

DOCTORAL THESIS

Reconstructing Physical Quantities from Sparse Measurements: Experimental Validation and Sensor-Based Inference in Hydraulic Environments

Wolf Iring Kösters

TALLINN UNIVERSITY OF TECHNOLOGY
DOCTORAL THESIS
30/2026

Reconstructing Physical Quantities from Sparse Measurements: Experimental Validation and Sensor-Based Inference in Hydraulic Environments

WOLF IRING KÖSTERS



TALLINN UNIVERSITY OF TECHNOLOGY
School of Information Technologies
Department of Computer Systems

The dissertation was accepted for the defence of the degree of Doctor of Philosophy on May 8, 2026

Supervisor: Prof. Maarja Kruusmaa,
Department of Computer Systems, School of Information Technologies,
Tallinn University of Technology
Tallinn, Estonia

Supervisor: Assoc. Prof. Stefan Hoerner,
Laboratoire des Écoulements Géophysiques et Industriels,
CNRS, Grenoble-INP, Université Grenoble-Alpes,
Grenoble, France

Supervisor: Assoc. Prof. Jeffrey A. Tuhtan,
Department of Computer Systems, School of Information Technologies,
Tallinn University of Technology
Tallinn, Estonia

Supervisor: Prof. Dominique Thévenin,
Institute of Fluid Dynamics and Thermodynamic,
Otto von Guericke University
Magdeburg, Germany

Opponents: Prof. Laurent David, University of Poitiers, Poitiers, France
Dr. Luiz Gustavo Martins da Silva, ETH Zürich, Zürich, Switzerland

Defence of the thesis: 13. May 2026, Tallinn

Declaration:

Hereby I declare that this doctoral thesis, my original investigation and achievement, submitted for the doctoral degree at Tallinn University of Technology, has not been submitted for any academic degree elsewhere.

Wolf Iring Kösters

signature

Copyright: Wolf Iring Kösters, 2026
ISSN 2585-6898 (publication)
ISBN ... (publication)
ISSN 2585-6901 (PDF)
ISBN 978-9916-80-502-2 (PDF)
<https://doi.org/10.23658/taltech.30/2026>

Kösters, W. I. (2026). *Reconstructing Physical Quantities from Sparse Measurements: Experimental Validation and Sensor-Based Inference in Hydraulic Environments* [TalTech Press]. <https://doi.org/10.23658/taltech.30/2026>

TALLINNA TEHNIKAÜLIKOOL
DOKTORITÖÖ
30/2026

**Füüsikaliste suuruste rekonstrueerimine
hõredatest mõõtmistest:
eksperimentaalne valideerimine ja
anduripõhine inferents hüdraulilistes
keskkondades**

WOLF IRING KÖSTERS



Contents

Glossary	7
List of Publications	9
Author's Contributions to the Publications	10
1 Introduction	1
1.1 Background and Motivation	1
1.1.1 Simultaneous Flow Measurement and Deformation Tracking	2
1.1.2 Design and Construction of an Experimental Blade Strike Rig	3
1.1.3 Evaluation of Strike Severity Metrics Derived from Sensor Probe Measurements	3
1.2 Research Questions	4
1.3 Structure of the Thesis and Contributions	5
2 Contribution I: Camera-Only Reconstruction of Flexible Hydrofoil Kinematics with Explicit Validity Bounds	11
2.1 Results & Discussion	12
2.2 Conclusions	15
3 Contribution II: An Open, Standardized Laboratory Platform for Reproducible Blade Strike Experiments	16
3.1 Results & Discussion	17
3.2 Conclusions	17
4 Contribution III: Systematic Evaluation of Strike Severity Models: Validity Bounds, Failures and Prospects for Improvement	21
4.1 Results & Discussion	22
4.2 Conclusions	26
4.3 My Contribution to the StrikeSense Project	26
5 Conclusion and Future Outlook	28
5.1 Context and Motivation	28
5.2 Flexible Hydrofoil Deformation	29
5.3 Fish-Friendly Hydraulic Design and the Strike Rig	29
5.4 Methodological Critique of the 95 g Threshold	31
List of Figures	33
List of Tables	33
References	38
Acknowledgments	39
Abstract	40
Kokkuvõte	41
A Appendix: Publications	42

A.1	Publication I	42
A.2	Publication II	60
A.3	Publication III	75
A.4	Publication IV	89
A.5	Publication V	107
A.6	Publication VI	121
	Curriculum Vitae	131
	Elulookirjeldus	132

Glossary

M_p metric

Strike severity metric based on the pressure time series proposed by Huang et al. (2025). (p. 24)

M_v metric

Strike severity metric based on the acceleration magnitude time series proposed by Huang et al. (2025). (p. 24)

2D2C

Two-dimensional, two-component measurement configuration capturing two in-plane velocity components. (p. 7)

95g-metric

3-axis acceleration magnitude threshold metric proposed in Deng et al. (2010) to identify severe acceleration events using sensor probes. (p. 3, 4, 22, 24)

BDS Barotrauma detection system: sensor probe developed at the Tallinn University of Technology (EST). (p. 10, 21, 22, 24)

CFD Computational fluid dynamics: simulates fluid flow and related physical phenomena using numerical methods on a computer. (p. 29)

CFTT cross-flow tidal turbine (p. 5–7)

EPRI Electric Power Research Institute (p. 17, 20, 33)

FSI Fluid–structure interaction: studies how fluids and solid structures influence each other’s motion and forces. (p. 1, 2, 4, 8, 11–15, 29)

L/t ratio

Fish length to blade thickness ratio. (p. 17, 20)

MRI Magnetic resonance imaging: a technique that produces images based on the response of different materials to strong magnetic fields and radiofrequency waves. (p. 2)

NACA0018

Symmetric NACA four-digit series airfoil profile with 18 % maximum thickness at 30 % chord and zero camber. (p. 7)

ORNL

Oak Ridge National Laboratory (p. 17, 20, 33)

PIV Particle image velocimetry: measures flow velocity by tracking the motion of tracer particles in a fluid using sequential images. (p. 2, 5–8, 11–15, 29)

RAPID

Robust Autonomous Pressure and Inertial Device: sensor probe developed at the Tallinn University of Technology (EST). (p. 9, 10, 21, 22, 24, 25)

RETERO

Project name: "Reduktion von Tierversuchen bei Turbinenpassagen durch Einsatz von Roboterfischen, Strömungssimulationen und Vorhersagemodellen". Translates to: Reduction of animal testing in turbine passages through the use of robotic fish, flow simulations, and prediction models. (p. 16, 17, 29)

RQ1 How can physical models be used to evaluate the complete [fluid-structure interaction \(FSI\)](#) on a hyper-flexible body when only sparse optical input from flow field measurements is available? (p. 2, 4, 5, 15)

RQ2 How can a standardized experimental platform for simulated turbine blade strikes be designed to provide precise and repeatable conditions while serving as a broadly comparable basis for validating sensor-based strike severity metrics used to assess fish mortality risk in hydraulic machinery? (p. 3, 5, 17)

RQ3 To what extent can existing strike severity metrics applied to different sensor probes reliably infer blade strike velocity under controlled experimental conditions, and can a data-driven approach offer a more accurate alternative within the biologically relevant velocity range? (p. 4, 5, 26)

Sensor Fish

Sensor probe developed at the Pacific Northwest National Laboratory (USA). (p. 10, 21, 22, 24, 25)

SSIM

Structural similarity index: metric that compares two images by sliding a window across both and computing local statistics (mean, variance, covariance) at each position, yielding a single score from 0 to 1. (p. 7)

StrikeSense

Project to investigate the use of sensor probes with compliant bodies for strike velocity prediction of sensor probes. (p. 24, 26, 27)

TSR Tip-speed ratio: Ratio of the tangential velocity at the blade tip to the free-stream flow velocity. (p. 7)

UNSW probe

Sensor probe developed at the University of New South Wales (AUS). (p. 10, 22, 24)

List of Publications

The present Ph.D. thesis is based on the following publications that are referred to in the text by Roman numbers.

- I S. Hoerner, W. I. Kösters, L. Vignal, O. Cleynen, S. Abbaszadeh, T. Maître, and D. Thévenin (2021). “Cross-Flow Tidal Turbines with Highly Flexible Blades—Experimental Flow Field Investigations at Strong Fluid–Structure Interactions”. In: *Energies* 14.4, p. 797. DOI: [10.3390/en14040797](https://doi.org/10.3390/en14040797)
- II W. I. Kösters and S. Hoerner (Aug. 2023). “Simultaneous flow measurement and deformation tracking for passive flow control experiments involving fluid–structure interactions”. In: *Journal of Fluids and Structures* 121, p. 103956. DOI: [10.1016/j.jfluidstructs.2023.103956](https://doi.org/10.1016/j.jfluidstructs.2023.103956)
- III W. I. Kösters, J. A. Tuhtan, D. Efimov, M. Kruusmaa, and S. Hoerner (Sept. 2025a). “An open laboratory blade strike rig to evaluate the risk of injury and mortality to fish and to test passive sensors”. In: *Sustainable Energy Technologies and Assessments* 81, p. 104427. DOI: [10.1016/j.seta.2025.104427](https://doi.org/10.1016/j.seta.2025.104427)
- IV W. I. Kösters, J. A. Tuhtan, S. Hoerner, M. Kruusmaa, and S. Abbaszadeh (Oct. 2025b). “Sensor Probes for Fish Passage Safety: Evaluating Strike Severity Metrics and Data-Driven Prediction”. HAL: <https://hal.science/hal-05314322>. Submitted to the *Journal of Ecohydraulics*

Additional publications

- V S. Hoerner, W. I. Kösters, S. Abbaszadeh, F. Wagner, and J. A. Tuhtan (May 2024). “Towards a reliable and validated toolbox to replace live fish tests for the assessment of injury and mortality during downstream passage”. In: *IAHR 15th International Symposium on Ecohydraulics and Fish Passage*. Quebec City, Canada
- VI S. Hoerner, T. Bennecke, W. I. Kösters, K. Ruiz-Hussmann, A. Jayaprakash, S. Abbaszadeh, J. A. Tuhtan, P.-L. Delafin, C. Bonamy, and R. Leidhold (Aug. 2, 2025). “Experimental Determination of the Hydrodynamic Loading on Vertical-Axis Cross-flow Tidal Turbines with Blade Embedded Autonomous Sensors”. In: 7th International Conference on Ocean Engineering. Chennai, India

Author's Contributions to the Publications

Publication I I developed the masking software and its methodology, created the PIV processing setup scripts and performed the processing of the data.

Publication II I developed the methodology, implemented and validated it using synthetic data for which I also created the methodology and supporting software, visualized the results and wrote the original draft, followed by review and revision.

Publication III I designed the strike rig, organized material procurement, built and validated the setup with respect to precision and variability of the achieved strike velocities, conducted the experiments, managed data collection and curation, developed the processing software, prepared visualizations and wrote the original draft, followed by review and revision.

Publication IV I co-developed the methodology, carried out the experiments, improved the data processing software from the previous study, curated and analyzed the data, created visualizations and wrote the original draft, followed by review and revision.

Publication V I carried out the experiments, curated and analyzed the data and created visualizations based on that.

Publication VI I was involved in setting up the experiment and in data curation.

1 Introduction

1.1 Background and Motivation

Compact, field-deployable instruments known as sensor probes have become a vital tool in both research and industry, allowing unobtrusive observations and long-term monitoring of parameters in locations that are otherwise difficult to access. A common application is in environmental sensing, where probes are deployed to record quantities such as temperature, rainfall, or humidity (Chan et al. 2021). The slow temporal variability of these parameters places minimal demands on the data acquisition system, making low sampling rates preferable to extend battery life and maximize deployment duration. Other types of sensors, such as animal-borne movement trackers or probes used to monitor transient phenomena like seismic activity, require higher sampling rates and durable construction to withstand physical stress during deployment.

Passive sensor probes used to assess stressor exposure in hydraulic machinery such as pumps and turbines act as instrumented surrogate bodies that are entrained in the flow path and record time-resolved signals. These measurements, most commonly pressure, acceleration and angular velocity, form the basis for evaluating mortality risk for fish during passage (Carlson and Duncan 2003; Deng et al. 2007; Pauwels et al. 2020). Here, measurements refer to estimations of physical quantities under controlled conditions. Such probes face particularly demanding requirements, they must be highly robust to withstand harsh conditions involving high pressures and blade impacts that generate extreme accelerations, while simultaneously operating at sufficiently high sampling rates to capture these transient events with adequate fidelity. At the same time, they must approximate the size and shape of juvenile fish, typically around 15 cm in length, to represent the life stage most likely to encounter such hazards during downstream migration, as in salmon. Constraints on size and power consumption favor compact, low-power sensors with limited bandwidth and dynamic range, leading to sparse, noisy, or partially corrupted data that fail to capture the fast dynamics of *FSI*.

Here, sparsity denotes limited observability from low-dimensional measurements. In the cases studied in this thesis, this manifests in distinct ways: in the hydrofoil application, the body shape must be inferred from tracer particles whose local density can drop below 300 particles per $100 \text{ px} \times 100 \text{ px}$ in separated flow regions, providing only partial coverage of the body boundary. In the strike severity application, accelerometers sampling at 2048 Hz capture as few as two to four data points during impact events lasting less than 2 ms, while probes with lower sampling rates of 100 – 400 Hz may record only a single sample or miss the peak entirely.

Model-based inference, which in this work refers specifically to the estimation of unmeasured forces from measured kinematics by inverting a prescribed mechanical model of the system response, offers a way to overcome these limitations by reformulating the problem as a physics-constrained inverse problem. As force cannot practically be measured directly, reliably observable kinematic quantities are recorded and used together with governing physical equations or data-driven surrogate models to infer the underlying loads. The reliability of these inferred quantities depends strongly on the integrity of the available data, as saturated or undersampled signals can produce biased, truncated, or highly variable estimates.

This dissertation examines three cases in which insufficient or degraded measurements are compensated by reformulating the task as a physics-constrained inverse problem. In each case, a limited set of observable kinematic or geometric quantities is combined with governing mechanical models to reconstruct stressor exposure, deformation, or interfaces. While the applications differ, all contributions follow this shared inverse-modeling framework.

Three specific research gaps motivate the investigations presented in this thesis, each corresponding to a distinct application domain but unified by the challenge of extracting reliable information from incomplete measurements.

1.1.1 Simultaneous Flow Measurement and Deformation Tracking

The first research gap lies in the field of experimental fluid dynamics, specifically in the investigation of flow fields using [particle image velocimetry \(PIV\)](#). In this technique, tracer particles are seeded into the fluid, illuminated within a plane and their displacements between consecutive image frames are used to compute the velocity field. The experimental case focuses on a highly flexible hydrofoil that cannot be directly distinguished from the surrounding flow in optical images and is only detectable through the deflection of the surrounding tracer particles. In [PIV](#) analysis, a structure distorts the flow velocity measurements in its immediate vicinity, making it essential to mask the hydrofoil body. While for rigid bodies this mask can often be derived from single-point measurements and known geometry, the study of flexible bodies, which involves the coupled interaction between the structure and the surrounding flow, known as [FSI](#), requires a different approach, as single-point measurements are no longer sufficient.

Using the existing camera images for both masking and deformation estimation, without requiring additional deformation-specific measurement hardware, is strongly preferred because it greatly simplifies the experimental setup. However, this introduces a complex image segmentation challenge. While extensive research has been conducted on segmentation for gas-liquid interfaces ([Cardwell et al. 2011](#); [Gui et al. 1997](#); [Dussol et al. 2016](#); [Jeon and Sung 2011](#); [Weheliye et al. 2012](#); [Sanchis and Jensen 2011](#)), these methods have not yet been extended to the segmentation of flexible solid bodies within a flow field. Instead, alternative solutions have been developed that rely on external measurement systems, including stereoscopic camera setups with surface markers ([Tregidgo et al. 2013](#); [Nikoueeyan and Naughton 2018](#); [Fatiha et al. 2019](#)), laser line scanners ([Ducoin et al. 2012](#); [Kalmbach and Breuer 2013](#); [Akcabay et al. 2014](#)), or even [magnetic resonance imaging \(MRI\)](#)-based approaches ([Hessenthaler et al. 2017](#)).

Developing a method that enables the use of a single-camera setup for [PIV](#) analysis of flexible bodies would provide substantial benefits to the research community by simplifying experimental setups and simultaneously yielding data on both the structural response of the body and the surrounding flow. This integration would allow deformation measurement and mask generation to be achieved in a single step. This leads to the first research question:

RQ1: *How can physical models be used to evaluate the complete FSI on a hyper-flexible body when only sparse optical input from flow field measurements is available?*

1.1.2 Design and Construction of an Experimental Blade Strike Rig

The second research gap is concerned with the investigation of blade strike mortality in fish passing through hydraulic turbines and pumps. The current standard for quantifying this risk relies on live fish tests conducted at specific sites, yet these experiments provide only cumulative mortality outcomes that indicate survival or death. As a result, they are limited to site- and operation-specific conditions and offer little insight into the mechanisms of injury. Passive in-stream sensor probes have been developed to overcome this limitation, but despite their widespread use, the existing models that link probe measurements to strike severity remain unvalidated (Kösters et al. 2025a).

This lack of validation may be attributed to the difficulty of creating repeatable strike conditions within turbines. It is challenging to ensure that a sensor probe experiences identical impact conditions in successive strikes or to precisely characterize key parameters such as the relative strike velocity, which represents the difference between the blade speed and the velocity of the entrained probe within the turbine or pump. Drawing inspiration from barotrauma research, where both fish and sensor probes were subjected to identical isolated stressors to establish injury thresholds (Brown et al. 2012), progress in this area would require comparable strike tests on both sensors and live fish. Fortunately, such live fish strike experiments have already been conducted (Hecker et al. 2007; Saylor et al. 2020a) and preliminary tests using a biomimetic probe have also been reported (Saylor et al. 2021). However, no further research has since been carried out to validate or refine strike severity models.

One likely reason is the lack of suitable experimental facilities. Only two turbine blade strike rigs have been built in the past twenty years, both located in the United States (Hecker et al. 2007; Bevelhimer et al. 2019), with a recent additional design developed in China (Meng et al. 2022). These rigs are labor intensive to operate because they rely on open-loop control systems that require iterative recalibration whenever test conditions such as strike velocity are changed. To advance sensor-based strike severity modeling, the research community would greatly benefit from a standardized strike rig design that incorporates closed-loop velocity control and provides openly accessible design data and documentation. Such a setup would eliminate the need for iterative calibration, ensure repeatable impact conditions and enable consistent validation across laboratories. This leads to the second research question:

RQ2: How can a standardized experimental platform for simulated turbine blade strikes be designed to provide precise and repeatable conditions while serving as a broadly comparable basis for validating sensor-based strike severity metrics used to assess fish mortality risk in hydraulic machinery?

1.1.3 Evaluation of Strike Severity Metrics Derived from Sensor Probe Measurements

The third research gap concerns the missing validation of current strike severity metrics for passive in-stream sensor probes and the limited understanding of how sensitive these probes are to strike velocity, as well as how their responses compare across different probe designs. The *95g-metric* is currently the most widely used strike severity metric (Knott et al. 2023; Martinez et al. 2019a; Deng et al. 2010; Fu et al. 2016; Martinez et al. 2019b; Salalila et al. 2019). It classifies acceleration events as either collision or shear flow events

based on event duration and further grades their severity by acceleration magnitude, with accelerations between 25 – 50 g considered slight, between 50 – 95 g considered moderate and equal to or above 95 g classified as severe (Deng et al. 2010). In practice, however, most studies have used only the 95 g threshold to distinguish severe events from non-severe ones.

The original validation of this metric was performed using biological threshold tests on juvenile Chinook salmon (*Oncorhynchus tshawytscha*) that were exposed to turbulent shear flow created by water jets, while their body accelerations were recorded with a high-speed camera (Richmond et al. 2009). Sensor probes were then subjected to the same conditions. Although these thresholds were derived under shear flow exposure, they were later adopted to describe collision events in the *95g-metric* without further validation (Deng et al. 2010). More recently, the same research group introduced a revised metric that, after filtering for events above 95 g, analyzes either the pressure or acceleration time series to infer strike severity (Huang et al. 2025). The calibration of this updated metric was performed by comparing sensor data with live fish test results obtained at the same site, yet no validation of the method has been reported.

This reveals a clear research gap: although strike severity metrics are widely used to interpret sensor probe data, none have been validated under controlled strike conditions. Furthermore, the relationship between acceleration measurements obtained from different sensor probe designs has not been established, making it difficult to compare results across studies. The sensitivity and variance of sensor probe measurements to strike velocity is also unknown, preventing any meaningful assessment of measurement uncertainty. Finally, the adequate sampling rates and dynamic ranges required to accurately capture strike events have not yet been defined, even though establishing these parameters would greatly accelerate the development of improved sensor probes by clarifying the necessary technical specifications. This leads to the third research question:

RQ3: To what extent can existing strike severity metrics applied to different sensor probes reliably infer blade strike velocity under controlled experimental conditions, and can a data-driven approach offer a more accurate alternative within the biologically relevant velocity range?

1.2 Research Questions

The problem addressed in this thesis is that physically relevant quantities in hydraulic fluid–structure interaction systems, specifically structural deformation, flow-field geometry and blade strike severity, cannot be measured directly with available sensor hardware and the metrics currently used to infer them from indirect measurements have not been validated under controlled conditions. Solving this problem requires both novel physics-constrained reconstruction methods and controlled experimental platforms that enable their evaluation.

This challenge is addressed through the following research questions:

RQ1 *How can physical models be used to evaluate the complete FSI on a hyper-flexible body when only sparse optical input from flow field measurements is available?*

Answered by Publication II (section A.2), see fig. 2 for a summary. The method

addressing this question was first applied in Publication I (summarized in fig. 1) to enable PIV processing of a cross-flow tidal turbine (CFTT) with highly flexible blades and was subsequently formalized and evaluated as a standalone contribution in Publication II, which therefore serves as the basis for answering this research question.

RQ2 *How can a standardized experimental platform for simulated turbine blade strikes be designed to provide precise and repeatable conditions while serving as a broadly comparable basis for validating sensor-based strike severity metrics used to assess fish mortality risk in hydraulic machinery?*

Answered by Publication III (section A.3), see fig. 3 for a summary.

RQ3 *To what extent can existing strike severity metrics applied to different sensor probes reliably infer blade strike velocity under controlled experimental conditions, and can a data-driven approach offer a more accurate alternative within the biologically relevant velocity range?*

Answered by Publication III (section A.3) & IV (section A.4), see fig. 3 and fig. 4 for a summary.

1.3 Structure of the Thesis and Contributions

The main content of this dissertation is organized into chapters that address each of the three key research questions and their associated contributions.

Section 2 addresses RQ1, investigating how high-speed recordings acquired for velocity field measurements around a highly flexible hydrofoil can also be used to reconstruct the foil's shape. This enables both the analysis of the coupling between the flow field and the hydrofoil's deflection and the generation of a body mask required for the flow field investigation. The principal challenge lies in the fact that the hydrofoil is not directly visible and can only be inferred through the deflection of sparsely seeded tracer particles. In addition, the wake region contains fewer visible tracers and the trailing edge of the foil undergoes rapid, transient changes in deflection angle during vortex shedding events.

Section 3 focuses on the development of an experimental setup capable of performing simulated turbine blade strikes on passive in-stream sensor probes. These probes are used to investigate the hydraulic conditions and collision events occurring within hydroturbines that contribute to fish injury and mortality. Although strike severity metrics have been proposed for such sensors, they have not been validated, even though they are widely used to estimate fish mortality. To evaluate the validity of these metrics, controlled strike experiments on sensor probes must be conducted to establish dose-response relationships that can be compared with those obtained from live fish experiments. No such validation study has yet been performed, likely due to the high entry barrier associated with constructing a suitable experimental rig. By designing, building and freely publishing all design files, this work aims to close that gap, facilitating metric validation and improving the quality of future sensor probes and strike severity models.

Section 4 uses the developed experimental strike rig to conduct such an investigation of existing strike severity metrics, comparing the results with biological dose-response studies and analyzing the sensitivity of the metrics to strike velocity, which has been identified as the primary factor influencing strike mortality. Four state-of-the-art sensor probe designs were tested under identical conditions to evaluate their mutual comparability. Such cross-

comparability has not previously been established, which has limited the interpretability of results across studies employing different probe designs. The insights gained from these experiments enabled the formulation of concrete recommendations for future hardware improvements.

The contributions to the respective research fields presented in this dissertation are derived from two first-author publications and one submitted manuscript:

Contribution I

Introducing a physics-informed method that simultaneously generates hydrofoil masks and retrieves deformation directly from [PIV](#) image data, enabling integrated fluid–structure interaction analysis of highly flexible structures.

The method was first applied in Publication I (section [A.1](#) summarized in [fig. 1](#)) to enable the [PIV](#) analysis of a [CFTT](#) with highly flexible blades, where it served as an essential component of the experimental workflow. Publication II (section [A.2](#)) then formalized, evaluated and documented the method itself. Because Publication II subsumes the methodological content of Publication I, only Publication II is used to describe the contribution in section [2](#).

Contribution II

Developing and openly sharing a standardized experimental setup for precise and repeatable simulated turbine blade strikes, enabling systematic validation and refinement of sensor-based strike severity metrics for assessing fish mortality.

Emerged from Publication III (section [A.3](#)), described in section [3](#) and summarized in [fig. 3](#).

Contribution III

Demonstrating the shortcomings of established strike severity metrics across multiple sensor probes and releasing an open-access dataset from controlled blade strike experiments to support the future development of more accurate and reliable metrics.

Emerged from Publication III (section [A.3](#)) & IV (section [A.4](#)), described in section [4](#) and summarized in [fig. 3](#) and [fig. 4](#).

Finally, the conclusions, limitations, future perspectives and closing remarks are presented in section [5](#). The publications are included in section [A](#), with additional publications listed to demonstrate practical applications and the broader impact of this research beyond the primary scope of the thesis.

Objective

Investigate the influence of highly flexible blades on the flow field of a CFTT at the blade level, using an oscillating hydrofoil surrogate model in a water tunnel. The study aims to characterize the passive flow control mechanism achieved through blade flexibility by comparing the flow fields around rigid and flexible NACA0018 hydrofoils undergoing forced pitch oscillations representative of a CFTT operating at tip-speed ratio (TSR) of $\lambda = 2$ and solidity $\sigma = 1.5$, conditions that induce deep dynamic stall.

Materials & Methods

Experiments were conducted in a closed-loop water channel at the LEGI labs in Grenoble with a test section of 1000 mm \times 175 mm \times 280 mm and an inlet velocity of 3.5 m s⁻¹. A NACA0018 hydrofoil with 66 mm chord length ($Re \approx 250,000$) was pitched sinusoidally at 2.25 Hz following the angle-of-attack trajectory of a single CFTT blade at a TSR of $\lambda = 2$. Flexible hydrofoils were constructed as multi-material compounds with a rigid aluminum leading edge and a carbon-fiber composite skeleton embedded in silicone. Time-resolved 2D2C PIV at 4 kHz was performed using two continuous lasers and a high-speed camera (1280 \times 800px). Raw data were processed with the open-source toolbox fluidimage and validated against the commercial software DaVis. An adaptive masking algorithm was developed to handle the simultaneously moving and deforming structure. Flow field periodicity was quantified using the structural similarity index (SSIM) between instantaneous and phase-averaged velocity fields across 9 oscillation periods.

Results

The rigid hydrofoil exhibited deep dynamic stall with flow separation onset at a pitch angle of $\alpha = 24^\circ$ on the upstroke and maximum wake extent at $\alpha = 27^\circ$ on the subsequent downstroke and flow reattachment delayed until $\alpha = -6^\circ$ due to pronounced hysteresis. The flexible hydrofoil showed significantly reduced wake size and shortened periods of flow separation, attributed to structural adaptation that passively controls the flow through profile deformation. A chordwise flapping effect was observed during vortex shedding. The SSIM analysis revealed that the flexible hydrofoil produced substantially more periodic flow fields (mean SSIM of 0.953 ± 0.02) compared to the rigid reference (mean SSIM of 0.893 ± 0.04), indicating reduced chaotic wake behavior. The average velocity difference between the open-source and commercial PIV codes was approximately -0.02 m s⁻¹, less than 1% of the mean flow speed.

Contribution

I developed the masking software and its methodology, created the PIV processing setup scripts and performed the processing of the data. I was not involved in designing the experiment, acquiring the raw data, or supervising the study.

Figure 1: Summary of Publication I (Hoerner et al. 2021): “Cross-Flow Tidal Turbines with Highly Flexible Blades—Experimental Flow Field Investigations at Strong Fluid–Structure Interactions”.

Objective

Develop a physics-informed, camera-based workflow that uses high-speed video frames acquired for PIV to simultaneously generate two outputs: a time-resolved hydrofoil mask required for the flow-field analysis and the cross-sectional deformation of a highly flexible hydrofoil. Because the hydrofoil is dark-coated and not directly visible in the images, its shape is inferred indirectly from the deflection of illuminated tracer particles in the surrounding flow. The method incorporates Euler–Bernoulli beam theory kinematics together with the known hydrofoil geometry to infer deformation without requiring an additional measurement system, thereby avoiding interference with the flow field analysis in conditions where tracer density is low and signal-to-noise ratio is poor.

Materials & Methods

Experimental data captured in a closed water channel using a hydrofoil with a rigid leading edge and a flexible trailing section at $Re \approx 2 \times 10^5 - 2.5 \times 10^5$ was used in this study. The hydrofoil was subjected to forced pitching motions of $\pm 30^\circ$ that induced dynamic stall. Recordings were obtained at 4000 Hz. A kernel-based image processing pipeline provided an initial segmentation which was refined using a beam bending model, from which body masks were generated. The robustness of the algorithm beyond the experimental setup was assessed with synthetic data spanning different tracer densities and including a case where the spatial distribution represented a flow separation event. Final validation under experimental conditions was carried out with a rigid hydrofoil, for which the true position could be determined from motor feedback and compared with the predictions of the developed image recognition method.

Results

We validated our physics-informed image segmentation method on synthetic and experimental datasets and found that it reliably reconstructs hydrofoil deformation while simultaneously enabling flow field measurement from a single image source. On synthetic data, the method maintained robustness across seed densities of 200 – 750 particles per $100 \text{ px} \times 100 \text{ px}$, yielding a mean angular error measured between determined and real profile chord line of approximately 1° . Applied to rigid foil experiments, the mean absolute angular error was 0.84° , with an increase to 2° under static stall conditions. Overall, the results demonstrate that augmenting kernel-based image filtering with Euler–Bernoulli beam theory enables simultaneous and reliable measurement of flow fields and structural deformation within a single experimental framework.

Contribution

I developed the methodology, implemented and validated it using synthetic data for which I also created the methodology and supporting software, visualized the results and wrote the original draft, followed by review and revision. I was not involved in designing or setting up the experiment or collecting the data.

Figure 2: Summary of Publication II (Kösters and Hoerner 2023): “Simultaneous flow measurement and deformation tracking for passive flow control experiments involving fluid–structure interactions”. The method was first applied in Publication I (section A.1), as described in section 2.

Publication III (Contribution II & III)

Objective

This study introduces and validates an open-access laboratory strike rig with electronically controlled blade velocity, providing a reproducible platform for simulating turbine blade strikes on both fish and sensor probes. The objective is to establish standardized experimental conditions for assessing injury and mortality risks and for testing the reliability of sensor-probe-based strike severity metrics.

Materials & Methods

The strike rig was realized as a motor-driven linear motion system with closed-loop servo control, enabling strike velocities between 1 – 10 m s⁻¹. The design was benchmarked against earlier blade strike simulators and all construction files, data processing routines and the strike protocol are released as open-access resources. As a demonstration case, strikes were performed on the **RAPID**, a sensor probe that records three-dimensional acceleration up to 300 g per-axis at 2048 Hz, to evaluate the widely used 95 g acceleration threshold, which defines a severe acceleration event for fish as one exceeding this value.

Results

The rig achieved accurate and repeatable velocity control with precision more than an order of magnitude higher than that of blade strike rigs used in previous biological threshold tests, substantially improving upon earlier designs in both accuracy and usability. Tests with the sensor probe showed that even strikes at only 1 m s⁻¹ produced peak accelerations greater than 95 g, contradicting biological studies that report measurable mortality rates in the tested fish species beginning only at strike velocities of approximately 4 m s⁻¹ and above. These findings demonstrate that the 95 g acceleration criterion does not reliably reflect biological risk and acceleration thresholds alone are unreliable indicators of strike severity. Controlled rig experiments are necessary to develop and validate inference models linking sensor data to biological outcomes.

Contribution

I designed the strike rig, organized material procurement, built and validated the setup with respect to precision and variability of the achieved strike velocities, conducted the experiments, managed data collection and curation, developed the processing software, prepared visualizations and wrote the original draft, followed by review and revision.

Figure 3: Summary of Publication III (Kösters et al. 2025a): “An open laboratory blade strike rig to evaluate the risk of injury and mortality to fish and to test passive sensors”. The contribution is described in detail in section 3.

Publication IV (Contribution III)

Objective

This study assesses the capability of established and newly proposed sensor-based strike severity metrics to infer relative blade strike velocity within the biologically relevant range for fish mortality and compares the performance of different sensor probes to examine the cross-comparability of their measurements. In addition, it investigates a data-driven approach as an alternative for improving the inference of blade strike velocity.

Materials & Methods

Experiments were conducted using the strike rig described in Publication III. Four sensor probes ([Sensor Fish](#), [RAPID](#), [UNSW probe](#) and [BDS](#)) were subjected to 30 strikes each. The [Sensor Fish](#) and [RAPID](#) record accelerations up to 200 g and 300 g per axis at 2048 Hz, while the [UNSW probe](#) and [BDS](#) have dynamic ranges of 16 g at 400 Hz and 250 Hz respectively. Strikes began at 1 m s^{-1} and continued until probe failure. Acceleration and pressure signals were analyzed with three metrics designed to estimate strike severity from sensor data and evaluated by their sensitivity to blade strike velocity, as biological threshold studies identified blade strike velocity as the dominant contributor to mortality due to collisions (Saylor et al. 2020b). For the data-driven approach, a Gaussian naïve Bayes classifier was trained on tri-axial acceleration time series to predict strike velocity classes.

Results

All three metrics exhibited saturation between $3 - 4 \text{ m s}^{-1}$, which prevented reliable discrimination between strikes associated with negligible mortality at 4 m s^{-1} and those causing near-complete mortality at 10 m s^{-1} . Measurements from the tested sensor probes differed substantially, indicating that metrics must be adapted to the specific probe system. The data-driven classifier predicted relative blade strike velocities over the range $1 - 10 \text{ m s}^{-1}$ with reasonable accuracy under laboratory conditions, although its transferability to turbine environments remains uncertain. The findings demonstrate that current metrics are unsuitable for field deployment and suggest that future probe designs may require either enhanced sampling rates and dynamic range or flexible bodies that prolong the duration of impact events.

Contribution

I co-developed the methodology, carried out the experiments, improved the data processing software from the previous study, curated and analyzed the data, created visualizations and wrote the original draft, followed by review and revision. The machine learning model, along with the corresponding text and figures in the manuscript, was developed by another contributor.

Figure 4: Summary of Publication IV (Kösters et al. 2025b): "Sensor Probes for Fish Passage Safety". The contribution is described in detail in section 4.

2 Contribution I: Camera-Only Reconstruction of Flexible Hydrofoil Kinematics with Explicit Validity Bounds

This chapter presents a physics-informed, camera-only method that simultaneously reconstructs hydrofoil deformation and generates body masks from PIV image data, eliminating the need for dedicated external measurement hardware.

PIV is an optical measurement technique widely employed to resolve instantaneous flow fields by seeding the fluid with tracer particles and recording their motion under laser illumination using high-speed cameras, yielding velocity vector fields such as those shown in fig. 6. The velocity field is reconstructed through cross-correlation of particle displacements between successive frames, which requires homogeneous seeding within the phase of interest. When additional phases or solid bodies such as hydrofoils or bubbles are present, they introduce spurious vectors in and around the phase, thereby corrupting the velocity field. Masking is therefore essential to remove non-seeded regions prior to correlation, ensuring that only true particle displacements contribute to the velocity calculation.

The state of the art in masking such regions can be divided into two methodological families. The first employs dedicated hardware operated alongside the PIV system to track deformation. While capable of providing accurate deformation measurements, this approach requires additional specialized equipment. Examples include laser line profiling (Ducoin et al. 2012; Kalmbach and Breuer 2013; Akcabay et al. 2014), which yields precise one-dimensional surface reconstructions, photogrammetry, where multiple cameras track body markers to reconstruct the three-dimensional shape of the body (Tregidgo et al. 2013; Nikoueeyan and Naughton 2018; Fatiha et al. 2019) and structured light techniques (Hoerner and Bonamy 2019). However, these methods involve complex setups, post-processing, or incompatibility with PIV when reflective surfaces are required.

The second family of methods applies image segmentation directly to PIV frames, a strategy extensively studied for bubble flows (Gui et al. 1997; Cardwell et al. 2011; Sanchis and Jensen 2011; Jeon and Sung 2011; Weheliye et al. 2012; Dussol et al. 2016). Bubble segmentation is facilitated by their bright reflective boundaries, which appear as luminous regions in images, while the gas-liquid interface is difficult to resolve through external measurement techniques. At the time of Publication III, however, this approach had not been transferred to masking solid bodies, where the problem is fundamentally different. Bodies are coated with non-reflective paint to prevent optical interference with PIV, rendering them nearly invisible except for the deflection of tracer particles, posing a challenge to a computer vision system akin to the Kanisza triangle, shown in fig. 5a. This challenge is compounded by non-uniform tracer seeding from flow separation and unavoidable internal reflections of the body.

The contribution of this work is the development of a camera-only solution in a PIV application field that has traditionally relied on external measurement setups for mask generation. By adapting morphological filtering techniques originally developed for bubble segmentation (Dussol et al. 2016) and embedding them within a physics-informed beam bending model, the method enables body masks to be generated directly from PIV frames. This approach not only provided accurate masking of the highly flexible hydrofoil but also, through the incorporation of structural physics, allowed two-way coupled FSI analyses of fluid flow and structural deformation. This capability is of particular importance for the

study of highly flexible structures which undergo large deformation.

The practical need for this method arose during the investigation of cross-flow tidal turbines with highly flexible blades, reported in Publication I (Hoerner et al. 2021). In that study, I developed and applied the masking software to enable PIV processing of the turbine flow field, which required accurate identification of the deforming blade at each time step. This application demonstrated the utility of the approach but also revealed the need for a formal validation framework, which motivated the systematic study presented in Publication II.

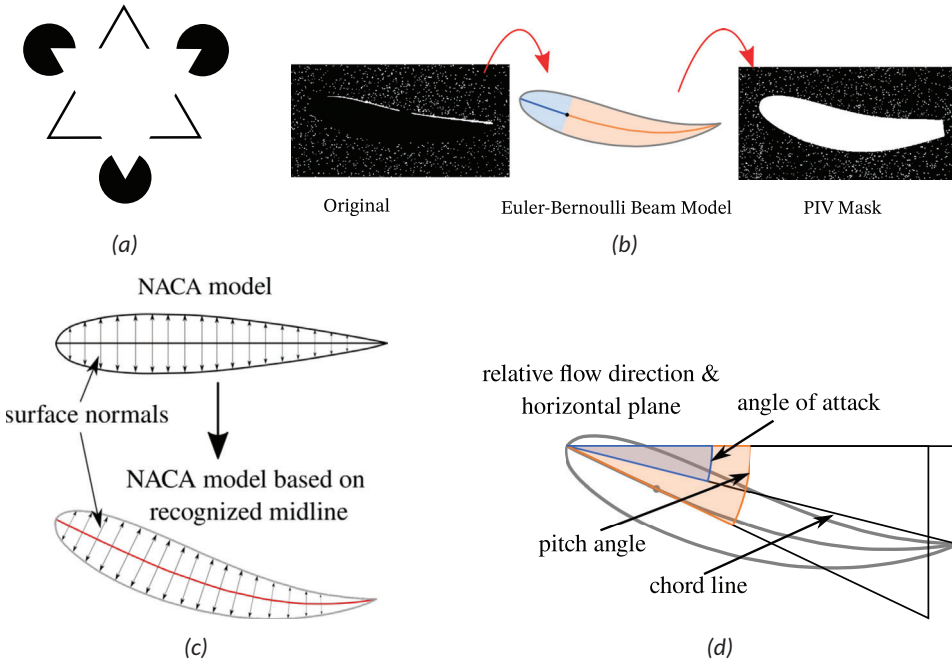


Figure 5: (a): Kanizsa triangle illustrating the segmentation challenge — clearly perceived by humans but difficult for computer vision to detect. (b): Processing workflow from high-speed image with enlarged tracer particles (first panel), through mean line extraction and beam model with third-degree polynomial deformation (second panel; orange/blue: flexible/rigid regions; black dot: pitching pivot), to PIV mask extended toward the trailing edge for three-dimensional deformation (third panel). (c): Reconstruction combining undeformed geometry with the deformed mean line via surface normals. Deformation reduces the effective angle of attack, defined relative to the fluid velocity vector. (d): Effective angle of attack used as response variable for FSI evaluation.

2.1 Results & Discussion

The developed method first stacks consecutive image frames to increase tracer particle density, then applies kernel-based image processing to segment the hydrofoil by exploiting the difference in illumination density between the foil body and the surrounding fluid. From the segmented body, a mean line is extracted and fitted using an Euler–Bernoulli beam model that assumes a third-degree polynomial bending characteristics from a distributed pressure load, thereby smoothing the mean line, as shown in fig. 5b. To reconstruct the

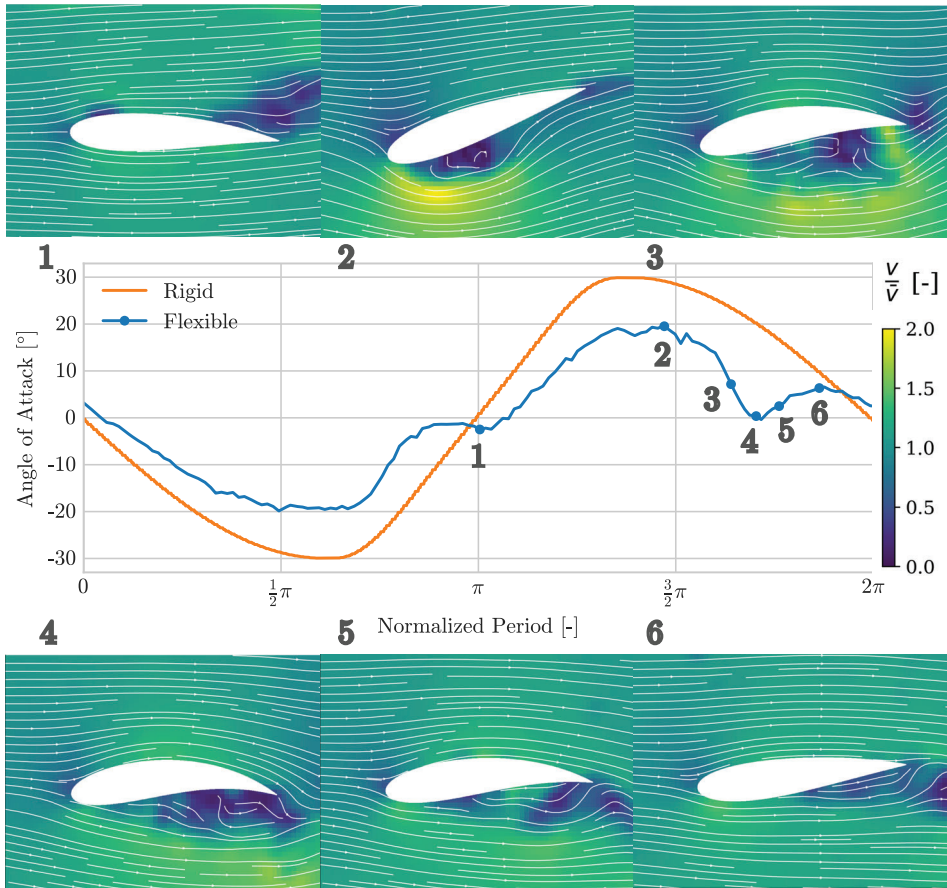


Figure 6: Combined *FSI* and *PIV* analysis from a single image source, showing the deformed foil body together with the surrounding deviation of the mean fluid velocity. A hypothetical rigid blade, shown in orange, is compared with the flexible blade, shown in blue, to illustrate the extent of deformation. The numbers 1 to 6 in the graph correspond to the images displayed above and below. Due to deformation, the effective pitch angles of the flexible blade remain below those of the rigid blade and between images 2 and 4 a flapping motion is observed that results from low pressure associated with the dynamic stall event. Reprint from Kösters and Hoerner (2023).

body geometry, surface normals are computed along the undeformed mean line of the original geometry and then applied to the deformed mean line, yielding the deformed body shape illustrated in fig. 5c. The resulting deformation causes a reduction in the effective angle of attack, which was used both as a response variable in subsequent FSI analysis and as a measure of the method's performance. This angle, defined as the inclination between the leading and trailing edges relative to the fluid velocity vector, is shown in fig. 5d.

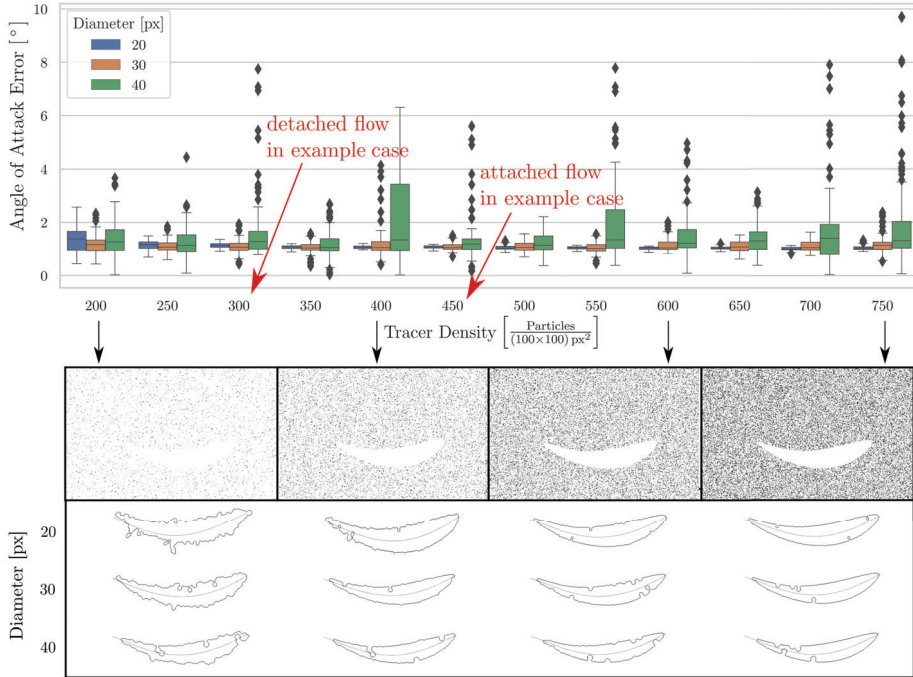


Figure 7: Error as a function of uniform tracer density estimated from synthetic data. The effect of summation kernel size is shown: a diameter of 30 performs better at low tracer density, while smaller kernels perform better at high seeding. Below, raw images and corresponding segmented foil outlines are shown for different kernel diameters and seeding densities. Red arrows mark the average tracer densities observed in experiments for attached and detached flow. Tracer particles are visually enlarged for clarity.

The results demonstrate that a physics-constrained segmentation of single camera PIV frames can recover the neutral axis and produce masks with sufficient fidelity to enable simultaneous flow and deformation analysis as shown in fig. 6, as validated through synthetic benchmarks and two experimental cases. Furthermore, the method was an essential component in a subsequent, more detailed FSI investigation, in which I performed the PIV postprocessing using the described approach (Hoerner et al. 2021), included among the additional publications in section A.1. On synthetic images, the algorithm maintained high accuracy across a wide range of seeding densities when the kernel diameter was appropriately chosen, as quantified by intersection over union and root mean square error. The error in angle of attack, defined as the angle between the leading and trailing edges, was close to one degree. This performance reflected a tradeoff between summation window size and particle density, as illustrated in the bottom of fig. 7, where the effect was systematically evaluated using synthetic data. Stacking consecutive frames improved

segmentation by increasing tracer density, though at the cost of temporal resolution proportional to the number of frames stacked. In a rigid foil validation with active pitching between ± 30 deg, where the body could be fully reconstructed from the pitching angle and the known geometry, the mean absolute error of the angle was approximately 0.84° , with a periodic bias that grew under detached flow and increased internal reflections. Under the worst case of static stall conditions, the error increased to about 2° . Although this is higher than the accuracy achieved by the structured light method applied to measure the deformation of highly flexible hydrofoils in the same setup, this approach relies on projecting light onto the surface and therefore requires a separate experimental setup that is incompatible with PIV measurements.

2.2 Conclusions

This work was able to give an answer to RQ1: *How can physical models be used to evaluate the complete FSI on a hyper-flexible body when only sparse optical input from flow field measurements is available?* by introducing a camera-only masking approach for deformable bodies in recordings intended for PIV analysis, eliminating the need for dedicated external measurement systems traditionally used to obtain structural deformation data. By adapting morphological image filtering techniques originally developed for multiphase flow segmentation and embedding them within a physics-based beam bending model, the method enables robust mask generation directly from single-camera frames. The results demonstrated that the proposed physics-constrained segmentation can accurately recover the neutral axis of a flexible hydrofoil and produce masks of sufficient fidelity to perform simultaneous FSI analyses from a single image source. Validation against synthetic benchmarks and controlled experiments confirmed that the method maintains high accuracy across a broad range of seeding densities, with angular errors on the order of one degree under dynamic motion and approximately 2° under especially challenging static stall conditions. While its accuracy is lower than systems with dedicated deformation-measurement hardware, with a mean angular error of 0.84° compared to 0.01° for a reference system, the presented method requires no additional hardware and remains fully compatible with PIV operation. It therefore provides a simple way to simultaneously measure the structural deformation of flexible hydrofoils and the surrounding flow field with a single measurement, helping with the analysis of FSI experiments, soft actuation or flexible underwater robotics.

3 Contribution II: An Open, Standardized Laboratory Platform for Reproducible Blade Strike Experiments

This chapter describes the design, construction and validation of an open-access strike rig that delivers reproducible simulated turbine blade strikes, enabling systematic evaluation of sensor-based strike severity metrics.

Hydropower plays a central role in renewable electricity generation by providing both base-load supply and grid stabilization, compensating for fluctuations in the output of other renewable sources (Vagnoni et al. 2024). However, it exerts substantial ecological pressure on river systems by fragmenting habitats and causing injury or mortality to fish that pass downstream through turbines, where a meta-analysis of 295 experiments from Europe and North America involving more than 275,000 fish reported an average mortality rate of 22% per turbine (Radinger et al. 2022). Because individual fish often encounter multiple turbines during migration, cumulative mortality may surpass species replacement rates, potentially leading to local population collapse (Van Treeck et al. 2021).

Although the European Union's Water Framework Directive requires Member States to maintain or restore river continuity as part of achieving good ecological status (The European Union 2000), current assessment standards continue to rely on live fish experiments as reflected in the Dutch Norm (Nederlandse Norm 2020) and a European standard which is underway (Deutsches Institut für Normung 2024). These experiments are costly and ethically problematic as they require exposing fish to extremely hazardous conditions, illustrated by a remark in the methodology of one such study noting that "in the case of decapitated or incomplete individuals, the number of fish was determined only by counting the number of heads" (Pauwels et al. 2024).

To address these limitations, researchers have developed computational models and passive in-stream sensor probes that record pressure, acceleration and rotation to characterize hydraulic conditions and infer strike severity (Carlson and Duncan 2003; Deng et al. 2007; Deng et al. 2014; Salalila et al. 2019; Pauwels et al. 2020; Saylor et al. 2021; Cox and Felder 2025; Salalila et al. 2025). However, the strike severity metrics used have not been directly validated against field observations of injury or mortality in live fish.

A commonly applied criterion, the 95 g threshold, designates accelerations above this threshold as indicative of severe acceleration events caused by collisions such as blade strikes or shear flow (Deng et al. 2010). However, while validated for shear-induced injuries in biological threshold studies (Richmond et al. 2009), this metric requires field validation, primarily due to the difficulty of reproducing controlled strike conditions in operational settings. To close this gap, we developed the **RETERO** strike rig, an open, electronically controlled laboratory platform capable of delivering reproducible simulated blade strikes at velocities between 1 – 10 m s⁻¹, shown in fig. 8. The design builds upon earlier strike rigs originally developed for live fish experiments, enhancing their functionality and precision while preserving sufficient similarity to ensure comparability between sensor-based and live fish strike experiments. In addition, we introduced a standardized strike protocol for sensor probe testing to enable consistent and reproducible experimental studies using the strike rig in future research.

Furthermore it can serve for the development of dose-response models for European fish

species, complementing existing data that to date concern only North American species. As all design files, rationale and cost estimates are openly accessible and detailed in Publication III (section A.4) (Kösters and Efimov 2025), the rig substantially lowers the entry barrier for conducting such studies. Consequently, it has the potential to expand the range of tested fish species, promote the design of more fish-friendly turbine blades and enhance the accuracy of sensor-based strike severity metrics, ultimately reducing reliance on live fish testing in the assessment of turbine-related mortality.

Additionally, we examined whether linear and rotary strikes yield comparable mortality outcomes in order to assess the comparability of strike-rig tests with live fish tests conducted on rotary strike rigs. To this end, we compared published live fish strike data for rainbow trout (*Oncorhynchus mykiss*) from Electric Power Research Institute (EPRI) (Amaral and Hecker 2008) and Oak Ridge National Laboratory (ORNL) (Saylor et al. 2020a) under overlapping conditions of fish length to blade thickness ratio (*L/t ratio*) and strike velocity.

3.1 Results & Discussion

The RETERO strike rig uses a servo-driven linear motion system with closed-loop control to set and maintain blade velocities between 1 – 10 m s⁻¹ and to actively compensate for the brief deceleration that occurs upon impact. This control strategy reproduces the behavior of a blade with substantially higher mass. The closed-loop design allows the blade strike velocity to be specified directly, representing an improvement over previous systems that required iterative calibration for each combination of blade and velocity. An overview of the trajectories across the entire velocity range is presented in fig. 9. These trajectories correspond to standard trapezoidal profiles in the time domain. The rig achieves highly repeatable blade strike velocities across the tested range of 1 – 10 m s⁻¹ with a maximum coefficient of variation of 0.12%, which is more than an order of magnitude lower than in earlier designs. Safety features are integrated into the setup, including a full enclosure and a hatch that permits operation only when securely closed. A clearance of 1 m from the ground enables the use of cameras with cost-effective lenses to record the strike event from below. Using existing biological threshold data for rainbow trout (*Oncorhynchus mykiss*) obtained from both rotary and linear strike rigs, we demonstrated that differences between rotary and linear strikes have no measurable effect on mortality outcomes. This was shown by comparing mortality rates across three overlapping experimental cases, which exhibited only minor discrepancies when controlling for *L/t ratio* and strike velocity, as summarized in fig. 10a and illustrated in fig. 10b. This result confirms that strike events in rotary machinery can be reliably approximated using linear blade strike experiments.

3.2 Conclusions

This contribution directly addresses RQ2: *How can a standardized experimental platform for simulated turbine blade strikes be designed to provide precise and repeatable conditions while serving as a broadly comparable basis for validating sensor-based strike severity metrics used to assess fish mortality risk in hydraulic machinery?* by introducing and validating a strike rig that replicates the experimental conditions of previous biological threshold studies and thereby enables the validation and further development of sensor-based blade strike severity metrics. It also facilitates continued refinement of sensor

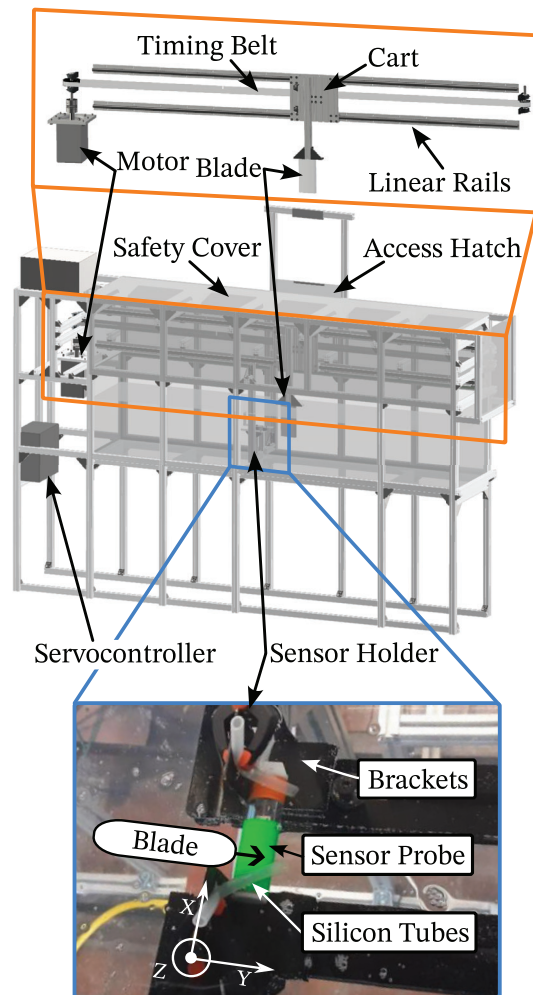


Figure 8: Rendered model of the strike rig with labeled components. During operation, the blade moves linearly from left to right and impacts the sensor probe mounted in the holder. To reduce drag and splashing, only the blade is submerged. At the end of its stroke, the blade decelerates to a predefined stop position governed by the servocontroller software. For safe handling, all moving parts are enclosed by acrylic glass, with an access hatch provided for inserting and removing sensor probes. The overall setup measures $3.84\text{ m} \times 0.72\text{ m} \times 2.61\text{ m}$ (length \times width \times height), while the basin itself is $3.04\text{ m} \times 0.58\text{ m} \times 0.69\text{ m}$. Below, a labeled photograph illustrates the sensor probe placement before a strike. Reprint from Kösters et al. (2025a).

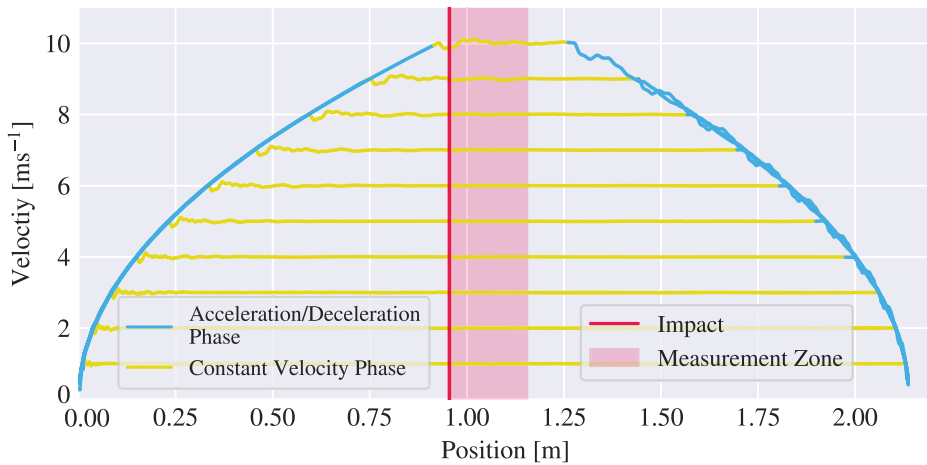
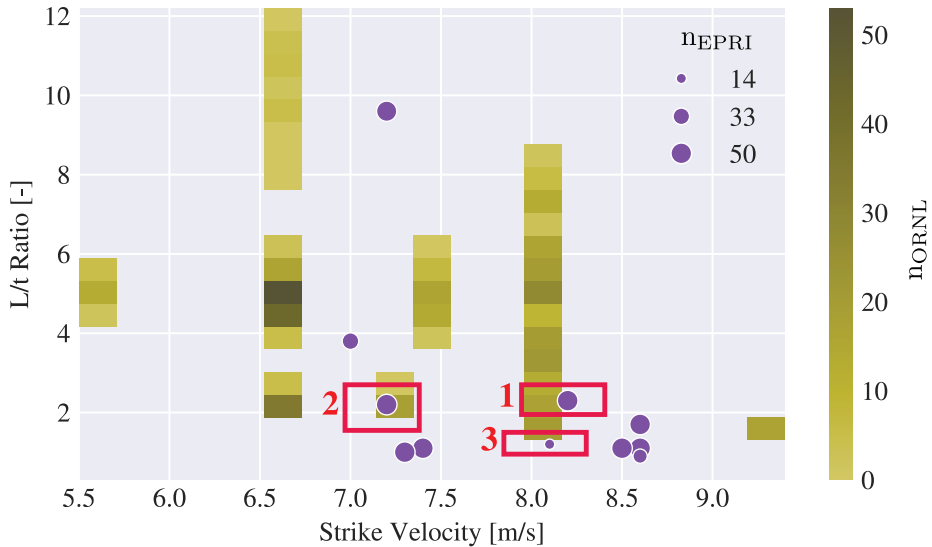


Figure 9: Blade velocity trajectories ranging from 1 – 10 m s⁻¹ without strike events across the full range of system motion. These trajectories follow standard trapezoidal velocity profiles in the time domain, where the trapezoid shape is defined by the selected stop position, acceleration, deceleration and target velocity, each of which is manually configured during motor setup. After this configuration, the operator only enters the desired strike velocity in the software for the experiments.

probe technology and the execution of threshold experiments on additional, ecologically relevant fish species. The introduction of a standardized strike protocol improves the cross-comparability of sensor strike experiments. In summary, this work provides an open-access tool designed to generate the biological threshold data required to estimate injury and mortality resulting from turbine blade strikes. It supports the advancement of fish-safe turbine designs and enhances the predictive reliability of sensor probes, offering biologists and engineers a more physically consistent understanding of the frequency and severity of blade strike events in hydropower systems worldwide.

	Strike Velocity [m/s]	L/t Ratio [-]	Amaral et al.				Bevelhimer et al.				Discrepancy [%pt.]
			n	Loc [%]	Orient [%]	Survival [%]	n	Loc [%]	Orient [%]	Survival [%]	
Box 1	7.8–8.6 (8.1)	2.0–2.7 (2.3)	50	4 H 74 M 22 T	64 L 22 D 14 V	32.0	20	10 H 90 M 0 T	100 L 0 D 0 V	30.0	2.0
				21 H 65 M 15 T	65 L 25 D 10 V	78.0	20	0 H 95 M 5 T	100 L 0 D 0 V	75.0	
				0 H 71 M 29 T	93 L 0 D 7 V	92.9	16	0 H 0 M 100 T	100 L 0 D 0 V	93.8	
Box 2	7.0–7.4 (7.2)	1.6–2.7 (2.2)	50	65 M 15 T 0 H	25 D 10 V 93 L	78.0	20	95 M 5 T 0 H	0 D 0 V 100 L	75.0	3.0
Box 3	7.9–8.3 (8.1)	1.0–1.5 (1.2)	14	71 M 29 T	0 D 7 V	92.9	16	0 M 100 T	0 D 0 V	93.8	0.9

(a) Table comparing experiments with overlapping conditions identified in fig. 10b, with the mean values reported by Amaral et al. in brackets. Strike location, reported as head (H), mid-body (M) and tail (T) and fish orientation, as lateral (L), dorsal (D) and ventral (V).



(b) Strike experiments conducted at EPRI as purple circles and ORNL shown in yellow, with overlapping experiments within the red boxes.

Figure 10: Comparison of blade strike experiments on rainbow trout conducted in the ORNL and EPRI studies across three overlapping experimental conditions. Individual ORNL results are shown as purple circles, averaged EPRI results as a yellow heatmap. For L/t ratio comparison, minimum and maximum values reported by EPRI were used. A 5% tolerance band around reported strike velocities defined overlap. Despite differences in strike location and fish orientation (summarized in the table), mortality rates show only minor discrepancies.

4 Contribution III: Systematic Evaluation of Strike Severity Models: Validity Bounds, Failures and Prospects for Improvement

This chapter uses the strike rig developed in the previous contribution to evaluate existing strike severity metrics across four sensor probe designs, revealing fundamental measurement limitations and proposing directions for improved probe design.

This contribution builds upon the previous one by using the developed strike rig to investigate the performance of current sensor probes designed to assess hydraulic conditions in turbines and pipe systems. The study evaluates their ability to capture the mechanics of blade strike impacts and examines the predictive capacity of existing strike severity metrics for fish mortality, focusing on their sensitivity to strike velocity, which has been identified as the primary driver of strike-induced mortality after accounting for species-specific effects (Saylor et al. 2020b).

Passive in-stream sensor probes such as the [Sensor Fish](#), the [RAPID](#) and the [BDS](#) were developed as a desired replacement for live fish tests, which remain the standard approach to assess fish passage risk in hydraulic machinery. Although live fish experiments can reliably quantify overall mortality risk, they present major limitations. Most importantly, they provide only cumulative mortality data across an entire structure, making it difficult to identify the specific mechanisms or sites of injury. This limitation hinders the development of more fish-friendly designs and requires that each site be tested under multiple operating conditions, which is prohibitively expensive and ethically problematic, particularly for endangered species such as the European eel.

Passive in-stream sensor probes typically integrate pressure sensors, gyroscopes and accelerometers (Carlson and Duncan 2003; Deng et al. 2007; Deng et al. 2014; Salalila et al. 2019; Pauwels et al. 2020; Saylor et al. 2021; Cox and Felder 2025; Salalila et al. 2025). Because pressure patterns during turbine passage can be matched with specific regions within the machine, these measurements allow researchers to localize recorded events and differentiate between potential causes of injury (Hou et al. 2018). This capability supports cross-site comparisons and provides valuable validation data for computational models used in turbine design (Romero-Gomez et al. 2024). However, the measurements do not directly yield mortality or injury rates; instead, they must be interpreted through metrics or models derived from live fish studies where exposure to specific stressors and the biological response were recorded.

This approach has been successfully applied to barotrauma, which occurs when fish experience pressures much lower than their acclimation level, leading to swim bladder rupture and decompression sickness (Brown et al. 2014). By studying the maximum rate of pressure change from a certain acclimatization point for injury in controlled barochamber experiments, researchers established criteria for evaluating turbine and pump safety (Stephenson et al. 2010; Boys et al. 2016; Yang et al. 2023; Pflugrath et al. 2021). Similarly, mortality associated with shear flow was investigated by exposing fish to controlled water jets and correlating their body accelerations with observed injuries (Deng et al. 2005). Although this methodology was originally developed for shear flow, the same thresholds have since been applied to evaluate blade strike exposure (Deng et al. 2010), despite the absence of a direct validation for impact events. Nevertheless, this metric, known as the 95 g threshold, has been widely adopted for interpreting strike severity (Knott et al. 2023; Martinez et al.



Figure 11: Photograph showing the four sensor probes evaluated in this study arranged side by side with a caliper included for scale. From left to right the probes are the UNSW probe, Sensor Fish, RAPID and BDS. A foam element is affixed to the UNSW probe to achieve neutral buoyancy, while colored tape markers are attached to the RAPID (orange) and BDS (green) probes to facilitate retrieval during field deployments. The pressure transducers are positioned on the upper surface of the UNSW probes, RAPID and BDS probes, whereas on the Sensor Fish the pressure port is oriented toward the camera.

2019a; Deng et al. 2010; Fu et al. 2016; Martinez et al. 2019b; Salalila et al. 2019).

Using the strike rig which entailed the previous contribution described in section 3, this last contribution provides such a validation, determining whether a simple threshold-based metric can in principle describe strike severity and testing an updated version proposed by Huang et al. (2025). In addition, the data is used to explore whether a data-driven model can accurately predict strike velocity and to identify design limitations in current sensor probes that must be addressed to achieve improved measurements.

We obtained four different sensor probe designs developed by three research groups, shown in fig. 11, with their respective physical and measurement specifications summarized in table 1. This collection enables an assessment of cross-comparability among their measurement results, as the relationship between the published acceleration values from the different probes has not yet been determined.

4.1 Results & Discussion

First, the 95g-metric was evaluated by subjecting the RAPID sensor probe to strikes at a velocity of 1 m s^{-1} . These strikes resulted in a median peak acceleration of 211 g, as shown in fig. 12, exceeding the threshold by 116 g and falling well within the range classified as severe according to the metric, where high mortality rates would be expected. To assess whether this prediction aligns with biological reality, we examined dose–response studies conducted on live fish, in which anesthetized individuals were exposed to controlled blade strikes at different velocities and the resulting mortality was modeled using logistic regression. These

Table 1: Table providing an overview of the sensors, including their physical characteristics and sensing modalities. The vertical bar separates the high acceleration sensor probes on the left from the low acceleration sensor probes on the right.

	Sensor Fish	RAPID	UNSW Sensor	BDS
Sensing modalities	total water pressure linear acceleration rate of rotation magnetic field	total water pressure linear acceleration	total water pressure linear acceleration	total water pressure linear acceleration rate of rotation magnetic field
Dimensions [mm]	cylindric, 89.9x24.5	cylindric, 100x25	cuboid, 34x26x14	cylindric, 140x40
Mass [g]	42	46	15	147
Sampling rate [Hz]	2048	2048 (acceleration) 100 (pressure)	400 (acceleration) 250 (pressure)	100 or 250 (acceleration) 100 (pressure)
Dynamic range (+/-)	± 200 g 0-12 bar ± 2000 deg/s	± 400 g 0-2 bar	± 16 g 0-14 bar	± 16 g 0-2 bar ± 2000 deg/s

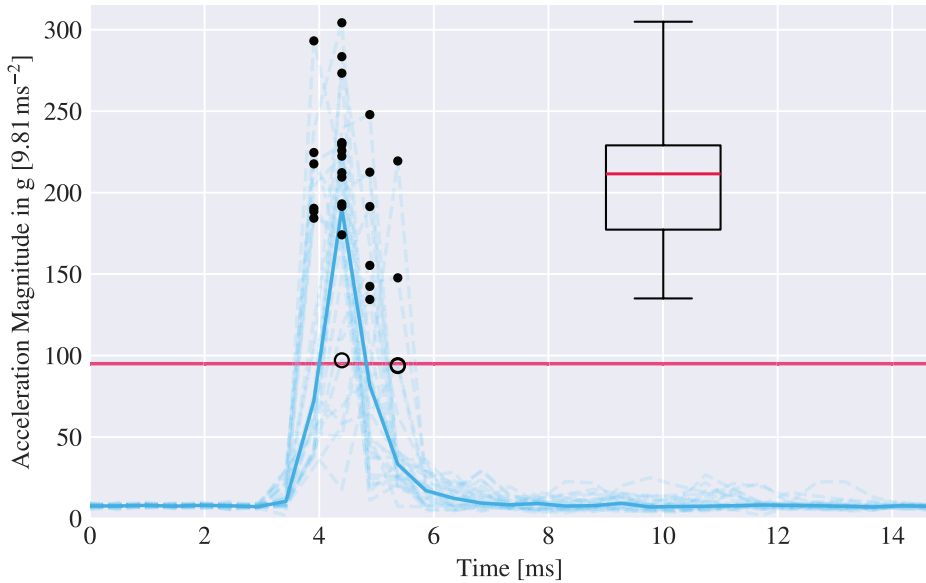


Figure 12: Acceleration time series for strikes at 1 m s^{-1} are displayed as transparent dashed blue lines ($n = 30$), with the median trace shown as a solid blue line. Black dots mark the peak acceleration of each individual strike, demonstrating that all measured values exceeded the 95 g threshold at 1 m s^{-1} . The distribution of these peak values is summarized in the box-whisker plot on the right, where whiskers extend to 1.5 times the interquartile range and outliers are shown as open circles. The median peak acceleration is 211 g , with the maximum reaching 304 g . In all but one strike the 95 g threshold was surpassed, highlighted by the horizontal red line. Post-impact accelerations are attributed to the flow disturbances generated by the blade wake. Reprint from Kösters et al. (2025a).

studies found no measurable mortality in any of the tested fish species below 4 m s^{-1} (Saylor 2021). Consequently, no mortality should occur at 1 m s^{-1} , indicating that the **95g-metric** does not provide accurate estimations of strike severity. These results were first presented at the International Symposium on Ecohydraulics and Fish Passage in Quebec, the leading global conference in this research field. The work attracted considerable interest from other researchers and led to the publication of a conference paper (Hoerner et al. 2024), as listed in section A.5.

Second, we investigated whether a higher acceleration threshold might yield better correspondence by subjecting the **RAPID** and **Sensor Fish** probes to strikes over the range $1 - 10 \text{ m s}^{-1}$ and recording their peak acceleration values. The results, presented in the upper panel of fig. 13, show that acceleration measurements saturate between $3 - 4 \text{ m s}^{-1}$, below the biological mortality threshold of 4 m s^{-1} and exhibit considerable variance and overlap throughout the velocity range. Therefore, peak acceleration cannot provide a reliable prediction of strike severity using the tested probes.

Third, the recently proposed **M_v metric** by Huang et al. (2025) was tested, which derives strike severity from the acceleration time series, as illustrated in the middle panel of fig. 13. This metric also saturates between $3 - 4 \text{ m s}^{-1}$, similar to the peak acceleration results. The accompanying **M_p metric**, which estimates strike velocity based on pressure time series, showed no clear correlation with strike velocity, as seen in the lower panel of fig. 13. The **RAPID** probe was excluded from this analysis due to its low sampling frequency of 100 Hz, which was insufficient to accurately capture the pressure dynamics. The **BDS** and **UNSW probe** were likewise unable to resolve strike events adequately because of their limited sampling rate and dynamic range.

Lastly, based on the observed failure modes and the measurement capabilities of each probe relative to their hardware specifications, I was able to formulate clear recommendations for future sensor design. Although rigid probes are easier to manufacture using conventional techniques, their short, high-intensity acceleration responses make accurate measurement difficult and pose challenges for mechanical robustness. None of the tested sensors survived strikes above 10 m s^{-1} and only the **RAPID** withstood a few such events before failing.

Measuring peak acceleration as a proxy for strike severity appears impractical in rigid sensor probes, as no small-scale commercial accelerometers offer the required dynamic range. Even if they did, the necessary sampling frequency would need to be at least an order of magnitude higher to capture the peak. Using the relationship between strike velocity and acceleration time series, a supervised machine learning algorithm was trained on the acceleration data of all axes and was able to predict strike velocity with reasonable accuracy (Kösters et al. 2025b). However, it remains uncertain how this approach would perform in real turbine environments where flow and strike conditions are more complex.

Future improvements should therefore focus on lengthening the impact duration by employing soft materials, which would reduce the need for extremely high sampling rates and wide dynamic ranges.

I contributed in a project dedicated to the development of such next-generation soft sensor probes (**StrikeSense**) under the guidance of Dr. Shokoofeh Abbaszadeh. The goal of this project is to design soft probes with enhanced capability to capture strike

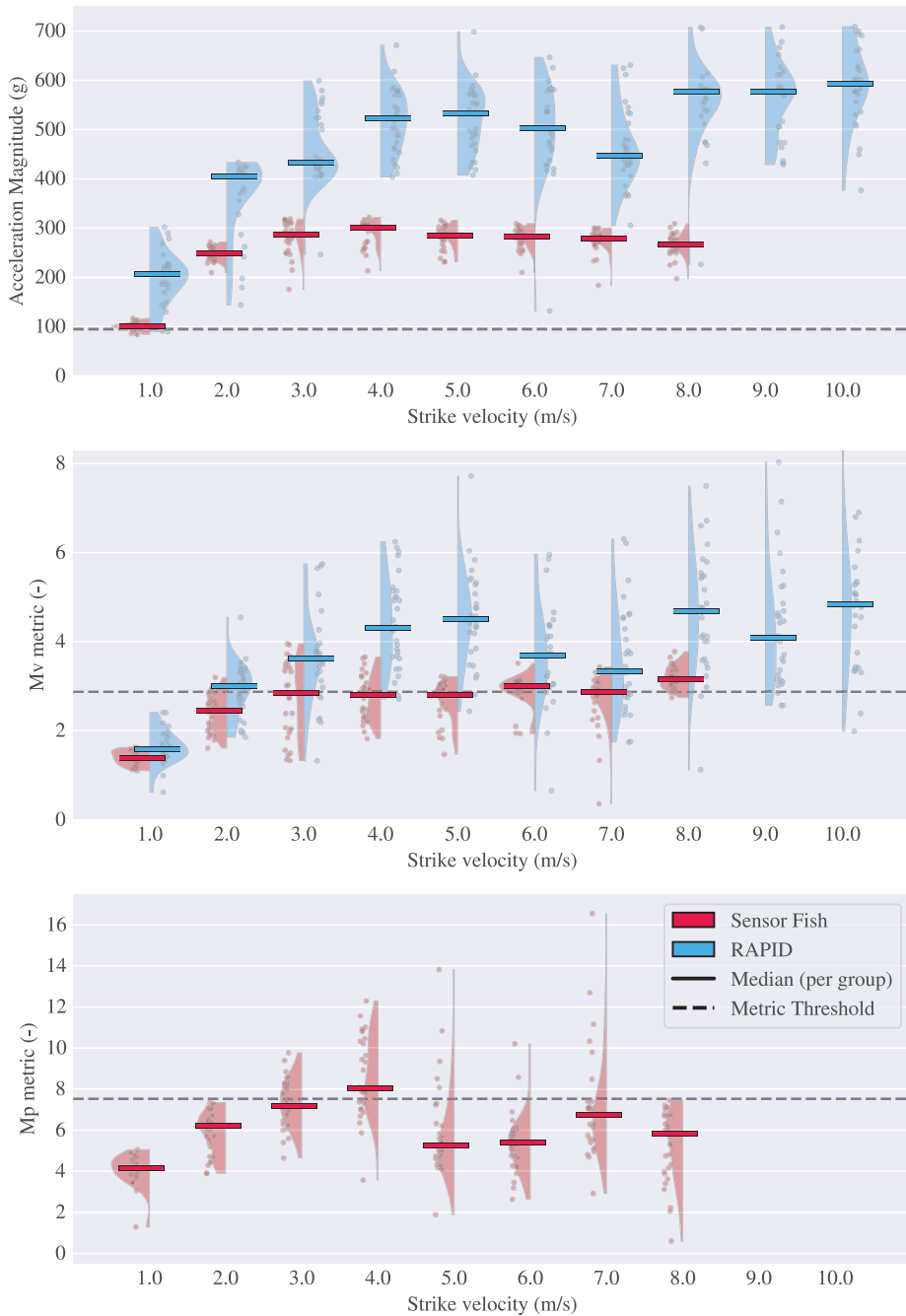


Figure 13: Peak acceleration magnitude, M_V and M_P metrics for the *Sensor Fish* and *RAPID* probes. Distributions are shown as violin plots using kernel density estimation, truncated at the outermost data points. Colored bars indicate group medians. Dashed lines mark published mortality thresholds: 95 g (peak acceleration), 2.87 (M_V) and 7.52 (M_P). The historically applied 95 g threshold for peak acceleration is included for reference. A conservative mortality threshold corresponds to approximately 4 m s^{-1} relative strike velocity. The *Sensor Fish* probe failed above 8 m s^{-1} and the *RAPID* above 10 m s^{-1} . Due to its 100 Hz pressure sampling frequency, the *RAPID* probe lacked sufficient resolution for M_P and was excluded from that analysis.

events accurately. Indeed, even the simple peak acceleration metric exhibited a clear, approximately linear relationship with strike velocity between $1 - 8 \text{ m s}^{-1}$, followed by saturation and increased variance at 8 and 9 m s^{-1} , as shown in fig. 14a. Additionally, probes incorporating strain gauges were developed to measure the rate and extent of bending, allowing the combined effects of blade thickness and impact velocity on strike severity to be assessed. Figure 14b presents a second-order polynomial regression between the maximum voltage deflection relative to steady state and the strike velocity. The quadratic term reflects the physical saturation of the bending response, which is limited by the maximum achievable deformation of the probe body.

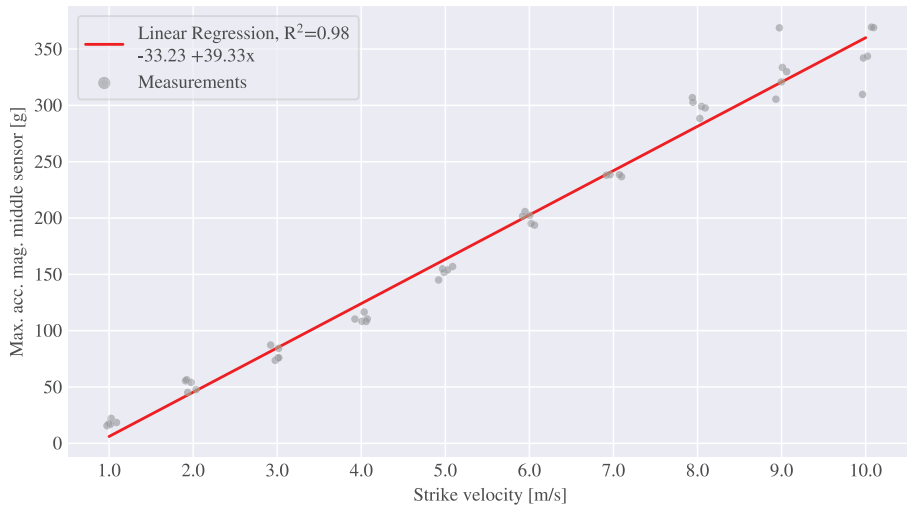
4.2 Conclusions

Based on the results of the study it can be said conclusively that current and newly introduced metrics to assess strike severity on the basis of passive in-stream sensor probes cannot assess strike severity of fish species tested so far in biological threshold tests. The data collected also served as a basis for a supervised machine learning model that could accurately predict strike velocity within the isolated setup of the strike rig. Moreover, the experience gained with testing the sensor probes led to concrete suggestions on the improvement of the sensor probes that would lead to better quality data. It thereby answers RQ3 conclusively and directly which states: *To what extent can existing strike severity metrics applied to different sensor probes reliably infer blade strike velocity under controlled experimental conditions, and can a data-driven approach offer a more accurate alternative within the biologically relevant velocity range?*.

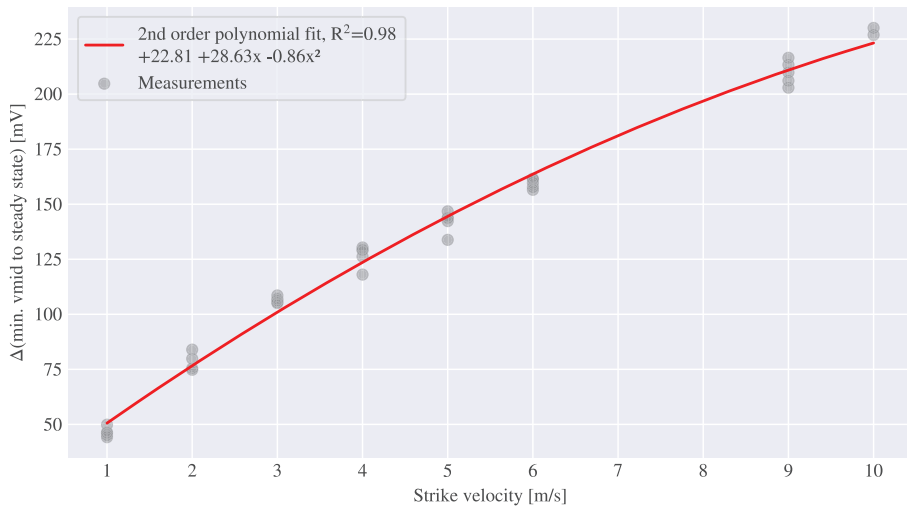
These findings motivated the development of next-generation sensor probes using compliant materials, to which I contributed as part of a dedicated project ([StrikeSense](#)).

4.3 My Contribution to the StrikeSense Project

Within the [StrikeSense](#) project, I was responsible for investigating different design variants of compliant strain gauge and accelerometer based sensor probes, with a focus on achieving appropriate stiffness for the tested velocity range and ensuring mechanical robustness of both the probe body and its electronic components, including cables, under large deformations. The use of compliant probe bodies extends the time scale over which acceleration occurs, which reduces peak acceleration magnitudes and mitigates bandwidth truncation and intersample peak loss. This principle was previously demonstrated by Saylor et al. (2021) and has seen further development in more recent work by Salalila et al. (2025). Early trials conducted within this project support this reasoning, showing clear differentiation across the tested strike velocity range when evaluating mid-body peak acceleration magnitude in the accelerometer based probe, as shown in fig. 14a and when assessing maximum bending in the strain gauge based probe, quantified as the maximum voltage difference between the undeformed state and the bent state, see fig. 14b.



(a) Peak acceleration magnitude in relation to strike velocity for a soft sensor probe with a hardness rating of Shore 16A with embedded accelerometers showing a clear linear relationship. Only the center acceleration magnitude is shown. The increase in variance at 8 and 9 m s^{-1} may be due to accelerometer saturation.



(b) Polynomial regression of the voltage difference of the middle strain gauge compared to the steady state in relation to strike velocity. Strike velocities of 7 and 8 m s^{-1} were excluded because of corrupted data. The sensor probe broke at 10 m s^{-1} after two recorded trials. The positive linear relationship is reduced by a negative 2nd degree component, likely a result of physical saturation of the degree of bending.

Figure 14: Preliminary strike tests on future sensor probes developed within the [StrikeSense](#) project with the measured quantity in relation to strike velocity.

5 Conclusion and Future Outlook

5.1 Context and Motivation

Across three conceptually connected studies in fluid mechanics, this dissertation examines how physics-informed, model-based reconstruction can extend what standard measurement systems reveal by deriving specific unmeasured quantities from incomplete image and sensor data. The cases encompass hydrofoil deformation together with its time-resolved fluid–structure interface geometry and acceleration-based estimators of turbine blade-strike severity. In each study, sparse measurements are paired with kinematic constraints to obtain physically admissible estimates, which both improves the interpretability of the underlying experiments and clarifies the limits imposed by partial observability.

This challenge cannot be met by relying solely on raw measurement quality. Instead, it requires the development of models capable of filtering noise and interpolating undersampled data in a physically meaningful way. Building and applying such models is therefore essential for extracting useful information from compact field-deployable sensors, especially when measuring transient events.

Compact, field-deployable instruments have become essential across a wide range of research areas, industrial applications and environmental monitoring efforts. They provide simple and efficient means of measuring quantities at specific locations over extended periods with minimal setup effort. For slowly varying environmental parameters such as temperature or humidity, the focus lies on maximizing deployment time and battery efficiency by using longer sampling intervals. Other types of probes, such as biologgers that record animal behavior and vital signs, or geophones that detect seismic activity, require much higher sampling rates to capture transient events and avoid missing important behavioral or seismic patterns. At the upper end of sampling rate requirements lie applications in predictive maintenance, where acceleration signals, acoustic emissions, or other vibration patterns are monitored to detect early signs of wear or failure before they cause damage or unplanned downtime. These sensors are often permanently integrated into the structure being monitored and form part of a larger sensor network with a centralized data acquisition system. This concept has since been adopted in hydromachinery research, where vertical hydraulic turbines present significant challenges due to cyclic vortex shedding caused by their rotation. Measuring these resulting vibrations is of considerable interest for the assessment of turbine loading. I contributed to this research by applying my expertise in sensor probe technology and helped incorporate them into the turbine blade, which led to the publication of a conference paper (Hoerner et al. 2025), included among the additional publications in section [A.6](#).

The study of fish passage through hydraulic machinery such as turbines and pumps presents a particularly demanding case. The relevant events, including turbine blade strikes, are highly transient, while the sensor probes must be small enough to mimic juvenile fish, extremely durable to withstand high pressures and accelerations and with a sampling rate and dynamic range high enough to capture these events with sufficient fidelity to assess injury and mortality risk. At the same time, they must remain cost-effective, since a large number of probes are often deployed simultaneously and may be lost during experiments due to uncertain field conditions.

In this dissertation, two cases were examined where sparse data were successfully rendered interpretable through the use of physics-informed modeling approaches.

5.2 Flexible Hydrofoil Deformation

In the study of highly flexible hydrofoils, an image-based method was developed that demonstrated how both deformation and masking information can be obtained directly from the motion of flow tracers. This approach allowed for a substantially simplified setup for generating [PIV](#) masks, which are essential for reconstructing the flow field, while simultaneously enabling the analysis of the coupled [FSI](#) behavior of flexible blades. By reducing experimental complexity, the method facilitates the study of flexible structures that combine high fatigue resistance with passive load shedding and contributes to the broader advancement of experimental research in the expanding field of [FSI](#).

The method is only suited for cases where the body has sufficient thickness. It is not applicable to very thin elastic sheets, which are more appropriately studied using existing techniques such as laser line scanning, as demonstrated by Kalmbach and Breuer (2013). In cases where there is a sharp change in light intensity, simpler image-based approaches that do not require physical modeling, such as those proposed by Dussol et al. (2016), may be more suitable. However, for the more complex case of deflection in highly flexible blades, the results indicate that sophisticated stereoscopic systems that track surface markers to reconstruct a three-dimensional model may not be necessary when the study focuses on two-dimensional deformation. As a logical next step, the proposed method could be validated directly and quantitatively for flexible structures, for example through laser interferometry along the trailing edge following Ducoin et al. (2012), or by using laser triangulation techniques such as those implemented by Kalmbach and Breuer (2013).

5.3 Fish-Friendly Hydraulic Design and the Strike Rig

In the area of fish-friendly hydraulic design, passive in-stream sensor probes are increasingly used to characterize hydraulic conditions within turbines and pumps as an alternative to live fish tests. Unlike live fish experiments, which provide only cumulative mortality outcomes after recapture, sensor probes record stressors such as pressure and acceleration at specific locations in the flow, allowing researchers to identify critical regions and mechanisms of injury. The use of sensors also addresses ethical and financial concerns associated with live testing, which would otherwise need to be repeated for every site, operating condition and species to yield reliable assessments regarding the local fish population. In addition, sensor data support the validation of [computational fluid dynamics \(CFD\)](#) simulations that accelerate the design of fish-safe hydraulic machinery. A persistent challenge, however, lies in linking sensor measurements to mortality outcomes across species.

To address this challenge, controlled strike experiments have been developed to simulate turbine blade impacts under isolated and repeatable laboratory conditions (Hecker et al. 2007; Bevelhimer et al. 2019). All rely on iterative calibration procedures that make them time-consuming to operate and difficult to reproduce consistently across measurement campaigns. By designing, constructing and openly publishing all design data, rationale and performance results of the [RETERO](#) rig, this work has significantly lowered the barrier to

systematically investigating strike severity metrics and assessing untested fish species.

Furthermore, using published strike data we could show that, in terms of strike mortality for the most commonly studied fish species, Rainbow trout (*Oncorhynchus mykiss*), the outcomes obtained with the new rig are fully compatible with biological threshold tests conducted using earlier designs. Although the rig is theoretically capable of performing live fish tests, it has not yet been used for this purpose. Such experiments would likely require modifications to the setup to regulate water quality parameters. For long-bodied species such as eels, the current basin width of 0.58 m may be insufficient, necessitating a redesign to accommodate a wider test chamber.

The strike rig is designed to deliver impacts up to 10 m s^{-1} , which results in complete mortality for all tested species except the American eel (*Anguilla rostrata*), which has been shown to survive strikes up to 13.6 m s^{-1} with a mortality rate of 13 % (n=90). Several modifications would be required to extend the rig's capability to eel testing:

- A wider test chamber to accommodate long-bodied species, as the current basin width of 0.58 m is insufficient.
- A more powerful servo drive, since the current system can provide only 30 A out of a possible 50 A at 400 V.
- A larger primary belt pulley to maintain operation within the motor's optimal torque range.
- Structural re-evaluation for mechanical strength under the increased load.

Another potential improvement lies in reducing the accelerated mass, particularly the sledge, which would shorten the travel length used for acceleration and deceleration. However, unless the diameter of the primary belt pulley—currently optimized for 10 m s^{-1} is increased, such a modification would mainly extend the duration of motion at maximum velocity rather than substantially increasing the attainable strike speed.

To facilitate further development, the model used for designing the strike rig has been made openly available on Github ¹. The repository includes updated measured parameters from the completed rig, enabling future researchers to make informed design and performance decisions when developing their own blade strike rigs.

Using this rig, a series of controlled experiments was conducted on existing sensor probes to assess the accuracy of current strike severity metrics used to estimate fish mortality in hydraulic machinery. The systematic evaluation revealed that prevailing metrics fail to predict strike severity within biologically relevant velocity ranges because the probes undersample the fast impact dynamics and saturate at higher loads. Some probes also exhibited mechanical fragility, failing at strike velocities as low as 2 m s^{-1} . These insights have guided the development of a new generation of sensor probes that employ soft or compliant materials to extend the duration of acceleration events, thereby reducing the required sampling rate and dynamic range—key steps toward miniaturization and cost efficiency.

¹<https://github.com/ikoesters/srdatacombiner>

To support continued progress in this field, the complete strike dataset comprising more than 750 individual experiments has been released as an open-access resource. This dataset allows other researchers to independently verify the findings and develop data-driven inference methods, continuing the open-science tradition established by Saylor et al., who publicly released their live fish strike dataset and thereby made a major contribution to the evaluation of the 95 g threshold, as discussed in Publication III (section A.3) (Kösters et al. 2025a).

5.4 Methodological Critique of the 95 g Threshold

During the investigation of strike severity thresholds, a broader and more concerning issue emerged: the most widely used metric, the 95 g threshold, had gained a false reputation of validity through repeated use in numerous studies. Despite this widespread adoption, none of these studies were designed to test or potentially falsify the validity of the metric, even though it was known to have never been properly validated. The repeated application of an unverified method in field experiments created an illusion of reliability, as the results have neither been challenged nor compared in a controlled way. This kind of methodological reinforcement, where an untested assumption becomes accepted as fact through repetition has also been observed in other scientific disciplines, including human behavioral research (West and Burton-Chellew 2025). The authors of that study cynically used “The emperor’s new clothes” as a memorable reference, drawing on Hans Christian Andersen’s tale to highlight this problem.

A similar pattern can be seen in more recent work by the same research group (Huang et al. 2025), where the metric score was derived from time-series data and a mortality threshold was defined as the value corresponding to 97.75% of the observed probability density function, based on live fish tests conducted at the same site. However, this percentile coincides with the sensor’s saturation limit, so the threshold value is determined by clipping rather than by the magnitude of the physical impact itself. As a result, the assigned severity level reflects the sensor’s measurement limit rather than a validated physical quantity. The physical validity of this metric was assumed without verification and consistency with two additional tests showing similar mortality rates was presented as proof of accuracy. The reason that these metrics have stood unchallenged may lie in the fact that realistic, controlled and repeatable strike tests are extremely difficult to perform and the only reason the strike rig can deliver consistent and measurable blade strikes is because it operates in a highly controlled, simplified environment far removed from real turbine conditions.

If acceleration-based strike-severity metrics are treated as precise without demonstrable validation, as shown by their repeated uncritical use documented earlier in this thesis, they risk producing misleading conclusions and, when used to inform turbine design or assessment strategies, contribute to unnecessary fish mortality in hydropower systems.

This work therefore establishes two necessary conditions for acceleration-based strike-severity metrics:

1. They must demonstrate predictable and low-variance responses to controlled impact velocities in an isolated blade-strike setup.
2. Only after satisfying this basic criterion can such metrics be assumed to reflect strike severity in the far more complex conditions of a turbine.

List of Figures

1	Summary of Publication I	7
2	Summary of Publication II	8
3	Summary of Publication III	9
4	Summary of Publication IV	10
5	Publication II: Segmentation challenge and foil tracking methodology	12
6	Publication II: Illustration of a combined FSI and PIV analysis	13
7	Publication II: Method's error estimation	14
8	Publication III: RETERO strike rig schematic	18
9	Publication III: Blade velocity trajectories	19
10	Comparison of ORNL and EPRI blade strike experiments on rainbow trout ..	20
11	Publication IV: Picture of all tested sensor probes side-by-side	22
12	Publication III: Sensor probe acceleration time series at 1 m s^{-1}	23
13	Publication IV: Sensitivity of strike metrics to relative blade velocity	25
14	Preliminary strike tests on soft sensor probes	27

List of Tables

1	Publication IV: Table providing an overview of their respective physical and measurement specifications	23
---	---	----

References

- Akcabay, D. T., E. J. Chae, Y. L. Young, A. Ducoin, and J. A. Astolfi (2014). "Cavity induced vibration of flexible hydrofoils". In: *Journal of Fluids and Structures* 49. DOI: [10.1016/j.jfluidstructs.2014.05.007](https://doi.org/10.1016/j.jfluidstructs.2014.05.007) (cit. on pp. 2, 11).
- Amaral, S. V. and G. E. Hecker (2008). "Evaluation of the effects of turbine blade leading edge design on fish survival". In: *Electric Power Research Institute* 1014937 (cit. on p. 17).
- Bevelhimer, M. S., B. M. Pracheil, A. M. Fortner, R. Saylor, and K. L. Deck (2019). "Mortality and injury assessment for three species of fish exposed to simulated turbine blade strike". In: *Canadian Journal of Fisheries and Aquatic Sciences* 76.12. DOI: [10.1139/cjfas-2018-0386](https://doi.org/10.1139/cjfas-2018-0386) (cit. on pp. 3, 29).
- Boys, C. A., W. Robinson, B. Miller, B. Pflugrath, L. J. Baumgartner, A. Navarro, R. Brown, and Z. Deng (2016). "A piecewise regression approach for determining biologically relevant hydraulic thresholds for the protection of fishes at river infrastructure". In: *Journal of Fish Biology* 88.5. DOI: [10.1111/jfb.12910](https://doi.org/10.1111/jfb.12910) (cit. on p. 21).
- Brown, R. S., B. D. Pflugrath, A. H. Colotelo, C. J. Brauner, T. J. Carlson, Z. D. Deng, and A. G. Seaburg (2012). "Pathways of barotrauma in juvenile salmonids exposed to simulated hydroturbine passage: Boyle's law vs. Henry's law". In: *Fisheries Research* 121-122. DOI: [10.1016/j.fishres.2012.01.006](https://doi.org/10.1016/j.fishres.2012.01.006) (cit. on p. 3).
- Brown, R. S., A. H. Colotelo, B. D. Pflugrath, C. A. Boys, L. J. Baumgartner, Z. D. Deng, L. G. M. Silva, C. J. Brauner, M. Mallen-Cooper, O. Phonekhampeng, G. Thorncraft, and D. Singhanouvong (2014). "Understanding Barotrauma in Fish Passing Hydro Structures: A Global Strategy for Sustainable Development of Water Resources". In: *Fisheries* 39.3. DOI: [10.1080/03632415.2014.883570](https://doi.org/10.1080/03632415.2014.883570) (cit. on p. 21).
- Cardwell, N. D., P. P. Vlachos, and K. A. Thole (2011). "A multi-parametric particle-pairing algorithm for particle tracking in single and multiphase flows". In: *Measurement Science and Technology* 22.10. DOI: [10.1088/0957-0233/22/10/105406](https://doi.org/10.1088/0957-0233/22/10/105406) (cit. on pp. 2, 11).
- Carlson, T. J. and J. P. Duncan (2003). *Evolution of the Sensor Fish Device for Measuring Physical Conditions in Severe Hydraulic Environments*. PNNL-15708, 878148. Richland, WA (United States): Pacific Northwest National Lab. (PNNL). DOI: [10.2172/878148](https://doi.org/10.2172/878148) (cit. on pp. 1, 16, 21).
- Chan, K., D. N. Schillereff, A. C. Baas, M. A. Chadwick, B. Main, M. Mulligan, F. T. O'Shea, R. Pearce, T. E. Smith, A. Van Soesbergen, E. Tebbs, and J. Thompson (2021). "Low-cost electronic sensors for environmental research: Pitfalls and opportunities". In: *Progress in Physical Geography: Earth and Environment* 45.3. DOI: [10.1177/0309133320956567](https://doi.org/10.1177/0309133320956567) (cit. on p. 1).
- Cox, R. X. and S. Felder (2025). "Injury-free transport of fish through closed conduit components". In: *Journal of Ecohydraulics*. DOI: [10.1080/24705357.2025.2462296](https://doi.org/10.1080/24705357.2025.2462296) (cit. on pp. 16, 21).
- Deng, Z. D., T. Carlson, J. P. Duncan, and M. Richmond (2007). "Six-Degree-of-Freedom Sensor Fish Design and Instrumentation". In: *Sensors* 7.12. DOI: [10.3390/s7123399](https://doi.org/10.3390/s7123399) (cit. on pp. 1, 16, 21).
- Deng, Z. D., T. J. Carlson, J. P. Duncan, M. C. Richmond, and D. D. Dauble (2010). "Use of an autonomous sensor to evaluate the biological performance of the advanced turbine at Wanapum Dam". In: *Journal of Renewable and Sustainable Energy* 2.5. DOI: [10.1063/1.3501336](https://doi.org/10.1063/1.3501336) (cit. on pp. 7, 3, 4, 16, 21, 22).
- Deng, Z. D., G. R. Guensch, C. A. McKinstry, R. P. Mueller, D. D. Dauble, and M. C. Richmond (2005). "Evaluation of fish-injury mechanisms during exposure to turbulent shear flow". In: *Canadian Journal of Fisheries and Aquatic Sciences* 62.7. DOI: [10.1139/f05-091](https://doi.org/10.1139/f05-091) (cit. on p. 21).

- Deng, Z. D., J. Lu, M. J. Myjak, J. J. Martinez, C. Tian, S. J. Morris, T. J. Carlson, D. Zhou, and H. Hou (2014). "Design and implementation of a new autonomous sensor fish to support advanced hydropower development". In: *Review of Scientific Instruments* 85.11. DOI: [10.1063/1.4900543](https://doi.org/10.1063/1.4900543) (cit. on pp. 16, 21).
- Deutsches Institut für Normung (2024). *DIN EN 18110:2024-08: Wasserbeschaffenheit - Verfahren zur Ermittlung der Fischdurchgängigkeit von Wasserförderschnecken, Pumpen und Spiralturbinen, die in Pumpwerken und Wasserkraftwerken verwendet werden*. DOI: [10.31030/3555890](https://doi.org/10.31030/3555890) (cit. on p. 16).
- Ducoin, A., J. A. Astolfi, and J.-F. Sigrist (2012). "An experimental analysis of fluid structure interaction on a flexible hydrofoil in various flow regimes including cavitating flow". In: *European Journal of Mechanics-B/Fluids* 36. DOI: [10.1016/j.euromechflu.2012.03.009](https://doi.org/10.1016/j.euromechflu.2012.03.009) (cit. on pp. 2, 11, 29).
- Dussol, D., P. Druault, B. Mallat, S. Delacroix, and G. Germain (2016). "Automatic dynamic mask extraction for PIV images containing an unsteady interface, bubbles, and a moving structure". In: *Comptes Rendus Mécanique* 344.7. DOI: [10.1016/j.crme.2016.03.005](https://doi.org/10.1016/j.crme.2016.03.005) (cit. on pp. 2, 11, 29).
- Fatiha, M. A., B. Augier, F. Deniset, P. Casari, and J. A. Astolfi (2019). "Morphing Hydrofoil Model Driven by Compliant Composite Structure and Internal Pressure". In: *Journal of Marine Science and Engineering* 7.12. DOI: [10.3390/jmse7120423](https://doi.org/10.3390/jmse7120423) (cit. on pp. 2, 11).
- Fu, T., Z. D. Deng, J. P. Duncan, D. Zhou, T. J. Carlson, G. E. Johnson, and H. Hou (2016). "Assessing hydraulic conditions through Francis turbines using an autonomous sensor device". In: *Renewable Energy* 99. DOI: [10.1016/j.renene.2016.08.029](https://doi.org/10.1016/j.renene.2016.08.029) (cit. on pp. 3, 22).
- Gui, L., R. Lindken, and W. Merzkirch (1997). "Phase-separated PIV measurements of the flow around systems of bubbles rising in water". In: *ASME FEDSM*. Vol. 97. Citeseer (cit. on pp. 2, 11).
- Hecker, G. E., S. V. Amaral, and P. S. Stacy (2007). *Investigation of Hydro-Turbine Leading-Edge Shapes Favorable to Fish Survival*. 102561. Palo Alto, CA: Electric Power Research Institute (cit. on pp. 3, 29).
- Hessenthaler, A., N. R. Gaddum, O. Holub, R. Sinkus, O. Röhrle, and D. Nordsletten (2017). "Experiment for validation of fluid-structure interaction models and algorithms: Experiment for validation of fluid-structure interaction models and algorithms". In: *International Journal for Numerical Methods in Biomedical Engineering* 33.9. DOI: [10.1002/cnm.2848](https://doi.org/10.1002/cnm.2848) (cit. on p. 2).
- Hoerner, S., T. Bennecke, W. I. Kösters, K. Ruiz-Husmann, A. Jayaprakash, S. Abbaszadeh, J. A. Tuhtan, P.-L. Delafin, C. Bonamy, and R. Leidhold (2025). "Experimental Determination of the Hydrodynamic Loading on Vertical-Axis Cross-flow Tidal Turbines with Blade Embedded Autonomous Sensors". In: 7th International Conference on Ocean Engineering. Chennai, India (cit. on pp. 9, 28, 121).
- Hoerner, S. and C. Bonamy (2019). "Structured-light-based surface measuring for application in fluid-structure interaction". In: *Experiments in Fluids* 60.11. DOI: [10.1007/s00348-019-2821-3](https://doi.org/10.1007/s00348-019-2821-3) (cit. on p. 11).
- Hoerner, S., W. I. Kösters, S. Abbaszadeh, F. Wagner, and J. A. Tuhtan (2024). "Towards a reliable and validated toolbox to replace live fish tests for the assessment of injury and mortality during downstream passage". In: *IAHR 15th International Symposium on Ecohydraulics and Fish Passage*. Quebec City, Canada (cit. on pp. 9, 24, 107).
- Hoerner, S., W. I. Kösters, L. Vignal, O. Cleyne, S. Abbaszadeh, T. Maître, and D. Thévenin (2021). "Cross-Flow Tidal Turbines with Highly Flexible Blades—Experimental Flow

- Field Investigations at Strong Fluid–Structure Interactions”. In: *Energies* 14.4. DOI: [10.3390/en14040797](https://doi.org/10.3390/en14040797) (cit. on pp. 9, 7, 12, 14, 42).
- Hou, H., Z. D. Deng, J. Martinez, T. Fu, J. P. Duncan, G. Johnson, J. Lu, J. Skalski, R. Townsend, and L. Tan (2018). “A Hydropower Biological Evaluation Toolset (HBET) for Characterizing Hydraulic Conditions and Impacts of Hydro-Structures on Fish”. In: *Energies* 11.4. DOI: [10.3390/en11040990](https://doi.org/10.3390/en11040990) (cit. on p. 21).
- Huang, T., A. Salalila, A. Meyers, T. Fu, J. Martinez, H. Hou, and Z. D. Deng (2025). “Velocity- and pressure-based metrics for estimating strike injuries during fish passage through hydro turbines”. In: *Results in Engineering* 25. DOI: [10.1016/j.rineng.2025.104535](https://doi.org/10.1016/j.rineng.2025.104535) (cit. on pp. 7, 4, 22, 24, 31).
- Jeon, Y. and H. Sung (2011). “PIV measurement of flow around an arbitrarily moving body”. In: *Experiments in Fluids* 50.4. DOI: [10.1007/s00348-010-0855-7](https://doi.org/10.1007/s00348-010-0855-7) (cit. on pp. 2, 11).
- Kalmbach, A. and M. Breuer (2013). “Experimental PIV/V3V measurements of vortex-induced fluid–structure interaction in turbulent flow—A new benchmark FSI-PfS-2a”. In: *Journal of Fluids and Structures* 42. DOI: [10.1016/j.jfluidstructs.2013.07.004](https://doi.org/10.1016/j.jfluidstructs.2013.07.004) (cit. on pp. 2, 11, 29).
- Knott, J., M. Mueller, J. Pander, and J. Geist (2023). “Ecological assessment of the world’s first shaft hydropower plant”. In: *Renewable and Sustainable Energy Reviews* 187. DOI: [10.1016/j.rser.2023.113727](https://doi.org/10.1016/j.rser.2023.113727) (cit. on pp. 3, 21).
- Kösters, W. I. and D. Efimov (2025). *Blade Strike Data: Sensor Probes for Fish Passage Safety: Evaluating Strike Severity Metrics and Data-Driven Prediction*. DOI: [10.5281/zenodo.16876012](https://doi.org/10.5281/zenodo.16876012) (cit. on p. 17).
- Kösters, W. I. and S. Hoerner (2023). “Simultaneous flow measurement and deformation tracking for passive flow control experiments involving fluid–structure interactions”. In: *Journal of Fluids and Structures* 121. DOI: [10.1016/j.jfluidstructs.2023.103956](https://doi.org/10.1016/j.jfluidstructs.2023.103956) (cit. on pp. 9, 8, 13, 60).
- Kösters, W. I., J. A. Tuhtan, D. Efimov, M. Kruusmaa, and S. Hoerner (2025a). “An open laboratory blade strike rig to evaluate the risk of injury and mortality to fish and to test passive sensors”. In: *Sustainable Energy Technologies and Assessments* 81. DOI: [10.1016/j.seta.2025.104427](https://doi.org/10.1016/j.seta.2025.104427) (cit. on pp. 9, 3, 18, 23, 31, 75).
- Kösters, W. I., J. A. Tuhtan, S. Hoerner, M. Kruusmaa, and S. Abbaszadeh (2025b). “Sensor Probes for Fish Passage Safety: Evaluating Strike Severity Metrics and Data-Driven Prediction”. HAL: <https://hal.science/hal-05314322> (cit. on pp. 9, 10, 24, 89).
- Martinez, J., Z. D. Deng, C. Tian, R. Mueller, O. Phonekhampheng, D. Singhanoung, G. Thorncraft, T. Phommavong, and K. Phommachan (2019a). “In situ characterization of turbine hydraulic environment to support development of fish-friendly hydropower guidelines in the lower Mekong River region”. In: *Ecological Engineering* 133. DOI: [10.1016/j.ecoleng.2019.04.028](https://doi.org/10.1016/j.ecoleng.2019.04.028) (cit. on pp. 3, 21).
- Martinez, J., Z. D. Deng, P. Titzler, J. Duncan, J. Lu, R. Mueller, C. Tian, B. Trumbo, M. Ahmann, and J. Renholds (2019b). “Hydraulic and biological characterization of a large Kaplan turbine”. In: *Renewable Energy* 131. DOI: [10.1016/j.renene.2018.07.034](https://doi.org/10.1016/j.renene.2018.07.034) (cit. on pp. 3, 22).
- Meng, L., R. Chen, X. Wang, C. Y. Zhang, Y. Zheng, and Y. J. Tian (2022). “Turbine blade strike tests for evaluation and optimization of fish-friendly turbine”. In: *IOP Conference Series: Earth and Environmental Science* 1037.1. DOI: [10.1088/1755-1315/1037/1/012058](https://doi.org/10.1088/1755-1315/1037/1/012058) (cit. on p. 3).
- Nederlandse Norm (2020). *NEN 8775:2020 Fish safety - Method for the determination of the fish safety of pumps, Archimedean screws and confined water turbines used in pumping stations and hydroelectric plants* (cit. on p. 16).

- Nikoueeyan, P. and J. W. Naughton (2018). "A photogrammetric approach for masking particle image velocimetry images around moving bodies". In: *Measurement Science and Technology* 29.10. DOI: [10.1088/1361-6501/aad9c8](https://doi.org/10.1088/1361-6501/aad9c8) (cit. on pp. 2, 11).
- Pauwels, I. S., R. Baeyens, G. Toming, M. Schneider, D. Buysse, J. Coeck, and J. A. Tuhtan (2020). "Multi-Species Assessment of Injury, Mortality, and Physical Conditions during Downstream Passage through a Large Archimedes Hydrodynamic Screw (Albert Canal, Belgium)". In: *Sustainability* 12.20. DOI: [10.3390/su12208722](https://doi.org/10.3390/su12208722) (cit. on pp. 1, 16, 21).
- Pauwels, I. S., S. Broos, L. Vandamme, J. Van Wichelen, J. Coeck, G. Toming, J. A. Tuhtan, and D. Buysse (2024). "A fish-friendly axial flow pump turns out to be eel safe, roach unfriendly and bream unsafe". In: *Scientific Reports* 14.1. DOI: [10.1038/s41598-024-81095-6](https://doi.org/10.1038/s41598-024-81095-6) (cit. on p. 16).
- Pflugrath, B. D., R. Saylor, K. M. Engbrecht, R. P. Mueller, J. R. Stephenson, M. Bevelhimer, B. M. Pracheil, and A. H. Colotelo (2021). *Biological Response Models: Predicting Injury and Mortality of Fish During Downstream Passage through Hydropower Facilities*. PNNL-30893. Pacific Northwest National Lab. (PNNL), Richland, WA (United States). DOI: [10.2172/1838202](https://doi.org/10.2172/1838202) (cit. on p. 21).
- Radinger, J., R. Van Treeck, and C. Wolter (2022). "Evident but context-dependent mortality of fish passing hydroelectric turbines". In: *Conservation Biology* 36.3. DOI: [10.1111/cobi.13870](https://doi.org/10.1111/cobi.13870) (cit. on p. 16).
- Richmond, M. C., Z. D. Deng, C. A. McKinstry, R. P. Mueller, T. J. Carlson, and D. D. Dauble (2009). "Response relationships between juvenile salmon and an autonomous sensor in turbulent flow". In: *Fisheries Research* 97.1. DOI: [10.1016/j.fishres.2009.01.011](https://doi.org/10.1016/j.fishres.2009.01.011) (cit. on pp. 4, 16).
- Romero-Gomez, P., T. Poomchaivej, R. Razdan, W. Robinson, R. Peyreder, M. Raeder, and L. J. Baumgartner (2024). "Sensor Fish Deployments at the Xayaburi Hydropower Plant: Measurements and Simulations". In: *Water* 16.5. DOI: [10.3390/w16050775](https://doi.org/10.3390/w16050775) (cit. on p. 21).
- Salalila, A., Z. D. Deng, J. J. Martinez, J. Lu, and L. J. Baumgartner (2019). "Evaluation of a fish-friendly self-cleaning horizontal irrigation screen using autonomous sensors". In: *Marine and Freshwater Research* 70.9. DOI: [10.1071/MF19194](https://doi.org/10.1071/MF19194) (cit. on pp. 3, 16, 21, 22).
- Salalila, A., J. Lu, J. J. Martinez, H. Hou, and Z. D. Deng (2025). "Autonomous sensor suite for evaluating fish-turbine interactions and environmental impacts in marine renewable energy and hydropower". In: *Science of The Total Environment* 966. DOI: [10.1016/j.scitotenv.2025.178710](https://doi.org/10.1016/j.scitotenv.2025.178710) (cit. on pp. 16, 21, 26).
- Sanchis, A. and A. Jensen (2011). "Dynamic masking of PIV images using the Radon transform in free surface flows". In: *Experiments in Fluids* 51.4. DOI: [10.1007/s00348-011-1101-7](https://doi.org/10.1007/s00348-011-1101-7) (cit. on pp. 2, 11).
- Saylor, R. K. (2021). "Susceptibility of riverine fishes to anthropogenically-linked trauma: Strikes from hydropower turbine blades". PhD thesis. USA: University of Tennessee (cit. on p. 24).
- Saylor, R. K., M. Bevelhimer, and B. Pracheil (2020a). *Fish injury and mortality caused by simulated impacts from turbine blades*. In collab. with A. Fortner, D. Sterling, K. Deck, E. Deck, I. Qsaquwa, and C. Anugwom. DOI: [10.21951/1755094](https://doi.org/10.21951/1755094) (cit. on pp. 3, 17).
- Saylor, R. K., D. Sterling, M. Bevelhimer, and B. Pracheil (2020b). "Within and Among Fish Species Differences in Simulated Turbine Blade Strike Mortality: Limits on the Use of Surrogacy for Untested Species". In: *Water* 12.3. DOI: [10.3390/w12030701](https://doi.org/10.3390/w12030701) (cit. on pp. 10, 21).

- Saylor, R. K., P. L. Wang, M. Bevelhimer, P. Lloyd, J. Goodwin, R. Laughter, D. Young, D. Sterling, P. Mhatre, C. Atkins, and B. Post (2021). "Creation of a prototype biomimetic fish to better understand impact trauma caused by hydropower turbine blade strikes". In: *PeerJ Materials Science* 3. DOI: [10.7717/peerj-matsci.16](https://doi.org/10.7717/peerj-matsci.16) (cit. on pp. 3, 16, 21, 26).
- Stephenson, J. R., A. J. Gingerich, R. S. Brown, B. D. Pflugrath, Z. Deng, T. J. Carlson, M. J. Langeslay, M. L. Ahmann, R. L. Johnson, and A. G. Seaburg (2010). "Assessing barotrauma in neutrally and negatively buoyant juvenile salmonids exposed to simulated hydro-turbine passage using a mobile aquatic barotrauma laboratory". In: *Fisheries Research* 106.3. DOI: [10.1016/j.fishres.2010.08.006](https://doi.org/10.1016/j.fishres.2010.08.006) (cit. on p. 21).
- The European Union (2000). *Directive 2000/60/EC of the European Parliament and of the Council of 23 October 2000 establishing a framework for Community action in the field of water policy* (cit. on p. 16).
- Tregidgo, L., Z. Wang, and I. Gursul (2013). "Unsteady fluid–structure interactions of a pitching membrane wing". In: *Aerospace Science and Technology* 28.1. DOI: [10.1016/j.ast.2012.10.006](https://doi.org/10.1016/j.ast.2012.10.006) (cit. on pp. 2, 11).
- Vagnoni, E., D. Gezer, I. Anagnostopoulos, G. Cavazzini, E. Doujak, M. Hočevár, and P. Rudolf (2024). "The new role of sustainable hydropower in flexible energy systems and its technical evolution through innovation and digitalization". In: *Renewable Energy* 230. DOI: [10.1016/j.renene.2024.120832](https://doi.org/10.1016/j.renene.2024.120832) (cit. on p. 16).
- Van Treeck, R., J. Radinger, R. A. Noble, F. Geiger, and C. Wolter (2021). "The European Fish Hazard Index – An assessment tool for screening hazard of hydropower plants for fish". In: *Sustainable Energy Technologies and Assessments* 43. DOI: [10.1016/j.seta.2020.100903](https://doi.org/10.1016/j.seta.2020.100903) (cit. on p. 16).
- Weheliye, W., M. Yianneskis, and A. Ducci (2012). "PIV measurements in a shaken cylindrical bioreactor". In: *16th international symposium on applications of laser techniques to fluid mechanics, Lisbon, Portugal* (cit. on pp. 2, 11).
- West, S. A. and M. N. Burton-Chellew (2025). "Replication of experiments and the canonisation of incorrect conclusions". In: *Evolution and Human Behavior* 46.6. DOI: [10.1016/j.evolhumbehav.2025.106749](https://doi.org/10.1016/j.evolhumbehav.2025.106749) (cit. on p. 31).
- Yang, C., Q. Li, D. Xu, J. Wu, Y. Zheng, Y. Zhang, and A. Yu (2023). "Fish damage due to tubular turbine: Experiments and CFD simulations". In: *Ocean Engineering* 272. DOI: [10.1016/j.oceaneng.2023.113881](https://doi.org/10.1016/j.oceaneng.2023.113881) (cit. on p. 21).

Acknowledgments

I am especially grateful to Maarja, Jeff, and Stefan for their patient supervision and academic guidance throughout this work. I also thank Jeff, Stefan, and Shokoofeh for initiating and securing the StrikeSense project funding that supported my research, with particular thanks to Shokoofeh for her continued supervision of this project. I am grateful to Maarja and Jeff for the opportunity to carry out my work in Tallinn.

I would like to thank Karla and Jessica for their help with assembling the strike apparatus and Danil for conducting the experiments. I thank Dirk, Christian and Helge for their support with mechanical and electrical installations and Peter for his assistance in setting up the high-speed camera system. I also thank Roberto for setting up the electric motor and for taking the time to explain its operation. I would further like to thank Andres for his help with microelectronics and Jaanus for his exceptional administrative support.

I would further like to thank Dominique, as head of the chair, for ensuring continued funding and steady progress of my work. I am also very thankful to Melanie for handling numerous orders and acquisitions and for making the administrative process feel straightforward.

Finally, I thank the members of my church for their support, encouragement and most of all prayer throughout this time.

Abstract

Reconstructing Physical Quantities from Sparse Measurements: Experimental Validation and Sensor-Based Inference in Hydraulic Environments

Many laboratory and field experiments rely on sensors that cannot directly measure the physical quantities of interest. Interpretation therefore depends on combining partial observations with physical constraints that restrict admissible behavior. This dissertation addresses how physically grounded reconstruction methods can recover unmeasured quantities from incomplete or noisy data, enabling simpler experiments without loss of interpretability.

The approach is first demonstrated for flexible hydrofoils, where structural deformation is reconstructed from image data by analyzing the motion of flow tracers. A beam-theory model constrains the solution, ensuring mechanical admissibility and removing the need for dedicated deformation-tracking systems. This yields a time-resolved description of both structure and flow geometry from standard imaging and simplifies mask generation for particle image velocimetry.

The framework is then applied to fish passage through hydraulic machinery, where direct observation is limited and live-fish tests provide only aggregate outcomes. Sensor probes offer detailed exposure data, but their signals are difficult to interpret physically. To address this, a reproducible blade strike rig with closed-loop velocity control was developed, enabling systematic and repeatable impact experiments. The open design facilitates comparability across studies.

Using this setup, commonly used acceleration-based strike severity metrics were evaluated against controlled impact conditions and published biological dose–response data. All tested metrics failed to resolve biologically relevant velocity ranges or distinguish safe from unsafe conditions. The resulting dataset was released openly.

A pilot study with soft-bodied probes showed improved sensitivity by extending impact duration and reducing signal saturation. This suggests that structural compliance can complement sensing and enable more robust, physically interpretable metrics. Future work should explore additional deformation-based measures and improve probe durability.

Taken together, these contributions show that enforcing explicit mechanical constraints during data analysis enables reconstruction of unmeasured physical quantities from limited observations. By developing and openly documenting a reproducible blade-strike rig and using it to evaluate widely used sensor-probe metrics, this work strengthens the methodological basis of experimental research in fluid–structure interaction and biohydraulic systems. Such controlled validation is a necessary step toward reducing fish injury and mortality in hydraulic machinery.

Kokkuvõte

Füüsikaliste suuruste rekonstrueerimine hõredatest mõõtmistest: eksperimentaalne valideerimine ja anduripõhine inferents hüdraulilistes keskkondades

Paljud laboratoorsed ja välitingimustes tehtavad katsed tuginevad anduritele, mis ei suuda otseselt mõõta huvipakkuvaid füüsikalisi suurus. Seetõttu sõltub tõlgendamine osalistest vaatlustest ja füüsikalistest piirangutest, mis määravad lubatava käitumise. Käesolev väitekiri käsitleb, kuidas füüsikaliselt põhjendatud rekonstrueerimismeetodid võimaldavad taastada mõõtmata suurus puudulike või mürarikaste andmete põhjal, võimaldades lihtsamaid katseid ilma tõlgendatavust kaotamata.

Lähene mist demonstreeritakse esmalt painduvate hüdrofiilide puhul, kus struktuurne deformatsioon rekonstrueeritakse pildipõhiste andmete abil, analüüsides voolujälgijate liikumist. Lahendust piirab talateooria mudel, mis tagab mehaanilise kooskõla ja välistab vajaduse spetsiaalsete deformatsiooni jälgimissüsteemide järele. Tulemuseks on ajas lahutatud kirjeldus nii struktuuri kui ka voolugeomeetria kohta standardse pildistamise põhjal ning lihtsustub maskide genereerimine osakeste pildikiiruse mõõtmiseks.

Seejärel rakendatakse raamistikku kalade läbipääsule hüdraulilistes masinates, kus otsene vaatlus on piiratud ja eluskalade katsed annavad vaid koondtulemusi. Andurproovid pakuvad detaileid kokkupuuteandmeid, kuid nende signaale on füüsikaliselt keeruline tõlgendada. Selle lahendamiseks töötati välja reprodutseeritava labalöögi katseseade suletud ahelaga kiiruse juhtimisega, mis võimaldab süstemaatilisi ja korduvaid löögikatseid. Avatud disain soodustab tulemuste võrreldavust erinevate uuringute vahel.

Selle seadistuse abil hinnati laialdaselt kasutatavaid kiirendusel põhinevaid löögitõsiduse mõõdikuid kontrollitud löögitingimuste ja avaldatud bioloogiliste doos–reaktsiooni andmete suhtes. Kõik uuritud mõõdikud ei suutnud eristada bioloogiliselt olulisi kiirusvahemikke ega teha vahet ohutute ja ohtlike tingimuste vahel. Saadud andmestik tehti avalikult kättesaadavaks.

Pilootuuring pehmekehaliste anduritega näitas paremat tundlikkust, kuna löögi kestus pikenes ja signaali küllastumine vähenes. See viitab, et struktuurne vastavus võib täiendada mõõtmist ja võimaldada robustsemaid, füüsikaliselt tõlgendatavaid mõõdikuid. Edasine töö peaks uurima täiendavaid deformatsioonipõhiseid mõõte ning parandama andurite vastupidavust.

Kokkuvõttes näitavad need tulemused, et selgesõnaliste mehaaniliste piirangute rakendamine andmeanalüüsis võimaldab taastada mõõtmata füüsikalisi suurus piiratud vaatlustest. Reprodutseeritava labalöögi katseseadme arendamine ja avatud dokumenteerimine ning selle kasutamine laialt kasutatavate andurimõõdikute hindamiseks tugevdab eksperimentaalse uurimistöö metoodilist alust vedeliku–struktuuri vastastikmõju ja biohüdraulika valdkonnas. Selline kontrollitud valideerimine on vajalik samm kalade vigastuste ja suremuse vähendamiseks hüdraulilistes masinates.

A Appendix: Publications






A.1 Publication I

S. Hoerner, W. I. Kösters, L. Vignal, O. Cleynen, S. Abbaszadeh, T. Maître, and D. Thévenin (2021). “Cross-Flow Tidal Turbines with Highly Flexible Blades—Experimental Flow Field Investigations at Strong Fluid–Structure Interactions”. In: *Energies* 14.4, p. 797. DOI: [10.3390/en14040797](https://doi.org/10.3390/en14040797)

This publication corresponds to Contribution I, discussed in section [2](#).

Article

Cross-Flow Tidal Turbines with Highly Flexible Blades—Experimental Flow Field Investigations at Strong Fluid–Structure Interactions

Stefan Hoerner ^{1,2,*} , Iring Kösters ¹ , Laure Vignal ², Olivier Cleynen ¹ , Shokoofeh Abbaszadeh ³ , Thierry Maître ² and Dominique Thévenin ¹ 

- ¹ Laboratory of Fluid Dynamics and Technical Flows, Institute of Fluid Dynamics and Thermodynamics, Otto von Guericke University Magdeburg, Universitätsplatz 2, 39106 Magdeburg, Germany; wolf.koesters@ovgu.de (I.K.); olivier.cleynen@ovgu.de (O.C.); thevenin@ovgu.de (D.T.)
 - ² Laboratory of Geophysical and Industrial Flows, University Grenoble Alpes, CNRS, Grenoble INP, LEGI, F-38000 Grenoble, France; laure.vignal@legi.cnrs.fr (L.V.); Thierry.Maitre@legi.grenoble-inp.fr (T.M.)
 - ³ Laboratory of Electrical Drive Systems, Institute of Electric Power Systems, Otto von Guericke University Magdeburg, Universitätsplatz 2, 39106 Magdeburg, Germany; abbaszadeh@ovgu.de
- * Correspondence: hoerner@ovgu.de

Abstract: Oscillating hydrofoils were installed in a water tunnel as a surrogate model for a hydrokinetic cross-flow tidal turbine, enabling the study of the effect of flexible blades on the performance of those devices with high ecological potential. The study focuses on a single tip-speed ratio (equal to 2), the key non-dimensional parameter describing the operating point, and solidity (equal to 1.5), quantifying the robustness of the turbine shape. Both parameters are standard values for cross-flow tidal turbines. Those lead to highly dynamic characteristics in the flow field dominated by dynamic stall. The flow field is investigated at the blade level using high-speed particle image velocimetry measurements. Strong fluid–structure interactions lead to significant structural deformations and highly modified flow fields. The flexibility of the blades is shown to significantly reduce the duration of the periodic stall regime; this observation is achieved through systematic comparison of the flow field, with a quantitative evaluation of the degree of chaotic changes in the wake. In this manner, the study provides insights into the mechanisms of the passive flow control achieved through blade flexibility in cross-flow turbines.

Keywords: fluid–structure interaction; deformable blades; NACA0018; particle image velocimetry; vertical-axis turbine; cross-flow turbine; dynamic stall



Citation: Hoerner, S.; Kösters, I.; Vignal, L.; Cleynen, O.; Abbaszadeh, S.; Maître, T.; Thévenin, D. Cross-Flow Tidal Turbines with Highly Flexible Blades—Experimental Flow Field Investigations at Strong Fluid–Structure Interactions. *Energies* **2021**, *14*, 797. <https://doi.org/10.3390/en14040797>

Academic Editor: Guillou Sylvain and Eric L. Bibeau

Received: 9 January 2021

Accepted: 28 January 2021

Published: 3 February 2021

Publisher's Note: MDPI stays neutral with regard to jurisdictional claims in published maps and institutional affiliations.



Copyright: © 2021 by the authors. Licensee MDPI, Basel, Switzerland. This article is an open access article distributed under the terms and conditions of the Creative Commons Attribution (CC BY) license (<https://creativecommons.org/licenses/by/4.0/>).

1. Introduction

Hydrokinetic energy in oceanic currents is an energy resource with large potential that remains largely unexploited. Sustainable exploitation technologies for marine and tidal streams are the focus of recent research, driven by the aim to reduce climate change and promote a greenhouse gas-neutral production of electrical energy. In this context, hydrokinetic turbines are of particular interest, as they might solve the most critical issues for a successful application in ocean energy engineering: sustainability and cost competitiveness against on-shore technologies.

Hydrokinetic vertical-axis or cross-flow tidal turbines (CFTTs)—the scope of this study—seem to be advantageous compared to classical axial, also called horizontal-axis turbines. They are predestined for array installations because of their rectangular cross-section and better fit in shallow water installations. This leads to high area-based power density as shown by Dabiri 2011 and others [1–3]. Additionally, they are in general of simple construction and operate independently of the stream direction, which is an important advantage for applications in tidal streams, featuring frequent variations in flow speed and direction [4].

1.1. State of Science and Technology

In spite of their simple geometry, CFTTs feature complex, unsteady flow in the rotor, as shown in Figure 1. The vertical axis of rotation translates into alternating angles of incidence α and relative velocities w for the blades as they rotate. The degree of unsteadiness at blade level is governed by (1) the solidity σ , the non-dimensional key parameter describing the robustness of the turbine shape, and (2) the operating point, expressed by the tip-speed ratio λ (see also Figure 2). Because of the high density of water, water turbines have higher solidities, they are of more robust design, compared to wind devices, and so they typically operate at lower λ . The turbines' optimal tip-speed ratio decreases along with their solidity, as shown by Shiono et al. 2000 [5]. Low- λ operating points result in high angles of attack on the turbine blades (see Figure 2). Dynamic blade stall may result from those flow conditions. The alternating angles of incidence will generate alternating hydrodynamic loads, which, together with the abrupt loss of lift and drag increase resulting from the periodic blade stall, can cause failure from material fatigue (Parashivoiu 2002 [6]), a serious challenge for this type of turbine.

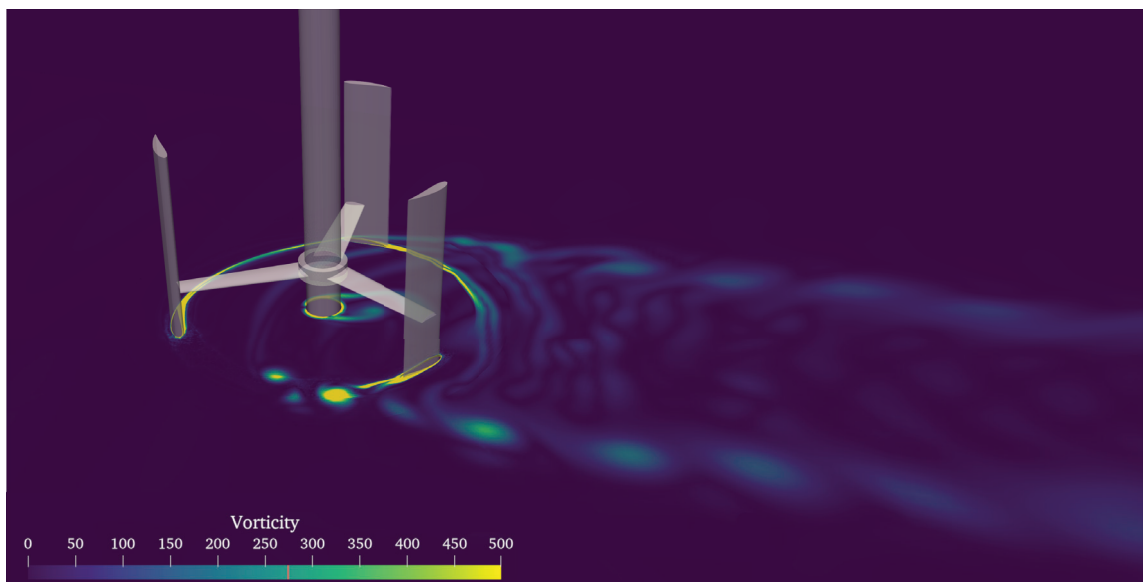


Figure 1. Three-dimensional computer-aided design (CAD) model of a three-bladed H-Darrieus cross-flow tidal turbine (CFTT) and vorticity field from numerical investigations at tip-speed ratio $\lambda = 2$. CFTTs generate a complex flow field due to the cross-flow design and the lack of a guiding structure (Software package OpenFOAM/Paraview).

In consequence, the control and inhibition of dynamic blade stall is key for an industrial application of CFTTs. It has been the topic of extensive studies for many years, beginning with Laneville and Vittecoq 1986 [7], with most recent progress published by Ferreira et al. 2009 [8], Gorle et al. 2016 [9], Buchner et al. 2017 and 2018 [10,11] or Miller et al. 2018 [12]. Dynamic stall itself is topic of recent, more fundamental research, such as Benton and Visbal 2019 [13]. The development of control strategies for blade stall is also of great interest not only for applications on CFTTs but a general challenge in unsteady aerodynamics (Müller et al. 2014 and 2016 [14,15]).

Different approaches exist to overcome dynamic stall in CFTTs. One is to control the angle of incidence of the rotor blades by active or passive pitch mechanisms on rigid blades. This most extensively studied method provides high improvements in the turbine efficiency and lowers the alternating load peaks, as reported by Lazauskas and Kirke 2012 [16], Khalid et al. 2013 [17], Mauri et al. 2014 [18] or Abbaszadeh et al. 2019 [19].

However, blade pitching requires complex mechanisms and adds an additional source of failure to the systems, reducing simplicity and robustness. New design approaches may deliver durable and sustainable solutions here in future.

A second, less investigated approach is based on an active control of the angular velocity (since α depends on the tangential velocity rotor velocity $\omega \times R$ and the azimuth angle θ). The dynamic adjustment of the angular speed therefore allows for control of the angle of attack [20]. This approach requires a sophisticated drive control in combination with a highly dynamic electrical drive, that may hinder cost competitiveness.

A third method is the deployment of adaptive structures—a bio-inspired method based on findings concerning sea mammals and fish, whose flexible fins significantly improve their propulsive efficiency, as reported by Fish 1993 [21] for bottlenose dolphins. The design of flexible blades is known to improve turbine efficiency, as reported by Zeiner-Gundersen 2015 [22] and McPhee and Beyene 2016 [23]. Additionally, it can increase the lifetime and help to reduce material deployment for these devices as shown by Hoerner et al. 2019 [24]. The deformations of the highly flexible rotor blades, which result from the flow adaptation, amount up to 20% of the chord length and provide passive control of the flow. Potential efficiency increases of 20% along with structural load reduction of 25% could be achieved, as shown experimentally by Hoerner et al. 2020 [25] on a reduced turbine model consisting of a pitching hydrofoil.

The present study focuses on the flow field surrounding a single CFTT blade, as investigated on a pitching flexible hydrofoil by means of high-speed particle image velocimetry measurements. An experimental approach for time-resolved particle image velocimetry (PIV) on the flow fields around a hyperflexible structure with the open-source toolbox fluidimage is presented and validated by comparison with a commercial reference code. The flow pattern and underlying fluid–structure effects on a CFTT equipped with flexible rotor blades are investigated. They provide new insights concerning passive flow control with adaptive structures for CFTT. Furthermore, the study reveals how dynamic stall can be controlled for this particular turbine type.

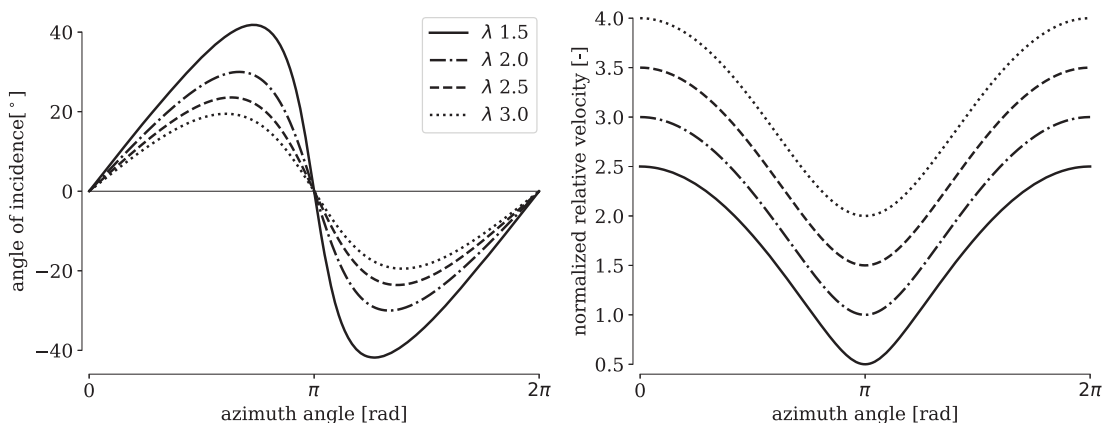


Figure 2. Alternating angle of incidence α (left) and relative velocity w (right) at blade level in dependence of azimuth angle θ and tip-speed ratio λ . The relative velocity w is normalized to the far-field velocity: w/v_∞ .

1.2. Blade Dynamics and Modeling

The flow field of a CFTT, at the blade level, is dominated by the highly unsteady variations of the angle of incidence α and the relative speed w (see Figures 1 and 2).

Equations (1) and (2) express their dependence on the azimuth angle θ and the operating point, given by the tip-speed ratio λ :

$$\alpha = \arctan\left(\frac{\sin \theta}{\lambda + \cos \theta}\right) \quad (1)$$

$$w = v_{\infty} \sqrt{1 + 2\lambda \cos \theta + \lambda^2} \quad (2)$$

The best efficiency operating point (BEP) depends on the turbine's solidity σ (see Equation (3)), a measure for the ratio between the areas covered by the blades and the rotor and expressed over the number of blades n , the turbine radius R and the blade chord length C :

$$\sigma = \frac{n \cdot C}{R} \quad (3)$$

The tip speed ratio λ is defined as the ratio between the tangential velocity of the blades, given as the product of the angular velocity ω and R , and the free-stream velocity v_{∞} :

$$\lambda = \frac{\omega R}{v_{\infty}} \quad (4)$$

For common design points of CFTTs with $\sigma = 1$, the BEP is found at roughly $\lambda = 2$ (Shiono et al. 2000 [5]).

The combination of values for σ and λ are crucial for the turbine characteristics:

1. a high solidity along with high tip-speed ratio will lead to strong blade-blade interaction. Blades then operate under unfavorable conditions, since the flow is not able to convect away the wake of the preceding blades;
2. a low solidity along with low tip-speed ratio will lead to profile stall and poor efficiency, due to high angles of incidence and a low "harvesting" area of the rotor.

At the blade level, the flow can be characterized by two parameters linked to σ and λ : The reduced frequency k and the trajectory of the angle of attack α . While the latter expresses the operating point (see Equation (1)), k combines both σ and λ into one dimensionless parameter, as will be shown subsequently:

$$k = \frac{C \cdot \dot{\alpha}_{\max}}{2 v_{\infty} \cdot \alpha_{\max}} = \frac{C \cdot \dot{\alpha}_{\max}}{\omega \cdot 2R \cdot \alpha_{\max}} \quad (5)$$

Neglecting blade-blade interaction and downstream wake effects of the cross-flow turbine, the flow field of a CFTT at blade level can be investigated with a surrogate model consisting of an oscillating hydrofoil [26].

2. Experimental Model and Setup

In this case, the hydrodynamic profile will perform a pitch motion in accordance to the trajectory of α (see Equation (1)). An advantage of this setup is the simplification of the experimental setup and the focus on the blade itself. Since the experiment was conducted in a closed water tunnel at LEGI Labs Grenoble, the alternating relative flow velocity w was replaced by the constant inlet velocity v_{ch} . This results in a constant Reynolds number, the effects of which on the results of this study are considered small. This comes along with a constant load and convection regime, which has to be considered for a transfer of the results to a real CFTT. The reduced frequency k for the given setup with constant v_{ch} and oscillation frequency f_o can be found by combining Equation (5) (left) with the motion law for α (Equation (1)), its temporal derivative $d\alpha/dt$ and the definition of λ (Equation (4)):

$$k = \frac{\pi \cdot f_o \cdot C}{v_{\text{ch}} \cdot (\lambda - 1) \cdot \arctan\left[(\lambda^2 - 1)^{-\frac{1}{2}}\right]} \quad (6)$$

The most interesting feature of the deployed surrogate model is the ability to investigate a full set of turbine designs by variation of k and α , according to Equation (6).

2.1. Experimental Facility

The water channel at LEGI Labs in Grenoble is operated in a closed loop with a maximum volume flow rate of 650 L/s at 20 m head. The facility is equipped with a test section of $1000 \times 175 \times 280$ (L \times W \times H in [mm]), shown in Figure 3. The turbulence intensity in the core flow was measured to be 0.5% based on flow field measurements using laser Doppler anemometry (LDA). The minimum achievable inlet velocity is of 3 m/s due to instabilities in the volume rate and overheating of the pump drive for lower drive speed. Therefore, in the study at hand, the channel's inflow velocity was set to 3.5 m/s.

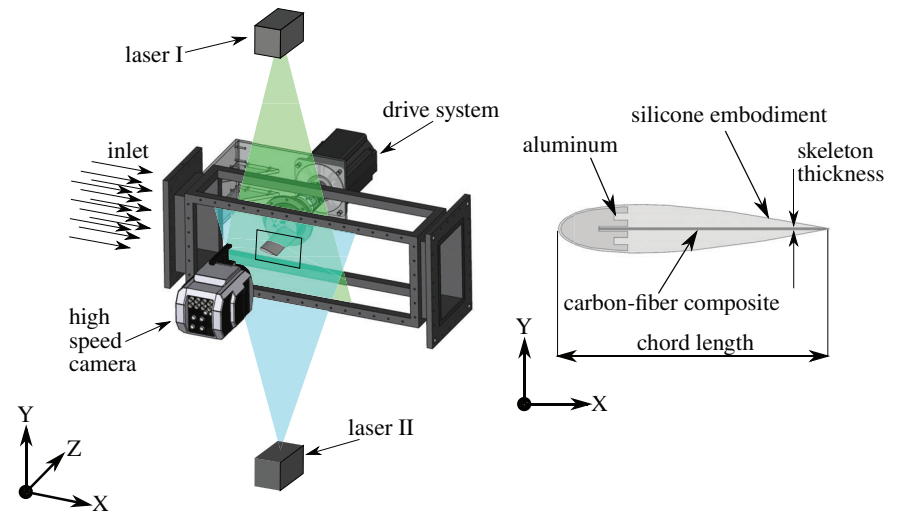


Figure 3. Experimental setup: (Left) The water tunnel test section is equipped with a servo-drive system allowing for a precise set-point control. A six-axis load cell captures the forces and moments acting on the profile. (Right) The stiffness of the flexible hydrofoils can be adjusted by the thickness of the carbon-fiber composite skeleton.

2.2. Highly Flexible Hydrofoils

The adaptive blades were designed as a multi-material compound (see Figure 3). The first quarter of the profiles is milled from aluminum and considered to be rigid. The remaining parts comprise a composite skeleton built from a thin (0.3 mm) plate of carbon fiber embedded in an epoxy resin matrix and an embodiment of high flexible silicone. This design allowed for a variation of the profile stiffness by only changing the skeleton thickness. The chord length of 66 mm of the NACA0018-shaped hydrofoil led to a chord-based Reynolds number of about 250,000 for the inlet velocity $v_{ch} = 3.5$ m/s in the experimental setup.

A detailed description of the experimental facility, hydrodynamic load measurement, and flexible hydrofoils can be found in Hoerner et al. 2019 [24].

2.3. Pitch Motion Setup

A servo-drive system of 5 kW and 143 Nm peak torque is fed by a power inverter, allowing the realization of any arbitrary rotational motion. To this purpose, a drive communication software was customized (Abbaszadeh et al. 2019 [19]). During the experiments, the drive performs an oscillating pitch motion according to Figure 2, highlighting the case $\lambda = 2$. This pitch motion leads, in addition to the main flow in the water channel, to a highly dynamic flow regime, comparable to the flow in the rotor of a single-bladed CFTT.

The position feedback of the drive for one period, describing the evolution of α , is shown along with the resulting flow field in Section 3.

2.4. PIV Hardware Setup

The instantaneous flow field was captured with a time-resolved, two-dimensional, two-component (2D2C) PIV setup with 4 kHz temporal resolution (see Figures 3 and 4). The light sheet of 2 mm thickness was built with two continuous lasers placed in parallel and pointing towards each other in the X-Y plane, in order to remove shadow effects from the hydrofoil. The plane was situated with a negative shift of 0.145 m in the Z-direction.

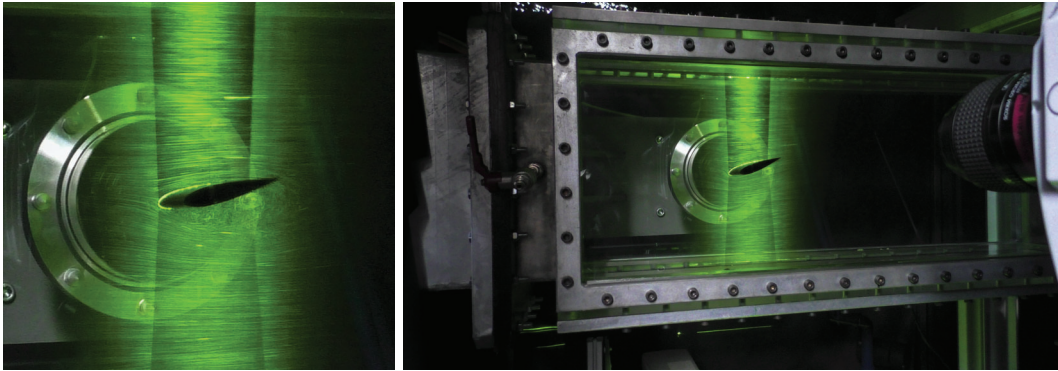


Figure 4. Setup of the two-dimensional, two-component (2D2C) particle image velocimetry (PIV) measurement with two synchronized lasers and high-speed camera at the LEGI labs closed-loop water tunnel. (Left) Detail of the inclined rigid hydrofoil, with flow separation. (right) The high-speed camera appears in the right of the image. Pathlines of particles are partly visible. Photos by Nicole Lambert, CNRS/LEGI 2017.

Both lasers were placed behind the test section: Laser I was equipped with an optical arm and a sheet generator which illuminated the measurement plane from the top, while Laser II generated the plane with a set of lenses from the bottom. The specifications of the lasers are given in Table 1; both were set to 500 mW power. The high-speed camera, a Phantom V2511 (see Table 2 for specifications) covers an area of $120 \times 74 \text{ mm}^2$ with 1280×800 pixel at 12 bit gray-scale depth. The data was acquired with lens aperture of focus/4 and an exposure time of $50 \mu\text{s}$. Each recording consists of 16,500 frames, amounting to 4.125 s. The flow was seeded with silver-coated hollow glass spheres of $10 \mu\text{m}$ diameter. The time synchronization of the position feedback and video recording is given by an external trigger signal from a pulse generator.

Table 1. Laser I and II specifications.

Spectra Physics Millennia		
Wave length	[nm]	532
Type		continuous NdYV04
Power	[W]	2 (pro 2 SJ)/5 (pro 5 SJ)

Table 2. High-speed camera specifications.

Phantom V2511					
Resolution	[px ²]	1280 × 800	Pixel size	[μm]	28
CMOS area	[mm ²]	35.8 × 22.4	Color depth	[bit]	12
Focus	[mm]	105	Acquisition rate	[fps]	25,000

The PIV measurements were performed for a reduced frequency $k = 0.24$, represented by variations of the oscillation frequency $f_o = 2.25 \text{ Hz}$ and a tip-speed ratio $\lambda = 2$. This

means that the flow field is dominated by a fully-dynamic stall regime. At first, measurements were performed for a rigid reference hydrofoil. Subsequently the experiment was repeated under exactly the same conditions for the flexible hydrofoil, which allows for a direct comparison of the influence of the passive stall control approach and consequences regarding the flow field.

2.5. Preprocessing and Masking

A particular challenge for the present study was the adhesion of particles to the silicone body, resulting in agglomerations on the surface. Reflections at the boundaries perturb the cross-correlation algorithm, so that the structure has to be masked. In the present case, the mask generation becomes a challenging task. The structure is in motion and simultaneously deforms, because the rigid body displacement is overlaid by an unknown and partly stochastic structural deformation. While the first can be easily predicted by the trajectory of the drive control or the position feedback, no reliable information is available for the deformation of the flexible body. To overcome this issue, a segmentation algorithm was developed to provide an adaptive mask for the PIV raw data. The algorithm and an additional technique used to measure cross-section deformation have been published as open-source code and are described in Hoerner 2020 [27].

The footage was taken by a camera perpendicular to the cross-section; therein, three-dimensional effects enlarge the projected area of the structure non-uniformly, as a result of non-uniform deformation of the hydrofoil itself across its span (in the Z-axis). This results in a sparser seeded (and hence darker) area, especially near the trailing edge. In consequence, a corrected mask (Figure 5), thicker than the NACA0018 geometry, was used during the PIV processing. This has a non-negligible effect on the measurements in the vicinity of the trailing edge and has to be considered in the evaluation of the results.

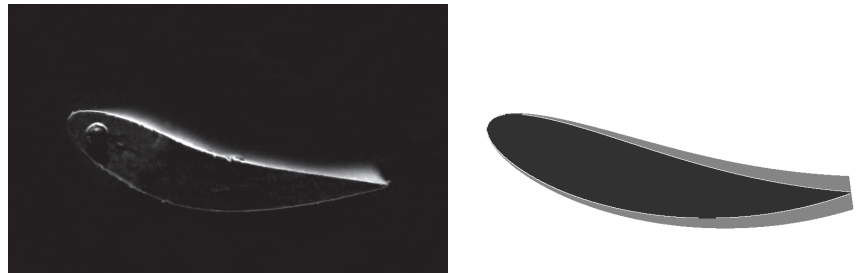


Figure 5. (Left) High-speed recording of the hydrofoil motion. The hyper-flexible hydrofoil encounters strong deformations for high angles of incidence. (Right) PIV mask generated from PIV raw data with thickened tail (grey) to cover three-dimensional deformation effects and recognized NACA0018 structure (black). The recordings belong to two different measurement campaigns.

2.6. Processing

Fluidimage, a PIV processing framework introduced by Augier et al. 2019 [28] was utilized to perform the PIV processing of the raw data.

The process starts with image preprocessing and mask generation. The main processing (the cross-correlation) is performed in a multi-step setup, starting with an initial window size of $128 \times 128 \text{ px}^2$ and a final window size of $32 \times 32 \text{ px}^2$. In the current state only quadratic interrogation windows are supported by the software. The windows overlap of 50% leads to one vector for each $16 \times 16 \text{ px}^2$, or $1.5 \times 1.5 \text{ mm}^2$ respectively. A correlation peak value of 0.3 was chosen as a threshold during the multi-step process to ensure reliable results. All vectors obtained with lower correlation values were discarded and replaced by the output of a thin-plate-spline (TPS) interpolation algorithm. The continuous laser source and the high sample rate made for challenging conditions. Subsequent

treatment methodology of the flow fields retrieved from the correlation was necessary and fully adapted to the data at hand.

2.7. Post-Processing

In a first step of data post-processing (see Figure 6), the (spatially) interpolated vectors (this is done by deploying thin-plate-spline radial basis functions during the processing in the Fluidimage software) for each time step with a correlation < 0.3 were discarded and replaced by NaN (see Figure 6 (far left)). Resulting vector gaps were subsequently filled up, exploiting the high temporal resolution of the recordings to increase the reliability of the data. A time-based rolling average with a window of four frames replaced most of the removed vectors with reliable values from the neighboring time steps (see Figure 6 (center left)). To this effect, the average value of all available velocities in a given coordinate was calculated. NaN were sorted out before averaging over the remaining data points.

In the next step, a Gaussian filter was applied to the field. In order to work around remaining NaN in the velocity field, the filter was applied once for a field containing the NaN values, and once for a field with NaN replaced by zeros. The division of the second field by the first removes the influence from the zero velocities (see Figure 6 (right)). The resulting field does not contain the masked region, which is simply treated as a tracer-free region (set to '0') while processing the raw footage. A second, NACA0018 foil-shaped mask without thickened trailing edge, generated in parallel to the processing mask during the preprocessing, is superposed on the velocity fields for optical convenience. In the subsequent figures, except where explicitly mentioned, flow velocities v are shown as a dimensionless values after division by the average incoming flow speed (v/\bar{v}), and the color scale is constant, ranging from $0 < v/\bar{v} < 2$ for all subsequent velocity plots and videos.

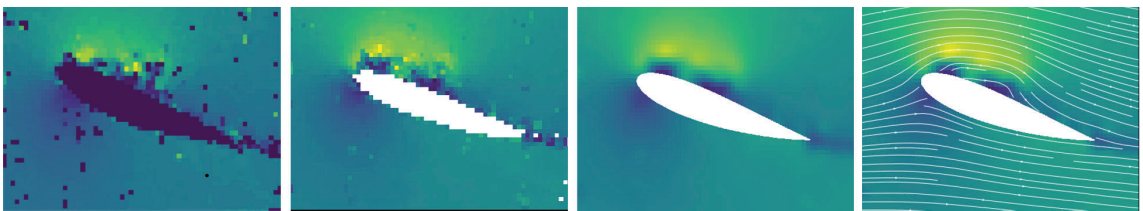


Figure 6. Postprocessing corrections on the vector field: (far left) Raw flow field with magnitude of the pixel shift and empty spaces from low correlation (< 0.3). (center left) Resulting field after application of the temporal rolling average with window size 4. (center right) final velocity field, after application of a Gaussian filter and calibration. (far right) Filtered vector field with streamlines: The velocity is displayed as non-dimensional velocity relative to the average flow speed v/\bar{v} .

2.8. Uncertainty Estimation

An uncertainty estimation for PIV measurements is challenging, due to the high abstraction level of the method and the multitude of processing steps. In order to evaluate the reliability of results and in particular of Fluidimage, results were compared with those obtained from the commercial software solution DaVis, and by using its uncertainty estimation function. The same adaptive masks were used in both processes. Table 3 shows the settings for the DaVis and Fluidimage software, which were chosen to be as similar as possible.

Table 3. DaVis and Fluidimage software settings used in the post-processing. Thin-plate-spline (TPS) stands for thin-plate spline interpolation.

	Davis		Fluidimage	
Denoise	counts subtraction	1000	threshold	counts > 85%
Vector calculation	time-series	multi-pass	time-series	multi-step
Window size/Steps	64 × 64	2	128 × 128	1
Overlap		0		50%
Smoothing	Gaussian weight	1:1	TPS	
Correction	standard		correl < 0.3	
Window size/Steps			64 × 64	1
Overlap				50%
Smoothing			TPS	
Correction			correl < 0.3	
Window size/Steps	32 × 32	2	32 × 32	1
Overlap		50%		50%
Smoothing	Gaussian weight	1:1	TPS	
Correction	standard		correl < 0.3	

The results of the comparison are visualized in Figure 7 where all the fields are displayed in m/s. The left half shows the velocity fields retrieved from each of the two software solutions. The right half shows the uncertainty of the PIV measurement obtained from DaVis, which is mainly based on the correlation peaks of the cross-correlation. In Figure 7, it becomes visible that the two software packages have a different treatment of masks. Fluidimage sets the masked area to zero velocity. This results in a smearing of the boundaries and produces artificially low velocities at the boundaries of the hydrofoil. This effect is not visible for DaVis where the mask seems to be treated explicitly with more sophisticated methods. This increases the reliability of the velocity fields close to the mask boundaries. Such a specific boundary treatment is not implemented in Fluidimage at this stage.

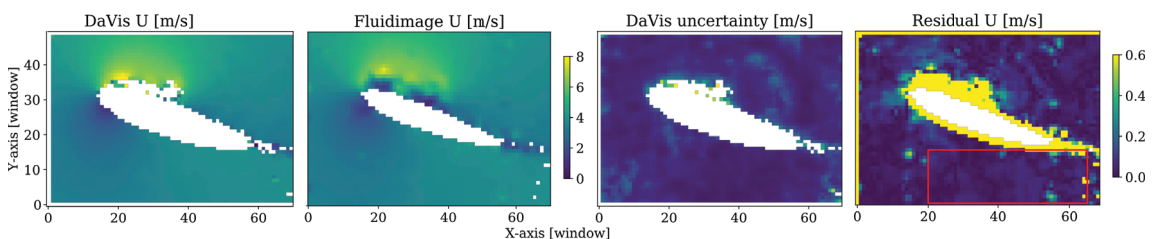


Figure 7. (Far left) Velocity field in m/s obtained by DaVis; (center left) Resulting field from Fluidimage with temporal rolling average with window size 4 and a Gaussian smoothing; (center right) Uncertainty of the PIV measurement in m/s from DaVis; (far right) difference between the magnitudes of the velocities from DaVis and Fluidimage, in m/s.

The differences between both reconstructed velocity fields were evaluated on a smaller window (the red rectangle in Figure 7) in order to avoid unrepresentative differences resulting from the mask treatment. In this window, the maxima of the magnitude were found to be a +0.16 m/s and -4.04 m/s (an outlier). The average difference was about -0.02 m/s, which is less than 1% of the average flow speed.

A further error source is related to the drive system and the accuracy of the position control. The position feedback is retrieved from the power inverter with a set-point precision of 0.058° by 0.0439° resolver resolution. The zero angle was calibrated with 0.014° accuracy (0.25 mm per meter) with a precision leveling tool.

3. Results and Discussion

3.1. The Influence of the Flexibility on Profile Stall

A systematic description of the influence of the hydrofoil flexibility on the macroscopic flow field is obtained in this study. The high measurement uncertainty in the boundary layer (see Section 2.8) does not allow for investigations of the propagation of the boundary layer separation in detail, and so precise mechanisms of hydrofoil stall are not in the focus of the present investigations.

In Figure 8, a stepwise evolution of the flow field is shown in discrete steps of 3° for one period for rigid and flexible hydrofoil. Instantaneous velocity fields are presented. In the upper left diagram, the trajectory of the pitch motion (black line) is shown along with the angles (red circles) corresponding to the flow fields shown below. Starting with the rigid hydrofoil, the reference for a conventional CFTT, deep dynamic stall characteristics are found: the flow stays attached while passing through the static stall angle of $\alpha = 15^\circ$ (NACA0018, $Re = 230,000$). The onset of flow separation can be observed on the trailing edge at $\alpha = 24^\circ$. The flow separation further grows and reaches its maximum, after passing $\alpha_{\max} = 30^\circ$, in the downward motion of the profile at $\alpha = 27^\circ$. Two counter-rotating vortices can be found in the wake structure. The size of the wake reduces as the angle of attack decreases. However, the flow remains detached until the hydrofoil gets in a clearly negative inclination ($\alpha = -6^\circ$), long after the static stall angle has been reached, the mark of a significant hysteresis. These effects are well described in literature as key characteristics of a dynamic stall regime (McCroskey 1976 [29]) and in former studies on pitching hydrofoils [30,31].

In the second half of the period, similar behavior can be reported (although some differences remain because the pitch velocity $\dot{\alpha}$ is higher in the downstroke). The largest profile wake zone appears again at $\alpha = -27^\circ$. The slower increase of the pitch angle allows for a faster reattachment of the flow ($\alpha = 3^\circ$). The hysteresis results in a regime where the flow only reattaches for very short parts of the oscillation period. This is in accordance to Gorle et al. 2016 [9] and their findings from PIV measurements on a four-bladed CFTT at $\lambda = 2$ and $k = 0.255$.

The flow field of the flexible hydrofoil shows different characteristics. The structural adaptation to the flow leads to a significant decrease of the size of the wake, even though the flow separates again near $\alpha \approx 27^\circ$. The hysteresis effects reported for the rigid hydrofoil appear for the flexible hydrofoil as well. However, the detached flow phase remains shorter in the period. In the second half, the deformation increases, the hydrofoil tail flaps, while shedding a main vortex at $\alpha = -27^\circ$ and the reattachment process is accelerated. This leads again to a shortened detached flow period. As shown in former studies, this structural adaptation and the resulting passive stall control leads to improved turbine efficiency [23,24]. The improvement is driven by drag reduction, which more than compensates for the reduction in lift resulting from the profile flexibility. The structural load also decreases because the structural deformation smoothens out the lift curves. This could translate into finer rotor geometries (reducing material usage) and longer lifetimes, due to decreased fatigue failure risks [24]. Beside this, a second, also remarkable point is the flow separation starting from the leading edge of the hydrofoil, which is a different behavior than observed for the rigid profile.

A chordwise flapping effect can be observed in the upwards motion from -12° to -6° , which is in accordance to the structural deformation measurements in a previous study [25,32]. This profile flapping is of stronger amplitude and can be linked to the shedding of the leading-edge vortex after convection of the profile, leading to significant deformations of the structure.

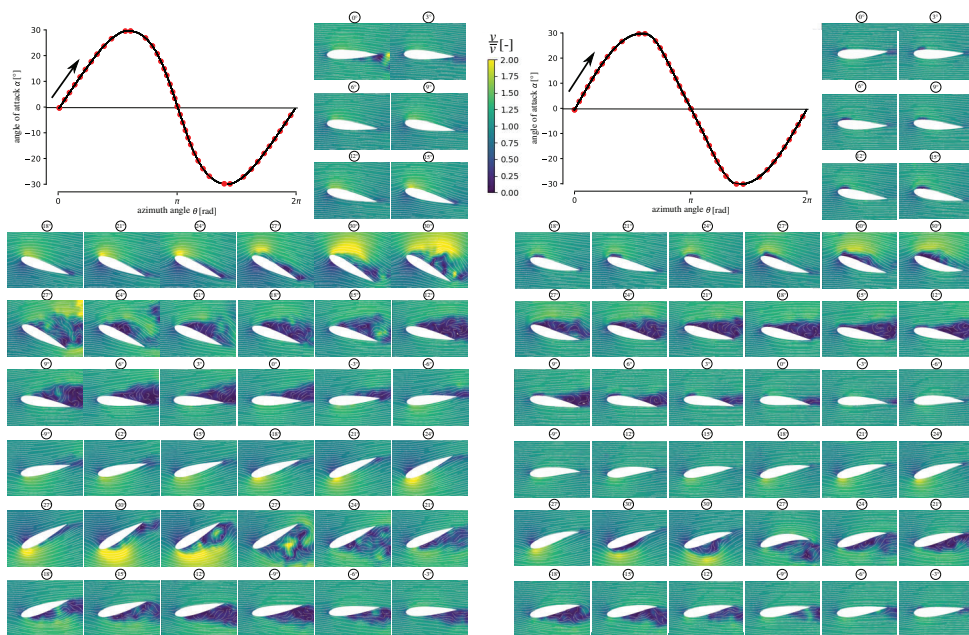


Figure 8. Flow fields for selected angles of incidence of one period of the oscillating pitch motion. The top-left diagram shows the pitch trajectory. The red points in the diagrams show the phase angle of the flow fields. **(Left)** Deep dynamic stall on a rigid NACA0018 hydrofoil at $k = 0.24$ for $\lambda = 2$ and $\sigma = 1.5$. Three-dimensional, chaotic structures with multiple, partly counter-rotating vortices are found in the separated zone. **(Right)** Flexible hydrofoil at $k = 0.24$ for $\lambda = 2$ and $\sigma = 1.5$.

3.2. The Influence of the Profile Flexibility on the Periodicity of the Flow Field

The influence of the flexibility on the phase angle based periodicity, or reproducibility of the flow is also investigated. The chaotic component of the flow field is observed through a comparison of the instantaneous flow fields with the average field for any one foil position. A high similarity of the flow field between individual periods is a desirable property, and is, following a hypothesis of the authors, likely to correlate with higher efficiencies in farm configurations. In such installations, reducing turbulence in the wake of an individual turbine may improve conditions for downstream turbines, enabling an increase in the power of the complete array. In this case, it could be taken as a measure for the efficiency of the energy conversion process.

A meaningful comparison of any flow fields shall not focus on microscale differences, but instead observe similarities in the main flow structure. The structural similarity index (SSIM), as proposed by Wang et al. 2004 [33] is a suitable tool to express the similarity of two images by the evaluation of luminance, contrast and structural similarity. In the case at hand it allows for the comparison of the flow fields using a single, averaged index, based on macro-scale—structural—similarities of the fields. Therefore, this tool, originally developed to assess the quality of image compression tools, serves as a fast and robust method for an assessment of the periodicity of the flow and the information loss in a phase-averaged flow field.

Figure 9 shows this comparison of the flow fields in multiple stages once for the rigid (left) and once for the flexible profile (right). As an example, a fully-detached flow at $\alpha = 28^\circ$ in the descending α motion is chosen using nine samples. The detached flow, a consequence of the dynamic stall regime induced by the periodic pitch motion, results in flow fields with significant stochastic properties. The number of periods for the set is limited to nine, due to the camera buffer size and the high sample frequency of the recording. However, this number of periods is sufficient to provide clear trends. The figure is divided in multiple sections. The averaged flow field is provided (top right) beside a diagram (top left) featuring the SSIM calculated between the instantaneous sample flow fields and the averaged one. Subsequently, pairs consisting of two images are shown: the instantaneous flow fields (numbered 1–9) and their difference relative to the averaged flow field (underneath). All velocity fields were initially uniformly scaled according to the averaged flow velocity v_{ch} .

In the case of the rigid foil, on the left, the wake area accounts for a significant share of the region captured with PIV measurements. The averaging of the flow field obviously suppresses small-scale structures originating from the instantaneous flow fields. As expected, significant differences appear in the wake region of the flow field and feature high variations in magnitude, structure, and size. The SSIM varies with a range of 0.04 from 0.874 to 0.912 with an average value of 0.893, which shows the strong variations for this case.

The flow fields of the flexible hydrofoil are generally characterized by a smaller wake size and a less complex flow structure. This can be found by visual examination and is also expressed by the SSIM, which varies in a smaller range of 0.02 from 0.943 to 0.963, around the generally higher average of 0.953. This is a clear metric for a significantly higher periodicity of the flow. Exploiting the results of the segmentation algorithm deployed for the raw PIV footage masking, the deflection of the flexible hydrofoil is a second parameter in the assessment of the periodicity. Figure 10 shows the differences in-between the deflected inclination angles β for the nine sample probes. The numbering of the periods is consistent with the numbering used in Figure 9. Variations of about 2° from the average can be reported. However, the bending characteristics are not correlated to the SSIM values. Further investigations of hydrodynamic loads and flow circulation around the profile could be appropriate in this case, but are out of the scope of this study.

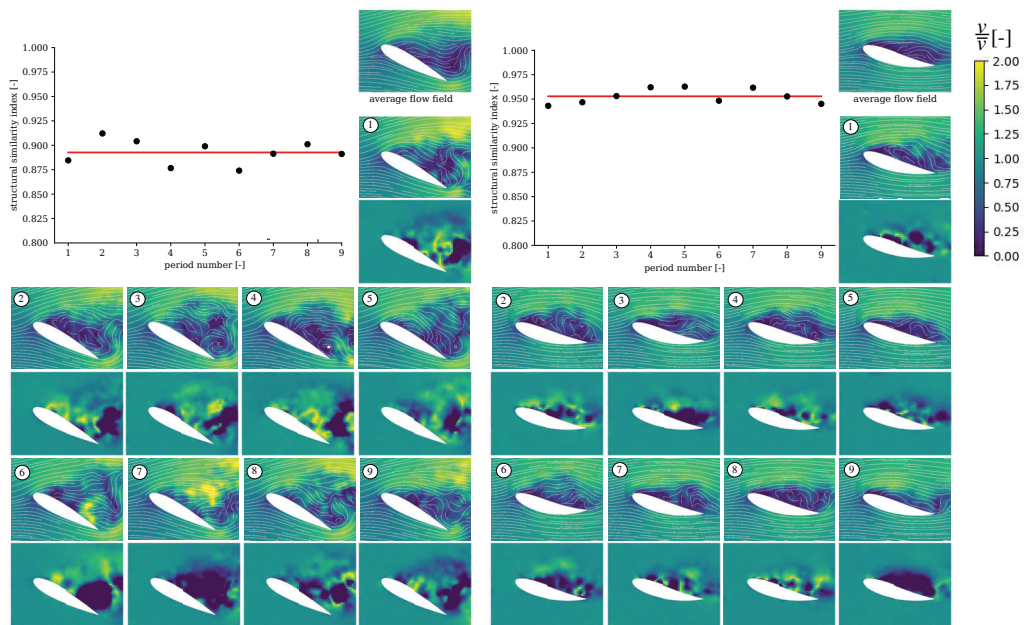


Figure 9. Averaged flow field (top plot), instantaneous flow fields (numbered 1–9) and relative velocity difference to the average (underneath) around the rigid (left) and the flexible (right) hydrofoil for an identical angle of incidence in multiple periods ($\alpha = 28^\circ$, $k = 0.24$). The diagrams show the structural similarity of the flow fields for each period.

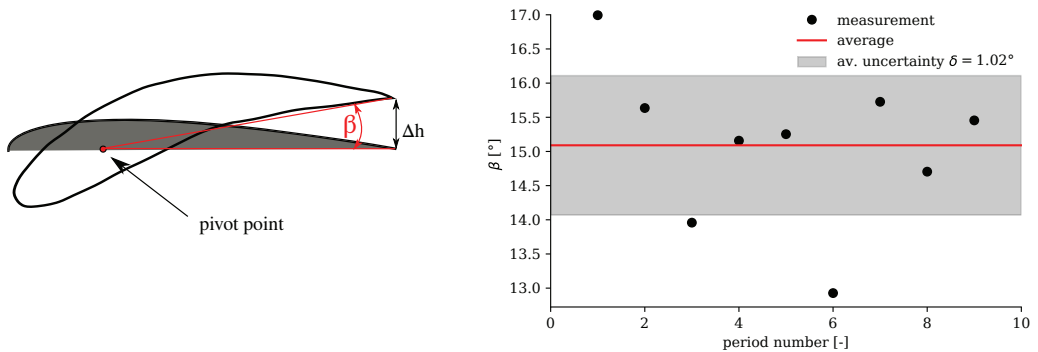


Figure 10. Definition of β . The profile tip was not considered to suppress errors from tip recognition uncertainty in the cross-section detection algorithm. Flexible profile deformation for multiple periods, expressed with the deformed angle of incidence β ($\alpha = 28^\circ$, $k = 0.24$).

4. Conclusions

A time-resolved 2D2C PIV study was performed on a hyperflexible pitching hydrofoil in a closed water tunnel. The open-source toolbox fluidimage and custom routines were deployed for post-processing the raw data after validation by comparison with a commercial reference code. This installation is deployed as a surrogate model for a CFTT. The flow field analysis allows for a clear description of the influence of the novel approach to deploy flexible turbine blades on CFTT. Furthermore, it provides a better understanding of the underlying mechanisms for these positive effects of passive flow control. The advantages of this model are the ability to closely investigate the CFTT rotor flow field at the blade level for multiple designs and operating points without hardware modifications. It could be shown that deployment of hyperflexible turbine blades attenuates the dynamic profile stall characteristics. This results in a smaller wake size during the fully stalled periods of a rotor revolution. Also, the periods of flow separation are shortened, which allows for a reduction of the drag and of the hydrodynamic loads. Chordwise flapping can be observed while the main vortex is shed after convection over the profile. In summary, it can be stated that the blade flexibility passively controls the flow by its adaptation. The hydrodynamic loads induce profile deformation, which reduces load peaks, ultimately leading to a damping of stall dynamics.

The flexibility of the blades is found to have significant effect on the structure of the wake. Beside a descriptive visual comparison of instantaneous and phase-averaged flow fields, the similarity between them was described quantitatively using the structural similarity index. The SSIM was found to be significantly higher (rising from 0.893 to 0.963) when using the flexible structure, showing fewer stochastic changes in wake features from period to period. This may be advantageous for farm installations.

In a parallel study using the same setup, surface tracking measurements were conducted; further work is intended to investigate the flow fields for multiple reduced frequencies and to link the results to the structural response and hydrodynamic loads. The effect of wake periodicity concerning energy harvesting will also be investigated in the future.

5. Materials

The data that supports the findings of the study are available from the corresponding author upon request.

Author Contributions: S.H. designed the experiment, acquired and post-processed the data. S.A. and S.H. designed and set up the drive and data acquisition system. I.K. coded the masking algorithm,

preprocessed and processed the PIV data. L.V. supervised the PIV setup. S.H. and O.C. analyzed the results. T.M. and D.T. supervised the study. All authors have read and agreed to the published version of the manuscript.

Funding: This research was funded by Rosa-Luxemburg-Stiftung Berlin PhD Scholarship, by the German Federal Ministry of Education and Research Wachstumskern Flusstrom Plus project (03WKC02B) and by the German-French-University Saarbrücken Cotutelle Scholarship.

Acknowledgments: The authors thank Michel Riondet (CNRS), Nicole Lambert (CNRS), Fabio Martins (OvGU), Anurag Misra (OvGU), Gabriel Moreau (CNRS) for their support. The authors are grateful for the support of Cyrille Bonamy (CNRS) and Pierre Augier (CNRS) regarding the use of the Fluidimage code.

Conflicts of Interest: The authors declare no conflict of interest.

Abbreviations

The following abbreviations are used in this manuscript:

2D2CV	Two dimensions two components
BEP	Best-efficiency point
CAD	Computer-aided design
CFTT	Cross-flow tidal turbines
PIV	Particle image velocimetry
LDA	Laser-Doppler anemometry
LEGI	Laboratoire des Écoulements Géophysiques et Industriels
NACA	National Advisory Committee for Aeronautics
NaN	Not-a-Number
SSIM	Structural Similarity Index
TPS	Thin plate spline
α	Angle of attack [°]
λ	Tip-speed ratio [-]
ρ	Density [kg/m ³]
σ	Rotor solidity [-]
Θ	Rotor azimuth angle [rad]
ω	Angular velocity [rad/s]
f	Frequency [Hz]
k	Reduced frequency [-]
n	Number of blades [-]
v	Absolute flow velocity [m/s]
w	Relative flow velocity [m/s]
C	Blade chord length [m]
H	Height [m]
L	Length [m]
R	Turbine radius [m]
W	Width [m]
Re	Reynolds number [-]
∞	free-stream condition
ch	water channel
max	maximum
o	oscillation
'	temporal derivation
-	average

References

1. Brownstein, I.; Kinzel, M.; Dabiri, J. Performance enhancement of downstream vertical-axis wind turbines. *J. Renew. Sustain. Energy* **2016**, *8*, 053306. [[CrossRef](#)]
2. Dabiri, J. Potential order-of-magnitude enhancement of wind farm power density via counter-rotating vertical-axis wind turbine arrays. *J. Renew. Sustain. Energy* **2011**, *3*. [[CrossRef](#)]

3. Whittlesey, R.; Liska, S.; Dabiri, J. Fish schooling as a basis for vertical axis wind turbine farm design. *Bioinspir. Biomimetics* **2010**, *5*, 035005. [[CrossRef](#)] [[PubMed](#)]
4. Jiang, C.; Shu, X.; Chen, J.; Bao, L.; Li, H. Research on Performance Evaluation of Tidal Energy Turbine under Variable Velocity. *Energies* **2020**, *23*, 6313. [[CrossRef](#)]
5. Shiono, M.; Suzuki, K.; Kiho, S. An experimental study of the characteristics of a Darrieus turbine for tidal power generation. *Electr. Eng. Jpn.* **2000**, *132*, 38–47. [[CrossRef](#)]
6. Paraschivoiu, I. *Wind Turbine Design: With Emphasis on Darrieus Concept*, 2nd ed.; Presses Internationales Polytechnique: Montréal, QC, Canada, 2002; ISBN 987-2-553-00931-0.
7. Laneville, A.; Vittecoq, P. Dynamic Stall: The Case of the Vertical Axis Wind Turbine. *J. Sol. Energy Eng. Trans. ASME* **1986**, *108*, 140–145. [[CrossRef](#)]
8. Ferreira, C.S.; van Kuik, G.; van Bussel, G.; Scarano, F. Visualization by PIV of dynamic stall on a vertical axis wind turbine. *Exp. Fluids* **2009**, *46*, 97–108. [[CrossRef](#)]
9. Gorle, J.; Chatellier, L.; Pons, F.; Ba, M. Flow and performance analysis of H-Darrieus hydroturbine in a confined flow: A computational and experimental study. *J. Fluids Struct.* **2016**, *66*, 382–402. [[CrossRef](#)]
10. Buchner, A.J.; Honnery, D.; Soria, J. Stability and three-dimensional evolution of a transitional dynamic stall vortex. *J. Fluid Mech.* **2017**, *823*, 166–197. [[CrossRef](#)]
11. Buchner, A.J.; Soria, J.; Honnery, D.; Smits, A. Dynamic stall in vertical axis wind turbines: Scaling and topological considerations. *J. Fluid Mech.* **2018**, *841*, 746–766. [[CrossRef](#)]
12. Miller, M.; Duvvuri, S.; Brownstein, I.; Lee, M.; Dabiri, J.; Hultmark, M. Vertical-axis wind turbine experiments at full dynamic similarity. *J. Fluid Mech.* **2018**, *844*, 707–720. [[CrossRef](#)]
13. Benton, S.; Visbal, M. The onset of dynamic stall at a high, transitional Reynolds number. *J. Fluid Mech.* **2019**, *861*, 860–885. [[CrossRef](#)]
14. Müller-Vahl, H.; Strangfeld, C.; Nayeri, C.; Paschereit, C.; Greenblatt, D. Control of thick airfoil, deep dynamic stall using steady blowing. *AIAA J.* **2014**, *53*, 277–295. [[CrossRef](#)]
15. Müller-Vahl, H.; Nayeri, C.; Paschereit, C.; Greenblatt, D. Dynamic stall control via adaptive blowing. *Renew. Energy* **2016**, *97*, 47–64. [[CrossRef](#)]
16. Lazauskas, L.; Kirke, B. Modelling passive variable pitch cross flow hydrokinetic turbines to maximize performance and smooth operation. *Renew. Energy* **2012**, *45*, 41–50. [[CrossRef](#)]
17. Khalid, S.; Liang, Z.; Sheng, Q.H.; Zhang, X.W. Difference between Fixed and Variable Pitch Vertical Axis Tidal Turbine—Using CFD Analysis in CFX. *Res. J. Appl. Sci. Eng. Technol.* **2013**, *5*, 319–325.
18. Mauri, M.; Bayati, I.; Belloli, M. Design and realisation of a high-performance active pitch-controlled H-Darrieus VAWT for urban installations. In Proceedings of the 3rd Renewable Power Generation Conference, Naples, Italy, 24–25 September 2014; [[CrossRef](#)]
19. Abbaszadeh, S.; Hoerner, S.; Maître, T.; Leidhold, R. Experimental investigation of an optimised pitch control for a vertical-axis turbine. *IET Renew. Power Gener.* **2019**, *13*, 3106–3112. [[CrossRef](#)]
20. Strom, B.; Brunton, S.; Polagye, B. Intracycle angular velocity control of cross-flow turbines. *Nat. Energy* **2016**, *2*, 1–9. [[CrossRef](#)]
21. Fish, F. Power output and propulsive efficiency of swimming bottlenose dolphins (*tursiops truncatus*). *J. Exp. Biol.* **1993**, *183*, 179–193.
22. Zeiner-Gundersen, D. A novel flexible foil vertical axis turbine for river, ocean and tidal applications. *Appl. Energy* **2015**, *151*, 60–66. [[CrossRef](#)]
23. MacPhee, D.; Beyene, A. Fluid–structure interaction analysis of a morphing vertical axis wind turbine. *J. Fluids Struct.* **2016**, *60*, 143–159. [[CrossRef](#)]
24. Hoerner, S.; Abbaszadeh, S.; Maître, T.; Cleynen, O.; Thévenin, D. Characteristics of the fluid–Structure interaction within Darrieus water turbines with highly flexible blades. *J. Fluids Struct.* **2019**, *88C*, 13–30. [[CrossRef](#)]
25. Hoerner, S.; Bonamy, C.; Cleynen, O.; Maître, T.; Thévenin, D. Darrieus vertical-axis water turbines: Deformation and force measurements on bioinspired highly flexible blade profiles. *Exp. Fluids* **2020**, *61*. [[CrossRef](#)]
26. Ly, K.; Chasteau, V. Experiments on an Oscillating Aerofoil and Applications to Wind-Energy Converters. *J. Energy* **1981**, *5*, 116–121. [[CrossRef](#)]
27. Hoerner, S. Characterization of the Fluid–Structure Interaction on a Vertical Axis Turbine with Deformable Blades. Ph.D. Thesis, University Otto-von-Guericke, Magdeburg, Germany, 2020; [[CrossRef](#)]
28. Augier, P.; Mohanan, V.; Bonamy, C. FluidDyn: A Python open-source framework for research and teaching in fluid dynamics by simulations, experiments and data processing. *J. Open Res. Softw.* **2019**, *7*. [[CrossRef](#)]
29. McCroskey, W.; Carr, L.; McAllister, K. Dynamic Stall Experiments on Oscillating Airfoils. *AIAA J.* **1976**, *57*–63. [[CrossRef](#)]
30. Ducoin, A.; Astolfi, J.A.; Sigrist, J.F. An experimental analysis of fluid structure interaction on a flexible hydrofoil in various flow regimes including cavitating flow. *Eur. J. Mech.-B/Fluids* **2012**, *36*, 63–74. [[CrossRef](#)]
31. Ducoin, A.; Deniset, F.; Astolfi, J.A.; Sigrist, J.F. Computational and experimental investigation of flow over a transient pitching hydrofoil. *Eur. J. Mech.* **2009**, *28*, 728–743. [[CrossRef](#)]

32. Hoerner, S.; Bonamy, C. Structured-light-based surface measuring for application in fluid—Structure interaction. *Exp. Fluids* **2019**, *60*, 168. [[CrossRef](#)]
33. Wang, Z.; Bovik, A.C.; Sheikh, H.R.; Simoncelli, E.P. Image quality assessment: From error visibility to structural similarity. *IEEE Trans. Image Process.* **2004**, *13*, 600–612. [[CrossRef](#)]

A.2 Publication II

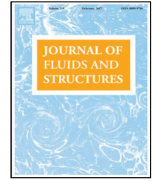
W. I. Kösters and S. Hoerner (Aug. 2023). “Simultaneous flow measurement and deformation tracking for passive flow control experiments involving fluid–structure interactions”. In: *Journal of Fluids and Structures* 121, p. 103956. DOI: [10.1016/j.jfluidstructs.2023.103956](https://doi.org/10.1016/j.jfluidstructs.2023.103956)

This publication corresponds to Contribution I, discussed in section 2.



Contents lists available at ScienceDirect

Journal of Fluids and Structures

journal homepage: www.elsevier.com/locate/jfs

Simultaneous flow measurement and deformation tracking for passive flow control experiments involving fluid–structure interactions



Wolf Iring Kösters^{a,b,*}, Stefan Hoerner^a

^a Laboratory of Fluid Dynamics and Technical Flows, Institute of Fluid Dynamics and Thermodynamics, Otto von Guericke University Magdeburg (OvGU), Universitätsplatz 2, 39106 Magdeburg, Germany

^b Center for Biorobotics, Tallinn University of Technology (Taltech), Akadeemia tee 15A, 12616 Tallinn, Estonia

ARTICLE INFO

Article history:

Received 10 January 2023

Received in revised form 12 July 2023

Accepted 18 July 2023

Available online 8 August 2023

Dataset link: [10.24352/UB.OVGU-2022-085](https://doi.org/10.24352/UB.OVGU-2022-085),
https://github.com/ikoesters/FSL_tracking

Keywords:

Fluid–structure interaction

Deformation tracking

PIV

Masking

NACA0018 hydrofoil

Passive flow control

ABSTRACT

Fluid–structure interactions (FSI) on highly flexible structures involve large deformations and require specific techniques for a thorough investigation of the flow field and structural deformation. To this purpose, a physics-informed method is introduced that allows for simultaneous determination of the flow fields and the structural deformation by using Particle Image Velocimetry (PIV) raw images. The method combines apriori knowledge of the mechanical characteristics of the flexible structure with classical image processing techniques for segmentation. PIV recordings of an actively pitched, highly deformable hydrodynamic profile experiment in a closed water tunnel serve as an example case. To achieve accurate results, the contour obtained from image segmentation is further defined under the assumption that its flexure can be described with the Euler–Bernoulli beam theory model. This makes it possible to determine the neutral fiber of the structure and the final reconstruction becomes possible from knowledge of the original geometry. The resulting procedure allows for a recognition of the structure itself and is suitable for cross-section deformation measurements and for masking of the structure in the raw images to improve the PIV processing. A test case comprising synthetic data similar to the application with a modeled profile geometry of known shape is used to investigate the accuracy of the method and its validity for deformation measurements. Under conditions of cyclic dynamic stall, a mean absolute error of 0.84° could be reached, with a deterioration up to 2° mean absolute error under static stall. The method has a major advantage compared to other technically more sophisticated and complex methods, such as the combination of Laser interferometers combined with Laser-Doppler Anemometry: the method allows for the usage of a single data source for both, fluid and solid in a unified measurement method. Therefore a direct comparison of instantaneous flow field and deformation is possible. In consequence it is in particular useful for highly dynamic multi-physical processes involving extreme deformations, such as passive flow control and soft actuated or flexible under water robotics.

© 2023 The Author(s). Published by Elsevier Ltd. This is an open access article under the CC BY license (<http://creativecommons.org/licenses/by/4.0/>).

* Corresponding author at: Laboratory of Fluid Dynamics and Technical Flows, Institute of Fluid Dynamics and Thermodynamics, Otto von Guericke University Magdeburg (OvGU), Universitätsplatz 2, 39106 Magdeburg, Germany.

E-mail address: wolf.koesters@ovgu.de (W.I. Kösters).

Nomenclature

2D2C	two directions, two components
C	normalized position on the mean-line (chord-line)
FSI	fluid–structure interaction
IoU	intersection over union
IQR	interquartile range
LEGI	Laboratoire des Ecoulements Geophysiques et Industriels
LIF	laser-induced fluorescence
MRI	magnetic resonance imaging
NACA	National Advisory Committee for Aeronautics
px	pixel within frames to be segmented
RMSE	root-mean-square error

1. Introduction

Flexible underwater structures are commonplace in nature. They are required for the undulatory locomotion of aquatic animals including fish, pinnipeds, and cetaceans. In the context of bio-inspired technologies they can also provide substantial benefits for technical applications including soft actuated and flexible underwater robots (Bozkurttas et al., 2006; Salumäe et al., 2014; Tangorra et al., 2011) and can be used for passive flow control methods, as investigated for vertical-axis turbines such as those presented by Zeiner-Gundersen (2015) or (Hoerner et al., 2019, 2021a). Indeed, the latter studies were originally the motivation for developing the method at hand.

The multi-physical interactions resulting from hyper-flexibility lead to a strong coupling between fluid forces and structural deformations. They are often found, for instance for fluid-induced vibrations or flutter. Numerical methods remain costly and challenging, in particular, if a complex, non-homogeneous structure is subjected to strong deformations (Fabbri, 2022). However, new experimental methods can provide simultaneous measurement of the instantaneous flow fields and structural deformations. This allows for deeper insights into the underlying physical mechanisms as well as investigations of more complex applications of fluid–structure interactions (FSI). Particle image velocimetry (PIV) analysis is the commonly employed method for the investigation of instantaneous flow fields. However, it typically considers a single phase containing the seed particles, so that other structures or phases cannot be tracked directly. Without proper preparation of the experimental setup and data treatment, the computed velocity fields will generally contain spurious vectors inside and in the vicinity of the additional phases and structures, thereby decreasing the reliability of the measurements and constraining the analysis of the whole vector field. To improve quality, it is crucial to mask the non-seeded phases and structures to correctly analyze the seeded phase.

Fujiwara et al. (2004) recognized that there is another advantage in doing so: the obtained masks can be used to reveal the movement of the other phase and its shape (air bubbles in water). Those can be directly used for FSI analysis, allowing for an investigation of the structural displacement or deformation and its relationship to the flow field. Therefore, the automated recognition and masking of non-seeded phases, such as bubbles or structures can improve and enhance experimental studies of multiphase flows and FSI configurations. Since the study of multiphase flows and of the flow around arbitrarily moving bodies or deforming phases (e.g., bubbles) is of much interest for many applications of fluid mechanics, many approaches have been developed to investigate them.

Examples of applications can in particular be found for tracking sand particles within a gas flow (Zhang et al., 2008; Muste et al., 2009; Capone et al., 2015), or for investigating trajectories in a bubble column (Fujiwara et al., 2004; Bröder and Sommerfeld, 2007; Rzehak et al., 2017; Kováts et al., 2017).

To perform a reliable PIV analysis of bubbles and bubble columns, the gas phase or bubbles have to be segmented. A popular method is to use laser-induced fluorescence (LIF) in combination with shadowgraphy (Boëdec and Simoëns, 2001; Lindken and Merzkirch, 2002; Fujiwara et al., 2004; Bröder and Sommerfeld, 2007).

The light scatter at the bubble interface often surpasses the intensity of the light scatter of the seed particles by an order of magnitude or more. This was exploited by several research groups that used digital image processing to derive masks (Cardwell et al., 2011; Gui et al., 1997; Dussol et al., 2016).

Methods relying on brightness intensity and size evaluation are used extensively when investigating particle flows (Muste et al., 2009; Cheng et al., 2010; Diez et al., 2011; Dearing et al., 2013; Capone et al., 2015). This is particularly well-suited when large differences exist between the size of the particles that interact with the flow – very often, sand is used – and the size of the PIV seed particles. In a recent development, purely data-driven methods for particle segmentation have emerged based on an autoencoder, a type of generative adversarial network (Vennemann and Rösgen, 2020). During the encoding step, the tracer particles are lost, while the shape of the sand particle is retained, and can thus be used as a mask. In experiments with free-surface flows, the sudden jump in local light intensity at the interface can be exploited (Sanchis and Jensen, 2011; Jeon and Sung, 2011; Weheliye et al., 2012; Vested et al., 2018).

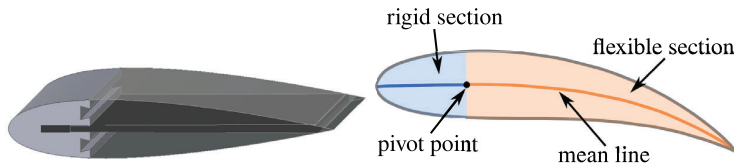


Fig. 1. (Left) Design of the flexible hydrofoil; (Right) Flexible and rigid section of the foil, with the pivot point at their interface and the mean line, here defined as the points midway between the upper and lower surfaces of the foil.

Markers on a body can be tracked with a stereoscopic camera setup, which allows for building a three-dimensional body that is then translated back to the image needed for masking (Tregidgo et al., 2013; Nikoueyan and Naughton, 2018; Fatiha et al., 2019). The differentiation between tracking points and tracer particles can be achieved by a minimum filter in the time domain if the body moves sufficiently slower compared the tracer particles within the fluid (Mitrotta et al., 2019). Deriving complex shapes from the deformation field of a projected pattern of structured light is also a well-known technique. It has been successfully implemented for surface deformation measurements of a flexible hydrofoil (Hoerner and Bonamy, 2019), which allows for capturing the 3D deformations of the surfaces from 2D single camera recordings. Commercially available laser-line profile scanners have been used to measure the deformation of a flexible sheet along one axis (Ducoin et al., 2012; Kalmbach and Breuer, 2013; Akcabay et al., 2014). The light scatter induced by the PIV light sheet was used for a similar purpose by several researchers (Rojratsirikul et al., 2009; Gomes et al., 2011; Nikoueyan and Naughton, 2018).

Finally, it should be noted that seed particle displacement does not necessarily have to be recorded by a camera: (Hessenthaler et al., 2017) used magnetic resonance imaging (MRI) to measure the position of seed particles without any need for masking the flexible rubber body present in the study.

It is often possible to generate accurate masks without tracking the second phase, thereby greatly simplifying the experimental setup. However, this translates into a segmentation problem for digital image processing. This issue has already been investigated extensively for gas-liquid phase segmentation (Gui et al., 1997; Cardwell et al., 2011; Sanchis and Jensen, 2011; Jeon and Sung, 2011; Weheliye et al., 2012; Dussol et al., 2016), but to the knowledge of the authors not yet for the segmentation of flexible bodies within a fluid flow acquired with a single-camera setup. Additionally, the suitability and precision of the computed masks for quantifying the deformation of the body have not been quantitatively assessed yet.

In this study, we aim to: (1) determine the body's deformation resulting from the fluid-structure interaction, and, (2) provide an exact masking of a highly flexible body based on the evaluation of the local light intensity. The central objective is to provide a simple and accurate tool to capture the full FSI from a single measurement and to improve the PIV results. The proposed physics-informed method uses apriori knowledge of the flexible structure in particular its bending characteristics, in conjunction with morphological image processing. As an application case, an actively pitched and highly deformable hydrofoil experiment in the water tunnel at LEGI Labs Grenoble is used. The results of the experiment's reference case with known shape serve as an evaluation case of the accuracy of the method itself deploying the PIV raw footage of the known geometry. A test case from synthetic data similar to this example has been created and allows for the quantitative determination of the accuracy of the developed procedure. Although the method is tailored towards this particular data set and may not be an out-of-the-box solution for a different body or a different experimental setup, many steps of the proposed method are universal. Consequently, this publication serves as a description of a general method and provides a computational framework adaptable to the specific needs of any other similar experimental work. This is of particular interest for FSI studies where a low-order structural model already exists which can be exploited to significantly improve the accuracy and reliability of the method.

2. Methodology

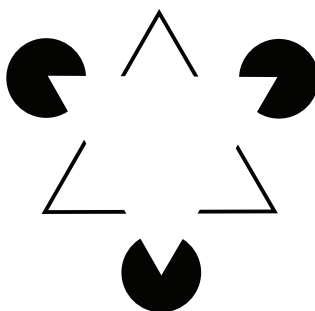
The data used in this study is based on an FSI case of a highly flexible hydrofoil for the passive flow control in cross-flow tidal turbines performed in a closed water tunnel in a fully turbulent flow (chord-based $Re \approx 250,000$). The hydrofoil with a NACA0018 shape consists of (1) a rigid front section from the leading edge to the pivot point (placed at $0.25C$), and (2) a flexible body in chord-wise direction in between the pivot point and the trailing edge, as can be seen in Fig. 1. The rigid tip section was milled from aluminum and can be considered rigid, while the flexible section consisted of a silicone body with a thin, carbon-fiber-enforced composite plate in the middle to provide adequate stiffness. The silicone body provides the external shape. Yet, its contribution to the stiffness is negligible as its Young's modulus is about 10 000 times lower than the modulus of the composite material. All details about the experimental base setup can be found in Hoerner et al. (2019, 2020).

For the PIV setup, a two-dimensional planar PIV high-speed setup (2D2C) with continuous recording at a frame rate of 4000 Hz was chosen, using a Phantom V2511 camera with specifications given in Table 1. Further details concerning the PIV measurements can be found in Hoerner et al. (2021b). The hydrofoil was actively pitched along a specific trajectory

Table 1

Specifications of the PIV setup.

chord-based Reynolds number	250 000
mean flow speed	3.5 m s^{-1}
maximal inclination	30°
image acquisition rate	4 kHz
force & angle acquisition rate	1 kHz
resolution	1280×800 pixel (px)
PIV type	high-speed 2D2C, single shot
illumination	continuous laser
flow field capture	instantaneous

**Fig. 2.** Kanizsa's triangle: a visual illusion comparable to how the foil is recognized by human perception (Kanizsa, 1955).

representing the variation of the angle of attack for a blade of a Darrieus vertical-axis turbine during each turn of the rotor. The angular position of the drive system performing the pitch motion was recorded by the drive encoder with a frequency of 1000 Hz. The light sheet generated by two opposite continuous lasers had a thickness of 2 mm. The seed particles were hollow glass spheres with a $10 \mu\text{m}$ diameter.

A detailed description of the process conditions (foil dimension, trajectory, measured signals) is provided in Hoerner et al. (2021a).

While looking for an appropriate algorithm that provided automated mask generation of the deforming structure, it became apparent that established methods that segment visible objects within a picture, e.g. bubbles, are not applicable here. The challenge of the problem stems from the fact that the contour of the foil, which is easily recognizable for a human being, is rather an 'illusory contour' – the visual illusion that evokes the perception of an edge where there is none (von der Heydt et al., 1984). Fig. 2 depicts a well-known example of this.

The task was therefore to recognize this illusory contour in the PIV raw data. Unfortunately, in contrast to the visual perception of human beings, identifying such contours poses a significant challenge to image recognition algorithms. All existing algorithms show specific shortcomings, as described next.

Edge detection as done by Bröder and Sommerfeld (2007) cannot be employed in this study, as there is no visible edge present in the image. Shape-matching of the whole body shape by (cross-)correlation (Gonzalez and Woods, 2008) could perhaps be done using numerous pre-processed bodies at various pitch angles and flexures, but seems impractical due to the sheer amount of cases that would need to be stored and loaded for this purpose. Feature matching would simplify the matching process by breaking the shape into smaller pieces (Jeon and Sung, 2011); however, the size of these pieces needs to be chosen according to the bending gradient of the foil. It is unclear whether these small features could still match at the end the overall foil geometry since, the smaller the representation, the more local seeding density will vary. Some spatial averaging would probably be required at the end, interfering with the procedure. Additionally, the occasional occurrence of outline reflections might lower the recognition ability.

Radon transform has been used with success for wave detection (Sanchis and Jensen, 2011), but is not straightforward to implement when handling closed objects. It would be necessary to either split the upper and lower surface of the foil before recognition or to reliably discern between the two from the results of the Radon transform. Otherwise, it would be unclear whether the recognized section comes from the upper or lower surface of the foil, and a closed body would not be suitably reconstructed.

The local variance of the illumination, as applied by Weheliye et al. (2012), was applied in this study as well; however, the method was not able to distinguish with sufficient accuracy between the body and the fluid.

A somewhat related masking challenge successfully used region-growing to delimit the particle-containing area (Dussol et al., 2016). However, our own results with this approach were disappointing: the seed density was not high enough to reliably return the shape of the foil.

The strongest bias comes from the foil's shape, while another comes from its non-homogeneous composition, with a rigid part at the leading edge (between position 0 and 0.25 on a normalized mean line (C)), and a flexible part between

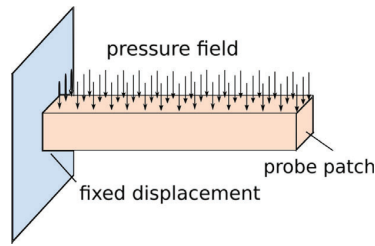


Fig. 3. Clamped beam as mechanical model for the flexure of the foil.

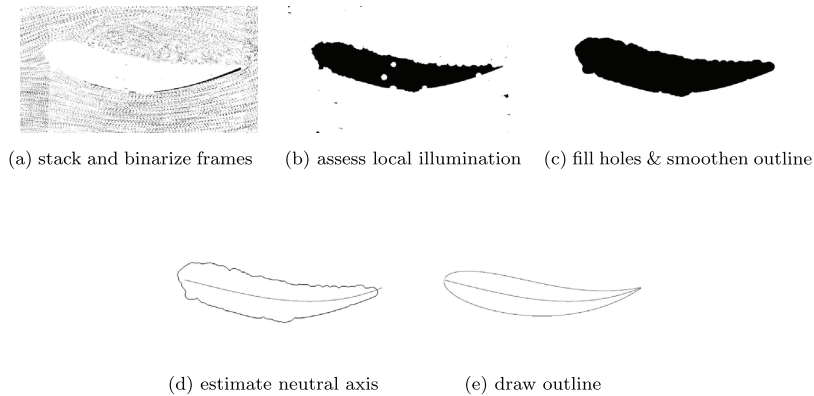


Fig. 4. Processing steps of the implemented algorithm for an exemplary foil position during its movement.

0.25 and 1 C. The pivot point lies at the interface between the two sections (at 0.25 C) and is located on the mean line (synonymously used for camber mean-line or camber line), which is the locus of points midway between the upper and lower surfaces.

The design considered in the study is shown in Fig. 1. Concerning foil thickness, the 4-digit NACA convention (Jacobs et al., 1933) will be used subsequently. It defines the thickness to be the distance between the upper and lower surface along the line normal to the mean line.

3. Procedure

Knowing the flexible and rigid sections of the foil, the neutral axis chord of the profile was modeled under the assumption of a clamped beam with its behavior described using the Euler–Bernoulli beam theory and illustrated in Fig. 3.

Even though the real structure is a plate rather than an Euler–Bernoulli beam, the primary objective of the experiment was to implement a case that allows for a simplified 1D model of the structure within a 2D flow that we measured using 2D2C high-speed PIV. 3D structural effects are generally present in the real system and have been investigated thoroughly in Hoerner and Bonamy (2019). For the method presented here, they have been considered to be negligible here, as we evaluate the hydrofoil only in the light sheet of the PIV system which has a thickness of less than 2 mm. The foil's outline was computed with the respective distance from the neutral axis for each point along the chord. Example images produced by each of the individual steps of the procedure are shown in Fig. 4.

The proposed method performs the subsequent steps to detect and mask the profile cross-section in a series of image processing stages:

Denoise, Stack & Binarize Frames (Fig. 4(a)): Initially, the image is denoised by setting a relative threshold, which regards pixel values above a certain percentile of the distribution of all pixel values within the image as signal and below as noise. Thereafter, consecutive frames are stacked to increase the difference in seed density between the flexible foil and the surrounding fluid. However, this step must be carefully implemented; while it increases recognition accuracy, it simultaneously reduces temporal resolution. Excessive stacking of frames blurs fast movements of the foil, thus diminishing detection accuracy. For subsequent processing with binary kernel operators, the image is binarized where anything above 0 is set to 1. Additionally, the image is cropped with a static window to the area of interest around the foil body to improve performance.

Assess Local Illumination Density (Fig. 4(b)): To assess the seed density within a certain area of the image, a convolution is applied with a matrix that contains ones exclusively arranged in a round shape. This is done by shifting this matrix or kernel successively over the image, multiplying corresponding elements, and summing them to create a new image. The area is regarded as foil body if it is above a threshold, or surrounding fluid if it is below, in our case best results are achieved if this threshold is 1. This method is comparable to the so-called majority filtering proposed by [Dussol et al. \(2016\)](#) and can be found in the reference work regarding digital image processing by [Gonzalez and Woods \(2008, p. 728\)](#). The associated threshold depends on the aggressiveness of the noise removal done in the previous step. In our case, the best strategy was finally found to denoise aggressively and put the threshold at 1 – the whole window will be regarded as fluid if one pixel is active.

Postprocess the Obtained Shape (Fig. 4(c)): Despite the foil body being recognized, holes within that body and islands within the fluid remain. In some parts of the fluid, no seed particles are found, while reflections within the foil body lead to falsely recognized fluid. The resulting artifacts are removed by morphological processing using the open-source toolbox called Scikit-image ([van der Walt et al., 2014](#)): The holes in the body are removed by binary closing, a combination of a binary dilation followed by a binary erosion; this also smoothens the shape. The islands in the fluid are removed by evaluating the size of all islands and remove all but the largest, the foil body. Unfortunately, as a result of the smoothing, the narrow leading edge got unintentionally removed as well which will be corrected in the proceeding step.

regions

Retrieve Meanline To compute the meanline, a Laplace filter first obtains the outline of the body. Then, for each index along the chordwise axis, the mean of the upper and the lower value is computed to obtain the meanline. As a result of the preceding binary closing operation, the trailing edge got removed. To restore it, the whole meanline is fitted with a third-degree polynomial fit which is extrapolated towards the trailing edge. This bending model stems from the assumption that the carbon-fiber composite can be considered to behave like a beam, clamped in the aluminum head, and bent by an end-load force. This is a standard case from the Euler–Bernoulli beam theory, in which the deflection curve is an exponential function of the third order. Several assumptions are required for this model: the beam must feature a constant bending stiffness, the elasticity must be linear, the bending must be purely axial, and the diameter must be invariant during flexure. In the case at hand, these premises were found to be met with negligible error ([Hoerner et al., 2019](#)). To give the meanline the correct length, it is first measured from the pivot point which serves as a fixed reference and then cut to the length known from the design specification.

Incorporate the Physics (Fig. 4(d)): Since the profile head consists of aluminum no bending occurs in this section. Thus, the mean line at the head is a straight segment with an inclination equal to the instantaneous pitch angle.

As data regarding the pitch angle exists from the drive's position feedback, the mean line between the rigid head and the pivot point is replaced by a straight line at the instantaneous pitch angle. To achieve a smooth transition between the two sections of the meanline, sample points are taken along both segments. All points are then fitted with a single polynomial fit of 4th order to account for the additional points in the rigid section. All points are then fitted with a single polynomial fit of 4th order to account for the additional points in the rigid section. An analysis of the data revealed negligible differences between 4th order and higher order fits, accordingly the lowest fit order was chosen. The amount of sample points is guided by the number of distinct samples needed to inconspicuously describe a linear regressive function. This is equal to the number of parameters that are estimated, as each sample reduces the degree of freedom in the linear system of equations by one. As shown by $\hat{y} = \hat{\beta}_0 + \hat{\beta}_1 x_1 + \hat{\beta}_2 x_2^2 + \dots$, the amount of parameters is equal to the degree of the fit function plus one. In our case, this leads to 4 sample points for the flexible section and 2 for the rigid section. However, the density of sample points from the rigid section is increased compared to the flexible section, as the confidence in the accuracy of the data is higher; shown in [Fig. 5](#) for the rigid front section of the profile. To locate the interface between the flexible and the rigid sections in the image as well as their respective beginnings and endings, the pivot point served as a reference.

Mitigate Image Recognition Errors: The points obtained from the mean line are filtered using a two-way (to remove an artificial phase shift), second-order low-pass Butterworth filter along the time axis (critical frequency/sample frequency = 0.1). This is done separately for both directions (x and y) in the image along the time axis. This process removes sudden jerks which can be considered as beyond the range of motion or acceleration and as an additional bias for the model. No filter was employed along the mean line itself, as this would violate the model assumptions.

Combine with NACA-Model & Postprocess (Fig. 4(e)): Using the mathematical description of a NACA0018 model, vectors from its mean line to the corresponding outline point were obtained. The number of points in the synthetic mean line was chosen equal to that of the recognized mean line. In consequence, for each point on the recognized mean line, a surface normal was computed and multiplied by the distance between meanline and outline of the undeformed NACA model from that particular chordwise position. The resulting vector was shifted to its respective, actual point along the mean line. In this manner, the NACA shape with the initially linear meanline can be projected onto the deformed mean line, as depicted in [Fig. 6 \(Left\)](#).

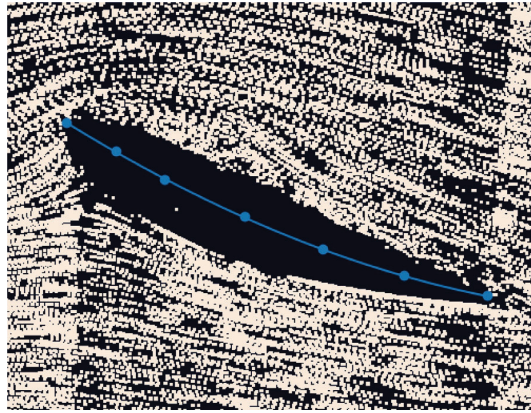


Fig. 5. The computed points along the mean line are shown interpolated by a 3rd-degree polynomial fit in a stacked frame. The seed particles are dilated for better visibility. Concerning the frontal rigid section, a larger number of points has been set to increase its relative effect in the fit.

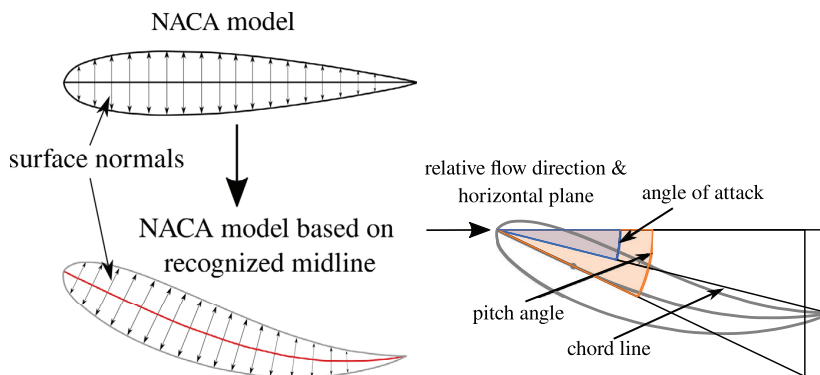


Fig. 6. (Left) Computation of the outline by the use of surface normals obtained from the NACA model; (Right) Angle of attack used in the comparison between measurements. The angle of attack is defined as the angle between the relative flow direction and the chordline. The chordline is defined as the straight line connecting the leading and trailing edges.

The source code has been made public and is available online,¹ licensed under GPLv3. It is written in Python and makes extensive use of the `scipy.ndimage` library (van der Walt et al., 2014), as well as of the Numerical Python (NumPy) package (van der Walt et al., 2011). The processing of 16,500 frames – the entire film length of the setup – with an output of one mean line for each frame, takes less than 20 min using an Intel Xeon CPU E5-2630 v3 at 2.40 GHz on a single thread. Generating and applying the respective mask takes about 5.5 h on the same system. This indicates that the bottleneck for the computation occurs in I/O operations, primarily from loading and saving the masked images to disk through a network drive. While the code is written for parallel execution, the parallelization is not implemented in practice, since performance gains are not to be expected as a consequence of the I/O limitation in the study presented here.

The framework with which the PIV computation was achieved, FluidImage (Augier et al., 2016), natively supports image pre-processing. This would allow for masking of the images without writing them to storage. After computing all mean lines, these lines could be saved and later accessed by FluidImage to create the instantaneous mask. Using this approach, high-performance gains are expected. The implementation of this parallelization feature will be considered as well as an integration of the source code into the FluidImage project in a future study.

4. Results & discussion

To assess the accuracy of the results, the algorithm is employed on synthetic data. This allows for a quantification of the limits of the methodology by implementing a stepwise reduction of the seed density.

¹ https://github.com/ikoesters/FSI_tracking

After the validation, the method is applied to real data of a rigid hydrofoil (with an exactly computable position), and finally on a flexible hydrofoil test case, where a qualitative assessment is performed.

4.1. Method validation with synthetic data

A significant factor in the usefulness of the method is its robustness regarding variations in seed density. Thus, an effort was made to quantify the influence of this parameter. The term summation window is used here for a convolution kernel consisting entirely of ones; effectively summing up all values within the window and storing the result in the window's center. The step size of this window, also called stride, is one pixel. The proposed method was employed on images considering different seed densities; additionally, a second parameter controlling the size of the summation window within the segmentation algorithm was set independently to study whether a larger window could counterbalance lower seed densities. To vary the seed density in a controlled and accurate manner, synthetic data was generated with a visual resemblance to the images for the final test case. A simple generation algorithm was chosen to reduce the underlying variability.

The algorithm first randomly initializes an array, serving as the particle-seeded background of the image. This array is binarized with a high threshold, resulting in a sparse particle seed with an area of 1 px each. Afterward, the array is dilated with a 3×3 px kernel for a realistic seed particle size and brightness variation. Different brightness emerges in cases where seed particles are generated in the direct vicinity and overlap. In the resulting image, these particles get deleted within an area corresponding to the geometry of a four-digit NACA profile (NACA15-5-18) according to [Jacobs et al. \(1933\)](#) to produce an illusory contour at a high inclination angle, somewhat comparable to the real data set (see raw images underneath the boxplot in [Fig. 7](#) for an illustration). This specific shape was chosen as it was manually determined from high-speed recordings of the load-deformed hydrofoils in the study at hand. The inclination angle of this foil is quantified by the angle from the leading to the trailing edge relative to the horizontal plane (as shown in [Fig. 6 \(Right\)](#)), which we will subsequently call the angle of attack. Its real value in the considered problem is 24.2° from the pivot point or 0° from the leading edge to the trailing edge.

Additionally, reflections and other false positives are added with the same method as the generated seed, but with an adjusted threshold. The area of a reflection is 1 px^2 with a value that is sufficient to trigger the algorithm; their number was chosen to visually resemble the real data at hand. This results, on average, in 3 (mean = 2.98, std = 1.84, N = 500) false positives, which amounts to an error rate of 50 ppm in relation to the foil size in pixels. A total of 100 images per seed density with randomly distributed seed particles were computed, without altering the foil shape or position over this period to give consistent and comparable results. The accumulated seed density in the real data can be freely chosen as a first step when employing our method, by controlling the number of stacked images in the process. Here, the seed density was set between $200 - 750 \frac{\text{particles}}{(100 \times 100) \text{ px}^2}$; the recognition quality below the lower limit is not adequate, while an excessive number of stacked frames would be necessary to exceed the upper limit. For the final example considered in our work, this range represents a stack size between 4 and 10 images, which is realistic. It should be noted that this leads to a time-averaging filter comparable to a rolling average in the deformation measurements, with a window in the stack size. To provide a realistic and conservative measure of the capabilities of the method, we chose a static case that does not employ any low-pass filtering, as cut-off frequency and gain are application-specific parameters. Lower movement speeds could potentially benefit from a reduced cut-off frequency, resulting in improved outcomes. Our decision to employ a static case without any filtering was made to circumvent this issue; this overestimates the error.

[Fig. 7](#) shows the recognition error (y-axis) of the algorithm in relation to different seed densities (x-axis) and the size of the summation window (colored bars). In the application at hand, the effective angle of attack for the deformation assessment is of interest, while for evaluating the masks we use intersection over union (IoU) as a metric, a similarity measure that computes how much two masks intersect relative to the area. It is the method performance measures in object detection commonly based upon ([Rezatofighi et al., 2019-06](#)). Additionally, we include the root-mean-square error (RMSE) to allow comparability to other methods.

It can be observed that within selected parameters the algorithm shows good performance over a wide range of seed densities. However, an average error of about 1° was observed in all cases. As can be seen in [Fig. 9](#), the angle of attack and the error on it are positively correlated. Since the foil only briefly reaches high angles of attack in the designated application, this level of error was considered uncritical, and no further effort was spent to investigate the source.

If the algorithm was to be applied, this problem can be circumvented by a correction function as the error was systematic and reproducible. However, to allow comparability this has not been done here.

While the larger window size has an increased chance that seed particles are present similar to a higher aperture of a camera, the greater size reduces the resolution of the segmented image available for the subsequent algorithm steps which diminishes the recognition quality. Additionally, the particles placed inside the structure have a much more pronounced effect. This can be observed at the lowest two seed densities where the medium-sized window balances out both effects and achieves the best error rate. At higher seed densities the benefit of the greater size diminishes and the smallest summation window performs markedly better than the others. The best results are therefore a trade-off between the two opposing effects and have to be determined in the specific case. The outliers within the investigation marked with diamonds, would likely be corrected by the low-pass filter, exploiting the structural similarity within small sections of the time-domain.

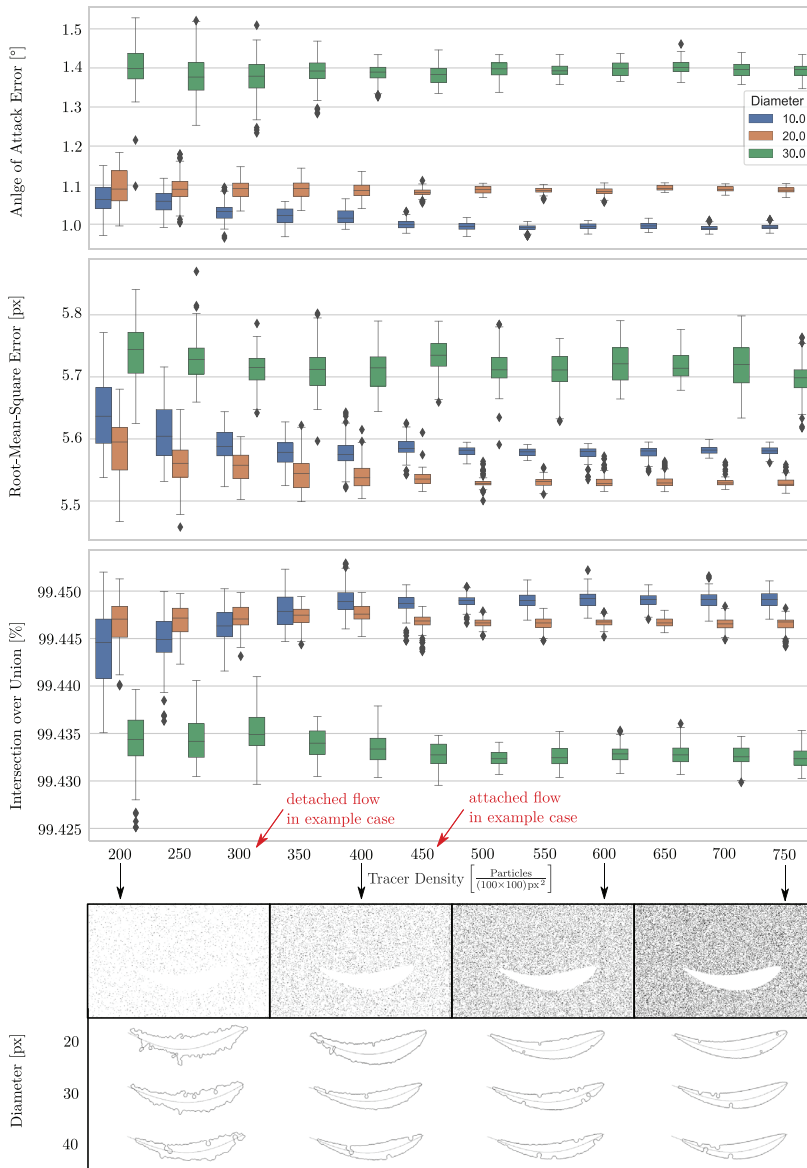


Fig. 7. Detection quality in relation to seed density and summation window diameter. The metrics used in our analysis include the difference in angle of attack, the intersection over union (IoU) for evaluating mask accuracy, and the root-mean-square error (RMSE) of the x–y distance between the true and identified points. Whiskers represent $1.5 \times$ IRQ (interquartile range), sample size is 100 images each. Recognized foils are shown below, selected from different source images to illustrate their respective differences.

In the next step, the impact on the recognition quality of regions with a reduced seed number density due to flow detachment or in a wake was simulated in a dedicated investigation. The image was artificially separated into two regions having distinct seed densities, with an interface roughly located along the camber line. The difference in the seed density was adjusted dynamically, the sparser side containing 66% of the density on the dense side. This ratio was derived from observations of real data, where a manual count performed on multiple regions and images produced an average seed density of around $75 \frac{\text{particles}}{(100 \times 100) \text{px}^2}$ in the attached flow, compared to $50 \frac{\text{particles}}{(100 \times 100) \text{px}^2}$ within the detached flow before stacking the frames to accumulate the seed density.

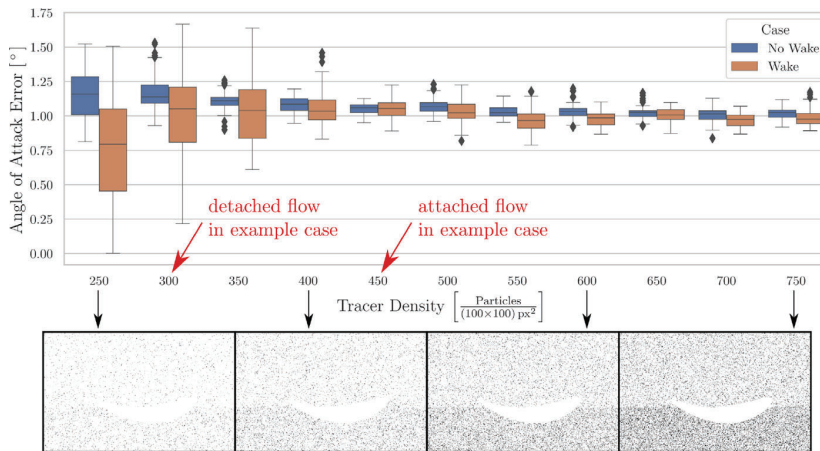


Fig. 8. Detection quality between a simulated region with low seeding density (detachment, wake) compared to the region with normal seeding density (attached flow). The seed density on the horizontal axis is that of the dense region. Whiskers represent $1.5 \times \text{IQR}$, the sample size is 100 images each.

The lower bound of 300 for the seed density in the tests was chosen as this results in a density of $300 \times 66\% = 200 \frac{\text{particles}}{(100 \times 100) \text{px}^2}$ in the detached flow. Higher measurement uncertainty is present in all investigations of the wake case, as can be observed in Fig. 8. Additionally, the bias observed in the last comparison is present as well, best visible in the densely seeded cases which experience low variance. If the value of 1° is assumed to be the correct measurement, the largest deviation of the $1.5 \times \text{inter-quartile range (IQR)}$ which includes 99.3% of all values is used as a rough estimate of quality. The largest difference is observed in the case with the lowest seed density where the largest deviation of the wake-case is 1° , while the non-wake-case experiences 0.5° leading to a disparity of 0.5° . Both were evaluated as non-significant for our case. In an exciting recent advancement, another solution to the problem of illusory contour segmentation problem has been proposed (Li et al., 2021); through creating an unstructured mesh in which each tracer particle represents a node. As the seeding density within the other phase is lower, the edges between nodes are longer and are removed through a threshold. Now unconnected nodes are pruned and a smooth curve is subsequently fitted over the division.

4.2. Application on real data

As aforementioned, experiments involving a hyper-flexible NACA0018 hydrofoil subjected to forced oscillation within a closed water tunnel at the LEGI laboratory in Grenoble have been performed (Hoerner et al., 2019; Hoerner and Bonamy, 2019; Hoerner et al., 2020, 2021b,a). The hydrofoil had a chord length of 66 mm, yielding a chord-based Reynolds number of $\text{Re} = 200,000$ when subjected to a flow velocity of 3 m s^{-1} . The forced oscillation was controlled by angle, following a predetermined trajectory that mimicked the flow experienced by a blade in a vertical-axis water turbine. The angle of incidence ranged from -30° to 30° . The entire experiment including set-up, blade models, and the resulting flow fields can be found in Hoerner et al. (2021a). To start with a validation case with known geometry, the algorithm was first employed on the rigid version of the foil. In that case, the mean line can simply be computed from the position feedback of the driver encoder, since no significant deformation occurs.

In Fig. 9 shows the mean measurement error in comparison to the position feedback from the driver encoder, with a mean absolute error of 0.84° . It has an apparent periodicity with the same frequency as the position feedback, however with a phase shift. Tests performed on a limited amount of different motion trajectories and frequencies could not yield a common set of parameters to fit their distinct error function. It was decided against a correction function, as the mechanics behind the error could not be narrowed down. However, the overall magnitude of the error correlates with: a) occurrence of detached flow and b) occurrence of reflections inside the foil. The sensitivity to detached flow has been studied with the help of synthetic data earlier and is also a challenge for the cross-correlation algorithm of the PIV algorithm. In a test case with static stall conditions, the most unfavorable conditions, the mean absolute error reached 2° . There is by the knowledge of the authors currently no available method to put this method into perspective. Dussol et al. (2016) used a very similar technique, however a validation of the segmentation accuracy was not performed. Hoerner and Bonamy (2019) used structured light to measure the deformation in 3D, while also performing a validation. They report a mean absolute error of 0.66 mm over a profile with a 66 mm chord line, which translates to an angular error of 0.01° . Even though this error is almost an order of magnitude lower, it requires a separate measurement setup while also being mutually exclusive to the PIV measurement due to the necessity of a reflective surface of the body.

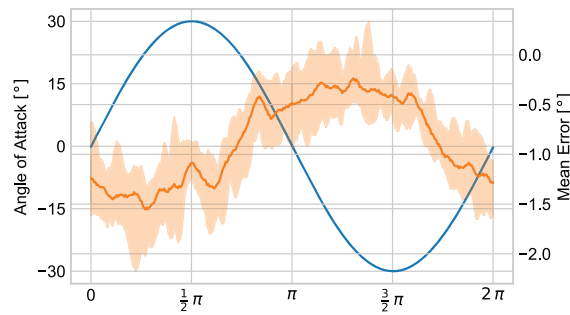


Fig. 9. The orange line shows the mean measurement error (right ordinate) over a full period at 3.1 Hz from a rigid hydrofoil averaged over 12 periods with the faded area representing the minimum and maximum value for each step. The blue line shows the sinusoidal position feedback from the drive system for comparison (left ordinate). (For interpretation of the references to color in this figure legend, the reader is referred to the web version of this article.)

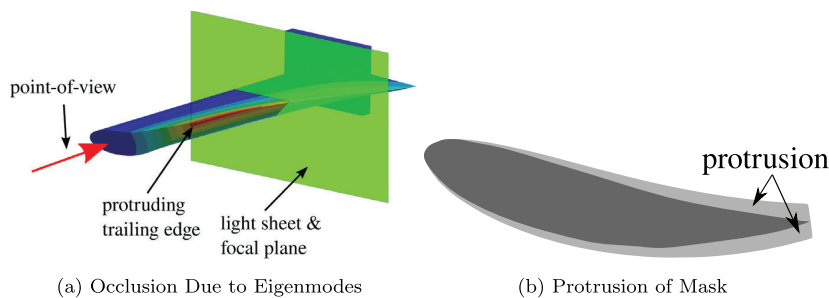


Fig. 10. Due to the eigenmodes of the structure, the body section closer to the camera's point-of-view occludes part of the deformation along the focal plane. Here, only one single eigenmode is shown for a better visibility. Mask after applying the linearly decreasing protrusion (i.e., artificial thickening).

4.3. Productive use in a flexible foil setup

Expanding on the aforementioned experiment, a highly flexible foil was used to investigate dynamic stall conditions between rigid and flexible foils. The dynamics of the dynamic stall event which occurred at every period of the enforced motion trajectory lead to a stochastic component in the deformation of the foil in the time domain. This made it impossible to independently quantify the accuracy of the method in this case without a second calibrated measurement data source. However, considering the previous investigations on the synthetic data of highly deformed foil and the tracking of a rigid foil on real data which yielded similar results, we can be confident about the adequacy of its performance. This was supported by visual inspection of the masked footage, which showed good tracking but revealed an apparent mismatch between the shape of the trailing edge in the footage and the mask. We determined this to be a result of the span-wise bending modes of the foil, as shown in Fig. 10(a). To account for this effect in the masking procedure, the recovered NACA shape was artificially enlarged by summation of a linearly decreasing term starting from the trailing edge, as shown in Fig. 10(b) for the final mask. Fig. 11 shows the combined PIV and FSI analysis for a flexible hydrofoil. While the diagram in the middle provides the reduced angle of attack due to the passive flow adaptation (blue line) for the instantaneous pitch angle of the blade (orange line). The diagram is embedded in the corresponding flow fields from the 2D2C high-speed PIV for particular points of interest during the oscillation period. The mask and the deflection were calculated with the methods at hand.

5. Conclusions

In this work, we showed that conventional image recognition can be constrained by physical assumptions of the system to greatly improve the recognition quality. The mentioned assumptions include kinematic assumptions on the bending shape, a dynamic assumption regarding the maximum oscillation frequency and morphological knowledge about the soft body. The benefit of the method is twofold: (a) providing a simple way to simultaneously measure the flow field and structural deformation with a single measurement, (b) creating the masks of the soft body undergoing FSI, which is a necessary part of the PIV analysis. The uncertainty of the method was found to be small enough to derive meaningful

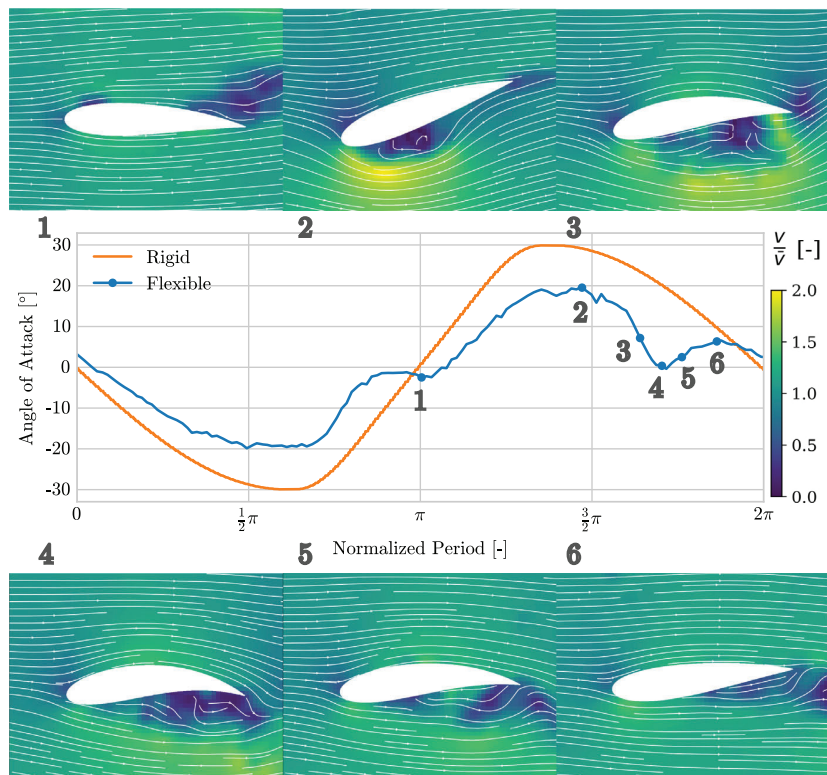


Fig. 11. Combined FSI and PIV analysis from a single image source. A hypothetical rigid blade for comparison to illustrate the degree of deformation.

conclusions for relevant FSI configurations. In a case study with a rigid hydrofoil actively pitched between -30° to 30° , the mean absolute error in the angle of attack was found to be sufficiently low at 0.8° . The presented method has already successfully been used in a recent FSI study to investigate the benefit of passive flow control with the use of a hyper-elastic structure (Hoerner et al., 2021b,a) by exploiting the mentioned benefits. However, certain requirements need to be met to yield satisfactory results: the body itself cannot be reflective or have reflective parts and sufficient particles need to be present for differentiation between body and surrounding in the image recognition step. Additionally, the method necessitates sufficient body thickness, rendering it unsuitable for elastic sheet models. An alternative approach, like the one used by Dussol et al. (2016), which leverages abrupt light intensity variations due to PIV light sheet scattering may be more fitting in this case. The subsequent enhancement of recognition through a kinematic model, as shown here, remains relevant. The sensitivity of the algorithm regarding the latter requirement was investigated through synthetic data controlled for seed density, as well as a wake case discrepancy in the seed density between the hydrofoil sides. Additionally, a naive approach to adapting the image recognition step to low seed densities were investigated by enlarging the kernel size, comparable to pupil dilation in low-light situations.

The method is set up in three distinct steps: (1) kernel-based image recognition, which is high in noise and can fail spectacularly in cases with an ill-arranged combination of reflection within the foil, (2) constrain the bending shape of the chord line to comply with the Euler-Bernoulli beam theory, (3) constrain the dynamic behavior of the deflection with a low-pass filter, (4) surround the obtained chord line with the known shape of the soft body.

As a next step, the method should be validated directly and quantitatively for flexible structures, either using laser interferometry along the trailing edge following (Ducoin et al., 2012), or by laser triangulation as implemented by Kalmbach and Breuer (2013).

Those steps will allow broader use of the method presented here, helping with the analysis of PIV data in fluid-structure experiments and soft actuation or flexible underwater robotics. The proposed method may be uniquely suitable to assess the kinematics of damaged flexible blades. For example, to assess blade motion before, during, and after impact damage with debris or after fatigue. This would allow for a more rapid laboratory assessment method for testing and validating the implementation of self-healing materials and condition monitoring for flexible blades in the future. Linking changes in the dynamic behavior to damage in a soft robotic gripper has recently been shown successfully with a nearly perfect detection and a 97% localization accuracy (Abdulali et al., 2022).

Declaration of competing interest

The authors declare the following financial interests/personal relationships which may be considered as potential competing interests: Wolf Iring Koesters reports financial support was provided by European Commission.

Data availability

A recent snapshot of the Python code along with a small segment of a high-speed video for testing is provided online in the open research data repository hosted by Otto-von-Guericke-University Magdeburg: [10.24352/UB.OVGU-2022-085](https://doi.org/10.24352/UB.OVGU-2022-085).

The code is under continuous development. The most recent version can be found on the author's git repository: https://github.com/ikoesters/FSL_tracking.

Acknowledgments

The authors thank Christian-Toralf Weber and Carsten Laddey (University of Applied Sciences Magdeburg) for providing the foundation for image material from structural mechanics analysis of the hydrofoil. The authors are grateful to Cyrille Bonamy and Pierre Augier (LEGI) for their work and their assistance regarding the incorporation of the PIV framework "FluidImage" into the workflow. Olivier Cleyner is thanked for language editing and commenting on the first manuscript of this article. The authors are grateful to the open science team of the University Magdeburg for their data repository services.

This project is part of the EU Marie Curie International Training Network on Soft, Self-responsive, Smart Materials for Robots (SMART-ITN) and has received funding from the European Union's Horizon 2020 research and innovation program under the Marie Skłodowska-Curie grant agreement No 860108.

References

- Abdulali, A., Terryn, S., Vanderborcht, B., Iida, F., 2022. Data-driven method for damage localization on soft robotic grippers based on motion dynamics. *Front. Robot. AI* 9, <http://dx.doi.org/10.3389/frobt.2022.1016883>.
- Akcabay, D.T., Chae, E.J., Young, Y.L., Ducoin, A., Astolfi, J.A., 2014. Cavity induced vibration of flexible hydrofoils. *J. Fluids Struct.* 49, 463–484. <http://dx.doi.org/10.1016/j.jfluidstructs.2014.05.007>.
- Augier, P., Bonamy, C., Campagne, A., Mohanan, A., 2016. FluidImage, a libre framework for scientific treatments of large sets of images. In: *Congrès Francophone de Techniques Laser (CFTL)*.
- Boëdec, T., Simoëns, S., 2001. Instantaneous and simultaneous planar velocity field measurements of two phases for turbulent mixing of high pressure sprays. *Exp. Fluids* 31 (5), 506–518. <http://dx.doi.org/10.1007/s003480100311>.
- Bozkurtas, M., Dong, H., Mittal, R., Madden, P., Lauder, G., 2006. Hydrodynamic performance of deformable fish fins and flapping foils. In: *44th AIAA Aerospace Sciences Meeting and Exhibit*. p. 1392.
- Bröder, D., Sommerfeld, M., 2007. Planar shadow image velocimetry for the analysis of the hydrodynamics in bubbly flows. *Meas. Sci. Technol.* 18 (8), 2513–2528. <http://dx.doi.org/10.1088/0957-0233/18/8/028>.
- Capone, A., Romano, G.P., Soldati, A., 2015. Experimental investigation on interactions among fluid and rod-like particles in a turbulent pipe jet by means of particle image velocimetry. *Exp. Fluids* 56 (1), 1. <http://dx.doi.org/10.1007/s00348-014-1876-4>.
- Cardwell, N.D., Vlachos, P.P., Thole, K.A., 2011. A multi-parametric particle-pairing algorithm for particle tracking in single and multiphase flows. *Meas. Sci. Technol.* 22 (10), 105406. <http://dx.doi.org/10.1088/0957-0233/22/10/105406>.
- Cheng, Y., Pothos, S., Diez, F.J., 2010. Phase discrimination method for simultaneous two-phase separation in time-resolved stereo PIV measurements. *Exp. Fluids* 49 (6), 1375–1391. <http://dx.doi.org/10.1007/s00348-010-0878-0>.
- Dearing, S.S., Campolo, M., Capone, A., Soldati, A., 2013. Phase discrimination and object fitting to measure fibers distribution and orientation in turbulent pipe flows. *Exp. Fluids* 54 (1), 1419. <http://dx.doi.org/10.1007/s00348-012-1419-9>.
- Diez, F.J., Torregrosa, M.M., Pothos, S., 2011. A comparison between round turbulent jets and particle-laden jets in crossflow by using time-resolved stereoscopic particle image velocimetry. *J. Fluids Eng.* 133 (9), 091301. <http://dx.doi.org/10.1115/1.4004815>.
- Ducoin, A., Astolfi, J.A., Sigrist, J.-F., 2012. An experimental analysis of fluid structure interaction on a flexible hydrofoil in various flow regimes including cavitating flow. *Eur. J. Mech. B Fluids* 36, 63–74. <http://dx.doi.org/10.1016/j.euromechflu.2012.03.009>.
- Dussol, D., Druault, P., Mallat, B., Delacroix, S., Germain, G., 2016. Automatic dynamic mask extraction for PIV images containing an unsteady interface, bubbles, and a moving structure. *Comptes Rendus Mécanique* 344 (7), 464–478. <http://dx.doi.org/10.1016/j.crme.2016.03.005>.
- Fabbri, T., 2022. Development of a high fidelity fluid-structure interaction solver : towards flexible foils simulation (Ph.D. thesis).
- Fatih, M.A., Augier, B., Deniset, F., Casari, P., Astolfi, J.A., 2019. Morphing hydrofoil model driven by compliant composite structure and internal pressure. *J. Mar. Sci. Eng.* 7 (12), <http://dx.doi.org/10.3390/jmse7120423>.
- Fujiwara, A., Danmoto, Y., Hishida, K., Maeda, M., 2004. Bubble deformation and flow structure measured by double shadow images and PIV/LIF. *Exper. fluids* 36 (1), 157–165. <http://dx.doi.org/10.1007/s00348-003-0691-0>.
- Gomes, J.P., Yigit, S., Lienhart, H., Schäfer, M., 2011. Experimental and numerical study on a Laminar fluid-structure interaction reference test case. *J. Fluids Struct.* 27 (1), 43–61. <http://dx.doi.org/10.1016/j.jfluidstructs.2010.09.004>.
- Gonzalez, R.C., Woods, R.E., 2008. *Digital Image Processing*, third ed., internat. ed In: Pearson Education, Pearson Education Internat, Upper Saddle River, NJ.
- Gui, L., Lindken, R., Merzkirch, W., 1997. Phase-separated PIV measurements of the flow around systems of bubbles rising in water. In: *ASME FEDSM*, Vol. 97. Citeseer, pp. 22–26.
- Hessenthaler, A., Gaddum, N.R., Holub, O., Sinkus, R., Röhrle, O., Nordsletten, D., 2017. Experiment for validation of fluid-structure interaction models and algorithms: Experiment for validation of fluid-structure interaction models and algorithms. *Int. J. Numer. Methods Biomed. Eng.* 33 (9), e2848. <http://dx.doi.org/10.1002/cnm.2848>.
- Hoerner, S., Abbaszadeh, S., Cleyner, O., Bonamy, C., Maître, T., Thévenin, D., 2021a. Passive flow control mechanisms with bioinspired flexible blades in cross-flow tidal turbines. *Exp. Fluids* 62 (5), 104. <http://dx.doi.org/10.1007/s00348-021-03186-8>.

- Hoerner, S., Abbaszadeh, S., Maître, T., Cleynen, O., Thévenin, D., 2019. Characteristics of the fluid– structure interaction within darrieus water turbines with highly flexible blades. *J. Fluids Struct.* 88, 13–30. <http://dx.doi.org/10.1016/j.jfluidstructs.2019.04.011>.
- Hoerner, S., Bonamy, C., 2019. Structured-light-based surface measuring for application in fluid–structure interaction. *Exp. Fluids* 60 (11), 168. <http://dx.doi.org/10.1007/s00348-019-2821-3>.
- Hoerner, S., Bonamy, C., Cleynen, O., Maître, T., Thévenin, D., 2020. Darrieus vertical-axis water turbines: Deformation and force measurements on bioinspired highly flexible blade profiles. *Exp. Fluids* 61 (6), 141. <http://dx.doi.org/10.1007/s00348-020-02970-2>.
- Hoerner, S., Kösters, I., Vignal, L., Cleynen, O., Abbaszadeh, S., Maître, T., Thévenin, D., 2021b. Cross-flow tidal turbines with highly flexible blades–experimental flow field investigations at strong fluid–structure interactions. *Energies* 14 (4), 797. <http://dx.doi.org/10.3390/en14040797>.
- Jacobs, E.N., Ward, K.E., Pinkerton, R.M., 1933. *The Characteristics of 78 related airfoil section from tests in the Variable-Density Wind Tunnel*, no. 460. US Government Printing Office.
- Jeon, Y., Sung, H., 2011. PIV measurement of flow around an arbitrarily moving body. *Exp. Fluids* 50 (4), 787–798. <http://dx.doi.org/10.1007/s00348-010-0855-7>.
- Kalmbach, A., Breuer, M., 2013. Experimental PIV/V3V measurements of vortex-induced fluid–structure interaction in turbulent flow–a new benchmark FSI-pfs-2a. *J. Fluids Struct.* 42, 369–387. <http://dx.doi.org/10.1016/j.jfluidstructs.2013.07.004>.
- Kanizsa, G., 1955. *Margini quasi-percettivi in campi con stimolazione omogenea*.
- Kováts, P., Thévenin, D., Zähringer, K., 2017. Investigation of mass transfer and hydrodynamics in a model bubble column. *Chem. Eng. Technol.* 40 (8), 1434–1444. <http://dx.doi.org/10.1002/ceat.201600679>.
- Li, Y., Blois, G., Kazemifar, F., Christensen, K.T., 2021. A particle-based image segmentation method for phase separation and interface detection in PIV images of immiscible multiphase flow. *Meas. Sci. Technol.* 32 (9), 095208. <http://dx.doi.org/10.1088/1361-6501/abf0dc>.
- Lindken, R., Merzkirch, W., 2002. A novel PIV technique for measurements in multiphase flows and its application to two-phase bubbly flows. *Exp. Fluids* 33 (6), 814–825. <http://dx.doi.org/10.1007/s00348-002-0500-1>.
- Mitrotta, F.M.A., Sciacchitano, A., Sodja, J., De Breuker, R., van Oudheusden, B.W., 2019. Experimental investigation of the fluid–structure interaction between a flexible plate and a periodic gust by means of robotic volumetric PIV. In: *13th International Symposium on Particle Image Velocimetry*. Universität der Bundeswehr München Neubiberg, Germany, pp. 645–656.
- Muste, M., Yu, K., Fujita, I., Ettema, R., 2009. Two-phase flow insights into open-channel flows with suspended particles of different densities. *Environ. Fluid Mech.* 9 (2), 161–186. <http://dx.doi.org/10.1007/s10652-008-9102-7>.
- Nikoueyan, P., Naughton, J.W., 2018. A photogrammetric approach for masking particle image velocimetry images around moving bodies. *Meas. Sci. Technol.* 29 (10), 105203. <http://dx.doi.org/10.1088/1361-6501/aa9c8>.
- Rezatofighi, H., Tsoi, N., Gwak, J., Sadeghian, A., Reid, I., Savarese, S., 2019-06. Generalized intersection over union: A metric and a loss for bounding box regression. In: *2019 IEEE/CVF Conference on Computer Vision and Pattern Recognition*. CVPR, IEEE, pp. 658–666. <http://dx.doi.org/10.1109/CVPR.2019.00075>.
- Rojratsirikul, P., Wang, Z., Gursul, I., 2009. Unsteady fluid–structure interactions of membrane airfoils at low Reynolds numbers. *Exp. Fluids* 46 (5), 859–872. <http://dx.doi.org/10.1007/s00348-009-0623-8>.
- Rzehak, R., Krauß, M., Kováts, P., Zähringer, K., 2017. Fluid dynamics in a bubble column: new experiments and simulations. *Int. J. Multiph. Flow* 89, 299–312. <http://dx.doi.org/10.1016/j.ijmultiphaseflow.2016.09.024>.
- Salumäe, T., Raag, R., Rebane, J., Ernits, A., Toming, G., Ratas, M., Kruusmaa, M., 2014. Design principle of a biomimetic underwater robot u-cat. In: *2014 Oceans-St. John's*. IEEE, pp. 1–5.
- Sanchis, A., Jensen, A., 2011. Dynamic masking of PIV images using the radon transform in free surface flows. *Exp. Fluids* 51 (4), 871–880. <http://dx.doi.org/10.1007/s00348-011-1101-7>.
- Tangorra, J., Phelan, C., Esposito, C., Lauder, G., 2011. Use of biorobotic models of highly deformable fins for studying the mechanics and control of fin forces in fishes. *Integr. Comp. Biol.* 51 (1), 176–189. <http://dx.doi.org/10.1093/icb/ict036>.
- Tregidgo, L., Wang, Z., Gursul, I., 2013. Unsteady fluid–structure interactions of a pitching membrane wing. *Aerosp. Sci. Technol.* 28 (1), 79–90. <http://dx.doi.org/10.1016/j.ast.2012.10.006>.
- van der Walt, S., Colbert, S.C., Varoquaux, G., 2011. The numpy array: A structure for efficient numerical computation. *Comput. Sci. Eng.* 13 (2), 22–30. <http://dx.doi.org/10.1109/MCSE.2011.37>.
- van der Walt, S., Schönberger, J., Nunez-Iglesias, J., Boulogne, F., Warner, J.D., Yager, N., Guillard, E., Yu, T., 2014. Scikit-image: Image processing in python. *PeerJ* 2, e453. <http://dx.doi.org/10.7717/peerj.453>.
- Vennemann, B., Rösgen, T., 2020. A dynamic masking technique for particle image velocimetry using convolutional autoencoders. *Exp. Fluids* 61 (7), 168. <http://dx.doi.org/10.1007/s00348-020-02984-w>, URL <https://link.springer.com/10.1007/s00348-020-02984-w>.
- Vested, M.H., Ergin, F.G., Carstensen, S., Christensen, E.D., 2018. High-resolution planar two-component PTV measurements in a breaking wave. In: *19th International Symposium on the Application of Laser and Imaging Techniques to Fluid Mechanics*. Springer-Verlag.
- von der Heydt, R., Peterhans, E., Baumgartner, G., 1984. Illusory contours and cortical neuron responses. *Science* 224 (4654), 1260–1262. <http://dx.doi.org/10.1126/science.6539501>.
- Weheliye, W., Yianneskis, M., Ducci, A., 2012. PIV measurements in a shaken cylindrical bioreactor. In: *16th International Symposium on Applications of Laser Techniques to Fluid Mechanics*. Lisbon, Portugal.
- Zeiner-Gundersen, D., 2015. A novel flexible foil vertical axis turbine for river, ocean, and tidal applications. *Appl. Energy* 151, 60–66. <http://dx.doi.org/10.1016/j.apenergy.2015.04.005>.
- Zhang, W., Wang, Y., Lee, S., 2008. Simultaneous PIV and PTV measurements of wind and sand particle velocities. *Exp. Fluids* 45 (2), 241–256. <http://dx.doi.org/10.1007/s00348-008-0474-8>.

A.3 Publication III

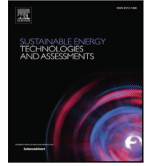
W. I. Kösters, J. A. Tuhtan, D. Efimov, M. Kruusmaa, and S. Hoerner (Sept. 2025a). "An open laboratory blade strike rig to evaluate the risk of injury and mortality to fish and to test passive sensors". In: *Sustainable Energy Technologies and Assessments* 81, p. 104427. DOI: [10.1016/j.seta.2025.104427](https://doi.org/10.1016/j.seta.2025.104427)

This publication corresponds to Contribution II, discussed in section 3.



Contents lists available at ScienceDirect

Sustainable Energy Technologies and Assessments

journal homepage: www.elsevier.com/locate/seta

Original article

An open laboratory blade strike rig to evaluate the risk of injury and mortality to fish and to test passive sensors

Wolf Iring Kösters^{a,b,1b,*}, Jeffrey A. Tuhtan^{b,1b}, Danil Efimov^{a,1b}, Maarja Kruusmaa^{b,1b}, Stefan Hoerner^{c,a,1b}^a Laboratory of Fluid Dynamics and Technical Flows, Institute of Fluid Dynamics and Thermodynamics, Otto von Guericke University Magdeburg (OvGU), Universitaetsplatz 2, 39106 Magdeburg, Germany^b Centre for Biorobotics, Tallinn University of Technology (TalTech), Akadeemia tee 15A, 12618 Tallinn, Estonia^c Laboratory of Geophysical and Industrial Flows (LEGI), CNRS, G-INP, University Grenoble-Alpes, F-38000 Grenoble, France

ARTICLE INFO

Dataset link: https://github.com/ikoesters/srda_tacombiner

Keywords:

Fish passage
Turbine passage
Fish-friendly turbine
Fish injury
Sensor probe

ABSTRACT

Hydropower is a key source of electricity that can negatively impact aquatic ecosystems. Fish passing downstream through hydropower facilities may face increased risks of injury and mortality from mechanical collisions with hydraulic structures and machinery. Laboratory tests provide a controlled environment to evaluate turbine blade strike risks, studying injury and mortality in live fish. Previous laboratory blade strike rigs vary substantially in design and implementation, lacking a standardized approach with controlled blade velocities for cross-comparable results. To address this, we propose an open laboratory blade strike test rig with electronically controlled blade velocities (1–10 m s⁻¹). In addition, rigid sensor tests were performed to investigate the recommendation that 95 g is suitable to assess the severity of the blade strike, which was exceeded at strike speeds as low as 1 m s⁻¹. This work is significant because it provides the hydropower, engineering and biological communities with the first open and standardized method to evaluate blade strikes on fish and sensor probes. The proposed test rig enables gathering biological threshold data to estimate injury and mortality to live fish, assessing turbine blade design for improved fish safety, and increasing sensor probe accuracy without relying on live fish field studies.

Introduction

Hydropower is a key source of electricity for base load power generation and plays a vital role in stabilizing electric grids, particularly in systems with a high share of renewable energy sources [1]. Despite the indisputable benefits of hydropower and the urgent need for resilient renewable energy infrastructure, the negative impacts of hydropower on river ecosystems has become increasingly evident, particularly on entrained fish [2,3], which can experience mortality rates exceeding the population's replacement rate, potentially leading to population collapse [4]. Hydropower has been identified as one driver behind a decline in migratory aquatic species through river fragmentation [5], affecting both potamodromous (solely living in fresh water) and diadromous (migrating between the sea and fresh water) fish species [6]. Many operators, manufacturers and authorities have made efforts to mitigate the environmental impact of hydropower in the last decades, and legislation puts increasing pressure on its operators by enforcing

measures for safe fish passage as through the Water Framework Directive in the European Union [7]. The importance of these challenges is also reflected in the fact that fish safety is presented as a key feature in the innovative in-stream turbines over classical hydropower [8].

In spite of the associated environmental impacts, the number of hydroelectric plants continues to rise, with 3909 hydropower plants under development as of 2022, representing 9% of the total capacity installed to date [9]. Yet half of all hydroelectric power plants worldwide were constructed over 40 years ago and are due for modernization [10], providing an important opportunity to introduce new turbine designs to reduce their environmental impacts. Examples of innovative turbines include the minimum gap runner turbine [11], Alden turbine [11,12], the very low head turbine [13] and the restoration hydro turbine [14].

In some cases, bypasses can be built which provide fish the opportunity to migrate around hydroelectric facilities, including fishways, bypasses, and screens. However, such mitigation solutions, such as surface bypasses, may be difficult to evaluate across study sites due to

* Corresponding author at: Laboratory of Fluid Dynamics and Technical Flows, Institute of Fluid Dynamics and Thermodynamics, Otto von Guericke University Magdeburg (OvGU), Universitaetsplatz 2, 39106 Magdeburg, Germany.

E-mail address: wolf.koesters@ovgu.de (W.I. Kösters).

<https://doi.org/10.1016/j.seta.2025.104427>

Received 23 January 2025; Received in revised form 23 May 2025; Accepted 24 June 2025

Available online 17 July 2025

2213-1388/© 2025 The Authors. Published by Elsevier Ltd. This is an open access article under the CC BY license (<http://creativecommons.org/licenses/by/4.0/>).

Nomenclature

Φ	Angular rotation
d_{rotor}	Rotor diameter
r	Coefficient of determination
s_{travel}	Length of relevant blade travel length
x_i	Peak acceleration magnitude value from a single experiment
X_{gv}	Array of peak acceleration magnitude values at one strike velocity
BDS	Barotrauma detection system
CAD	Computer-aided design
CFD	Computational Fluid Dynamics
CV	Coefficient of variation
EPRI	Electric Power Research Institute
HBET	Hydropower Biological Evaluation Toolset
L/t ratio	Fish length to blade thickness ratio
MAD	Mean absolute deviation
MSWR	Minimum strike window requirement
ORNL	Oak Ridge National Laboratory
PC	Polycarbonate
PCB	Printed circuit board
PU	Polyurethane
RAPID	Robust Autonomous Pressure and Inertial Device
RETERO	Project name
RPM	Revolutions per minute

a lack of standardized performance criteria [15]. Recent field studies have shown that at some sites, between 35–88% of fish passed through the turbine despite the presence of bypasses and the installation of fine screens [16]. Additionally, such structures can result in elevated predation rates at these choke points [17].

Once entrained in a turbine, fish mortality is typically high: in a study summarizing 249 experiments reported in 91 studies on downstream migration through hydropower turbines in North America and Europe, Radinger et al. [18] estimated the average mortality rate at 22.3%. Even sites employing new turbine designs, such as the previously mentioned very low head turbine, can still result in considerable passage mortality [19]. In cases where the mortality rates from turbine passage are higher than the reproduction rate, populations may face a risk of collapsing. To estimate large-scale impacts, ecological risk screening at the population level can be carried out using the European Fish Hazard Index (EFHI), developed by Van Treeck et al. [4].

Live fish tests remain the state-of-the-art method for assessing and quantifying the risk of injury and mortality to fish during downstream turbine passage, which is reflected in the current draft for a European standard [20] and the national Dutch standard [21] from 2020. Furthermore, such assessments may be mandated as a consequence of national regulations and policies such as the European Water Framework Directive [7], as hydropower operators are required to meet legal obligations related to their ecological impacts. A key advantage of using live fish is their ability to account for all sources of mechanical injury and mortality during passage, including barotrauma, shear, and collision events such as pinching, grinding, and blade strikes [22,23]. However, live fish tests can be prohibitively expensive for small hydropower plant operators and are subject to increasing ethical concerns, as demonstrated by the restriction of such tests in Switzerland via the Animal Welfare Act [24] and the Animal Experimentation Ordinance [25]. Additionally, live fish field tests only provide the cumulative outcome of physical damage, making it difficult

or impossible to infer the precise locations within the hydraulic structure and machinery where damages occur, and can be highly species-, size-, life stage-, site- and operation point dependent.

To address the limitations and shortcomings of live fish testing, researchers have developed numerical models to investigate the hydraulic conditions to which fish would be exposed [26–30], which is a valuable guide for the design of environmentally enhanced turbines [31] and pumps [32,33]. However, the flow field in hydraulic machinery is extremely complex, and computational fluid dynamics (CFD) models require physical validation. Furthermore, most current CFD models do not take fish swimming activity into account.

Sensor probes, which were first patented by researchers at the US Army Corps [34] to study fish behavior near hydropower intakes. Subsequently, the ‘Sensor Fish’ was developed by Carlson and Duncan [35] for turbine passage studies and was later enhanced by Deng et al. [36] and Deng et al. [37] to measure the physical environment, focusing primarily on pressure, acceleration and rotational rate. These measurements have since been used in several studies to assess dam hydraulic conditions in situ (e.g. [38–42]) and to investigate new or unconventional turbine designs [43–45]. They have also been used to estimate the risk of barotrauma in juvenile salmon [46], including a recent improvement which includes a dynamic model of swim bladder size as proposed by Kerr et al. [47].

A significant limitation of passive sensor probe devices is their inability to account for fish behavior, which has been demonstrated to substantially influence outcomes. Geiger et al. [48] investigated the influence of behavior of river trout (*Salmo trutta fario*) on turbine passage mortality by conducting experiments in a model laboratory turbine. They modified fish behavior by either sedating the fish or using a device that induced an electric field at the turbine intake. Their findings demonstrated an approximately 50% reduction in mortality rates for fish of 15 cm and 29 cm length in the electric field group compared to the control group. Sedation also reduced mortality, although its effect was smaller yet still significant. Additionally, Vowles and Kemp [49] studied the influence of lighting conditions on the passage of brown trout (*Salmo trutta*) and reported substantial delays due to avoidance behaviors triggered by light exposure. Nonetheless, passive sensor probes are increasingly employed to quantify hydrodynamic parameters beyond their original application in hydraulic machinery, supporting broader fish-protection research efforts — such as recent investigations into closed-conduit systems [50].

To establish an equivalent model for shear events, Deng et al. [51] measured the acceleration and subsequent mortality of smolts subjected to shear flow induced by a high-velocity water jet. High-speed cameras measured the whole-body movement of the fish, from which velocity, acceleration, and jerk were calculated and compared to respective mortality for each velocity of the water jet. Based on these experiments, they classified events by peak acceleration magnitude of the sensor probe into three risk categories: low (25–50 g), medium (50–95 g), and high (greater than 95 g) for shear and collision events, distinguished by their magnitude and duration [38]. Events with a duration of less than 7.5 ms, measured as at least 70% of the maximum value, were classified as collisions, while those exceeding 7.5 ms were considered shear events. In addition to the development of this method [51], further information can be obtained in Richmond et al. [52], where fish and sensors were subjected to the same shear conditions and fish mortality was correlated with the full-body sensor acceleration. The results of this study were presented as a logistic regression with confidence intervals for the probability of minor and major injuries. However, the interpretation of the boundaries for these classes remains unclear as in one shear case (slow fish – fast water) 95 g the logistic regression curve already predicts major injuries with a mean probability close to 100%. Finally, these thresholds were also applied for collision events, even though the sensor did not experience a shock event during shear flow in the same way as it would have experienced during a collision. Thus, the use of the 95 g threshold may lead to an overestimation

of the severity of collision events as highlighted by Bercovitz et al. [53]. To further investigate acceleration thresholds, the authors have presented preliminary results from laboratory strike rig experiments related to acceleration maxima on 10 cm long 2.5 cm outer diameter plastic cylindrical sensors [54].

Currently, the acceleration-threshold concept, based on Richmond et al. [52] and introduced in Deng et al. [38], remains as the most common methodology to assess the severity of blade strike events; however an alternative based on the kinetic energies of translation and rotation was proposed in Pauwels et al. [44]. The acceleration-threshold model of Deng et al. [38] is used by the commercial software “Hydropower Biological Evaluation Toolset” (HBET) [55] accompanying the ATS Sensor Fish [37] to evaluate the passage through hydro-structures. With over 520 publications (using Google Scholar with the keyword “Sensor Fish”), this device can be estimated as the most widely used and is the only commercialized sensor model. It samples data at 2 kHz using a 3-axis gyroscope, a pressure sensor, and a 3-axis accelerometer with a measurement range of up to 112.5 g. The device has a cylindrical shape with a diameter of 24.5 mm, a length of 90 mm, and is neutrally buoyant at 43 g [36]. Recent publications using the 95 g rule for collisions [41,43,45,56] illustrate its widespread application, despite a clear validation case of the 95 g criteria based on field or strike rig lab studies.

To address the absence of a biological response model for turbine blade strikes on fish, data from existing blade strike experiments conducted over the past three decades [14,57–62] can be used to link relative blade strike velocity with injury and mortality.

These blade strike rigs can be broadly categorized by their design as either electric motor-powered or spring-driven, and by their motion as either rotary or linear. The original design by Turnpenny et al. [57] featured a spring-driven blade with linear motion, although detailed replication information is scarce [63]. In 2007, Hecker et al. [64] employed a motor-powered linear motion rig, subsequently called Alden rig, identifying a key relationship between the blade-to-fish length ratio and mortality, and establishing the now-standard semicircular blade shape. A decade later, Bevelhimer et al. [63] introduced a compact spring-powered rig with rotary motion, subsequently called ORNL rig. Their extensive research on strike angle, location, fish rotation, and species impact on mortality was later compiled by Saylor et al. [65]. Most recently, Meng et al. [62] presented a rig similar to the ORNL rig design.

Ideally, these experiments can be replicated with sensors in order to infer the risk of injury and mortality from sensor measurements, following a potential methodology illustrated in Fig. 1. In the figure, the model only accounts for blade speed, omitting the L/t ratio (fish length to blade thickness ratio), which has been identified as another critical factor in blade strike mortality [64]. However, just as the model correlates strike velocity with acceleration, the L/t ratio can be incorporated the same way. The idea of performing simulated blade strikes on sensor probes to infer a mortality risk for fish, although not explicitly proposed, was first introduced by Bevelhimer et al. [59] who performed strike tests on the Sensor Fish. Recently, Saylor et al. [66] proposed and tested flexible, fish-shaped sensor probes outfitted with accelerometers embedded in ballistic gelatin-molded bodies. However, in these studies, the relative velocity of the blade-strike was not estimated using the probe data to the knowledge of the authors.

The main contributions of this work are two-fold: (a) provide an open blade strike rig design, the RETERO rig, that may be used as a standardized testing and comparison environment for blade strikes on sensor probes and live fish alike, and (b) evaluate the suitability of the 95 g acceleration magnitude threshold as an indicator of blade strike severity using sensor probes.

The major findings of this work can be used to collect biological threshold data required to estimate injury and mortality caused by blade strikes, aid in the development of new fish-safe turbine designs, and increase the predictive accuracy of sensor probes to provide biologists and engineers with a more physically accurate representation of the frequency and severity of blade strike events in hydropower plants world-wide.

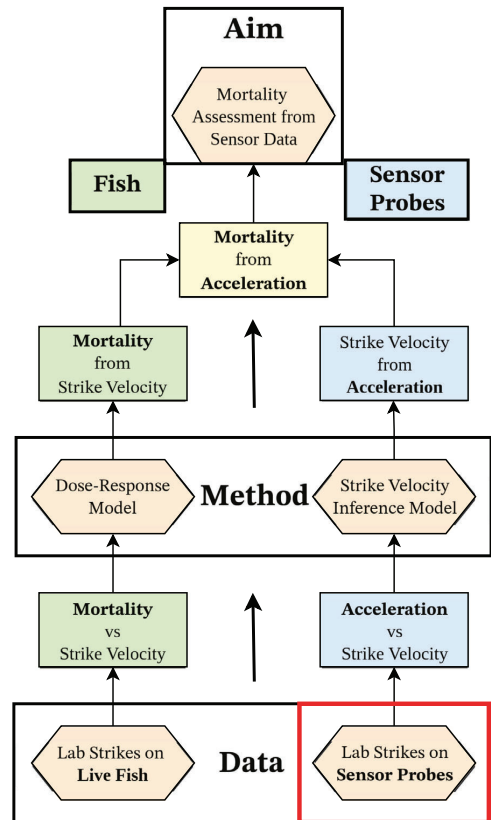


Fig. 1. Flow diagram illustrating the methodology for inferring fish mortality from sensor probe data by integrating dose–response studies with a strike velocity inference model. The sensor’s acceleration time series is connected to fish mortality via the mediating variable of strike velocity. To enable this inference, data from blade strikes with known velocities (highlighted in red) is required, the means and methodology of generating these represents the primary contribution of this work.

Methodology

In this section, we compare the different strike rig designs, outline the requirements for a new strike rig, describe the proposed system, and provide a strike test protocol.

Drive system comparison. All strike rigs consist of a single turbine blade model accelerated within a static water tank. The primary objective of the rig is not to fully replicate all aspects of the hydraulic conditions within a turbine, but instead to offer a controlled testing environment that consistently generates reproducible blade strikes, facilitating the development of reliable dose–response relationships. We assessed the main difference in the existing strike rigs to be the drive system, which are electric motor-driven or spring loaded. The rig from Turnpenny et al. [57] was excluded in our study due to the difficulty in obtaining detailed information on their design, as well as the rig from Meng et al. [62] because the manuscript lacked sufficient detailed comparative design and performance data. Although spring-loaded design allows for a more compact and purely mechanical setup, the strike speed cannot be set directly. Rather, the spring tension needs to be adjusted iteratively by checking the realized strike velocity and manually changing the tension according to Bevelhimer et al. [59]. This has to be done for each velocity and blade type as the drag and probably also the inertia

of the blade changes. Furthermore, the researchers faced the challenge of a minimum spring tension that still resulted in excessive velocities, which was solved by attaching drag-increasing fixtures to the blade arm for low velocities [63]. A spring-loaded strike arm is also not able to maintain a stable velocity of the blade after collision, which can result in a significant decrease in the post-collision blade velocity. This strike characteristic differs from in-situ turbine blade collisions where the blade inertia is commonly very high. The motorized system at Alden Laboratory was therefore not faced with these challenges. The rig incorporated an additional clutch and brake system. Although the original rationale for increasing the complexity with these components was not explicitly stated, it can be inferred that their inclusion reduced the required distances for acceleration and deceleration, thus allowing for a shorter basin length. As the motor did not provide feedback, the researchers used a magnetic sensor to measure the strike velocity. As in the spring-loaded version, a stable post-strike blade velocity could not be maintained due to the lack of a closed-loop drive control. The Alden rig is considerably larger than the ORNL rig with 16.5 m versus 0.9 m, although this could potentially have been reduced by using a more powerful motor.

System requirements. We identified a number of design requirements that are necessary to ensure comparability between sensor strike experiments and live fish strike tests. However, despite differences in their underlying mechanisms, the results from both methodologies demonstrated remarkable consistency within overlapping ranges of strike velocities and fish-length-to-blade-thickness (L/t) ratios, as detailed in Section “Design challenges”. We first chose the database compiled by Saylor et al. [65] which contains approximately 2300 strike tests and 250 controls which were not subjected to a blade strike [65]. We determined the fish retainer, the blade shape and the velocity range and the repeatability of the strike velocity, which need to be made as closely as possible as the retainer used in the live fish tests. The retainer applies just enough force to secure the fish or sensor probe in place while minimizing resistance to movement during strike. It also reduces variability in the input conditions but intentionally does not eliminate it entirely, as illustrated in Fig. 2. The shape of the blade had a semicircular leading edge, as introduced by Hecker et al. [64] and adopted in all ORNL rig experiments. The strike velocities of the ORNL rig range between $6.1\text{--}8.2\text{ m s}^{-1}$ with a 52 mm blade and have a coefficient of variation (CV) of maximum 4% of the strike velocity. In addition, it should be safe to operate even in periods of inattention, which might arise during the hundreds or thousands of tests performed, which consist of highly repetitive tasks and can lead to a potentially higher risk of human error. We strongly encourage the development of a highly elaborated security concept for this device in case of planned copy built. Although the authors provide a detailed description of the measures taken in their lab, they cannot assume responsibility for any damage or harm in other laboratories.

Design implementation. From this point forward, the developed strike rig will be referred to as the *RETERO rig*, named after the research project within which it was developed. Fig. 2 provides an overview of the *RETERO rig*, illustrating the overall setup in the center. The top section details the drivetrain, featuring the linear motion system, while the bottom section depicts the sensor probe retaining system prior to a strike. The novelty of the proposed strike rig is its software configurable strike velocity, and the capacity to maintain a stable blade velocity before, during and after the impact occurs. The standoff distance of about 1 m between the basin and the ground accounts for the use of lenses with standard focal lengths in the high-speed measurement. We based our design on the motor-powered Alden rig, but improved on it by utilizing modern electronic hardware; most importantly, by using a servo drive with closed loop control. Due to its excellent starting torque and the ability to exert high breaking force, the need for an external clutch and break system is eliminated. In its software, a position control algorithm allows for setting up velocity profiles which are controlled

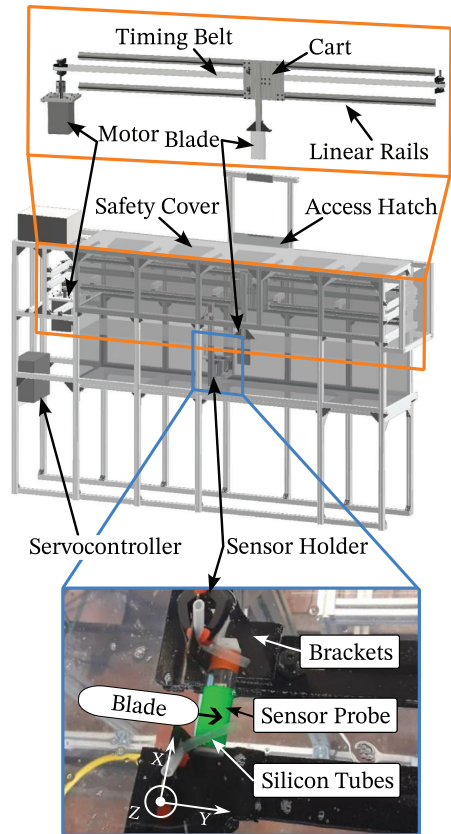


Fig. 2. Overview of the strike rig setup, with key components labeled. During operation, the blade travels linearly from left to right, striking the sensor probe positioned in the sensor holder. To minimize drag and splashing, only the blade is submerged. At the end of its travel, the blade decelerates to a predefined stop position, controlled by the servocontroller software. For safe operation, all moving parts are enclosed within acrylic glass, with an access hatch provided for sensor probe placement and retrieval. The complete setup measures $3.84\text{ m} \times 0.72\text{ m} \times 2.61\text{ m}$ (length \times width \times height), while the basin alone is $3.04\text{ m} \times 0.582\text{ m} \times 0.69\text{ m}$. Below a labeled photograph showing the sensor probe positioning prior to a strike. Along the X -axis, rotation is not constrained and lateral variation in the positioning is permitted. The sensor probe is secured before impact using silicon tubes, which apply minimal force during the strike. The brackets holding the probe are 50 mm wide and 99 mm high, with a 60 mm gap between them.

and maintained using an encoder from the motor as position feedback which is fed into a closed control loop. This makes it possible to directly set the desired strike velocity by the software, without the need to iteratively find the right configuration. Additionally, through the closed loop control system, it is able to achieve a high degree of repeatability in between strikes, either performed consecutively or with intervals of days or months in between. During blade setup, the maximum achievable acceleration value must be determined, followed by fine-tuning the feedback control loops to the highest stiffness setting without inducing oscillation. This was accomplished using the ‘Slider Tuning’ feature in the servocontrol software (Kollmorgen Workbench), which provided more effective results compared to the ‘Autotune’ feature. Finally, it actively compensates for the loss of the post strike blade velocity during the strike event, which cannot be achieved with Alden or the ORNL systems as they lack the feedback for a controller. This mimics a much higher blade inertia, which is closer to reality, while

Table 1

Summary of the technical characteristics of blade strike rigs used to evaluate the risk of injury and mortality during hydropower turbine passage. The coefficient of variation (CV) for the Alden Lab rig is an own calculation based on experiment ID 21, identified as the case with maximum variance in the published data.

	Alden [58]	ORNL [59,63]	RETERO
Length × Width × Height	16.5 m × 0.91 m × 0.91 m	0.9 m × 0.6 m × 0.6 m	3.84 m × 0.72 m × 2.61 m
Drive chain	AC motor	Mechanical spring	Servomotor
Blade motion	Linear	Circle segment	Linear
Blade speed	0–12 m s ⁻¹ @ 150 mm	7.3–12.2 m s ⁻¹ @ 26 mm	0–9 m s ⁻¹ @ 26 mm
@ Blade diameter		6.1–8.2 m s ⁻¹ @ 52 mm	
Strike speed estimation	Automatic (Magnetic sensors)	Manual (Motion tracking)	Automatic (Motor feedback)
Repeatability as CV	max. 1.8%	max. 4%	max. 0.12%
Control over fish orientation & Strike angle	No	Yes	Yes
Additional features	External brake delivers high breaking force	No electronic actuation required	High-res position feedback and blade deceleration compensation

the high resolution position feedback of the motor is able to precisely quantify this effect.

The deceleration phase poses the highest risk of damage to the device itself or injury to the operators during its use, as the stored momentum of the blade must be safely dissipated. To mitigate potential damage in case of malfunction, three security measures are in place: software control ensures the blade stops near the end of its range; a limit switch positioned beyond this point cuts power to the motor; and stiff foam blocks at either end absorb the impact, preventing the cart from striking the frame or the blade from hitting the basin walls. Despite the aforementioned improvements, the RETERO rig remains affordable at 7000 € (see full cost breakdown in the appendix, Table A.3). However, even though the dimensions are more compact compared to the Alden rig, with 4.1 m × 0.7 m × 2.3 m, it is not as compact as the ORNL design.

Test protocol. The RETERO rig test protocol involved either placing the sensor probe in the holder and activating it there, or turning it on outside the water and then inserting it into the holder after verifying it was active. Sensor probes were activated using an external magnet, which when placed next to the housing in the vicinity of the magnetic switch, activated the sensor probe. The sensor probes were positioned laterally onto the strut profile and held in place using two silicone tubes, so that the blade would strike the middle of the body as shown in Fig. 2. As the effective impact stiffness of the sensor probe depends on the orientation of the printed circuit board (PCB) relative to the blade strike location, the PCB orientation was randomly set for each strike event. This is necessary to avoid a systematic bias in the accelerometer readings due to a fixed PCB orientation when the sensor probe is struck. This is an important aspect to consider when conducting strike tests in a lab because in field studies, it is not possible to ascertain the absolute orientation of the sensor probe PCB relative to the blade. By randomizing the orientation, the lab impact data are as cross-comparable with field data as possible. The longitudinal strike location within the water tank was determined and confirmed for each strike event using motor feedback to verify that the sensor probes were struck at the same position along the blade's path of motion. Sensor data quality was evaluated for further processing, to remove outliers that were indicated by acceleration magnitudes outside the measurement range or faulty recordings. Data were excluded from the strike evaluation if the acceleration magnitude peak fell outside of three times the median absolute deviation (MAD) from the median at that strike velocity, in accordance with the recommendations of Leys et al. [67,68]. The MAD is defined as: $MAD = \text{median}(|x_i - \text{median}(X_{sv})|)$ where X_{sv} is the array of all acceleration magnitude peak values at one strike velocity and x_i is the peak value from a single experiment at that velocity, hence every strike velocity produces a different threshold.

The water level was maintained at 160 mm above the brackets on which the sensor probe is positioned prior to a strike, illustrated in Fig. 2. The blade was carefully aligned vertically during attachment, as any

slant would impart a vertical velocity to the sensor probe, potentially causing it to forcefully hit the bottom of the basin or become airborne.

After reviewing the high-speed video recordings, with exemplary cases provided in the supplementary material, we conservatively set the window in which a strike occurs to 20 cm of the blade travel length. Consequently, the maximum achievable strike velocity is defined as the velocity the rig can sustain during this interval, with the same or lower velocity deviation as the rig used by Bevelhimer et al. [63], who measured the blade velocity immediately before impact. We refer to this as the minimum strike window requirement (MSWR), set at 20 cm.

Data processing. To combine and process data from the sensor probes, servocontroller, and high-speed video, a series of Python scripts have been developed and made openly available.¹ These scripts are bundled into a Python package, which can be installed easily via the Python package manager pip. The overall workflow, illustrated in the Github repository, begins by importing the data and checking for corruption or outliers caused by technical faults or operator errors, as described in the above paragraph.

The dataset is trimmed to the strike event by identifying the first collision point where the acceleration magnitude reaches the dynamically adjusted threshold determined in accordance to [68]. This value is also used to verify data integrity, and then including an additional 4 ms prior to this point to ensure no relevant information is lost.

The processed data is then organized along three dimensions: strike velocity, trial, and time, using the Xarray Python package.²

RETERO rig repeatability

High repeatability between strikes is achieved through a 4kHz closed-loop feedback control system between the servocontroller and motor. To assess the rig's repeatability, we conducted tests without a sensor probe, measuring the strike velocity at the impact position for velocities between 1 m s⁻¹ to 10 m s⁻¹, with five repetitions per velocity. The coefficient of variation (CV), used as a repeatability metric by Bevelhimer et al. (see Table 1), was 0.12% at 1 m s⁻¹ in our rig, significantly lower than their reported 4%. Achieving high precision is crucial, as we aim for equal or better repeatability to ensure reliable comparison with previous strike rig study results. Additional metrics for each strike velocity can be found in Table 2.

Results & discussion

To illustrate the trajectory of the strike blade at velocities ranging from 1 m s⁻¹ to 10 m s⁻¹, Fig. 3 presents the corresponding velocity

¹ github.com/ikoesters/srdatacombiner.

² docs.xarray.dev.

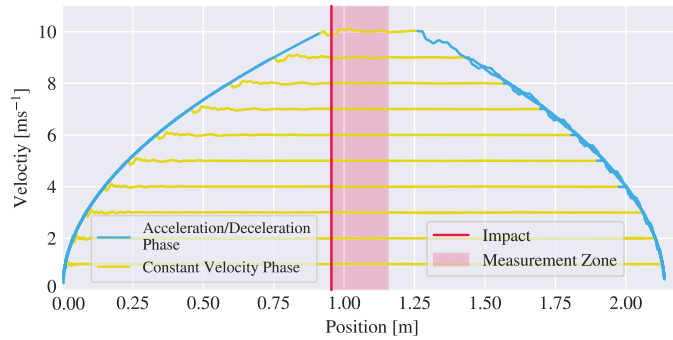


Fig. 3. Blade velocity trajectories from 1–10 ms⁻¹ without strike events over the whole range of motion of the system. These trajectories represent standard trapezoidal velocity profiles in the time domain. The trapezoid shape is determined by the stop position, the acceleration and deceleration, and the velocity, which are manually set during the motor configuration. Gain factors for the control loop are automatically determined during startup.

Table 2

Overview of the various metrics assessing precision and repeatability across target strike velocities ranging from 1 m s⁻¹ to 10 m s⁻¹ at 0.955 m along the path of travel of the blade. The coefficient of variation (CV) is equivalent to the relative standard deviation, the median absolute deviation (MAD) was normalized by the strike velocity as well.

Target velocity [m s ⁻¹]	Mean [m s ⁻¹]	CV [%]	Median [m s ⁻¹]	Rel. MAD [%]
1	1.00	0.12	1.00	0.05
2	2.00	0.02	2.00	0.01
3	3.00	0.05	3.00	0.03
4	4.00	0.03	4.00	0.01
5	5.01	0.02	5.00	0.02
6	6.00	0.01	6.00	0.01
7	7.00	0.02	7.00	0.02
8	8.01	0.03	8.01	0.02
9	8.98	0.01	8.98	0.00
10	9.89	0.02	9.89	0.01

profiles over the strike path without collision. Initially, the blade accelerates with 55 m s⁻² (0–10 m s⁻¹ in 0.18 s) to the target velocity, maintaining it as consistently as possible despite any disturbances. With a 9.5 mm blade, mechanical losses and drag losses combined use between 4% (1 m s⁻¹) and 13% (10 m s⁻¹) of the available 30 A power budget, with the remaining power used to overcome the inertia of the system. These values were calculated on the constant velocity part of corresponding trajectories without strikes between 1–8 m s⁻¹ with a coefficient of determination of $r^2 = 0.990$. At the moment of impact, a brief deceleration occurs, which is promptly counteracted by the servocontroller, increasing the motor power to restore the target velocity. The velocity loss during the strike was calculated as the difference between the target strike velocity and the minimum velocity observed during the strike, ranging from 3.1–5.3 % of the strike velocity measured directly before impact. Finally, the blade decelerates with 57 m s⁻² and comes to a complete stop at a predefined location. To investigate performance during strike tests with large and heavy sensor probes, a trout model (33 cm in length, 620 g) was constructed as described in [69]. The model is built from a 0.2 mm carbon fiber composite sheet as a mid-plane, a body made of two-component silicone (Zhermack Elite Double 8), and a stiff 3D-printed head.

Example use-case

To showcase a practical application of the strike rig we performed strike tests on sensor probes. The investigation aims to shed light on the challenges associated with the use of an acceleration magnitude threshold to assess the severity of a strike event. In this investigation, the sensor probe was subjected to blade strikes of 1 m s⁻¹ with 30 repetitions each. The position of the sensor probe before the strike

was controlled as shown in Fig. 2. The blade featured a semicircular leading edge with a 9.5 mm diameter, made from 3D-printed impact-resistant polycarbonate (PC) and reinforced by stainless steel threaded rods. The sensor probe used is the Robust Autonomous Pressure and Inertial Device (RAPID), developed at the Tallinn University of Technology and are certified for impacts according to the M802:01.03.2022 shock test procedure (peak accelerations from 10–400 g) and ECSS-E-ST-10-03C(2012) test standard with the test certificate nr. 8-009-22/13.04.2022. It is neutrally buoyant, 25 mm in diameter, 100 mm long, and has a mass of 24 g, which are similar dimensions to those of the Sensor Fish of Deng et al. [36], and records the acceleration in three axes over a range of 400 g at a rate of 2 kHz. The time of peak acceleration magnitude varies across four measurement points, or approximately 1.5 ms, with a median strike duration of 3 ms, considering values above 10 g. Following the convention of Deng et al. [38], where values within 70% of the peak are counted, the strike duration ranges between 0.5–1 ms (1–2 data points). Additionally, not all time series exhibited a single distinct peak; many showed two peaks, separated by a data point significantly lower than the adjacent values.

Fig. 5 presents the results of our experiment, in which strikes at 1 m s⁻¹ produced a mean acceleration peak of 200 g, well above the 95 g threshold, though still within the 7.5 ms time window used to classify a strike event [38]. A left-tailed 95% confidence interval, calculated using the Student's t-distribution to determine the margin of error, provides a lower bound of 184 g. Strikes exceeding this threshold have been associated with severe injuries according to [38]. However, the database compiled by Bevelhimer et al. [63], which includes over 2500 live fish blade strike tests of a variety of fish species, reports minimal mortality even at velocities of 5 m s⁻¹, with only one fatality out of 55 fish tested. In the comprehensive overview study by Pflugrath et al. [70], an extended model based on strike tests involving seven different fish species with varying mean body sizes (*Alosa* spp.: 7.6 cm; Gizzard shad: 16 cm; Paddlefish: 26.7 cm; Rainbow trout: 11.6 cm and 16.1 cm; Hybrid striped bass: 18 cm; Bluegill: 11.6 cm and 16.1 cm; Brook trout: 24.8 cm) resulted in dose–response curves predicting zero mortality for strike velocities below 5 m s⁻¹ across all tested species and sizes. This suggests that while the 95 g criterion has been a valuable guideline, its reliability as a predictor of mortality, already being subjected to increasing scrutiny regarding its accuracy [53], is not likely that it is a reliable threshold to evaluate mortality from simulated turbine strikes. This is further supported by Bevelhimer et al. [59] which noted that the maximum accelerations observed in their strike apparatus were higher than those reported in field studies of that period using the Sensor Fish device. This leads to the authors hypothesis that this overestimation is a systematic problem and not related to the specific sensor technology used in this study as it appears in both sensor probe designs, using two different strike rigs by independent investigators. Consequently, further refinement of a strike parameter on sensor probes is necessary to more reliably infer blade strike velocity from acceleration measurements.

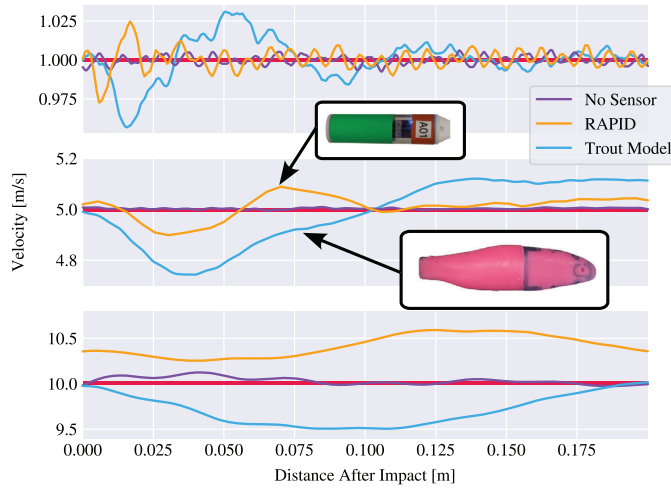


Fig. 4. Average blade speed, measured by the servocontroller in relation to its position post-impact, was recorded for cases with no sensor, the RAPID sensor (described in the following example use-case), and the trout model at strike velocities of 1 m s^{-1} , 5 m s^{-1} , and 10 m s^{-1} (indicated by the red bar) struck mid-body, laterally. At 5 m s^{-1} , it can be observed that, despite the substantial weight and size differences between the RAPID sensor (24 g, 90 mm) and the trout model (620 g, 330 mm), the additional reduction in strike velocity due to drag and impulse transfer for the trout model is only 0.16 m s^{-1} . At 10 m s^{-1} , the trout model exhibited a maximum deceleration of 0.5 m s^{-1} , compared to 0.05 m s^{-1} for the RAPID sensor. A systematic error of 0.3 m s^{-1} or 3% in the realized strike velocity can be observed in the RAPID sensor measurements due to an improper servocontroller configuration, however, it was deemed negligible to the overall results considering the variation in measured acceleration, shown in the subsequent Section “Example use-case”.

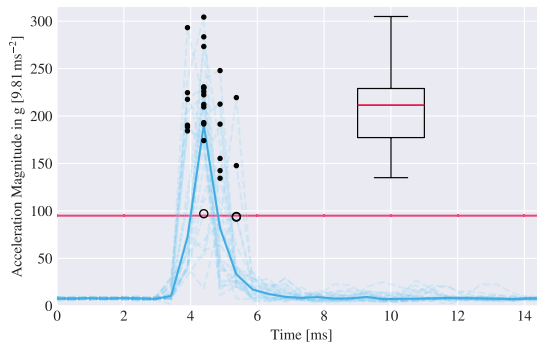


Fig. 5. Acceleration time series for strikes at 1 m s^{-1} are shown as transparent dashed blue lines ($n = 30$), with the median acceleration represented by a solid blue line. Black dots indicate peak acceleration values for each time series, where it can be seen that all acceleration magnitudes exceeded the 95 g threshold at 1 m s^{-1} . The distribution of peak values is represented in the box-whisker plot on the right, with whiskers extending to 1.5 times the interquartile range and outliers indicated by empty circles. The median peak acceleration is 211 g , with one strike reaching 304 g . In all but one trial the 95 g threshold was exceeded, highlighted by the horizontal red line. The post-impact acceleration is caused by the blade’s wake.

Design challenges

Several challenges were identified during the development and operation of the RETERO rig. These include limitations related to maximum velocity, motor interaction, and structural stability, which are detailed below. The differences between the turbine environment and the strike rig do not necessarily constitute a limitation. Rather, the rig was deliberately designed not to replicate the precise physical conditions of turbine passage, but instead to simulate blade strikes in the controlled and reproducible manner of a lab environment while minimizing confounding factors.

Maximum velocity. Although the ORNL strike rig is capable of achieving velocities up to 12.2 m s^{-1} , our current design is limited to a maximum strike velocity of 10 m s^{-1} . This constraint arises from the minimum strike window requirement (MSWR) of 20 cm, set in our test protocol. Achieving higher velocities would reduce the strike window

below this threshold. Nonetheless, this limitation might be not of major concern, as average mortality rates provided in dose–response studies reported very high to total mortality risks already below 10 m/s for many species and live stages such as shown by [65] for small (11–12.5 cm) and larger (22–26 cm) rainbow trout. If higher impact speeds became necessary for a specific experimental campaign, a more powerful servo controller and motor would be required to deliver additional power. Beside this reducing the accelerated mass is another potential strategy to lower power demands. A script for evaluating these scenarios, calibrated using real-world data from our rig, is available in the code repository.

Stability. To prevent excessive vibration during operation, which increases with strike velocity and blade thickness, the rig should be supported by a stable foundation which is an important consideration when selecting the location for the RETERO rig. Ideally, this support should also be provided at the top of the rig for maximum leverage.

Additionally, we recommend that the high-speed camera setup be mounted separately from the rig's frame to prevent interference. Even though shaking cannot be completely eliminated, image sharpness was not adversely affected by post-strike vibrations in our tests, suggesting that most of the vibrations occurs after the strike.

Comparability rotary motion and linear motion strikes. The design of the linear motion strike rig is based on the assumption that tangential motion during impact is a reasonable approximation for impacts in rotary machines. While this may hold true for hard-bodied sensor probes, where the strike may be characterized primarily by the initial impact, soft-bodied objects, such as fish or soft-bodied sensor probes, can experience significantly longer interactions with the blade. In the worst-case scenario, where the interaction spans the entire strike window of 20 cm, the angular rotation is given by $\phi = \frac{2s_{\text{travel}}}{d_{\text{rotor}}}$, where s_{travel} is the 20 cm strike window and d_{rotor} is the rotor diameter. The resulting deviation perpendicular to the strike direction is given by $x_{\text{deviation}} = (1 - \cos(\phi)) \cdot s_{\text{travel}}$. For typical machine dimensions, such as a turbine with a 8.6 m rotor [42] and a pump with a 0.8 m [32] rotor, this deviation ranges from 0.22 mm for the turbine to 24 mm for the pump or 0.1 % and 12.2 % in relation to the travel length respectively. According to Bevelhimer et al. [59], the blade swept through 0.5 m of water before impact. Assuming an approximate angular rotation of 90°, this corresponds to an estimated rotor with a 0.64 m diameter with a resulting geometric deviation of 40 mm (or 19%) when compared to linear motion.

Additionally, we compared compiled results from live fish strike tests on rainbow trout (*Oncorhynchus mykiss*) conducted by Electric Power Research Institute (EPRI) [58] and ORNL [65] for overlapping values of the L/t ratio and strike velocity. While ORNL reported data for individual strikes, EPRI provided averaged results, leading to a comparative approach where EPRI datasets encompassing similar experimental conditions to ORNL were included, as illustrated in Fig. 6(b). Both studies used a blade with a semicircular leading edge and assessed mortality at 1 h post-strike. ORNL reported fish length as total length (from the tip of the snout to the tips of the caudal fin), while EPRI reported fork length (measured from the tip of the snout to the middle caudal fin rays) [64]. This methodological difference is expected to have minimal impact for rainbow trout, as this species has relatively short fin tips, resulting in a nearly truncate caudal fin. EPRI's experiments varied strike location, primarily targeting the mid-body, and did not control for fish orientation, though both parameters were documented. In contrast, ORNL's selected strikes had a consistent lateral orientation but varied in strike location, with box 3 in Fig. 6(b) consisting entirely of strikes to the tail region, which is summarized in Fig. 6(a). Despite methodological differences, mortality discrepancies across the three overlapping cases were minimal, showing that the rigs with linear motion show good comparability to those with rotary motion.

Deviation of the impact location. In Fig. 4, it can be observed that the impact position shifts towards the rear between strike velocities of 1 m s^{-1} to 10 m s^{-1} by 10 cm. In Table 2, we assumed a constant impact position, corresponding to the impact location for a strike velocity of 1 m s^{-1} . This assumption introduces inaccuracies at higher velocities, as the impact occurs later than expected. However, given the high repeatability of the strike event and the significant variability in the measured acceleration magnitude of the sensor probe following the strike, correcting for this rather small positional error was deemed to have little meaningful impact on the measurements.

Conclusions & Outlook

Hydropower is a vital component of global renewable energy strategies. However, its ecological challenges, in particular the risk of injury and mortality to fish during downstream passage, pose an obstacle for a continued use in the face of the increased awareness of its ecological

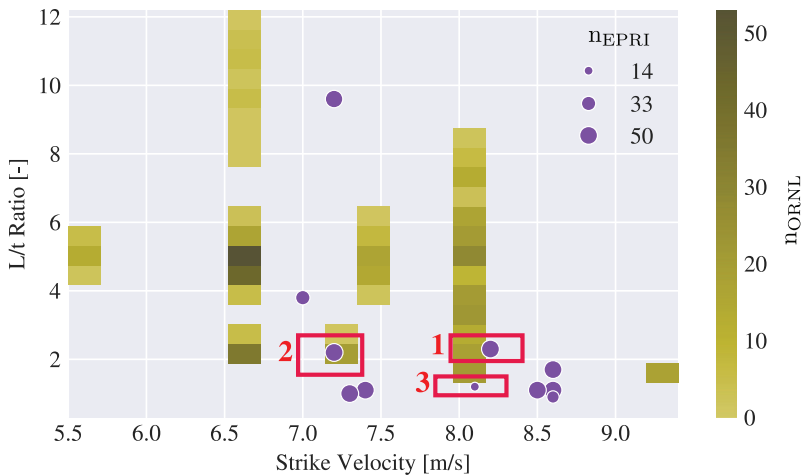
impact and the loss of biodiversity. The test rig presented in this work bridges a critical gap in hydropower research by offering a reproducible platform for studying the dynamics of blade strikes on sensor probes and live fish data. In this work, we introduced a digitally controlled, open-access laboratory test rig design for the collection of biological threshold data necessary for estimating fish injury and mortality due to turbine blade strikes, with detailed design information available online [71]. The rig also allows for an enhancement of the predictive accuracy of passive collision sensors, providing biologists and engineers with a more accurate depiction of the frequency and severity of blade strike events. This tool is especially valuable for developing new fish-safe turbine designs, because it allows for impact testing multiple blade geometries across a range of strike velocities. With precise control over blade velocity, ranging from 1 m s^{-1} to 10 m s^{-1} , it offers a reliable method for studying both fish injury and the physical conditions experienced during strikes. The open-access design significantly lowers the barrier to entry by reducing the need for specialized engineering expertise, making it more accessible to researchers from various fields.

Existing laboratory methods to research strike events, such as live fish experiments and sensor-based testing, have been constrained by the lack of precise control over blade velocity and the absence of a standardized test rig. Our rig addresses these limitations with electronically controlled blade velocity, improved reproducibility between strikes, minimal and quantified deceleration during impact, self-resetting mechanisms, and high-resolution position feedback—all within a compact and cost-efficient design. The fact that even strikes at 1 m s^{-1} , which are insufficient to cause severe injury to fish, produced acceleration values exceeding the 95 g threshold by more than double, not only challenges the current reliance on this threshold for determining injury severity but more importantly shows the need of improved sensor development and the benefit of having access to a system like ours, which allows researchers to verify blade strike models under controlled conditions. This setup isolates strike events from other confounding effects of a real flow field, focusing exclusively on strike velocity and blade thickness which are two critical variables influencing mortality to provide data specifically suited for estimating strike severity in field conditions using sensor probes. This approach could significantly enhance ecological impact assessments of hydropower facilities by enabling the use of dose-response relationships to estimate strike-induced mortality for specific fish species solely from sensor data — an application not currently feasible in field investigations. Current live fish testing methods, involving extensive fieldwork and intensive data processing, are highly time-consuming and challenging to scale. For instance, one of the authors participated in a recent live-fish experiment involving over 1800 fish, combined with sensor probes, to investigate changes in passage mortality for three fish species in a pump modified specifically to reduce fish mortality [72]. This study required several weeks of fieldwork followed by more than nine months of data cleaning and analysis.

Looking ahead, the development and use of this test rig offer new opportunities to refine injury and mortality models based on sensor data as well as aid in advances of sensor development regarding the prediction of strike velocity. Future work could focus on expanding the rig's capabilities to test a broader range of conditions and sensor types. Additionally, the open design allows for collaboration within the hydropower, engineering, and biological communities to further enhance the predictive models used in assessing fish injury and mortality. By refining sensor probe accuracy, the need for live fish testing in field studies can be reduced, promoting more ethical and efficient research methods. Ultimately, the continued evolution of such test rigs will contribute to more sustainable and ecologically responsible hydropower development worldwide.

	Strike Velocity [m/s]	L/t Ratio [-]	Amaral et al.				Bevelhimer et al.				Discrepancy [%pt.]
			n	Loc [%]	Orient [%]	Survival [%]	n	Loc [%]	Orient [%]	Survival [%]	
Box 1	7.8–8.6 (8.1)	2.0–2.7 (2.3)	50	4 H 74 M 22 T	64 L 22 D 14 V	32.0	20	10 H 90 M 0 T	100 L 0 D 0 V	30.0	2.0
			50	21 H 65 M 15 T	65 L 25 D 10 V	78.0	20	0 H 95 M 5 T	100 L 0 D 0 V	75.0	
			14	0 H 71 M 29 T	93 L 0 D 7 V	92.9	16	0 H 0 M 100 T	100 L 0 D 0 V	93.8	
Box 2	7.0–7.4 (7.2)	1.6–2.7 (2.2)	50	65 M 15 T	25 D 10 V	78.0	20	95 M 5 T	0 D 0 V	75.0	3.0
Box 3	7.9–8.3 (8.1)	1.0–1.5 (1.2)	14	71 M 29 T	0 D 7 V	92.9	16	0 M 100 T	0 D 0 V	93.8	0.9

(a) Table comparing experiments with overlapping conditions identified in fig. 6b, with the mean values reported by Amaral et al. in brackets. Strike location, reported as head (H), mid-body (M), and tail (T), and fish orientation, as lateral (L), dorsal (D), and ventral (V).



(b) Strike experiments conducted at EPRI as purple circles, and ORNL shown in yellow, with overlapping experiments within the red boxes.

Fig. 6. Comparison of strike experiments on rainbow trout between the ORNL and EPRI experiments, with three identified overlapping conditions. ORNL results, reported individually, are represented as a yellow heat map, while EPRI's averaged results are shown as purple circles. For comparing L/t ratios (ratio of fish length to blade thickness), the minimum and maximum values reported from EPRI for that experiment were used, while a 5% range around the reported strike velocity was applied to identify overlapping conditions. Despite notable variations in strike location and fish orientation (as shown in the table), the discrepancy in reported mortality rates remains minimal.

CRedit authorship contribution statement

Wolf Iring Kösters: Writing – original draft, Visualization, Validation, Software, Methodology, Investigation, Data curation. **Jeffrey A. Tuhtan:** Writing – review & editing, Validation, Supervision, Methodology, Conceptualization. **Danil Efimov:** Investigation. **Maarja Kruusmaa:** Writing – review & editing, Supervision, Resources, Project administration, Funding acquisition. **Stefan Hoerner:** Writing – review & editing, Validation, Supervision, Resources, Project administration, Methodology, Funding acquisition, Conceptualization.

Declaration of competing interest

The authors declare that they have no known competing financial interests or personal relationships that could have appeared to influence the work reported in this paper.

Acknowledgments

The authors would like to express their sincere gratitude to Karla Ruiz-Hussmann, Jessica Dafis, Yanneck Kiiski, Shokoofeh Abbaszadeh, Christian Kisow, and Dirk Meinecke for their invaluable assistance in the construction of the strike rig. Special thanks are extended to Yanneck Kiiski and Johannes Frank for their contributions to the creation

and maintenance of the CAD design. Finally, we are deeply appreciative of Roberto Leidhold for his crucial support in the setup and tuning of the power electronics and servomotor, without which this project would not have been possible.

This project is part of the EU Marie Curie International Training Network on Soft, Self-responsive, Smart Materials for Robots (SMART-ITN) and has received funding from the European Union's Horizon 2020 research and innovation program under the Marie Skłodowska-Curie grant agreement No 860108. It is also funded by the German Federal Ministry of Education and Research (BMBF) under project number 031L0152A - D/16LW019 ("Alternative Methods to Animal Testing"), which ran between March 2019 to March 2024 and received funding by the Deutsche Forschungsgemeinschaft (DFG, German Research Foundation, Germany – 444994527. Jeffrey A. Tuhtan and Maarja Kruusmaa's contributions were funded in part by the Estonian Research Council, Estonia Grant PRG2198.

Appendix A. Detailed design description

Detailed instructions for constructing the strike rig are provided in this section. Table A.3 shows a cost breakdown for each assembly group, while individual part names, numbers and additional info on these parts important for building the strike rig can be obtained in the bill of materials table available online [71].

Table A.3

Cost breakdown of the strike rig and its assembly components as of late 2022. Prices have remained largely stable as of 2024.

Assembly group	Main items in group	Approximate price
Frame	aluminum strut profiles, brackets, fasteners	1800 €
Basin	PC plates, PU adhesive, primer	1200 €
Drive system mechanics	rail, belt, linear bearings, pulleys, bushings	900 €
Drive system electronics	motor, servo-drive, break resistor	3100 €
	Total	7000 €

The strike rig is a linear motion system with supported rail, as this combines high stiffness and load capacity with low cost. The drive system is a servo-motor, it allows for high-accuracy motion control and the ability to engage with the maximum torque from rest. The torque is transmitted through a timing belt; this is much lighter and does not need lubrication compared to a chain. The frame is comprised of aluminum strut profiles 45 mm × 45 mm in size that allow easy modification and construction while being decently stiff.

The strike rig employs a linear motion system with supported rails, offering a combination of high stiffness, load capacity, and cost-efficiency. The drive system consists of a servo motor, providing high-accuracy motion control and the capability to deliver maximum torque from rest. Torque is transmitted via a timing belt, which is lighter and requires no lubrication compared to a chain. The frame is constructed from 45 mm × 45 mm aluminum strut profiles, ensuring ease of modification and assembly while maintaining sufficient stiffness.

To estimate the required motor power, the motion system was initially modeled using differential equations that accounted for mass, acceleration, and fluid drag. Following the rig's construction, these values were updated to include real-world mechanical losses. For research groups interested in building a similar system, the Python script used for these calculations is available in the GitHub repository.³

Frame and basin. The basin is constructed from polycarbonate (PC) due to its superior impact resistance compared to glass or acrylic glass. Standard PC plates are produced in dimensions of 3050 mm × 3050 mm, which determined the basin length of 3 m to eliminate the need for additional seals. To address expected pressure peaks, sloshing effects, and wave-induced deformation, a flexible polyurethane adhesive (Sika Sikaflex 295UV) was used. To enhance stiffness, the PC plates were reinforced with aluminum angle profiles along their edges. The basin is supported by a frame of aluminum strut profiles, which bear the basin's load and provide mounting points for other system components.

Motor. The maximum motor speed and effective pulley diameter determine the system's maximum strike speed and should be selected to achieve the desired performance. An excessively large pulley diameter increases the required translational force, leading to higher torque demands and necessitating a more powerful motor and servo drive. The motor selected for the system is a Siemens 1FT6102-8AC71, which provides a maximum speed of 1500 RPM at full torque. This corresponds to an optimal pulley diameter of 127 mm.

Servocontroller. The servocontroller used (Kollmorgen AKD-P01207) is capable of delivering a peak current of 30 A for up to 1 s, resulting in motor power of 10.4 kW when supplied with three-phase current at 400 V. A key advantage of this controller is its compatibility with Python, enabling the development of an interface to adjust parameters within predefined safe limits. Additionally, more advanced velocity trajectories can be programmed and fed through the PC interface. During deceleration, the motor operates as a generator, with the generated energy dissipated as heat through an external resistive load.

Belt and pulleys. A belt drive was selected over a chain drive or spool system, as used by the Alden rig, due to its lower weight compared to a chain drive and its ability to enable automatic resetting, which is not feasible with a spool system. The HTD (high-torque drive) system was chosen for its high availability and superior circumferential force capacity. The specific belt used is an HTD-8M-30, featuring a 8 mm tooth pitch and a 30 mm width. Proper belt tension is achieved by adjusting the axial distance, moving the motor setup backward as necessary.

The pulley is not mounted directly to the motor shaft because the radial forces generated exceed the shaft's maximum allowable force. Instead, the pulley is mounted on a separate shaft connected to the motor via a backlash-free metal bellows coupler, which is critical for avoiding resonance in the system. The shaft, with a diameter of 20 mm, is made from X46Cr13 stainless steel and is supported by two UCP204 industry-standard pillow bearings. Its dimensions were determined using the von Mises yield criterion with a safety factor of 1.4.

The closest available match to the effective diameter in the HTD-8M system is a 48-tooth motor pulley, which allows for a maximum speed of 9.6 m s⁻¹. Although slightly below the desired speed of 10 m s⁻¹, the torque loss associated with this discrepancy is minimal and does not significantly affect performance.

Rail and cart. A shaft-guidance system of type TBS25, featuring 25 mm diameter shafts with a length of 3200 mm, was used. This system is compatible with the aluminum strut profile raster, ensuring seamless integration. The cart is connected to the rail through low-friction recirculating ball bearings (SBR25UU), providing smooth and efficient motion.

The cart itself is constructed from planar aluminum strut profiles, allowing for rapid attachment or replacement of the blade arms. The belt is secured to the cart using clamping plates.

Strike arm and blade. The strike arm is constructed from an aluminum strut profile, onto which 3D-printed impact-resistant polycarbonate (PC) blades are attached. The 3D-printed blades are reinforced with two stainless steel threaded rods, which are epoxied into the structure and serve as connection points to the strut profile. A plastic lid positioned between the blade and the strike arm acts as a splash shield.

To ensure comparability with the data from Saylor et al. [65], the blade's leading edge is constrained to a semicircular shape. However, the supporting body and trailing edge of the blade can be optimized to reduce drag and, more importantly, to minimize entrained air, which negatively affects high-speed video quality.

Sensor retainer. The sensor mounting setup follows the design established by ORNL [63]. Two angled aluminum sheets, each 50 mm wide, are mounted on the front side of an aluminum strut profile, as illustrated in Fig. 2. The strike angle can be adjusted by repositioning the aluminum platforms and securing them with wing nuts. The distance between the platforms is adjustable by moving the strut profile to which the platforms are attached.

Data synchronization. The servocontroller is programmed to emit a digital pulse before impact, serving as a trigger signal for the high-speed cameras. Additionally, this signal activates a device that generates a magnetic pulse via a copper coil on the basin wall adjacent to sensors that feature Hall effect sensors. This pulse is detected by a magnetic

³ github.com/ikoesters/srdatacombiner.

sensor on the probe and is later used for synchronizing the data from the servo-drive, cameras, and sensor probe. For sensors without a Hall effect sensor, the sudden increase in acceleration magnitude upon impact may be used to achieve synchronization.

Safety considerations. To reiterate what has been said in the methodology section, ensuring safe operation is paramount, even in cases of user inattention. To this end, the rig is fully enclosed in acrylic glass, and the access hatch is equipped with a safety switch that disables the motor when opened. Additionally, a Python-based graphical user interface is under development to restrict access to the servocontroller software, allowing only safe and predefined user inputs.

Incorrect parameter settings in the servocontroller software can lead to potentially catastrophic outcomes, particularly concerning the end-of-motion point. This setting allows the motor to operate at full speed up to the limit switch, which cuts power if exceeded. However, the momentum stored in the system can cause the motor to crash into the wall beyond the limit switch. While buffer material has been successfully used to soften such impacts and prevent structural damage, this mitigation measure cannot be guaranteed to protect against all scenarios.

Appendix B. Supplementary data

The supplementary material [73] includes high-speed videos of the fish dummy discussed in Section 3 and the rigid RAPID sensor probe impacted at 5 m s^{-1} , recorded from the bottom and side, along with a strike video at normal speed, available at <https://doi.org/10.5281/zenodo.15864853>.

Data availability

The CAD data are publicly available online [71], and the software used for data processing and integration can be accessed via GitHub at <https://github.com/ikoesters/srdatacombiner>. Videos demonstrating the RETERO strike rig tests are included in the supplementary materials. Additionally, the datasets used to generate Figures 4, 5, and 6 in this paper are openly accessible online [74].

References

- Vagnoni E, Gezer D, Anagnostopoulos I, Cavazzini G, Doujak E, Hočevár M, Rudolf P. The new role of sustainable hydropower in flexible energy systems and its technical evolution through innovation and digitalization. *Renew Energy* 2024;230:120832. <http://dx.doi.org/10.1016/j.renene.2024.120832>, URL <https://linkinghub.elsevier.com/retrieve/pii/S0960148124009005>.
- Cox RX, Kingsford RT, Suthers I, Felder S. Fish injury from movements across hydraulic structures: A review. *Water* 2023;15(10):1888. <http://dx.doi.org/10.3390/w15101888>, URL <https://www.mdpi.com/2073-4441/15/10/1888>.
- Iho A, Soiminen N, Vehviläinen I, Koljonen S, Artell J, Belinskij A. Rivers under pressure: Interdisciplinary feasibility analysis of sustainable hydropower. *Environ Policy Gov* 2023;33(2):191–205. <http://dx.doi.org/10.1002/eet.2013>, URL <https://onlinelibrary.wiley.com/doi/10.1002/eet.2013>.
- Van Treecck R, Radinger J, Noble RA, Geiger F, Wolter C. The European fish hazard index – an assessment tool for screening hazard of hydropower plants for fish. *Sustain Energy Technol Assessments* 2021;43:100903. <http://dx.doi.org/10.1016/j.seta.2020.100903>, URL <https://linkinghub.elsevier.com/retrieve/pii/S2213138820313308>.
- Larinier M. Contributing paper dams and fish migration. In: World commission on dams. 2001, URL <https://www.semanticscholar.org/paper/Contributing-Paper-Dams-and-Fish-Migration-Larinier/e4ab7319c3a47876392607a3277fe03a64fc6b1>.
- Błońska D, Tarkan AS, Andreou D, Bolland JD, Davies P, Dodd JR, Gillingham P, Roberts CG, Amat-Trigo F, Aksu S, Hinds A, Palder OJ, Yeldham M, Britton JR. Restoration of river connectivity enables long-distance spawning migrations in a potamodromous fish. *J Environ Manag* 2025;377:124646. <http://dx.doi.org/10.1016/j.jenvman.2025.124646>, URL <https://linkinghub.elsevier.com/retrieve/pii/S030147972500622X>.
- Union TE. Directive 2000/60/EC of the European Parliament and of the Council of 23 October 2000 establishing a framework for Community action in the field of water policy. 2000, URL <https://eur-lex.europa.eu/eli/dir/2000/60/oj>.
- Brown E, Sulaeman S, Quispe-Abad R, Müller N, Moran E. Safe passage for fish: The case for in-stream turbines. *Renew Sustain Energy Rev* 2023;173:113034. <http://dx.doi.org/10.1016/j.rser.2022.113034>, URL <https://linkinghub.elsevier.com/retrieve/pii/S1364032122009157>.
- Uria-Martinez R, Johnson M. U.S. hydropower market report (2023 edition). Technical report, Oak Ridge National Laboratory (ORNL), Oak Ridge, TN (United States); 2023, URL <https://www.energy.gov/eere/water/hydropower-market-reports>.
- Quaranta E, Aggidis G, Boes RM, Comoglio C, De Michele C, Ritesh Patro E, Georgievskaja E, Harby A, Kougiaris I, Muntean S, Pérez-Díaz J, Romero-Gomez P, Rosa-Clot M, Schleiss AJ, Vagnoni E, Wirth M, Pisticchio A. Assessing the energy potential of modernizing the European hydropower fleet. *Energy Convers Manage* 2021;246:114655. <http://dx.doi.org/10.1016/j.enconman.2021.114655>, URL <https://linkinghub.elsevier.com/retrieve/pii/S0196890421008311>.
- Schwevers U, Adam B. Fish-friendly turbines. In: Schwevers U, Adam B, editors. *Fish protection technologies and fish ways for downstream migration*. Cham: Springer International Publishing; 2020, p. 203–10. http://dx.doi.org/10.1007/978-3-030-19242-6_6.
- Foust J, Hecker G, Li S, Allen G. Fish-Friendly hydropower turbine development & deployment: alden turbine preliminary engineering and model testing. Technical report DOEGOI8167-1, Electric Power Research Institute; 2011, <http://dx.doi.org/10.2172/1050066>, URL <https://www.osti.gov/biblio/1050066>.
- Quaranta E, Baheini A, Riasi A, Revelli R. The very low head turbine for hydropower generation in existing hydraulic infrastructures: State of the art and future challenges. *Sustain Energy Technol Assessments* 2022;51:101924. <http://dx.doi.org/10.1016/j.seta.2021.101924>, URL <https://www.sciencedirect.com/science/article/pii/S2213138821009383>.
- Amaral SV, Watson SM, Schneider AD, Rackovan J, Baumgartner A. Improving survival: Injury and mortality of fish struck by blades with slanted, blunt leading edges. *J Ecohydraulics* 2020;5(2):175–83. <http://dx.doi.org/10.1080/24705357.2020.1768166>, URL <https://www.tandfonline.com/doi/full/10.1080/24705357.2020.1768166>.
- Klopries E-M, Deng ZD, Lachmann TU, Schüttrumpf H, Trumbo BA. Surface bypass as a means of protecting downstream-migrating fish: Lack of standardised evaluation criteria complicates evaluation of efficacy. *Mar Freshwater Res* 2018;69(12):1882–93. <http://dx.doi.org/10.1071/MF18097>, Publisher: CSIRO PUBLISHING. URL <https://www.publish.csiro.au/mf/MF18097>.
- Knott J, Mueller M, Pander J, Geist J. Downstream fish passage at small-scale hydropower plants: Turbine or bypass? *Front Environ Sci* 2023;11:1168473. <http://dx.doi.org/10.3389/fenvs.2023.1168473>, URL <https://www.frontiersin.org/articles/10.3389/fenvs.2023.1168473/full>.
- Norman J, Reeds J, Wright RM, Bolland JD. Impact of anthropogenic infrastructure on aquatic and avian predator-prey interactions in a modified lowland river. *Freshwater Biol* 2024;69(1):157–71. <http://dx.doi.org/10.1111/fwb.14201>, URL <https://onlinelibrary.wiley.com/doi/10.1111/fwb.14201>.
- Radinger J, Van Treecck R, Wolter C. Evident but context-dependent mortality of fish passing hydroelectric turbines. *Conserv Biol* 2022;36(3):e13870. <http://dx.doi.org/10.1111/cobi.13870>, URL <https://onlinelibrary.wiley.com/doi/10.1111/cobi.13870>.
- Mueller M, Knott J, Pander J, Geist J. Experimental comparison of fish mortality and injuries at innovative and conventional small hydropower plants. *J Appl Ecol* 2022;59(9):2360–72. <http://dx.doi.org/10.1111/1365-2664.14236>, URL <https://besjournals.onlinelibrary.wiley.com/doi/10.1111/1365-2664.14236>.
- für Normung e.V. DI. DIN EN 18110:2024-08: Wasserbeschaffenheit - Verfahren zur Ermittlung der Fischdurchgängigkeit von Wasserförderschnecken, Pumpen und Spiralturbinen, die in Pumpwerken und Wasserkraftwerken verwendet werden. 2024, <http://dx.doi.org/10.31030/3555890>, URL <https://www.dinmedia.de/de/-/381721727>.
- (NEN) NN. NEN 8775:2020 fish safety - method for the determination of the fish safety of pumps, archimedean screws and confined water turbines used in pumping stations and hydroelectric plants. 2020.
- Čada G, Coutant C, Whitney R. Development of biological criteria for the design of advanced hydropower turbines. Idaho Fall, ID (United States): U.S. Department of Energy; 1997, <http://dx.doi.org/10.2172/1218126>, pages DOE/ID-100578, 1218126, 3738. Report Number: DOE/ID-100578, 1218126, 3738. URL <https://www.osti.gov/servlets/purl/1218126>.
- Coutant CC, Whitney RR. Fish behavior in relation to passage through hydropower turbines: A review. *Trans Am Fish Soc* 2000;129(2):351–80. [http://dx.doi.org/10.1577/1548-8659\(2000\)129<0351:FBIRTP>2.0.CO;2](http://dx.doi.org/10.1577/1548-8659(2000)129<0351:FBIRTP>2.0.CO;2), URL [http://doi.wiley.com/10.1577/1548-8659\(2000\)129<0351:FBIRTP>2.0.CO;2](http://doi.wiley.com/10.1577/1548-8659(2000)129<0351:FBIRTP>2.0.CO;2).
- of the Swiss Confederation TFA. Swiss animal welfare act. 2005, URL <https://fedlex.data.admin.ch/eli/cc/2008/414>.
- of the Swiss Confederation TFA. FSVO ordinance on laboratory animal husbandry, the production of genetically modified animals and methods of animal experimentation. 2010, URL <https://fedlex.data.admin.ch/eli/cc/2010/207>.
- Zangiabadi E, Masters I, Williams AJ, Croft TN, Malki R, Edmunds M, Mason-Jones A, Horsfall I. Computational prediction of pressure change in the vicinity of tidal stream turbines and the consequences for fish survival rate. *Renew Energy* 2017;101:1141–56. <http://dx.doi.org/10.1016/j.renene.2016.09.063>, URL <https://linkinghub.elsevier.com/retrieve/pii/S0960148116308539>.

- [27] Klopries E-M, Schüttrumpf H. Mortality assessment for adult European eels (*Anguilla Anguilla*) during turbine passage using CFD modelling. *Renew Energy* 2020;147:1481–90. <http://dx.doi.org/10.1016/j.renene.2019.09.112>, URL <https://linkinghub.elsevier.com/retrieve/pii/S0960148119314508>.
- [28] Stoltz U, Geiger F, Tuhtan JA. Influence of operation modes and fish behavior on fish passage through turbines. *IOP Conf Ser: Earth Environ Sci* 2021;774(1):012125. <http://dx.doi.org/10.1088/1755-1315/774/1/012125>, URL <https://iopscience.iop.org/article/10.1088/1755-1315/774/1/012125>.
- [29] Powalla D, Hoerner S, Cleynen O, Thévenin D. A numerical approach for active fish behavior modelling with a view toward hydropower plant assessment. *Renew Energy* 2022;188:957–66. <http://dx.doi.org/10.1016/j.renene.2022.02.064>, URL <https://linkinghub.elsevier.com/retrieve/pii/S0960148122002063>.
- [30] Zhu G, Guo Y, Feng J, Gao L, Wu G, Luo X. Analysis and reduction of the pressure and shear damage probability of fish in a Francis turbine. *Renew Energy* 2022;199:462–73. <http://dx.doi.org/10.1016/j.renene.2022.08.158>, URL <https://linkinghub.elsevier.com/retrieve/pii/S0960148122013349>.
- [31] Hogan TW, Cada GF, Amaral SV. The status of environmentally enhanced hydropower turbines. *Fisheries* 2014;39(4):164–72. <http://dx.doi.org/10.1080/03632415.2014.897195>, URL <http://doi.wiley.com/10.1080/03632415.2014.897195>.
- [32] Hoerner S. Critical areas for fish passage in large axial flow pumps. In: *Proceedings of the 40th IAHR world congress (vienna, 2023)*. Vienna; 2023.
- [33] Pan Q, Weihs Z, Zhang D, Shi W, van Esch BPM. Locomotion and strike damage of fish passing through a fish friendly tubular pump using computational fluid dynamics and discrete element coupling method. *Phys Fluids* 2024;36(8):087129. <http://dx.doi.org/10.1063/1.5216564>.
- [34] Ahmad F, Evans J, Nestler JM. Multiple sensor fish surrogate for acoustic and hydraulic data collection. 1997.
- [35] Carlson TJ, Duncan JP. Evolution of the sensor fish device for measuring physical conditions in severe hydraulic environments. Technical report PNNL-15708, 878148, Richland, WA (United States): Pacific Northwest National Lab. (PNNL); 2003. <http://dx.doi.org/10.2172/878148>, URL <http://www.osti.gov/servlets/purl/878148-DIWgVE/>.
- [36] Deng ZD, Carlson T, Duncan JP, Richmond M. Six-degree-of-freedom sensor fish design and instrumentation. *Sensors* 2007;7(12):3399–415. <http://dx.doi.org/10.3390/s7123399>, URL <http://www.mdpi.com/1424-8220/7/12/3399>.
- [37] Deng ZD, Lu J, Myjak MJ, Martinez JJ, Tian C, Morris SJ, Carlson TJ, Zhou D, Hou H. Design and implementation of a new autonomous sensor fish to support advanced hydropower development. *Rev Sci Instrum* 2014;85(11). <http://dx.doi.org/10.1063/1.4900543>, URL <http://aip.scitation.org/doi/10.1063/1.4900543>.
- [38] Deng ZD, Carlson TJ, Duncan JP, Richmond MC, Dauble DD. Use of an autonomous sensor to evaluate the biological performance of the advanced turbine at Wanapum Dam. *J Renew Sustain Energy* 2010;2(5). <http://dx.doi.org/10.1063/1.3501336>, URL <http://aip.scitation.org/doi/10.1063/1.3501336>.
- [39] Fu T, Deng ZD, Duncan JP, Zhou D, Carlson TJ, Johnson GE, Hou H. Assessing hydraulic conditions through Francis turbines using an autonomous sensor device. *Renew Energy* 2016;99:1244–52. <http://dx.doi.org/10.1016/j.renene.2016.08.029>, URL <https://linkinghub.elsevier.com/retrieve/pii/S0960148116307303>.
- [40] Martinez J, Deng ZD, Tian C, Mueller R, Phonekhampheng O, Singhanoung D, Thorncraft G, Phommavong T, Phommachan K. In situ characterization of turbine hydraulic environment to support development of fish-friendly hydropower guidelines in the lower Mekong River region. *Ecol Eng* 2019;133:88–97. <http://dx.doi.org/10.1016/j.ecoeng.2019.04.028>, URL <https://linkinghub.elsevier.com/retrieve/pii/S0925857419301454>.
- [41] Martinez J, Deng Z, Titzler P, Duncan J, Lu J, Mueller R, Tian C, Trumbo B, Ahmann M, Renholds J. Hydraulic and biological characterization of a large Kaplan turbine. *Renew Energy* 2019;131:240–9. <http://dx.doi.org/10.1016/j.renene.2018.07.034>, URL <https://linkinghub.elsevier.com/retrieve/pii/S0960148118308310>.
- [42] Romero-Gomez P, Poomchaivej T, Razdan R, Robinson W, Peyreder R, Raeder M, Baumgartner LJ. Sensor fish deployments at the Xayaburi hydropower plant: Measurements and simulations. *Water* 2024;16(5):775. <http://dx.doi.org/10.3390/w16050775>, URL <https://www.mdpi.com/2073-4441/16/5/775>.
- [43] Martinez JJ, Daniel Deng Z, Klopries E-M, Mueller RP, Scott Titzler P, Zhou D, Beirao B, Hansten AW. Characterization of a siphon turbine to accelerate low-head hydropower deployment. *J Clean Prod* 2019;210:35–42. <http://dx.doi.org/10.1016/j.jclepro.2018.10.345>, URL <https://linkinghub.elsevier.com/retrieve/pii/S0959652618333821>.
- [44] Pauwels IS, Baeyens R, Toming G, Schneider M, Buysse D, Coeck J, Tuhtan JA. Multi-species assessment of injury, mortality, and physical conditions during downstream passage through a large archimedes hydrodynamic screw (Albert Canal, Belgium). *Sustainability* 2020;12(20):8722. <http://dx.doi.org/10.3390/su12208722>, URL <https://www.mdpi.com/2071-1050/12/20/8722>.
- [45] Knott J, Mueller M, Pander J, Geist J. Ecological assessment of the world's first shaft hydropower plant. *Renew Sustain Energy Rev* 2023;187:113727. <http://dx.doi.org/10.1016/j.rser.2023.113727>, URL <https://linkinghub.elsevier.com/retrieve/pii/S1364032123005841>.
- [46] Brown RS, Pflugrath BD, Colotelo AH, Brauner CJ, Carlson TJ, Deng ZD, Seaburg AG. Pathways of barotrauma in juvenile salmonids exposed to simulated hydrotrauma passage: Boyle's law vs. Henry's law. *Fish Res* 2012;121–122:43–50. <http://dx.doi.org/10.1016/j.fishres.2012.01.006>, URL <https://linkinghub.elsevier.com/retrieve/pii/S0167838612000379>.
- [47] Kerr JR, White PR, Leighton TG, Silva LGM, Kemp PS. Boyle's Law ignores dynamic processes in governing barotrauma in fish. *Sci Rep* 2023;13(1):19125. <http://dx.doi.org/10.1038/s41598-023-46125-9>, URL <https://www.nature.com/articles/s41598-023-46125-9>.
- [48] Geiger F, Cuchet M, Peter R. Zur Verringerung von Fischschäden in Turbinen mittels Verhaltensbeeinflussung. *WASSERWIRTSCHAFT* 2020;110(12):41–5. <http://dx.doi.org/10.1007/s35147-020-0756-5>, URL <https://www.springerprofessional.de/doi/10.1007/s35147-020-0756-5>.
- [49] Vowles AS, Kemp PS. Effects of light on the behaviour of brown trout (*Salmo trutta*) encountering accelerating flow: Application to downstream fish passage. *Ecol Eng* 2012;47:247–53. <http://dx.doi.org/10.1016/j.ecoeng.2012.06.021>, URL <https://linkinghub.elsevier.com/retrieve/pii/S0925857412002200>.
- [50] Cox RX, Felder S. Injury-free transport of fish through closed conduit components. *J Ecohydraulics* 2025;1–16. <http://dx.doi.org/10.1080/24705357.2025.2462296>, URL <https://www.tandfonline.com/doi/full/10.1080/24705357.2025.2462296>.
- [51] Deng ZD, Guensch GR, McKinstry CA, Mueller RP, Dauble DD, Richmond MC. Evaluation of fish-injury mechanisms during exposure to turbulent shear flow. *Can J Fish Aquat Sci* 2005;62(7):1513–22. Publisher: NRC Research Press Ottawa, Canada.
- [52] Richmond MC, Deng ZD, McKinstry CA, Mueller RP, Carlson TJ, Dauble DD. Response relationships between Juvenile Salmon and an autonomous sensor in turbulent flow. *Fish Res* 2009;9(1–2):134–9. <http://dx.doi.org/10.1016/j.fishres.2009.01.011>, URL <https://linkinghub.elsevier.com/retrieve/pii/S016783860900040X>.
- [53] Bercovitz Y, Tissot L, Sagnes P, Courret D, Lebert F, Lagarige T, Mataix V, Dumond L. Evaluation of fish injuries at the outlet of downrun passage devices: Preliminary in situ and laboratory experiments with Sensor Fish. In: *Proceedings of the 39th IAHR world congress. International Association for Hydro-Environment Engineering and Research (IAHR); 2022*, p. 1237–45. <http://dx.doi.org/10.3850/IAHR-39WC25217119202255>, URL <https://www.iahr.org/library/infor?pid=20868>.
- [54] Hoerner S, Kösters WI, Abbaszadeh S, Wagner F, Tuhtan JA. Towards a reliable and validated toolbox to replace live fish tests for the assessment of injury and mortality during downstream passage. In: *IAHR 15th international symposium on ecohydraulics and fish passage*. Quebec City, Canada; 2024. URL <https://hal.science/hal-04642604>.
- [55] Hou H, Deng ZD, Martinez J, Fu T, Duncan JP, Johnson G, Lu J, Skalski J, Townsend R, Tan L. A hydropower evaluation toolset (HBET) for characterizing hydraulic conditions and impacts of hydro-structures on fish. *Energies* 2018;11(4):990. <http://dx.doi.org/10.3390/en11040990>, URL <http://www.mdpi.com/1996-1073/11/4/990>.
- [56] Salalila A, Deng ZD, Martinez JJ, Lu J, Baumgartner LJ. Evaluation of a fish-friendly self-cleaning horizontal irrigation screen using autonomous sensors. *Mar Freshwater Res* 2019;70(9):1274. <http://dx.doi.org/10.1071/MF19194>, URL <http://www.publish.csiro.au/?paper=MF19194>.
- [57] Turpenny AW, Davis MH, Flemming JM, Davies JK. Experimental studies relating to the passage of fish and shrimps through tidal power turbines. *Mar Freshw Res Unit, Natl Power* 1992.
- [58] Amaral SV, Hecker GE. Evaluation of the effects of turbine blade leading edge design on fish survival. *Electr Power Res Inst* 2008;(1014937).
- [59] Bevelhimer MS, Pracheil BM, Fortner AM, Saylor R, Deck KL. Mortality and injury assessment for three species of fish exposed to simulated turbine blade strike. *Can J Fish Aquat Sci* 2019;76(12):2350–63. <http://dx.doi.org/10.1139/cjfas-2018-0386>, URL <http://www.nrcresearchpress.com/doi/10.1139/cjfas-2018-0386>.
- [60] Saylor RK, Fortner A, Bevelhimer M. Quantifying mortality and injury susceptibility for two morphologically disparate fishes exposed to simulated turbine blade strike. *Hydrobiologia* 2019;842(1):55–75. <http://dx.doi.org/10.1007/s10750-019-04026-x>, URL <http://link.springer.com/10.1007/s10750-019-04026-x>.
- [61] Saylor RK, Sterling D, Bevelhimer M, Pracheil B. Within and among fish species differences in simulated turbine blade strike mortality: Limits on the use of surrogacy for untested species. *Water* 2020;12(3):701. <http://dx.doi.org/10.3390/w12030701>, URL <https://www.mdpi.com/2073-4441/12/3/701>.
- [62] Meng L, Chen R, Wang X, Zhang CY, Zheng Y, Tian YJ. Turbine blade strike tests for evaluation and optimization of fish-friendly turbine. *IOP Conf Ser: Earth Environ Sci* 2022;1037(1):012058. <http://dx.doi.org/10.1088/1755-1315/1037/1/012058>, URL <https://iopscience.iop.org/article/10.1088/1755-1315/1037/1/012058>.
- [63] Bevelhimer MS, Pracheil BM, Fortner AM, Deck KL. An overview of experimental efforts to understand the mechanisms of fish injury and mortality caused by hydropower turbine blade strike. Technical Report ORNL/TM-2017/731, 1425338, Oak Ridge, TN (United States): Oak Ridge National Laboratory (ORNL); 2017. <http://dx.doi.org/10.2172/1425338>, URL <http://www.osti.gov/servlets/purl/1425338/>.

- [64] Hecker GE, Amaral SV, Stacy PS. Investigation of hydro-turbine leading-edge shapes favorable to fish survival. Technical Report 102561, Palo Alto, CA: Electric Power Research Institute; 2007.
- [65] Saylor RK, Bevelhimer M, Pracheil B. Fish injury and mortality caused by simulated impacts from turbine blades. 2020, <http://dx.doi.org/10.21951/1755094>, URL <https://www.osti.gov/servlets/purl/1755094/>.
- [66] Saylor RK, Wang PL, Bevelhimer M, Lloyd P, Goodwin J, Laughter R, Young D, Sterling D, Mhatre P, Atkins C, Post B. Creation of a prototype biomimetic fish to better understand impact trauma caused by hydropower turbine blade strikes. *PeerJ Mater Sci* 2021;3. <http://dx.doi.org/10.7717/peerj-matsci.16>, URL <https://peerj.com/articles/matsci-16>.
- [67] Leys C, Ley C, Klein O, Bernard P, Licata L. Detecting outliers: Do not use standard deviation around the mean, use absolute deviation around the median. *J Exp Soc Psychol* 2013;49(4):764–6. <http://dx.doi.org/10.1016/j.jesp.2013.03.013>, URL <https://www.sciencedirect.com/science/article/pii/S0022103113000668>.
- [68] Leys C, Delacre M, Mora YL, Lakens D, Ley C. How to classify, detect, and manage univariate and multivariate outliers, with emphasis on pre-registration. *Int Rev Soc Psychol* 2019;32(1). <http://dx.doi.org/10.5334/irsp.289>, URL <https://riips-irsp.com/articles/10.5334/irsp.289>.
- [69] Abbaszadeh S, Hoerner S, Leidhold R. Experimental optimization of a fish robot's swimming modes: A complex multiphysical problem. *Exp Fluids* 2024;65(4):51. <http://dx.doi.org/10.1007/s00348-024-03786-0>, URL <https://link.springer.com/10.1007/s00348-024-03786-0>.
- [70] Pflugrath BD, Saylor R, Engbrecht KM, Mueller RP, Stephenson JR, Bevelhimer M, Pracheil BM, Colotelo AH. Biological response models: Predicting injury and mortality of fish during downstream passage through hydropower facilities. Technical Report PNNL-30893, Pacific Northwest National Lab. (PNNL), Richland, WA (United States); 2021, <http://dx.doi.org/10.2172/1838202>, URL <https://www.osti.gov/biblio/1838202>.
- [71] Kösters WI, Tuhtan J, Efimov D, Kruusmaa M, Hoerner S. CAD data: An open laboratory blade strike rig to evaluate the risk of injury and mortality to fish and to test passive sensors. 2025, <http://dx.doi.org/10.5281/ZENODO.15078947>, URL <https://zenodo.org/doi/10.5281/zenodo.15078947>.
- [72] Pauwels IS, Broos S, Vandamme L, Van Wichelen J, Coeck J, Toming G, Tuhtan JA, Buysse D. A fish-friendly axial flow pump turns out to be eel safe, roach unfriendly and bream unsafe. *Sci Rep* 2024;14(1):30234. <http://dx.doi.org/10.1038/s41598-024-81095-6>, URL <https://www.nature.com/articles/s41598-024-81095-6>.
- [73] Kösters WI. Supplementary Data: An open laboratory blade strike rig to evaluate the risk of injury and mortality to fish and to test passive sensors. 2025, <http://dx.doi.org/10.5281/ZENODO.15864853>, URL <https://zenodo.org/doi/10.5281/zenodo.15864853>.
- [74] Kösters WI, Efimov D. Figure data: An open laboratory blade strike rig to evaluate the risk of injury and mortality to fish and to test passive sensors. 2025, <http://dx.doi.org/10.5281/ZENODO.15078904>, URL <https://zenodo.org/doi/10.5281/zenodo.15078904>.

A.4 Publication IV

W. I. Kösters, J. A. Tuhtan, S. Hoerner, M. Kruusmaa, and S. Abbaszadeh (Oct. 2025b). “Sensor Probes for Fish Passage Safety: Evaluating Strike Severity Metrics and Data-Driven Prediction”. HAL: <https://hal.science/hal-05314322> (*under review*)

This manuscript corresponds to Contribution III, discussed in section 4.

Sensor Probes for Fish Passage Safety: Evaluating Strike Severity Metrics and Data-Driven Prediction

Wolf Iring Kösters^{1,2,*}, Jeffrey A. Tuhtan², Stefan Hoerner^{1,3}, Maarja Kruusmaa², and Shokoofeh Abbaszadeh⁴

¹Laboratory of Fluid Dynamics and Technical Flows, Institute of Fluid Dynamics and Thermodynamics, Otto von Guericke University Magdeburg (OvGU), Universitätsplatz 2, 39106 Magdeburg, Germany

²Department of Computer Systems, Tallinn University of Technology (TalTech), Akadeemia tee 15A, 12616 Tallinn, Estonia

³Laboratory of Geophysical and Industrial Flows (LEGI), CNRS, G-INP, University Grenoble-Alpes, F-38000 Grenoble, France

⁴Institute of Electric Power Systems, Otto von Guericke University Magdeburg (OvGU), Universitätsplatz 2, 39106 Magdeburg, Germany

*wolf.koesters@ovgu.de

ABSTRACT

Hydropower turbines and pumping stations may pose a significant risk to fish during downstream passage, with blade strikes as a major cause of injury and mortality. Sensor probes are used to assess downstream passage risk due to rapid decompression, shear, turbulence and strike events. However, there has been no systematic physical validation of the metrics used to assess the risks posed by blade strike. Since biological threshold models indicate that the relative blade strike velocity is the primary driver of mortality, in this work we focus on evaluating how well existing metrics predict the relative blade strike velocity within a biologically relevant range. To do so, we subjected multiple sensor probes to controlled, simulated turbine blade strikes at velocities from 1–10 m/s to assess metric performance, explore a data-driven alternative, and identify priorities for future sensor design. Our results show that existing metrics, as well as the peak acceleration magnitude, saturate between 3–4 m/s for current sensor probes and often exhibit substantial variance, limiting their ability to distinguish between biologically safe (≤ 4 m/s) and unsafe (> 4 m/s) blade strikes. To address this shortcoming, we propose a simple machine learning classifier trained on tri-axial acceleration data to predict the relative blade strike velocity with sufficient accuracy, and validate its use under laboratory conditions.

1 Introduction

Hydropower plays a crucial role in the worldwide energy network with increasing importance in terms of grid balancing as the share of fluctuating wind and solar power continues to grow¹. It supplies about 14 % of global electricity and nearly half of South America's demand, making it the largest renewable energy source worldwide². However, hydropower installations contribute to river fragmentation, which has reached an alarming density of 0.74 barriers per river kilometer in Europe³. Hydraulic machinery can kill or injure entrained fish⁴, which has dramatic effects on local and migrating fish populations⁵.

Recognizing these substantial negative impacts on freshwater fish biodiversity, European legislation has been enacted to reduce the number of barriers⁶.

While the exact number of hydropower facilities is difficult to quantify, a World Wildlife Fund (WWF) report of 2019 gives a number of over 21,000 hydropower facilities in Europe⁷, while Belletti et al. (2020)³ estimated over 61,000 European dams with or without turbines. The sheer number of these structures makes it impractical to provide alternative migration routes at every site, as the costs would be prohibitively high. Even where downstream passage mitigation measures are implemented, effectively guiding fish toward them and away from hydraulic machinery and infrastructure remains a significant challenge⁸. Given these constraints, rethinking the design of pumps and turbines to actively facilitate fish passage may offer a more viable solution for at least a third of these installations⁹.

Live fish tests are commonly used to assess the risks posed by hydraulic structures reflected in the current Dutch norm¹⁰, and a European standard which is underway¹¹, but these tests can only provide cumulative injury and mortality rates for a given installation. Moreover, live fish studies come with significant ethical and financial costs, limiting their application across different operating conditions and locations. To address these limitations, sensor probes are increasingly being used in comparative studies to evaluate the risks to migrating fish^{8,9,12–14}. These sensors align with the 3R principles of animal welfare

Nomenclature

ρ	Fluid density
$ a $	Acceleration magnitude
BDS	Barotrauma Detection System
DOF	Degrees of freedom
FNR	False negative rate
IMU	Inertial measurement unit
L/t ratio	Fish length to blade thickness ratio
MAD	Mean absolute deviation
PC	Polycarbonate
POM	Polyoxymethylene
RAPID	Robust Autonomous Pressure and Inertial Device
TPR	True positive rate
UNSW	University of New South Wales
WWF	World Wildlife Fund

in experimental testing (Replace, Reduce, Refine) by minimizing or replacing the need for live fish tests while providing more insight from the collected data.

Various sensor probes have been developed for different hydraulic environments. These include devices designed for high-speed conditions, such as the Sensor Fish¹⁵ and the RAPID sensor¹⁶, as well as those tailored for low-speed environments, such as the Barotrauma Detection System (BDS)¹⁷, the Fish Backpack Sensor¹⁸, which focuses on monitoring fish behavior in and around hydraulic structures, and the UNSW sensor¹⁹, which has been developed specifically for use in conduit systems. Sensors designed for low-velocity conditions typically operate at a lower sampling rate of around 100–250 Hz and include accelerometers with lower dynamic range of around 16 g, compared to high-velocity sensor probes that sample at around 2000 Hz and a dynamic range of 200 g (Sensor Fish) or 400 g (RAPID).

These sensor probes have been used in numerous studies to assess the frequency and severity of the blade strike during turbine passage using metrics that use acceleration magnitude to infer severity^{8,13,20–23}. Although the metric proposed by Deng et al. (2010)²⁰ pioneered the use of sensors systems to assess collisions using the peak value value of an impact event with a threshold of 95 g as a threshold for a severe acceleration event. The group recently updated this approach by including the 3 preceding and subsequent points around a peak at 95 g in the analysis and integrating them over them. This is based on the assumption that the sudden increase in velocity of the sensor probe caused by the blade impact can be implicitly quantified by the accelerometer through its time series.

Saylor et al. (2020)²⁴ investigated the effects of fish length, blade thickness, relative blade strike velocity, site of impact, and angle of impact. These studies concluded that strikes that transfer more energy to fish increase lethality, which means midbody lateral strikes at 90° had the highest rates of mortality²⁵. In addition, thinner and faster blades were always more deadly than thicker and slower blades. In Francis and Kaplan turbines, the blade thickness does not change significantly along the blade diameter, and for stiff sensor systems the fish length can be modeled during post processing of the collision data. This leaves relative blade strike velocity, site of impact and angle of impact as remaining unknowns, that need to be investigated using sensor probes. Of these, the angle of impact and relative blade strike velocity were determined to be the most important in a logistic regression of strikes on brook trout (*Salvelinus fontinalis*) and rainbow trout (*Oncorhynchus mykiss*). With every 1 m/s increase in relative blade strike velocity, these fish were around 6 times more likely to die and around 3 times more likely to die if struck at 90° compared to 135°²⁴. Other species have not yet been tested with blade strikes at different angles, while strike speed had high and significant influence in the case of Gizzard shad (*Dorosoma cepedianum*), American Shad (*Alosa sapidissima*), Blueback Herring (*Alosa aestivalis*). Consequently, the relative velocity of the blade can be regarded as a main parameter required to predict strike-induced mortality.

Acceleration magnitude increases with strike velocity, forming the basis of the original acceleration magnitude metric²⁰ as well as a more recent extension proposed by Huang et al. (2025)²⁶, in which the acceleration time series surrounding a

peak event is analyzed rather than relying solely on the peak value. For strike identification, the established 95 g threshold was applied to classify strike events. Following this classification, the acceleration magnitude time series and the pressure time series associated with the event were evaluated independently, resulting in the M_v metric and the M_p metric, evaluating the ram pressure on the sensor probe's pressure sensor, respectively. In the publication, these metrics were treated independently and were not combined into a single estimate of mortality. Importantly, all three metrics were validated against mortality rates in live fish rather than through a systematic evaluation of their sensitivity to changes in strike velocity.

Measuring the sensitivity of a metric to relative blade strike velocity in a systematic way has not yet been done and represents an important research gap to address. Accordingly, the primary objective of this work is to evaluate existing sensor-based strike metrics that have been widely used as proxies for strike severity. Specifically, we assess whether these metrics provide a reliable measure of relative blade strike velocity and associated injury risk under controlled impact conditions. For the fish species mentioned above, the logistic regression model predicts an increase in mortality beginning at 4 m/s²⁴, which may be considered a mortality threshold. This threshold can serve as a reference point for calibrating existing metrics and as a benchmark for assessing their ability to predict whether a blade strike occurs below or above 4 m/s.

Connecting strike speeds with mortality for a given blade thickness, angle, species, and size would open up the possibility of connecting a mortality rate with an accelerometer measurement, as described in²⁷. The main research questions of this work are as follows:

1. Can the 95 g-rule be amended by using a different threshold?
2. How sensitive is the newly proposed metric by Huang et al. (2025)²⁶ to relative impact velocities measured in a laboratory strike rig?
3. Can a data-driven model trained on laboratory strike data reliably predict relative blade strike velocity?
4. Which challenges in sensor probe design need to be overcome to provide better measurements for field assessments of relative blade strike velocities?

This work is significant because it presents the first comprehensive analysis of how widely used metrics respond to changes in relative blade strike velocity and offers concrete recommendations for future developments in both software and hardware. The findings of this research also provide key information to improve sensor design and standardize sensor-based strike measurements with the long-term aim of replacing live fish tests with sensors in order to systematically assess the risk of injury and mortality of fish passing downstream at hydraulic structures and through hydroelectric turbines and pumping stations. Additionally, we provide a practical example of how the relative blade strike velocity from a lab rig may be reliably predicted using machine learning classifiers.

2 Methodology

All experiments were carried out using a custom-built strike rig developed in 2020, for which detailed designs, design rationale, and operational descriptions are openly available²⁷, depicted in fig. 1.

2.1 Strike Rig

The rig comprises a linear motion system that accelerates a blade within a water-filled basin measuring 4.1 m × 0.7 m × 2.3 m. The system is driven by a servomotor, ensuring a stable, highly repeatable, and precisely controlled velocity during strikes through a closed-loop control mechanism. The servomotor control actively counteracts momentum loss as a result of sensor probe acceleration, effectively replicating the inertial characteristics of a high-mass blade under realistic conditions. The blade used in the experiments has a semicircular leading edge, a standard configuration for live fish strike studies²⁸. It has a diameter of 9.5 mm and is fabricated from 3D printed impact-resistant polycarbonate (PC) reinforced with stainless steel threaded rods for enhanced structural integrity. The position of the sensor probe was secured prior to impact of the blade using a retainer adapted from Bevelhimer et al. (2019)²⁹, previously validated in similar studies. The retainer was designed to exert minimal force, ensuring that the probe remained fixed while reducing resistance to movement during impact. This configuration minimizes variability in initial conditions, although slight variations in lateral position and rotational freedom were allowed to facilitate robust predictive model development.

2.2 Metric Evaluation

We included three different metrics in the evaluation: the magnitude of the maximum acceleration and the metrics recently published M_v and M_p by Huang et al. (2025)²⁶. Relative blade strike velocities between 1 – 10 m/s were tested and compared with biological threshold data from lateral strikes of the middle body at a 90° angle.

The fish species and their respective average lengths in these biological tests were: Paddlefish (27.9 cm), *Alosa* spp. (7.7 cm), Gizzard shad (16.0 cm), Rainbow trout (11.5 and 26.0 cm), Brook trout (24.8 cm), Hybrid striped bass (18.0 cm), and Bluegill (11.8 and 16.1 cm)³⁰.

Comparable tests have not been performed on chinook salmon smolts, which have an average body length of 14.4 cm for yearlings and 11.3 cm for subyearlings³¹, the species and life stage with which the metrics M_v and M_p metrics have been calibrated. The authors of the metric note that threshold values may differ for other hydraulic structures beyond the Kaplan turbines used in their study, as well as for fish with markedly different morphologies, such as eels.

Therefore, our evaluation does not focus on the absolute value of the mortality threshold, as no directly comparable case is available. Instead, we assess whether the proposed metrics are capable of distinguishing between relative blade strike velocities that are relevant for fish mortality based on the biological threshold tests described previously.

Acceleration Magnitude This metric uses the peak acceleration magnitude of a time series, calculated by first computing the Euclidean norm of the acceleration along the x, y, and z axes. It differentiates between shear and collision events based on the duration for which the acceleration remains above 70 % of the maximum value. If this duration exceeds 7.5 ms, the event is classified as a shear event; if it is shorter, the event is classified as a collision. In a second step, a threshold is applied above which mortality from acceleration magnitude can be expected.

M_v Metric This approach follows classical Newtonian mechanics, where the change in velocity is given by: $\Delta v = \int a(t) dt$, with v denoting velocity, a acceleration, and t time. Acceleration events are selected if they are above 95 g, in which case three data points preceding and succeeding the peak value are selected which is around 1.5 ms at the sampling rate of the Sensor Fish of 2048 Hz or 3 ms in total. From these values, the acceleration magnitude is computed through the Euclidean norm: $a_{\text{mag}} = \sqrt{a_x^2 + a_y^2 + a_z^2}$, and the values are integrated over the time window.

M_p This approach is based on the Bernoulli principle, which relates the hydrodynamic pressure to the fluid flow acting on the pressure sensor, and assumes that the sensor is oriented directly toward the oncoming flow. It works by calculating the difference between a presumed steady state immediately before the impact and the maximum pressure encountered during the impact. The impact event is found through the accelerometer data and to account for a shift between the peak acceleration and the peak pressure event, two points before and after the location of the acceleration peak are taken into account when locating the maximum pressure. This difference is then calculated by $M_p = \sqrt{\frac{2}{\rho} |P_{\text{max}} - P_{\text{steady state}}|}$, where ρ is the fluid density in kg/m³ and P the pressure in Pa which would in theory yield the velocity causing the pressure change.

2.3 Sensor Probes & Test Protocol

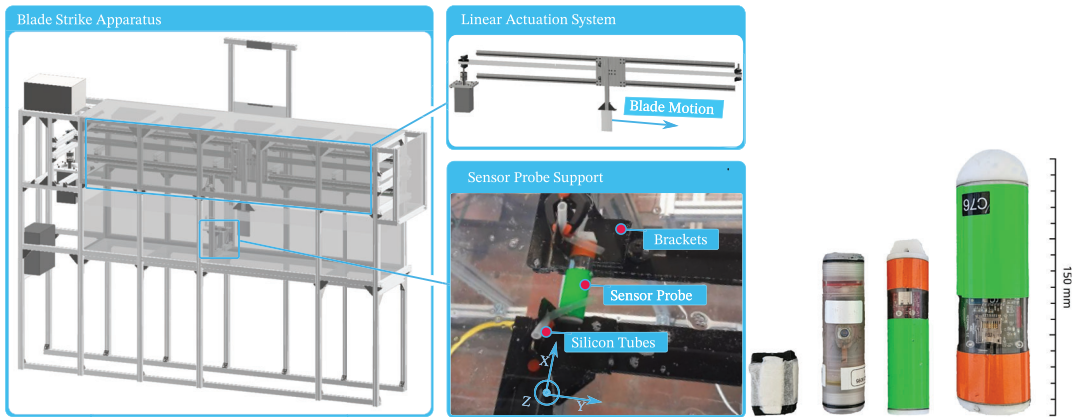


Figure 1. Left: Overview of the strike rig with labeled components. The blade moves linearly from left to right to strike the sensor probe mounted in the holder, with only the blade submerged to reduce drag and splashing. Blade motion, including deceleration to a predefined stop position, is governed by the motor controller. All moving parts are enclosed for safety with an access hatch for probe handling. The setup measures $3.84\text{ m} \times 0.72\text{ m} \times 2.61\text{ m}$ (length \times width \times height). Reproduced from Kösters et al. (2025)²⁷. **Right:** Photograph of all tested sensor probes side-by-side, with a caliper included for scale. The sensors from left to right are: UNSW sensor probe, Sensor Fish, RAPID, and BDS. The foam attached to the UNSW sensor ensures neutral buoyancy. The orange and green tapes on the RAPID and BDS sensors facilitate retrieval in field deployments. The pressure sensors are located on the top surface of the UNSW, RAPID, and BDS sensors, whereas on the Sensor Fish, it faces the camera.

Sensors The sensor probes used in this study comprise four different devices, previously applied in field investigations of hydraulic environments around hydraulic structures, and in the case of the UNSW probe, in laboratory studies, shown on the left in fig. 1. Most of such studies have been conducted with the Sensor Fish. The initial design was developed at the US Army Corps of Engineers³² and was later refined at the Pacific Northwest National Laboratory³³, followed by a further iteration introduced in 2014¹⁵. A recent update introduced the Marine Sensor Fish in February 2025 adding a larger battery, a salinity sensor, and a gyroscope and magnetometer with extended dynamic range³⁴, while all other components remain unchanged. Because current blade strike severity metrics are based on acceleration and pressure, this study and its conclusions remain unaffected by this modification.

The sensor probes used in this study are not designed to mimic the material properties of fish tissue. Their purpose is to record acceleration and pressure signals from which calibrated metrics can then predict fish injury. Our investigation is grounded in the assumption that blade strike velocity can serve as a proxy for fish injury and mortality when combined with biological threshold data. Accordingly, the probes were tested in their standard configuration, without coatings or compliant layers, as this reflects their current use in conjunction with these velocity- and impulse-based metrics.

The RAPID sensor probe was developed in 2021 by Tallinn University of Technology¹⁶. This device was preceded by the BDS sensor probe, developed in 2016 by the same group¹⁷ to evaluate the potential of barotrauma in large and medium-sized hydropower turbines. The UNSW sensor probe was developed in 2022 at the University of New South Wales (Australia) to investigate hydraulic conditions in pipe flows³⁵.

When sensor probes are used for fish surrogate studies, their design is typically adapted to the conditions of the deployment environment. In low-acceleration environments, changes occur over longer time scales and acceleration events are of lower magnitude. Based on these specifications, the sensor probes available to us were grouped into two categories:

- **High-acceleration sensor probes:** Sensor Fish and RAPID
- **Low-acceleration sensor probes:** BDS and UNSW sensor probes

Although the UNSW and BDS probes were primarily developed for pressure measurements in low-acceleration conditions, the Sensor Fish and RAPID both incorporate high-dynamic-range accelerometers in addition to pressure sensors, making them suitable for hydraulic environments in which entrained bodies experience high accelerations. Table 1 lists the sensors along with their sensing modalities, technical and physical specifications.

Table 1. Table providing an overview of the sensors, including their physical characteristics and sensing modalities. The vertical bar separates the high acceleration sensor probes on the left from the low acceleration sensor probes on the right.

	Sensor Fish	RAPID	UNSW Sensor	BDS
Sensing modalities	total water pressure			total water pressure
	linear acceleration	total water pressure	total water pressure	linear acceleration
	rate of rotation	linear acceleration	linear acceleration	rate of rotation
Dimensions (mm)	magnetic field			magnetic field
	cylindric, 89.9x24.5	cylindric, 100x25	cuboid, 34x26x14	cylindric, 140x40
Mass (g)	42	46	15	147
Sampling rate (Hz)	2048	2048 (acceleration)	400 (acceleration)	100 or 250 (acceleration)
		100 (pressure)	250 (pressure)	100 (pressure)
Dynamic range (+/-)	± 200 g	±400 g	± 16 g	± 16 g
	0-12 bar	0-2 bar	0-14 bar	0-2 bar
	± 2000 deg/s			± 2000 deg/s

Test Protocol The strike rig test protocol involved two sensor probe activation methods: (i) activating the probe while secured in the holder, or (ii) activating it prior to the placement and outside the water, verifying operation, and subsequently inserting it into the holder. Activation was achieved using an external magnet placed adjacent to the housing near the magnetic switch.

Sensor probes were subjected to blade strikes at initial velocities of 1 m/s, incrementally increased in 1 m/s steps until all available sensors experienced malfunction. Each velocity condition was tested through 30 independent trials to ensure statistical robustness.

The sensor probes were secured in a holder prior to each strike. The holder design was inspired by Bevelhimer et al. (2019)²⁹ and has been previously described in detail²⁷. It exerts only the minimal force required to keep the sensor securely in position before impact. Two versions of the holder were employed: one designed for the BDS, ATS, and RAPID sensors, and another specifically developed for the smaller-sized UNSW sensor, which necessitated a separate design. All sensor probes completed data acquisition before removal from the water, reducing acceleration events and facilitating automated strike detection. To assess data integrity, sensor recordings were examined for anomalies, and outliers were identified based on acceleration magnitudes that exceeded the sensor's measurement range or exhibited faulty signal patterns. Strike data were excluded from further analysis if the peak acceleration magnitude exceeded three times the median absolute deviation (MAD) from the median at a given relative blade strike velocity, following the methodology recommended by Leys et al. (2019)³⁶. The MAD was computed as: $MAD = \text{median}(|X_i - \text{median}(X)|)$ where X represents the vector of all peak acceleration magnitudes at a given relative blade strike velocity, and X_i denotes the peak acceleration value from an individual test at that velocity³⁷.

The water level in the tank was maintained at 160 mm above the brackets on which the sensor probe is positioned prior to a strike. Blade alignment was carefully controlled to ensure vertical positioning during attachment, as misalignment could introduce unintended vertical velocity components, causing secondary impacts with the basin floor or becoming airborne.

Data Retrieval & Cleaning To ensure consistent alignment across trials, a fixed, sensor-specific acceleration magnitude threshold was established to identify the onset of each strike event, as specified in table 2. This threshold was set above accelerations encountered during handling but below accelerations experienced at 1 m/s strikes. To ensure that the onset of the strike was captured, a constant time offset of -5 ms was then applied for all sensors so that the start of the time series preceded any strike-induced acceleration, with the exact number of indices to subtract calculated from each sensor's sampling rate. This proved a robust method, resulting in excellent temporal alignment across trials.

For the low acceleration sensors, the sampling rate was piecewise linearly interpolated prior to alignment to improve temporal precision. After the impact event, a fixed window of 100 ms was analyzed, even though the strike itself typically lasted less than 25 ms (see fig. 2).

Despite best efforts, sensor malfunctions meant that not all velocities have exactly 30 repetitions. Faulty datasets were repeated when identified; however, in most cases the sensor probe had already failed, and a replacement was not available. The total number of experiments conducted at each velocity is provided in table 2.

Table 2. Overview of the valid experimental data analyzed, including the individual acceleration magnitude thresholds used to identify strike events. The horizontal line between the RAPID and UNSW sensor probes marks the division between high acceleration and low acceleration sensor probes.

Sensor	Strike threshold (g)	Repetitions (-) per strike velocity (m/s)									
		1	2	3	4	5	6	7	8	9	10
Sensor Fish	70	30	30	30	30	30	30	30	30	-	-
RAPID	30	30	30	30	30	30	28	30	30	30	29
UNSW	12	21	14	-	-	-	-	-	-	-	-
BDS	25	30	30	30	30	30	-	-	-	-	-

2.4 Sensor Fish

Hardware The Sensor Fish sensor probe is a cylindrical housing with a pressure sensor on the side and end caps that can drop masses at a pre-programmed state to make it positively buoyant and come up to the surface. Under these, connection pins are located, which require a custom connector cable. The relevant sensing modalities include a three-axis accelerometer ((ADXL377, Analog Devices, Inc., Norwood, MA, USA), a pressure sensor (MS5412-BM, Measurement Specialties, Inc., Hampton, VA, USA), and a three-axis gyroscope (ITG-3200, InvenSense, Inc., San Jose, CA, USA) as well as an inertial measurement unit (IMU) (LSM303DLHC, STMicroelectronics, Geneva, Switzerland) for orientation determination. All sensors undergo laboratory calibration prior to the experiments, as stated in³⁸.

Usage The sensor is turned on with a magnet held in the vicinity of the onboard sensor, a red LED turns on indicating that measurements are being taken. When the set measurement time is over, bright white LEDs flash, which facilitates in-field retrieval. To download the data the cap that stores the droppable mass is removed, revealing a custom connector that has to be carefully rotationally aligned with a custom connector to USB cable and pressed in. Communication with the sensor probe is done with custom software, that handles downloading, calibration, setting date and time and resetting the sensor probe, which is necessary to take another measurement. Charging is done through the same connector cable.

Test Protocol The sensor probe was turned on outside of the water before it was placed into the sensor holder. It was removed from the water, when the LEDs started flashing, indicating that the measurement had ended.

2.5 RAPID

Hardware The Robust Autonomous Pressure and Inertial Device (RAPID) is a cylindrical, neutrally buoyant sensor probe with a polycarbonate housing and a flat POM end cap, developed at the Tallinn University of Technology. It is certified for impacts in accordance with the M802:01.03.2022 shock test procedure (peak accelerations from 10–400 g) and the ECSS-E-ST.10-03C (2012) test standard, with test certificate no. 8-009-22 / 13.04.2022.

The sensing modalities include an absolute pressure sensor (MS5837-2BA, TE Connectivity, Switzerland) and a three-axis accelerometer (H3LIS331DL, STMicroelectronics, Switzerland). An updated version, released shortly after completion of our experiments, also incorporates a gyroscope and a magnetic field sensor.

Data are stored in a removable microSD card and saved in two separate files: one containing high-frequency acceleration data and the other containing lower-frequency pressure data, which is done to reduce overall file size. The two files are aligned via shared timestamps.

Usage The sensor probe is activated by swiping a magnet in a smooth motion near the onboard Hall sensor. Upon activation, the device performs a self-calibration of the pressure sensor, indicated by a blue LED. When the LED switches to blinking green, the measurement has begun.

To retrieve data, the tube is opened to access the USB-C port on the circuit board. When connected, the device is recognized as a mass storage unit, allowing direct access to the data files. Configuration files stored as plain text can be modified to adjust

measurement length, date, and time. The device is recharged through the same USB-C port; during charging, the blinking green LED changes to a constant red light once charging is complete. The microSD card can store hundreds of datasets before reaching capacity, eliminating the need to download data after every measurement.

Test Protocol The sensor probe was either activated outside the water before being placed in the holder or turned on after being positioned in the setup. The probe was removed from the water when the LEDs stopped blinking, indicating that the measurement had ended and the device had shut down.

2.6 UNSW

The sensors developed by the University of New South Wales are of cuboid shape and housed within a custom 3D-printed enclosure, which has been waterproofed using an electronics potting compound. To achieve neutral buoyancy, polystyrene foam was attached to the exterior of the housing.

These sensor is based on the MbitLab MetaMotionR v0.5, with an accelerometer and gyroscope (BMI160, Bosch Sensortec, Reutlingen, Germany) and a pressure sensor (MS580314BA01-00, TE-Connectivity, Galway, Ireland). Data recording was initiated via Bluetooth using the sensor-specific TinyTracker software installed on an iPad.

The data has to be downloaded via Bluetooth from the device, each time a measurement has been taken.

Test Protocol The sensor probe was activated before being placed in the setup, as it required a bluetooth signal for starting the measurement. For determining when to remove the sensor from the water, a timer was used that was started at the same time as the sensor probe with the measurement time as the timer value.

2.7 BDS

Hardware The Barotrauma Detection System (BDS) sensor probe is neutrally buoyant, consists of a cylindrical polycarbonate housing with two machined polyoxymethylene (POM) end caps, one side flat and the other spherical, enclosing the sensor electronics. The device is powered by two AAA alkaline batteries, to avoid that the batteries loose contact during the strike event, they are constrained by a plastic clip. The data are stored in a removable microSD card.

The BDS is equipped with a digital nine-degree-of-freedom (DOF) IMU (BNO055, Bosch Sensortec, Reutlingen, Germany) and three pressure sensors (MS5837-2BA, TE Connectivity, Galway, Ireland) located on the spherical end. The inclusion of multiple pressure sensors provides triple modular redundancy, enhancing fault tolerance in case of individual sensor failure. Additionally each of these sensors can be programmed with a different pressure range.

Before experimental deployment, each BDS sensor's accuracy was verified through laboratory calibration using a custom-built barochamber. Sensors were tested at total pressures up to 5500 hPa, 2.75 times their maximum rated pressure. A commercial reference pressure sensor (HOBO U20-001-02, Onset Computer Corp., USA) was used to log chamber pressure and validate the accuracy of each BDS unit.

Usage To start the measurement a magnet is held close to the onboard magnetic switch. After that the sensors starts up and performs a self-calibration of the pressure sensors where the current pressure is set at 100 kPa. This is visible through an LED rapidly changing colors in the order red - blue - green. When the LED switches to a constant red color, the measurement has started.

For retrieving the data after the strike, a magnet needs to constantly activate the magnetic switch. This turns on the WiFi mode, in which the sensor probe is discoverable with another WiFi capable device. By accessing a website, all recorded data files can be viewed and downloaded. Additionally, the measurement frequency can be set here. The microSD card can store hundreds of datasets before reaching capacity, eliminating the need to download data after every measurement.

Test Protocol The BDS was exclusively used in the 250 Hz mode. The BDS was put in the sensor holder and turned on in place with a strong magnet on a stick. The data was not downloaded after every strike, but in an interval decided by the experimenter in accordance to its risk of failure. The LED turning off marks the end of the measurement and the sensor probe shutting off subsequently, after which it was retrieved for data download or another strike.

Usage To start a measurement, a magnet is held close to the onboard magnetic switch. The sensor then powers on and performs a self-calibration of the pressure sensors, setting the current pressure to 100 kPa. This process is indicated by an LED cycling rapidly through red, blue, and green. When the LED changes to a constant red, the measurement has begun.

To retrieve data after a strike, the magnetic switch must be continuously activated with a magnet. This enables WiFi mode, making the sensor probe discoverable by another WiFi-capable device. By accessing the device's interface through a web browser, all recorded data files can be viewed and downloaded. The interface also allows configuration of the measurement frequency. The microSD card can store hundreds of datasets before reaching capacity, so data does not need to be downloaded after every measurement.

2.8 Data-Driven Classification of the Relative Blade Strike Velocity

The relative blade strike velocity was estimated for each class, ranging from 1–10 m/s, in 1 m/s increments, based on the high-g accelerometer data. This was done using the Gaussian naive Bayes approach, which was chosen due to its previous use in accelerometer-based human fall classification³⁹ with an accuracy of 80 % and in high-frequency (12,800 Hz) mechanical fault detection true positive rates exceeding 90 %⁴⁰. First, 15 measurements from each of the three accelerometer axes were aligned for all recordings such that the initial acceleration event begins from the third data point, where the first two data points correspond to the acceleration readings of the sensor at rest, used as a reference to visually verify that the input time series were correctly aligned. This simple protocol was chosen as it is easy to identify the initial up-ramping of the accelerometer data across all datasets, and allows for a rapid and efficient alignment method. Next, for each relative blade strike velocity, the continuous set of 15 single-axis acceleration measurements for each axis (x,y,z) were concatenated into a single feature vector of length 45. This ensures that data from all three axes are included in the velocity estimation, which is important because previous methods based on acceleration magnitude mix the signals from each of the three axis when calculating the magnitude. Because the acceleration time series data along each axis can have distinct characteristics due to the geometric and physical properties of the sensor probe, we chose to create a feature vector which uses data from all three axes in lieu of the magnitude. Finally, the naive Bayes classification was performed using 10-fold cross-validation, and the results were reported as a confusion matrix using the mean value of the 10 models, where 20 % of the data were withheld to validate the classifier.

3 Results & Discussion

In this comparison, four different sensor types were used: the UNSW sensor, the Sensor Fish, the RAPID, and the BDS, see fig. 1 for a photograph and table 1 for an overview of their capabilities. These sensors have previously been employed in studies assessing hydraulic conditions within turbine environments, and in the case of the UNSW sensor, in pipe-flow investigations. The velocity range tested was limited by the sensor probes survivability to the simulated blade strikes. The target of obtaining 30 repetitions per relative blade strike velocity could not always be achieved due to sensor malfunctions caused by the high acceleration forces during impact, combined with the limited number of available devices. The tested strike velocities for each sensor, along with the minimum number of repetitions at any given velocity, are summarized in table 2.

Strike-induced mortality depends on multiple interacting factors, including impact location, angle, blade geometry, and fish morphology. In the following analysis, relative blade strike velocity is used as the primary evaluation variable, as it shows a strong and monotonic association with mortality under controlled blade-strike conditions. Existing metrics are therefore assessed by their ability to differentiate relative blade strike velocity, rather than by direct comparison to biological mortality thresholds.

On this basis, the following analysis proceeds in three steps. First, the measured sensor probe responses to simulated blade strikes are reported, focusing on the observed characteristics of the recorded time series. Second, the behavior of the strike severity metrics as a function of relative blade strike velocity is described. Within each subsection, these observations are followed by an interpretation of their implications. Finally, a data-driven approach for predicting relative blade strike velocity from the impact time series is presented, followed by a separate discussion of consequences for future sensor design.

Time Series Analysis Figure 2 compares the acceleration magnitude readings over time during a blade strike for the Sensor Fish, RAPID, UNSW and BDS sensor probe. Dashed lines are indicating the sensor-specific saturation limits, which are higher than the single-axis saturation limits because the acceleration magnitude is the Euclidean norm for the three axes: $a_{\text{mag}} = |a| = \sqrt{a_x^2 + a_y^2 + a_z^2}$, simplifying to $|a|_{\text{max}} = \sqrt{3} \cdot a_{\text{max}}$ if all the axis values are equal. However, if the acceleration vector and the measurement axis of the sensor are aligned, the sensor can go into saturation at the single-axis saturation limit itself, which may be the reason behind the plateau of the maximum values of the Sensor Fish at 5 m/s. Although the Sensor Fish and RAPID probes are similar in size, shape, and weight, their responses to blade strikes differ markedly: they vary in both peak acceleration magnitude and signal shape over time. This contrast is not observed when the UNSW and BDS sensor probes are compared. However, their signals are heavily undersampled and saturated. This is evident when comparing the strikes at 1 m/s and 2 m/s, where the acceleration magnitude shows little difference despite the doubling of the velocity.

To evaluate differences in measurement performance relevant to this application, we used peak acceleration magnitude alongside two metrics recently proposed by Huang et al. (2025)²⁶. Figure 3 presents the distribution of these metric scores as a function of relative blade strike velocity, including the respective medians in comparison to the thresholds proposed to indicate the onset of mortality.

The Sensor Fish and RAPID sensor probe were tested under slightly different conditions. To avoid premature damage, the Sensor Fish was always struck on the side opposite the pressure sensor, as the opening in the cylinder was considered a potential structural weak point. In contrast, the RAPID sensor was tested at random rotational orientations to broaden the data base for a machine learning model. Consequently, variability in sensor output is not directly comparable between the two devices, although comparisons of average values remain valid. Likewise, the UNSW sensor was constrained along all axes prior

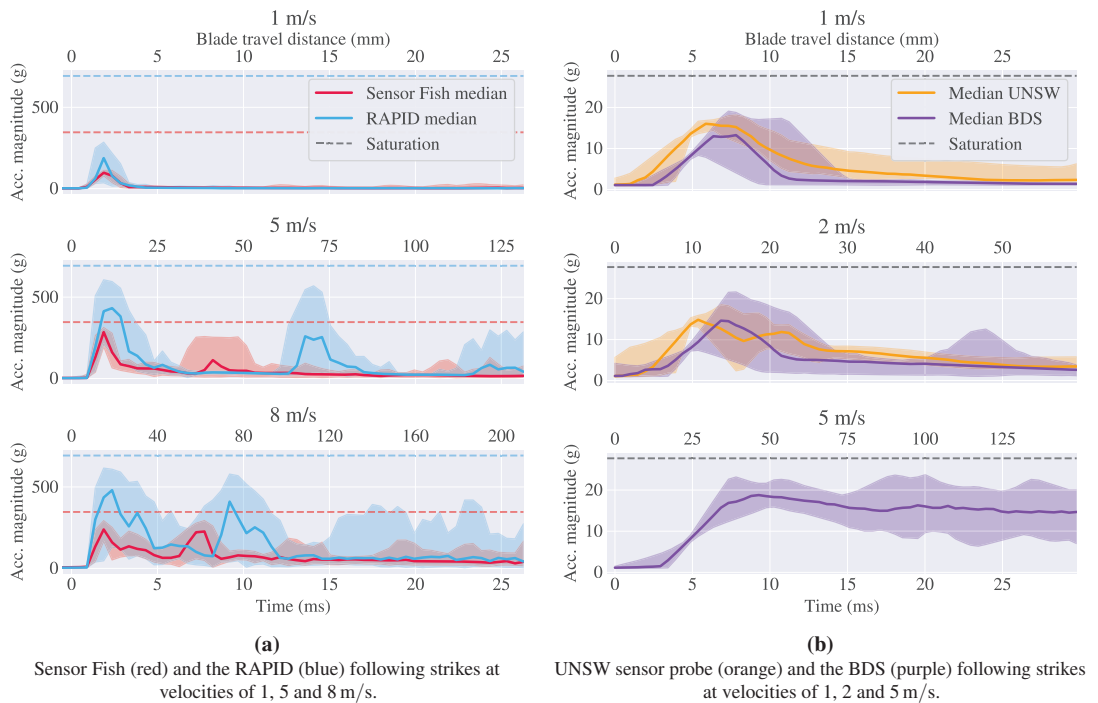


Figure 2. Comparison of acceleration magnitude time-series distributions ($n = 30$) of the tested sensor probes designed for environments with high acceleration events: (a) Sensor Fish & RAPID, and low acceleration events: (b) UNSW sensor probe & BDS. The corresponding blade travel distance for each relative blade strike velocity is shown at the top of the plot. Shaded areas represent the 95 % confidence intervals, estimated using linear interpolation. The dashed line indicates the threshold beyond which all three sensor axes are fully saturated, equal to $|a|_{\max} = \sqrt{3} \cdot a_{\text{single-axis}}$. In some cases, such as with the Sensor Fish or the BDS at 5 m/s, there seems to be clear signs of saturation, even though the complete saturation value is not met. This may be due to saturation happening earlier when one or two axes clip, as described before.

to the strike because of the difficulty of targeting it given its small size, while the BDS was tested under the same conditions as the RAPID.

The relevant velocity range to differentiate the severity of a strike should, at a minimum, allow the distinction between strikes above and below 4 m/s. This threshold corresponds to the appearance of observed mortality in multiple species during simulation of turbine strike experiments in anesthetized fish²⁴. The upper limit of the relevant range is considered to be around 10 m/s, beyond which most species do not survive, as reported by Pflugrath et al. (2021)²⁵. However, an important exception is the eel, which appears unusually resistant to blade strikes. In publicly available strike data⁴¹, American eel (*Anguilla rostrata*) demonstrated a survival rate of 87 % at a relative blade strike velocity of 13.6 m/s ($n = 90$).

Low acceleration sensor probes were not included in this comparison, as their tested relative blade strike velocity range (1–2 m/s for the UNSW sensor) lies outside the scope of this application. Nonetheless, these probes may still be useful for determining whether a blade strike has occurred, regardless of its severity, since quantifying strike probability alone can already provide valuable insight.

Peak Acceleration Magnitude Analysis In our previous study²⁷, we showed that relative blade strike velocities as low as 1 m/s can generate peak acceleration magnitudes that exceed the commonly referenced threshold of 95 g, which has been associated with a severe exposure event connected to fish mortality based on work by Deng et al. (2010)³⁰. However, biological threshold models, such as those proposed by Pflugrath et al. (2021)²⁵, predict no mortality at this velocity. This indicates that the commonly used 95 g threshold can be exceeded at strike velocities that are predicted to be biologically non-lethal, suggesting that this threshold is not a reliable indicator of strike-induced mortality.

This discrepancy raises the question of whether the threshold may have been set too conservatively and the metric could be revised by adopting a higher threshold. The upper plot in fig. 3 compares peak acceleration magnitude measurements from the Sensor Fish and the RAPID sensor probe, which have single-axis saturation limits of 200 g and 400 g, respectively. A decrease in acceleration magnitude between 5–7 m/s was observed for the RAPID sensor probe, followed by a sudden increase at 8 m/s. The Sensor Fish plateaus at approximately 3 m/s, while the RAPID sensor does so around 4 m/s, consistent with partial axis clipping and bandwidth limits, so peak acceleration magnitude is no longer a reliable proxy for relative strike velocity beyond these points. As a result, strikes at the 4 m/s threshold which do not lead to mortality cannot be reliably distinguished from strikes at 8 m/s, a velocity at which observed fish mortality rates reached 80 % or higher in most tested species³⁰.

A plausible explanation of the decrease in acceleration magnitude, would be that this pattern may be explained by the drag crisis, in which the drag coefficient drops sharply as the Reynolds number increases by up to a factor of three⁴². Pasam et al. (2023) reported that this transition occurs at a critical Reynolds number of approximately $Re \sim 2.3 \times 10^5$ for smooth cylinders, with surface roughness lowering this threshold⁴².

The sensor related Reynolds number is given by:

$$Re = \frac{L \cdot u}{\nu} = \frac{25 \cdot 10^{-3} \cdot 8}{1 \cdot 10^{-6}} = 200,000 \quad (1)$$

where L is the tube diameter, u is the relative fluid velocity, and ν is the kinematic viscosity of water. The mechanism may be described as follows: when drag is reduced, the probe is accelerated more easily by the blade. At higher drag coefficients, the probe resists motion, resulting in greater deformation and a longer impact duration. By contrast, reduced resistance shortens the impact time scale, thereby increasing the maximum acceleration. Because peak acceleration magnitude is affected by clipping beyond 3–4 m/s, the Reynolds-number explanation is presented as a hypothesis about impact dynamics, since peak magnitude ceases to uniquely encode strike velocity once clipping begins. Testing this hypothesis would require acceleration measurements that do not clip in the examined velocity range.

Interpreting this result, saturation of the sensor probes propagates directly into metric saturation because the metric is defined solely by the maximum acceleration magnitude, thereby limiting its ability to differentiate relative blade strike velocities within the range most relevant for assessing fish mortality risk. Furthermore, the wide spread of peak acceleration magnitude values in the RAPID sensor probe, where for example a strike at 2 m/s produced a higher value than at 8 m/s, further reduces the reliability of peak acceleration magnitude as a metric for strike velocity even below the saturation level.

Although the Sensor Fish appears to show lower variance in its readings, this may be influenced by differences in experimental conditions, as previously discussed.

M_v Metric Analysis The M_v metric²⁶ is calculated by integrating the three data points before and after a peak that exceeds 95 g. This threshold is used solely for strike event detection and in all tests it correctly identified the occurrence of a strike. As shown in the middle plot of the figure, this metric saturates at approximately 3 m/s for the Sensor Fish and 4 m/s for the RAPID sensor, similar to the saturation observed in peak acceleration magnitude measurements. Interpreting this result, the stated metric threshold of 2.87 coincides with the point at which the metric ceases to vary systematically with relative blade strike velocity and therefore cannot be assigned a physical meaning in terms of strike severity.

M_p Metric Analysis This metric calculates the difference between steady-state pressure before the strike and the maximum pressure during the strike resulting from ram pressure of the fluid on the pressure sensor given its direction is aligned with acceleration vector of the sensor probe, and estimates the corresponding velocity using the Bernoulli equation. For the M_p metric²⁶, only Sensor Fish data were used. The RAPID sensor was excluded from this analysis because its pressure sensor samples at only 100 Hz, which is insufficient to capture the rapid pressure fluctuations required for this calculation. While the pressure conditions in the strike rig differ from those in real turbine environments, the metric is based on hydrodynamic pressure caused by the sensor accelerating through the surrounding fluid. Therefore, it is expected to function in line with the intentions of its original authors.

While there is a linear relationship between the metric and the relative blade strike velocity from 1–4 m/s, the metric value decreases significantly at higher velocities, similar to the dip observed in the RAPID results. As a possible interpretation, this decrease may be linked to the previously discussed flow transition associated with the critical Reynolds number. Because the Sensor Fish has greater surface roughness, its critical Reynolds number would be expected to be lower than in the case of the RAPID, which is consistent with the observed decrease appearing at 5 m/s. However, the observed behavior could also be explained without invoking a flow transition. At higher strike velocities, larger impact forces amplify the rotational moment generated by small residual misalignments, so that the probe rotates more during impact, intermittently misaligning the pressure port, underestimating pressure peaks, and increasing scatter. Importantly, the pressure signal does not exhibit hard sensor saturation analogous to the acceleration measurements. Nevertheless, the presence of this dip, together with the large spread in

metric values at each velocity, results in substantial overlap across the full range of tested strike velocities, rendering the metric unable to reliably distinguish between biologically safe (≤ 4 m/s) and unsafe (>4 m/s) relative blade strike velocities under the tested conditions.

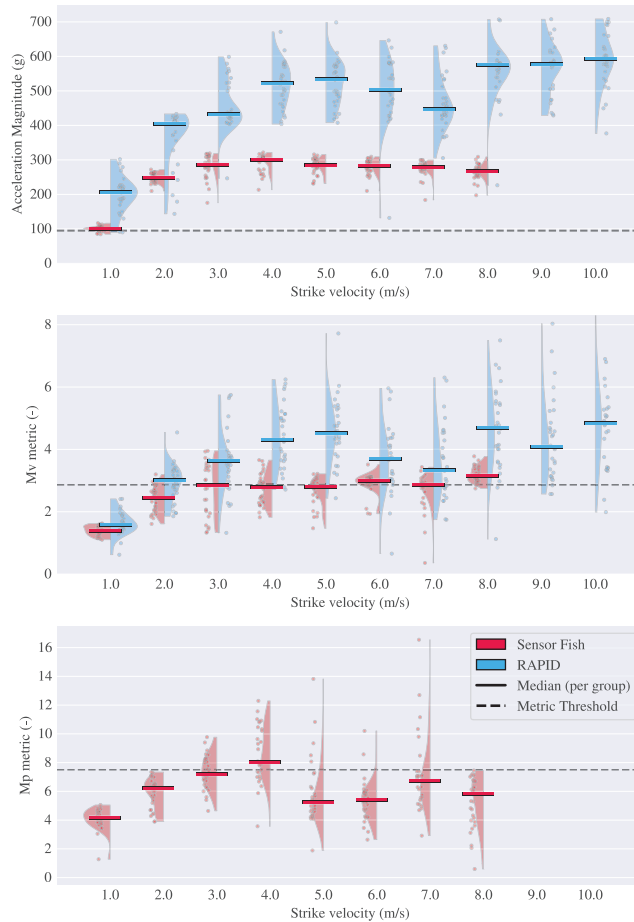


Figure 3. Results of the peak acceleration magnitude, the M_v and the M_p metrics calculated for the Sensor Fish and the RAPID. Each distribution is shown as a violin plot, estimated using kernel density estimation and truncated at the extreme data points to avoid non-physical extrapolations. For each relative blade strike velocity and sensor probe, a bar in the corresponding color shows the median metric value for this group. This may be compared with the metric thresholds for mortality, which are given as 2.87 (M_v), and 7.52 (M_p), respectively. For reference, the 95 g threshold for the peak acceleration magnitude metric was also included, although it can now be considered obsolete. A conservative relative blade strike velocity threshold for mortality is 4 m/s²⁴. The Sensor Fish did not withstand strikes above 8 m/s, while the RAPID failed at a relative blade strike velocity of 10 m/s. The RAPID’s pressure sensor operates at 100 Hz, providing insufficient resolution for the M_p metric; it was therefore excluded from that analysis.

Data-Driven Model Because the three evaluated metrics were found to not be suitable to relate the accelerometer and pressure data to the relative velocity of the blade strike, we investigated an alternative approach. Based on our evaluation of existing methods using the strike rig, we found that the total duration of laboratory strike events on the rigid cylinders had durations ranging from 0.005 to 0.007 seconds. Robust statistical approaches must therefore be able to make use of a small time window with high variance. As the relative velocity is the main variable of interest, the selected method must also be able to provide

continuous or categorical numerical results that are easy to interpret. Based on these restrictions and requirements, a naïve Gaussian Bayes classifier was used to estimate the relative blade strike velocity using both the Sensor Fish and RAPID sensors fig. 4. The authors first tested several well-known inference methods including multiple linear regression, elastic net, lasso and kernel ridge methods, none of which provided relative strike velocity estimates with errors less than 30%, which was deemed to high for practical use. This classifier was chosen because it is computationally efficient to implement, is robust for small datasets and provides class probabilities, which can be used for uncertainty estimation. The Sensor Fish data range from 1 – 8 m/s, and the RAPID sensor probes were the only devices which were not destroyed at the higher velocities, capturing data across the 1 – 10 m/s full range. For each dataset, a feature vector consisting of the accelerometer data from each of the three axes was taken with a length of 15 datapoints. For each feature vector, the second datapoint was the onset of acceleration due to the strike. This leads to a feature vector with a total length of 45 (15 datapoints, three axes each) for each recorded strike event. The lowest true positive rate of the RAPIDs of 60 % was for the relative blade strike velocities of 3, 4 and 9 m/s, and was as high as 96.7 % for 1 m/s. Considering the Sensor Fish, the lowest true positive rate was found to be 70 % was for the relative blade strike velocities of 3, 4 and 5 m/s, and was as high as 96.7 % for 1 m/s. This indicates that although the sensors themselves record physically distinct acceleration time series from the blade strikes, the errors associated with the velocity classification remain similar.

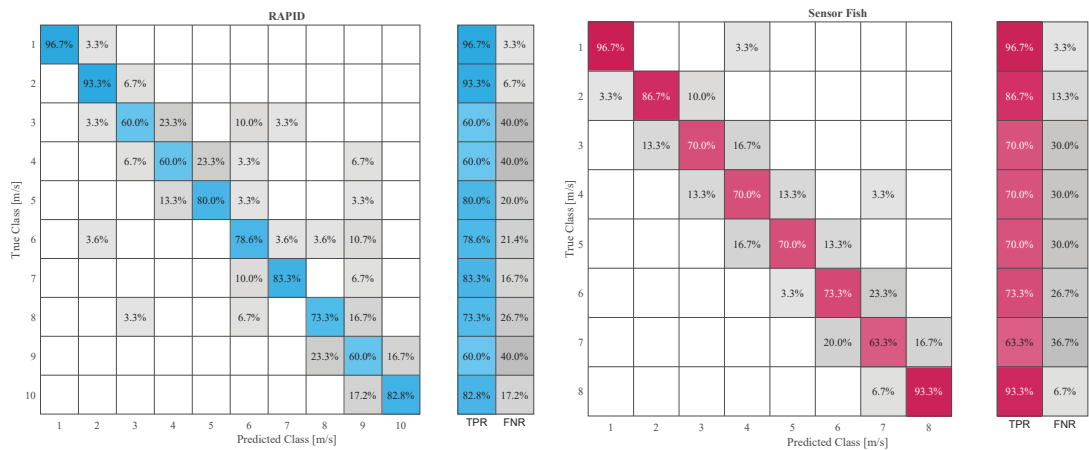


Figure 4. Confusion matrices of the Gaussian naïve Bayes classifier results (RAPID n = 297, Sensor Fish n = 240). The percentage of correctly classified relative blade strike velocity classes is shown along the diagonal, and the off-diagonal entries are the percentages of incorrect classifications. The True Positive Rate (TPR) and False Negative Rate (FNR) are indicated on the right of each confusion matrix, and sum to 100 % across each row.

Suggestions for Future Sensor Probes The strike data from the sensor probes were affected by saturation and insufficient temporal resolution, resulting in inter-sample peak loss and bandwidth truncation, which made them unsuitable for maximum value analysis or for deriving velocity through integration of the acceleration signal. Nevertheless, a machine learning algorithm was able to predict the relative blade strike velocity with reasonable accuracy. Both the high and low acceleration sensor probes lacked sufficient sampling rates and dynamic range to capture human interpretable dynamic behaviour during stiff body impacts. Increasing the dynamic range may be difficult, as the 400 g single axis saturation threshold of the RAPID is close to the maximum currently achievable value with compact, commercially available sensors. By contrast, increasing the sampling rate is less constrained by physical limits, though it comes with added integration cost during sensor development. Such an improvement may be valuable if better resolved impact dynamics are required.

For the Sensor Fish, RAPID and BDS sensor probes, the plastic housing tubes did not sustain physical damage; failures were instead attributed to faults arising from damaged electronic components. The UNSW sensor probe was an exception: its glued seam failed, and, possibly due to an air cavity in the potting compound, it experienced water ingress at the battery charging port.

Limitations of the Study The main limitation of this study lies in its transferability to real-world turbine environments. The strike rig was specifically designed to deliver precise and repeatable blade strikes, which would not have been feasible in a

model turbine. While this controlled set-up enables consistent testing, it also introduces limitations, particularly the absence of realistic fluid flow conditions.

Although we have shown that the difference between the motion of the straight and rotary blades is negligible at typical machine dimensions within the short time frame of a strike, the influence of the surrounding fluid field cannot be replicated. One way to approximate this is by assuming a relative blade strike velocity. For example, if a fish and the surrounding fluid are moving at 5 m/s and the blade at 8 m/s, the effective relative blade strike velocity could be modeled as 3 m/s. However, this assumes a perfectly straight flow, which does not reflect the complex high turbulent flow conditions inside turbines or pumps.

Additionally, although the motion of the blade can be approximated locally as linear at the point of impact, real turbine blades can strike at varying angles due to a curved blade. This could result in force vectors acting on the sensor probe that differ significantly from those in our setup. Since the actual range of blade angles in operational turbines is out of the scope of such a study, we chose to carry out all strikes with a vector aligned normal to the sensor probe surface at the midpoint of the blade.

Because the probes do not replicate fish tissue mechanics, the measured acceleration and pressure signals are not direct representations of what a fish experiences during a blade strike. Instead, they are used to support prediction of strike velocity, which serves as a proxy for injury risk. Consequently, the present results do not resolve how differences in material compliance between sensor probes and live fish influence strike mechanics.

4 Conclusion & Outlook

In this study, we subjected sensor probes that were designed to assess passage mortality for hydraulic structures to simulated turbine strikes ranging between 1 – 10 m/s.

Metric Analyses We evaluated two recently proposed M_v & M_p metrics²⁶ along with the long-established acceleration magnitude metric, all of which aim to estimate the severity of a blade strike. We found that the M_v & M_p metrics as well as the acceleration magnitude saturate at velocities of 3–4 m/s. Higher relative blade strike velocities cannot be distinguished from these saturation levels. Biological threshold tests that subjected anaesthetized fish to simulated turbine strikes show that strikes below 4 m/s do not result in immediate or 48 h delayed mortality, and strikes above 8 m/s result in 100 % mortality for all species of fish tested²⁴, while probably being higher for eels⁴³. Unfortunately, this makes the application of these metrics challenging to justify in-field use cases.

Data-Driven Approach to Infer the Relative Blade Strike Velocity We could show that a data-driven approach that uses the acceleration data of all three axes, instead of the acceleration magnitude, can under laboratory conditions be used to estimate the relative blade strike velocity with reasonable accuracy; see fig. 4. In order to apply the data-driven approach on field data, it is first necessary to subject identical sensors in a more realistic yet controlled test environment with high-speed cameras where the sensor orientation and strike location can be visually confirmed. For rotating blades, the relative velocity can then be determined using the videos which provide the sensor and blade surface velocity at the recorded point of impact. Afterwards, the corresponding strike time series data and relative strike velocities obtained from the camera footage can be used to re-train the classifier in the same manner as the proposed laboratory-based method. However, in the interim, the author's suggest that in cases where the relative blade strike velocity estimation is constrained to being above or below 4 m/s, it may be feasible to apply the data-driven approach to provide a more simplified threshold for strike events with little to no risk of mortality to those with some risk of mortality.

Lessons for Future Sensor Design Our experiments indicate that, for reliable detection of stiff-body impacts, future sensor designs should employ sampling rates of at least 2000 Hz, coupled with a data-driven algorithm capable of inferring relative blade strike velocity. Across most devices, the dominant failure modes were electrical rather than mechanical, suggesting that improvements in internal electrical robustness should be prioritized over further strengthening of the external housing. If the data-driven approach does not yield sufficient accuracy in in-field applications, an alternative solution could be to embed the sensor in a thick soft coating. This would extend the time scale over which acceleration occurs, thereby reducing the peak acceleration values, reducing bandwidth truncation and intersample peak loss. This approach was demonstrated by Saylor et al. (2021)⁴⁴ and has seen further development recently by Salalila et al. (2025)³⁴.

We demonstrated that current sensor probes are unable to capture the underlying dynamics of a blade strike within the biologically relevant range. As a result, any metric that depends on resolving these dynamics, such as threshold-based or physical models, is unlikely to succeed. To address this limitation, we propose the use of data-driven models, which can identify hidden patterns in the data that are inaccessible to current approaches, thereby enabling the estimation of relative blade strike velocity with sufficient accuracy under laboratory conditions. Whether this performance can be replicated in the complex environment of a hydroturbine or pump, and how reliable access to relative blade strike velocity can be achieved in practice, remains to be determined.

Data availability

The raw and aggregated datasets are available online⁴⁵, along with the code used for aggregation, cutting, and alignment. Additionally, this software is also accessible on GitHub at <https://github.com/ikoesters/srdatacombiner>.

Acknowledgement

The authors are very grateful to Pedro de Jesus Gomez Romero with the turbine manufacturer Andritz (Austria) for providing us with the Sensor Fish devices, as well as to Stefan Felder and Reilly Cox at UNSW (Australia) for providing us with their sensors for testing in the study. The authors gratefully acknowledge Danil Efimov for his contributions to data collection.

This project is part of the European Union Marie Curie International Training Network on Soft, Self-responsive, Smart Materials for Robots (SMART-ITN) and has received funding from the European Union's Horizon 2020 research and innovation program under the Marie Skłodowska-Curie grant agreement No 860108. It is also funded by the German Federal Ministry of Education and Research (BMBF) under project number 031L0152A - D/16LW019 ("Alternative Methods to Animal Testing"), which ran between March 2019 to March 2024. Wolf Iring Kösters has been partially funded by means of the Deutsche Bundesstiftung Umwelt (DBU) in terms of the "StrikeSense" project with grant number AZ 39399/01. Jeffrey A. Tuhtan and Maarja Kruusmaa's contributions were funded in part by the Estonian Research Council Grant PRG2198.

Author contributions statement

W.I.K. and provided the original draft with J.A.T. providing the sections concerning the data-driven model. W.I.K. collected, curated and visualized the data including all software development. S.H., J.A.T. and W.I.K. developed the methodology. All authors reviewed and edited the manuscript. S.A. administered and provided funding for the project.

Competing Interests

The authors declare no competing interests.

References

1. Vagnoni, E. *et al.* The new role of sustainable hydropower in flexible energy systems and its technical evolution through innovation and digitalization. *Renew. Energy* **230**, 120832, DOI: [10.1016/j.renene.2024.120832](https://doi.org/10.1016/j.renene.2024.120832) (2024).
2. International Hydropower Association. *2024 World Hydropower Outlook: Opportunities to Advance Net-Zero* (International Hydropower Association, 2024).
3. Belletti, B. *et al.* More than one million barriers fragment Europe's rivers. *Nature* **588**, 436–441, DOI: [10.1038/s41586-020-3005-2](https://doi.org/10.1038/s41586-020-3005-2) (2020). Publisher: Nature Publishing Group.
4. Cox, R. X., Kingsford, R. T., Suthers, I. & Felder, S. Fish Injury from Movements across Hydraulic Structures: A Review. *Water* **15**, 1888, DOI: [10.3390/w15101888](https://doi.org/10.3390/w15101888) (2023).
5. He, F. *et al.* Hydropower impacts on riverine biodiversity. *Nat. Rev. Earth & Environ.* **5**, 755–772, DOI: [10.1038/s43017-024-00596-0](https://doi.org/10.1038/s43017-024-00596-0) (2024). Publisher: Nature Publishing Group.
6. European Commission. Directorate General for Environment. Biodiversity strategy for 2030: barrier removal for river restoration. *Publ. Off. Eur. Union* DOI: [10.2779/181512](https://doi.org/10.2779/181512) (2022).
7. WWF. Hydropower pressure on European rivers: The story in numbers. Tech. Rep. (2019).
8. Knott, J., Mueller, M., Pander, J. & Geist, J. Ecological assessment of the world's first shaft hydropower plant. *Renew. Sustain. Energy Rev.* **187**, 113727, DOI: [10.1016/j.rser.2023.113727](https://doi.org/10.1016/j.rser.2023.113727) (2023).
9. Evans, O. J. *et al.* Rethinking fish-friendliness of pumps by shifting focus to both safe and timely fish passage for effective conservation. *Sci. Reports* **14**, 17888, DOI: [10.1038/s41598-024-67870-5](https://doi.org/10.1038/s41598-024-67870-5) (2024).
10. (NEN), N. N. NEN 8775:2020 Fish safety - Method for the determination of the fish safety of pumps, Archimedean screws and confined water turbines used in pumping stations and hydroelectric plants (2020).
11. für Normung e.V., D. I. DIN EN 18110:2024-08: Wasserbeschaffenheit - Verfahren zur Ermittlung der Fischdurchgängigkeit von Wasserförderschnecken, Pumpen und Spiralturbinen, die in Pumpwerken und Wasserkraftwerken verwendet werden, DOI: [10.31030/3555890](https://doi.org/10.31030/3555890) (2024).

12. Pflugrath, B. D., Boys, C. A., Cathers, B. & Deng, Z. D. Over or under? Autonomous sensor fish reveals why overshot weirs may be safer than undershot weirs for fish passage. *Ecol. Eng.* **132**, 41–48, DOI: [10.1016/j.ecoleng.2019.03.010](https://doi.org/10.1016/j.ecoleng.2019.03.010) (2019).
13. Martinez, J. *et al.* In situ characterization of turbine hydraulic environment to support development of fish-friendly hydropower guidelines in the lower Mekong River region. *Ecol. Eng.* **133**, 88–97, DOI: [10.1016/j.ecoleng.2019.04.028](https://doi.org/10.1016/j.ecoleng.2019.04.028) (2019).
14. Romero-Gomez, P. *et al.* Sensor Fish Deployments at the Xayaburi Hydropower Plant: Measurements and Simulations. *Water* **16**, 775, DOI: [10.3390/w16050775](https://doi.org/10.3390/w16050775) (2024).
15. Deng, Z. D. *et al.* Design and implementation of a new autonomous sensor fish to support advanced hydropower development. *Rev. Sci. Instruments* **85**, DOI: [10.1063/1.4900543](https://doi.org/10.1063/1.4900543) (2014).
16. Hoerner, S., Kösters, W. I., Abbaszadeh, S., Wagner, F. & Tuhtan, J. Towards a reliable and validated toolbox to replace live fish tests for the assessment of injury and mortality during downstream passage (2024).
17. Pauwels, I. S. *et al.* Multi-Species Assessment of Injury, Mortality, and Physical Conditions during Downstream Passage through a Large Archimedes Hydrodynamic Screw (Albert Canal, Belgium). *Sustainability* **12**, 8722, DOI: [10.3390/su12208722](https://doi.org/10.3390/su12208722) (2020).
18. Evans, O. *et al.* The effectiveness of a fish-friendly pumping station for critically endangered European eel; An assessment using live eels, fish-mounted sensors and passive sensors. *Ecol. Eng.* **213**, 107526, DOI: [10.1016/j.ecoleng.2025.107526](https://doi.org/10.1016/j.ecoleng.2025.107526) (2025).
19. Cox, R. X. & Felder, S. Injury-free transport of fish through closed conduit components. *J. Ecohydraulics* 1–16, DOI: [10.1080/24705357.2025.2462296](https://doi.org/10.1080/24705357.2025.2462296) (2025).
20. Deng, Z. D., Carlson, T. J., Duncan, J. P., Richmond, M. C. & Dauble, D. D. Use of an autonomous sensor to evaluate the biological performance of the advanced turbine at Wanapum Dam. *J. Renew. Sustain. Energy* **2**, DOI: [10.1063/1.3501336](https://doi.org/10.1063/1.3501336) (2010).
21. Fu, T. *et al.* Assessing hydraulic conditions through Francis turbines using an autonomous sensor device. *Renew. Energy* **99**, 1244–1252, DOI: [10.1016/j.renene.2016.08.029](https://doi.org/10.1016/j.renene.2016.08.029) (2016).
22. Martinez, J. *et al.* Hydraulic and biological characterization of a large Kaplan turbine. *Renew. Energy* **131**, 240–249, DOI: [10.1016/j.renene.2018.07.034](https://doi.org/10.1016/j.renene.2018.07.034) (2019).
23. Salalila, A., Deng, Z. D., Martinez, J. J., Lu, J. & Baumgartner, L. J. Evaluation of a fish-friendly self-cleaning horizontal irrigation screen using autonomous sensors. *Mar. Freshw. Res.* **70**, 1274, DOI: [10.1071/MF19194](https://doi.org/10.1071/MF19194) (2019).
24. Saylor, R. K., Sterling, D., Bevelhimer, M. & Pracheil, B. Within and Among Fish Species Differences in Simulated Turbine Blade Strike Mortality: Limits on the Use of Surrogacy for Untested Species. *Water* **12**, 701, DOI: [10.3390/w12030701](https://doi.org/10.3390/w12030701) (2020).
25. Pflugrath, B. D. *et al.* Biological Response Models: Predicting Injury and Mortality of Fish During Downstream Passage through Hydropower Facilities. Tech. Rep. PNNL-30893, Pacific Northwest National Lab. (PNNL), Richland, WA (United States) (2021). DOI: [10.2172/1838202](https://doi.org/10.2172/1838202).
26. Huang, T. *et al.* Velocity- and pressure-based metrics for estimating strike injuries during fish passage through hydro turbines. *Results Eng.* **25**, 104535, DOI: [10.1016/j.rineng.2025.104535](https://doi.org/10.1016/j.rineng.2025.104535) (2025).
27. Kösters, W. I., Tuhtan, J. A., Efimov, D., Kruusmaa, M. & Hoerner, S. An open laboratory blade strike rig to evaluate the risk of injury and mortality to fish and to test passive sensors. *Sustain. Energy Technol. Assessments* **81**, 104427, DOI: [10.1016/j.seta.2025.104427](https://doi.org/10.1016/j.seta.2025.104427) (2025). Publisher: Elsevier BV.
28. Hecker, G. E., Amaral, S. V. & Stacy, P. S. Investigation of Hydro-Turbine Leading-Edge Shapes Favorable to Fish Survival. Tech. Rep. 102561, Electric Power Research Institute, Palo Alto, CA (2007).
29. Bevelhimer, M. S., Pracheil, B. M., Fortner, A. M., Saylor, R. & Deck, K. L. Mortality and injury assessment for three species of fish exposed to simulated turbine blade strike. *Can. J. Fish. Aquatic Sci.* **76**, 2350–2363, DOI: [10.1139/cjfas-2018-0386](https://doi.org/10.1139/cjfas-2018-0386) (2019).
30. Saylor, R. K. *Susceptibility of riverine fishes to anthropogenically-linked trauma: Strikes from hydropower turbine blades*. Ph.D. thesis, University of Tennessee, USA (2021).
31. Skalski, J. *et al.* Compliance Monitoring of Yearling and Subyearling Chinook Salmon and Juvenile Steelhead Survival and Passage at John Day Dam, 2012. Tech. Rep. PNNL-22152, 1083413, 400403209 (2013). DOI: [10.2172/1083413](https://doi.org/10.2172/1083413).

32. Ahmad, F., Evans, J. & Nestler, J. M. Multiple Sensor Fish Surrogate for Acoustic and Hydraulic Data Collection (1997).
33. Deng, Z. D., Carlson, T., Duncan, J. P. & Richmond, M. Six-Degree-of-Freedom Sensor Fish Design and Instrumentation. *Sensors* **7**, 3399–3415, DOI: [10.3390/s7123399](https://doi.org/10.3390/s7123399) (2007).
34. Salalila, A., Lu, J., Martinez, J. J., Hou, H. & Deng, Z. D. Autonomous sensor suite for evaluating fish-turbine interactions and environmental impacts in marine renewable energy and hydropower. *Sci. The Total. Environ.* **966**, 178710, DOI: [10.1016/j.scitotenv.2025.178710](https://doi.org/10.1016/j.scitotenv.2025.178710) (2025).
35. Cox, R., Peirson, W. & Felder, S. Investigating the hydrodynamic risk for fish injury in pipe entries. DOI: [10.26190/UNSWORKS/28424](https://doi.org/10.26190/UNSWORKS/28424) (UNSW Sydney, Sydney, 2022).
36. Leys, C., Delacre, M., Mora, Y. L., Lakens, D. & Ley, C. How to Classify, Detect, and Manage Univariate and Multivariate Outliers, With Emphasis on Pre-Registration. *Int. Rev. Soc. Psychol.* **32**, DOI: [10.5334/irsp.289](https://doi.org/10.5334/irsp.289) (2019).
37. Leys, C., Ley, C., Klein, O., Bernard, P. & Licata, L. Detecting outliers: Do not use standard deviation around the mean, use absolute deviation around the median. *J. Exp. Soc. Psychol.* **49**, 764–766, DOI: [10.1016/j.jesp.2013.03.013](https://doi.org/10.1016/j.jesp.2013.03.013) (2013).
38. Deng, Z. D. *et al.* Evaluation of fish-injury mechanisms during exposure to turbulent shear flow. *Can. J. Fish. Aquatic Sci.* **62**, 1513–1522, DOI: [10.1139/f05-091](https://doi.org/10.1139/f05-091) (2005). Publisher: NRC Research Press Ottawa, Canada.
39. Qiu, H., Rehman, R. Z. U., Yu, X. & Xiong, S. Application of Wearable Inertial Sensors and A New Test Battery for Distinguishing Retrospective Fallers from Non-fallers among Community-dwelling Older People. *Sci. Reports* **8**, 16349, DOI: [10.1038/s41598-018-34671-6](https://doi.org/10.1038/s41598-018-34671-6) (2018). Publisher: Nature Publishing Group.
40. Jaiswal, V., T. N. B., Murugan, P. & D, R. P. Fault analysis on deep groove ball bearing using ResNet50 and AlexNet50 algorithms. *Sci. Reports* **15**, 12962, DOI: [10.1038/s41598-025-97410-8](https://doi.org/10.1038/s41598-025-97410-8) (2025).
41. Saylor, R. K., Bevelhimer, M. & Pracheil, B. Fish injury and mortality caused by simulated impacts from turbine blades, DOI: [10.21951/1755094](https://doi.org/10.21951/1755094) (2020).
42. Pasam, A., Tudball Smith, D., Holmes, J. D., Burton, D. & Thompson, M. C. The influence of surface roughness on postcritical flow over circular cylinders revisited. *J. Fluid Mech.* **975**, A36, DOI: [10.1017/jfm.2023.846](https://doi.org/10.1017/jfm.2023.846) (2023).
43. Pauwels, I. S. *et al.* A fish-friendly axial flow pump turns out to be eel safe, roach unfriendly and bream unsafe. *Sci. Reports* **14**, 30234, DOI: [10.1038/s41598-024-81095-6](https://doi.org/10.1038/s41598-024-81095-6) (2024).
44. Saylor, R. K. *et al.* Creation of a prototype biomimetic fish to better understand impact trauma caused by hydropower turbine blade strikes. *PeerJ Mater. Sci.* **3**, DOI: [10.7717/peerj-matsci.16](https://doi.org/10.7717/peerj-matsci.16) (2021).
45. Kösters, W. I. & Efimov, D. Blade Strike Data: Sensor Probes for Fish Passage Safety: Evaluating Strike Severity Metrics and Data-Driven Prediction, DOI: [10.5281/zenodo.16876012](https://doi.org/10.5281/zenodo.16876012) (2025).

A.5 Publication V

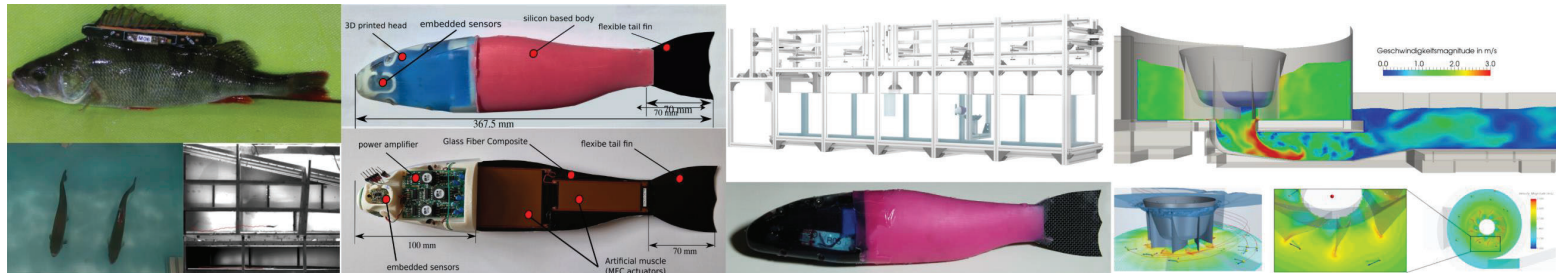
S. Hoerner, W. I. Kösters, S. Abbaszadeh, F. Wagner, and J. A. Tuhtan (May 2024). "Towards a reliable and validated toolbox to replace live fish tests for the assessment of injury and mortality during downstream passage". In: *IAHR 15th International Symposium on Ecohydraulics and Fish Passage*. Quebec City, Canada



15th International Symposium on Ecohydraulics and Fish Passage 2024

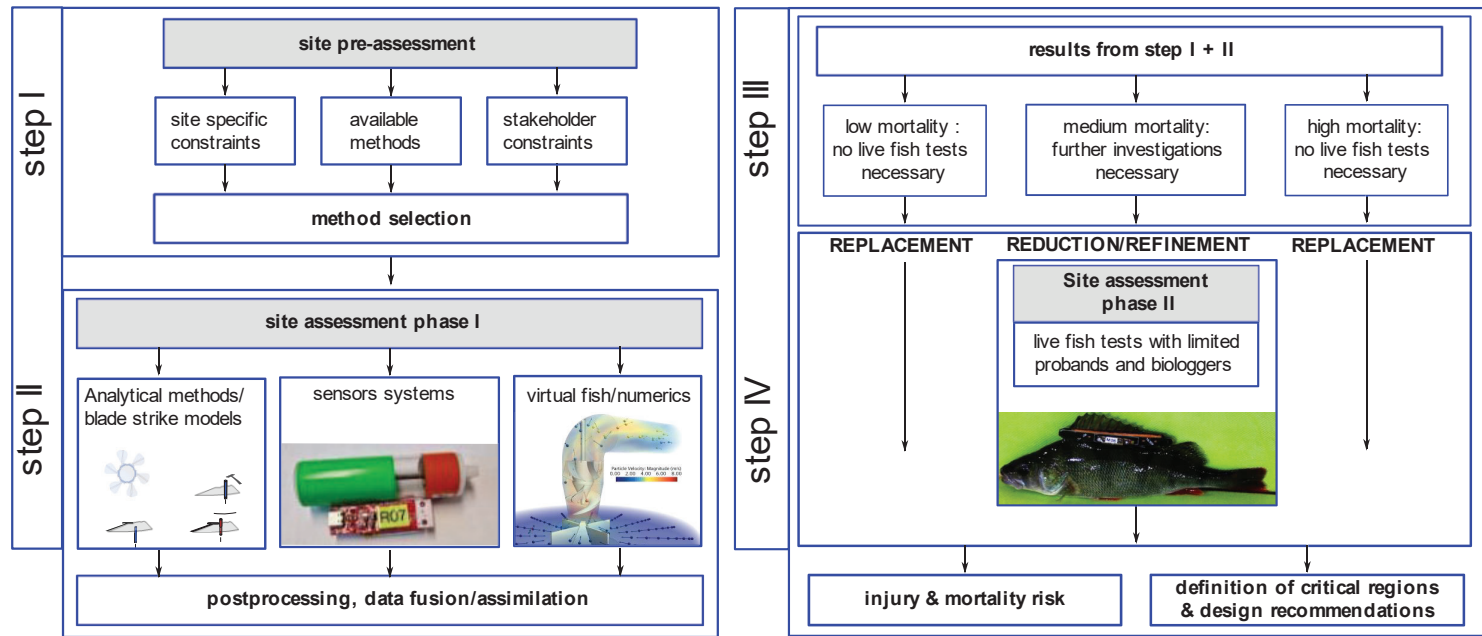
Towards a reliable and validated toolbox to replace live fish tests for the assessment of injury and mortality during downstream passage

S. Hoerner^{1,2}, W. I. Kösters^{2,3}, S. Abbaszadeh², F. Wagner⁴, J. A. Tuhtan³



¹LEGI, CNRS, Grenoble-INP, Université Grenoble-Alpes, France, ²Otto-von-Guericke-Universität Magdeburg, Germany,

³Department of Computer Science, Taltech, Tallinn, Estonia, ⁴Institute of Aquatic Ecology and Fish Biology, Jena, German



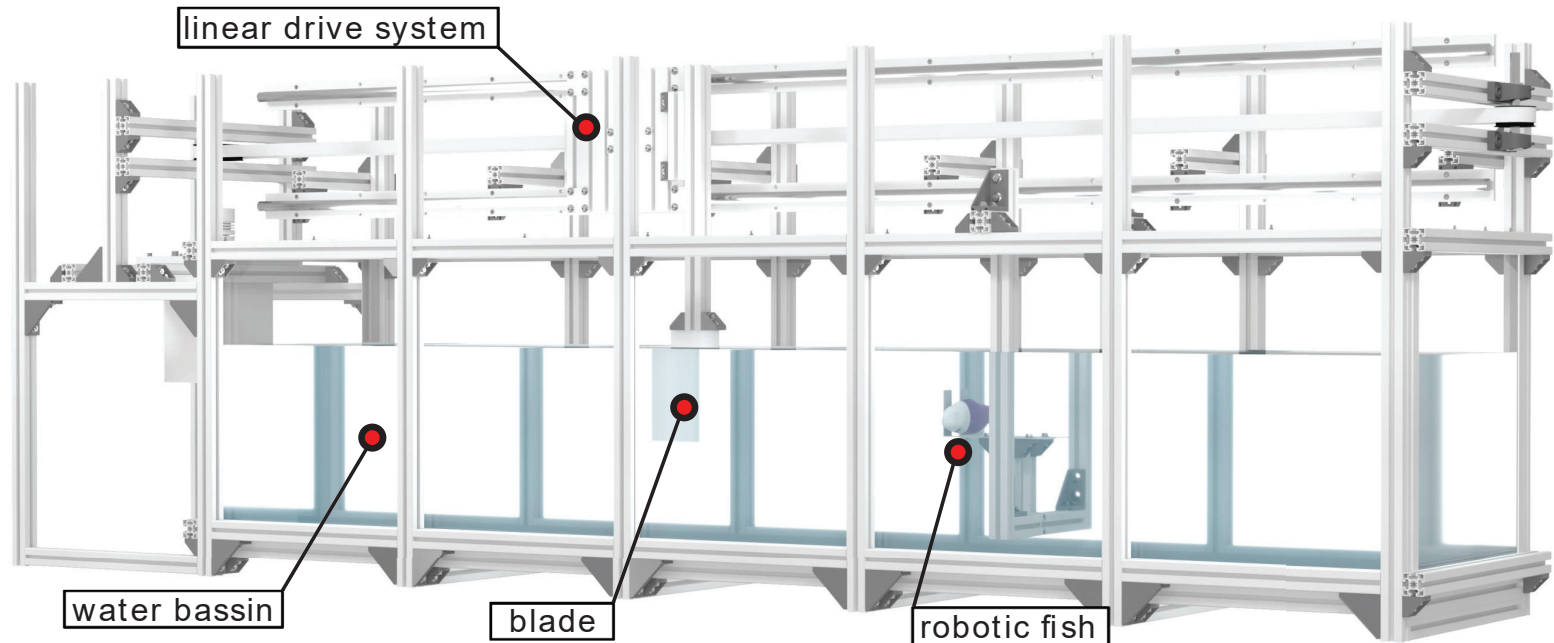
Replacement of live animal tests & integration of new methods in the standards requires faith by evidence

- what are the criteria for injury, e.g. thresholds, parameters, etc. ?
 - biological well studied for some species, what about others ?
 - good knowledge and transferability from fish to surrogate system for barotrauma but challenging for blade strike and collision
- how can we link sensor data to injury and provide evidence ?
- what about different sensor types/vendors or modeling methods ? Are results comparable and reliable ?
- for experimental methods : reference data from test sites with
 - mortality rates from live fish (*limited but feasible*)
 - known & reproduceable boundary conditions (*difficult*)
 - continuous access for repetition with new/novel devices (*very difficult*)

or : lab tests with standardised protocols (*easier ?*)

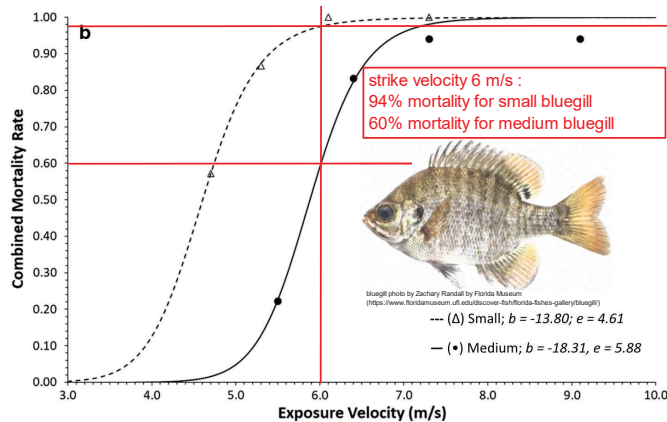
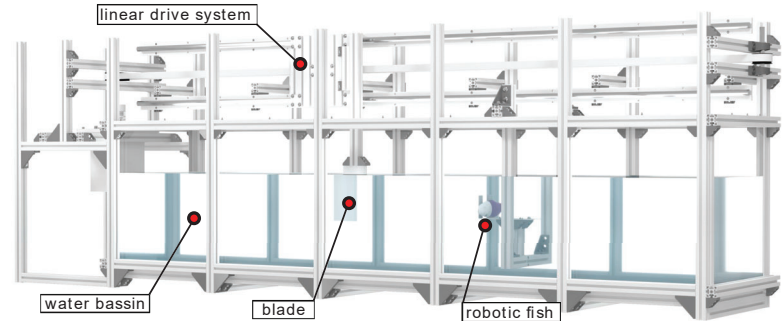
Replacement of live animal tests & integration of new methods in the standards requires faith by evidence

lab tests with standardised protocols : **blade strike test rig**



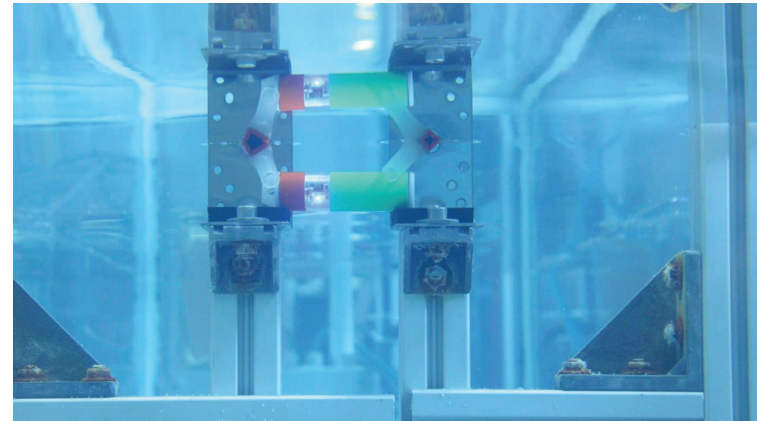
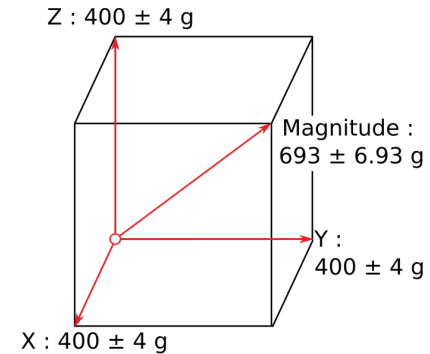
Lab tests with standardised protocols : blade strike test rig

- inspired by ORNL¹ and EPRI² test benches
- motorized fully controlled linear drive system
- high strike repeatability (< 0.02% variation)
- 0-9 m/s strike velocity
- **aim : repetition of fish tests with sensors and correlation to injury**
- e.g. Saylor *et al.* 2019 on bluegill³ :



Lab tests with standardised protocols : blade strike test rig

- RAPID sensors from TalTech
tech specs : 6-axis IMU, magnetic field, absolute pressure
2kHz sampling rate, polycarbonate housing
(see: <https://biorobotics.pages.taltech.ee/edf/en/>)
 - IMU accelerations $400 \text{ g} \pm 0.5\% \text{ F.S.}$ uncertainty per axis (uncertainty retrieved from own lab tests)
 - translatory motion => 3 axis
=> acceleration magnitude = $693 \text{ g} \pm 0.5\% \text{ F.S.}$
- data from 60 samples for each strike velocity : 1 to 9 m/s
- Hypothesis : criteria for severe injury acceleration magnitude > 95 g
(according to Deng *et al.* 2010⁴, time component to differ from collision to shear was not assessed)



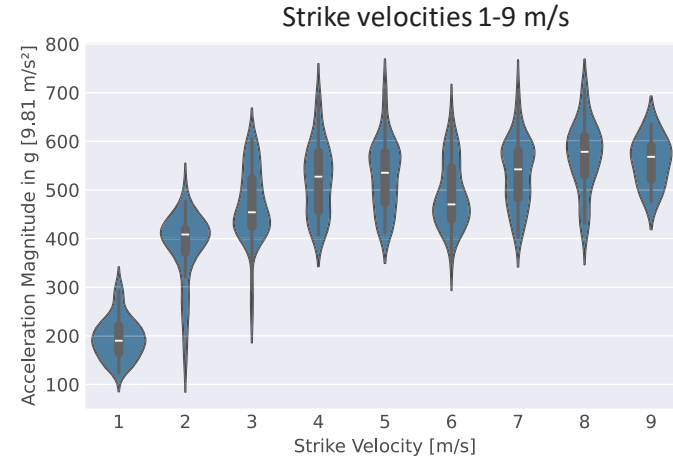
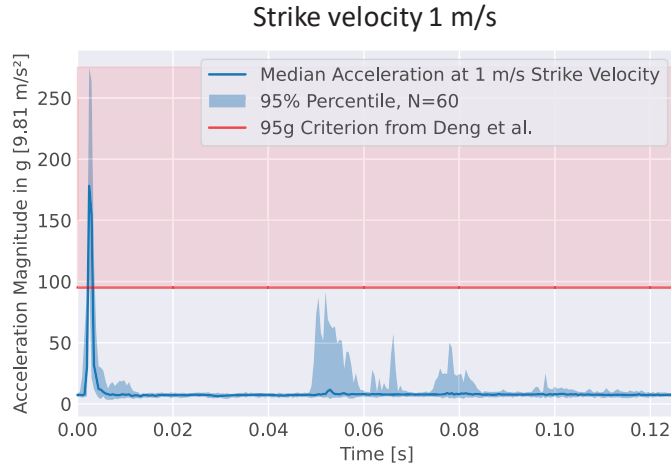
Lab tests with standardised protocols : blade strike test rig



Lab tests with standardised protocols : blade strike test rig



Lab tests with standardised protocols : blade strike test rig



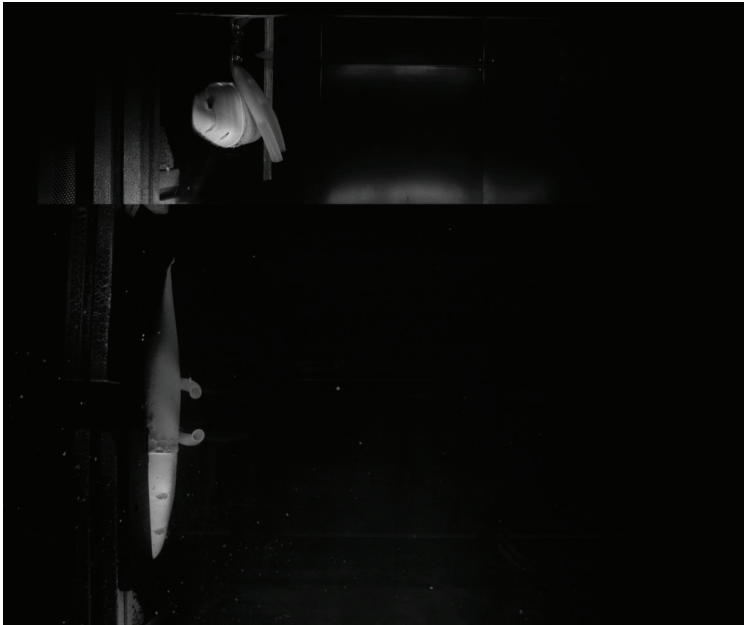
- for 1 m/s and bluegill mortality 0% : all measured sensor acceleration magnitudes exceed 95 g.
Max of the median 178 g (95% data percentile : min 123g/max 275 g, max of all samples= 304 g)
- very fast saturation of the sensors starting from 4 m/s. Strike velocities of more than 4 m/s provide similar magnitudes.
Relative strike velocity of 1m/s can produce same acceleration magnitude as 6 m/s
- **conclusions:**
- **(1) acceleration magnitudes cannot provide quantifiable strike velocity data and**
- **(2) the 95 g rule is not applicable (at least for the tested sensors)**

Summary

- standardized tests for collision sensor systems are necessary to provide evidence and faith in the new methods to the community
- a blade strike test rig for repeatable sensor testing has been built (a publication with technical details is in submission)
- up to now no correlated strike acceleration thresholds to estimate injury are available, strike velocities hardly quantifiable
- TalTech RAPID sensor measurements do not match with the 95 g threshold for severe injury (Deng *et al.* 2010⁴) when comparing to live fish data (Saylor et al. 2019¹). What about other market available sensors such as ATS sensor fish ?
- open questions remain :
 - cross-comparability: how do sensors from different vendors behave for the same strike ?
Extended strike testing with standardized protocols on various sensor types are necessary to ensure suitability and cross comparability
 - method suitability: can injury risk probabilities be quantified from acceleration magnitudes in general ?
Do we need other measures ? Are rigid sensor bodies appropriate to replace fish for strike test surrogate systems ?

Outlook

Are flexible bodies closer to fish body characteristics and do they provide better data for risk probability quantification, such as shown in Saylor *et al.* 2021⁵?



Thank you very much for your attention !

contact :

stefan.hoerner@univ-grenoble-alpes.fr





...there are more RETERO presentations at the congress:

Hoerner et al. - *Towards a reliable and validated toolbox to replace live fish tests for the assessment of injury and mortality...*, Monday, 16:00, Session 11 “Fish screening techniques”

Wagner et al. - *Behavior analysis for fish...*, Tuesday, 14:30, Session 22 “Safe downstream passage”

Abbaszadeh et al. - *Bio-inspired robotic fish for assessment of injury ...*, Wednesday, 11:45 Session 33 “Fishway monitoring & evaluation 1”

Kopecki et al. - *Estimating fish swimming speed using non-invasive backpack sensors...*, Wednesday, 11:15 Session 34 “Fish locomotion in unsteady flow”



References

- ¹ M.S. Bevelhimer, B. M. Pracheil, A. M. Fortner, R. Saylor, K.L. Deck, Mortality and Injury Assessment for Three Species of Fish Exposed to Simulated Turbine Blade Strike, *Canadian Journal of Fisheries and Aquatic Sciences*, 2019
- ² G. E. Hecker, S. V., Amaral, and P.S. Stacy, Investigation of Hydro-Turbine Leading-Edge Shapes Favorable to Fish Survival. 102561. Palo Alto, CA: Electric Power Research Institute, 2007.
- ³ R. Saylor . A. Fortner . M. Bevelhimer, Quantifying mortality and injury susceptibility for two morphologically disparate fishes exposed to simulated turbine blade strike, *Hydrobiologia*, 2019
- ⁴ Z. Deng, T. J. Carlson, J. P. Duncan, M. C. Richmond, and D. D. Dauble, Use of an autonomous sensor to evaluate the biological performance of the advanced turbine at Wanapum Dam, *Journal of Renewable & Sustainable Energy*, 2010
- ⁵ R. Saylor . P.L. Wang, M.S. Bevelhimer, P. Lloyd , J. Goodwin , R. Laughter , D. Young, D. Sterling, P. Mhatre, C. Atkins and B. Post, Creation of a prototype biomimetic fish to better understand impact trauma caused by hydropower turbine blade strikes, *PeerJ Material Science*, 2021

A.6 Publication VI

S. Hoerner, T. Bennecke, W. I. Kösters, K. Ruiz-Hussmann, A. Jayaprakash, S. Abbaszadeh, J. A. Tuhtan, P.-L. Delafin, C. Bonamy, and R. Leidhold (Aug. 2, 2025). "Experimental Determination of the Hydrodynamic Loading on Vertical-Axis Cross-flow Tidal Turbines with Blade Embedded Autonomous Sensors". In: 7th International Conference on Ocean Engineering. Chennai, India

Experimental Determination of the Hydrodynamic Loading on Vertical-Axis Cross-flow Tidal Turbines with Blade Embedded Autonomous Sensors

Stefan Hoerner^{1,2}, Timo Bennecke², Wolf I. Kösters^{2,3} Karla Ruiz-Husmann^{1,2}, Adhithiyam Jayaprakash⁴, Shokoofeh Abbaszadeh⁴, Jeffrey A. Tuhtan³, Pierre-Luc Delafin¹, Cyrille Bonamy¹, and Roberto Leidhold⁴

¹ Laboratoire des Écoulements Géophysiques et Industriels (LEGI), G-INP, CNRS, Université Grenoble-Alpes, Grenoble, France,
stefan.hoerner@universite-grenoble-alpes.fr,

² Institute of Fluid Dynamics and Thermodynamics, Otto-von-Guericke-University Magdeburg, Germany

³ Department of Computer Systems, Tallinn University of Technology (TalTech), Tallinn, Estonia

⁴ Institute of Electrical Power Systems, Otto-von-Guericke University Magdeburg, Germany

Abstract. Hydrokinetic vertical-axis cross-flow turbines (CFTT) can efficiently harness tidal and ocean currents but are prone to vibrations and fatigue due to complex flow dynamics, especially at low rotational speeds where blade stall occurs. To study these effects, a lab-scale rotor was developed with strain gauges on the support structure and embedded miniaturized sensors in the blades. These sensors measure accelerations, rotational speed, pressure, and magnetic fields, capturing blade bending, torsion, and overall rotor motion. They can be calibrated in situ and can serve as a plug-and-play system for advanced rotor monitoring in future designs.

Keywords: Tidal energy, Vertical axis turbines, Cross-flow turbines, Experiments, Fluid-structure interactions, complex instrumentation

1 Introduction

The first mature ecologically compatible technologies based on hydrokinetic energy converters are now available for tidal streams. In recent years, extensive field tests have been conducted successfully, and a first 17.5 MW pilot farm is currently being built in the English Channel¹. However, the available sites remain limited [1],[4], and the power density and energy conversion efficiency of hydrokinetic turbines are generally low [11].

Vertical-axis cross-flow tidal turbines (CFTT) promise higher power density per area than classic axial tidal turbines, which are often referred to as horizontal-axis turbines. For wind turbines, it has been shown numerically and experimentally that a higher power density can be achieved by an order of magnitude [5]. Due to fluid mechanical similarity laws, it can be assumed that this also applies to tidal turbines. However, CFTTs pose technical challenges as a result of their rotation axis being perpendicular to the flow. The rotor blades are subject to a continuous periodic change in the angle of attack α_b [rad], as shown in Fig. 1

¹ for example see www.hydroquest.fr/en/flowatt-en/

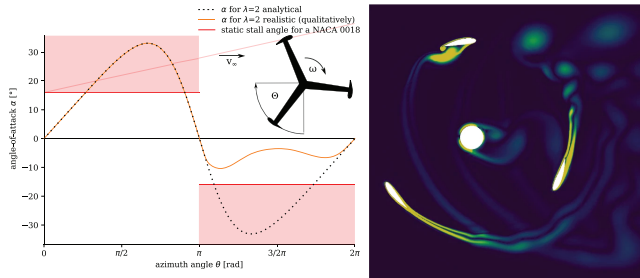


Fig. 1. (left) Analytical model of the angle of attack α_b (black dashed). (right) Numerical 2D simulations (OpenFOAM, URANS, $k-\omega$ -SST model) ([8] CC BY 4.0)

(left). An analysis using velocity triangles results in a non-sinusoidal periodic curve, which is given by (1). The values of α_b depend on the operating point, which is expressed by the dimensionless tip speed ratio λ_r . (2).

$$\alpha_b = \arctan\left(\frac{\sin \theta_r}{\lambda_r + \cos \theta_r}\right) \quad (1)$$

where θ_r [rad] is the azimuth angle of the rotor (Fig. 1 (left) for the coordinate system).

$$\lambda_r = \frac{\omega_r R}{v_\infty} \quad (2)$$

where ω_r is the angular velocity of the rotor in [rad/s] and R is the turbine radius in [m], whose vector product reflects the tangential velocity, and v_∞ [m/s] is the velocity of the free flow. Tidal turbines are typically operated at $\lambda_r \approx 2$, as they have relatively solid construction due to the high density of water compared to wind turbines. This requires a low λ_r value for the optimal operating point [14]. The low value λ_r in turn leads to very high α_b values (30° for $\lambda=2$), which are significantly above the static stall angle of a common rotor blade profile. However, the rotor dynamics and the resulting high flow instabilities, expressed in high reduced frequencies, lead to an increase in the dynamic stall angle. In earlier work [8], this angle was shown to reach well over 20° in a common turbine design as presented in [9]. Therefore, simple turbine models based on static profile data and calculations allow for only a very rough estimate of the mechanics of such turbines, and the rotor dynamics are key for the turbine characteristics. Numerical models show high values for α_b and dynamic blade separation in the upstream region of the rotor (Fig. 1 (right)), which are comparable to analytical predictions, while α_b in the downstream region of the turbine is significantly smaller due to the wake of the upstream region of the rotor in the flow field [6]. In summary, it can be said that the periodic angle change and flow separation generate alternating hydrodynamic loads that lead to vibrations and, in the worst case, to failure of the rotor structures. CFTTs have long been known for their vulnerability to fatigue failure [10]. However, fluid-structure interactions have been studied in less detail and most studies are numerical in nature [12]. Therefore, we

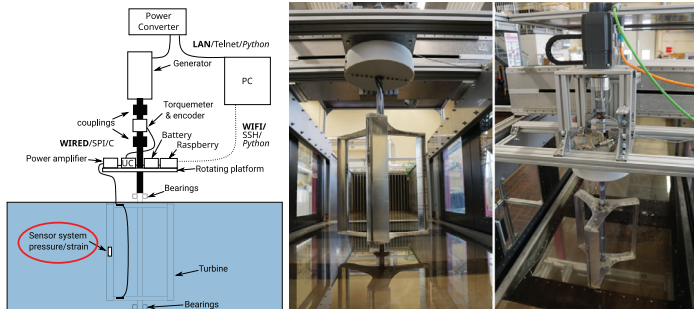


Fig. 2. (left) Instrumentation of the turbine flume model. (middle) Experimental model in the lab flume. (right) Power uptake is realized with a velocity controlled servo drive.

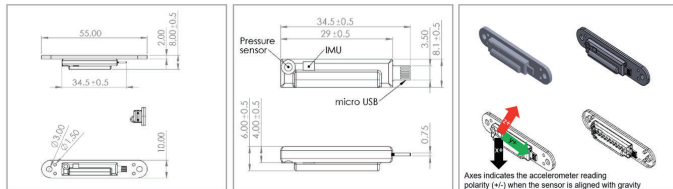


Fig. 3. Technical drawings and dimensions in mm of the microtag devices (from [15])

have developed a flume-scale turbine model using extensive weak coupled fluid-structure interaction simulations by employing 2D CFD simulations mapped to 3D FEA [3] with suitable profile shapes [12] equipped with strain gauges [2] to assess hydraulic loads and experimentally analyse fluid-structure interactions. In this study, we present an autonomous microsensors system embedded in the blades of the flow channel model. The aim is to demonstrate a calibration process and the benefits and limitations of the current system, which represents a step forward in our development of a cost-effective measuring instrument for academic and industrial applications in the field of fluid-structure interaction.

2 Methodology

2.1 General instrumentation setup

The instrumentation and measurement concept of the test setup is shown in Fig. 2. The turbine is a straight-bladed Darrieus CFFT with three blades and mountings at both blade tips. The design is based on an aluminum skeleton with 3D-printed fairings. The NACA0018 rotor blade profiles are slightly curved in accordance with the circumference of the turbine to take into account the flow curvature resulting from rotation [9]. The diameter and height (blade length) of the turbine are 400 mm, and the blade chord length is 72.5 mm.

All relevant parameters, such as torque, azimuth angle and blade support load, are recorded via microcontrollers on a rotating platform and transmitted by

Table 1. Technical specifications microtags [15]. The sensor measures absolute pressure, 3D acceleration, angular velocities and magnetic fields.

Pressure sensor	MS5837-2BA (TE Connectivity)	
pressure range	0-2000	mbar
Inertial Measurement Unit (IMU)	BMX160 (Bosch Sensortech)	
linear acceleration range	16	g [9.81 m/s ²]
linear acceleration accuracy	0.01	g [9.81 m/s ²]
gyroscope data range	2000	deg/s
gyroscope data accuracy	+/-2	deg/s
magnetic field data range (x,y / z)	1300 / 2500	μ T
magnetic field accuracy (x,y / z)	5 / 10	μ T
Overall weight & dimensions		
weight	1.6	g
length x height x width	35 x 8.15 x 6.1	mm
Data logging frequency		
logging rate	100	Hz

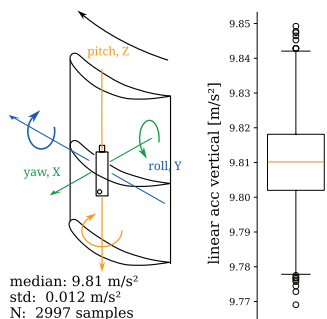
WiFi from a Raspberry Pi 3A + [13] to a desktop computer. The strain measurement system, consisting of five full bridges with strain gauges, enables the determination of individual blade load components. This system records loads synchronously with flow fields, which are currently measured using high-speed particle image velocimetry (PIV). Details were presented in [2]. The turbine scaling was a trade off in between flow similarity (Reynolds number) and confinement (currently 20%). The blade based Reynolds number varies from 50,000 to 100,000 depending on the operation point.

2.2 Embedded FSI sensors

In addition, autonomous embedded FSI microsensors (microtag) were installed in one blade. Technical specifications and drawings are shown in Fig. 3 & Tab. 1. Sensor was installed 11 mm toward the leading edge from the quarter chord of the hydrofoil. Vertical distance from upper blade tip is 150 mm. The opening for the pressure transducer diaphragm has a 2 mm diameter. A silicone tube connects the pressure transducer to blade surface. The cavity for the sensor is filled with ultra-soft silicone to fix the position. The blade stiffness is assured using a metal rod (stainless steel) as reinforcement. Thus it is hypothesised that the modification has negligible influence to the structural characteristics, such as bending modes or deformation.

The sensors provide linear acceleration, angular velocity and the magnetic field flux density. In addition, a temperature-compensated sensor measures the total surrounding pressure. The data was streamed via the microUSB connection to the Raspberry Pi on the rotating platform and time-stamped to synchronize the microtag with the other data collected on the turbine.

2.3 Bias removal and calibration

**Fig. 4.** Coordinate system and Z-axis data (gravity) after bias removal and calibration

The sensor is embedded into the blade and cannot be removed easily. Therefore it is not possible to calibrate the sensor using standard methods such as [7]. As a consequence, the bias from the sensor tilt is removed and the sensor is calibrated based on a reference measurement in the installed position. A series of measurements ($N = 2997$ samples)

without any motion and without water (in air) is performed. The aim of the bias removal is to reorient the coordinate system of the data from the tilted installation towards the rotating reference X, Y, Z (Z is aligned with gravity, origin is the sensor, see Fig. 4). The tilt is determined with linear acceleration. (3) allow to determine the

time-averaged values for the tilt angles, pitch $\bar{\rho}_s$, roll $\bar{\phi}_s$, and yaw/azimuth $\bar{\theta}_s$.

$$\begin{aligned}\bar{\rho}_s &= \frac{1}{N} \sum_{i=0}^N \left(\tan^{-1} \left(\frac{a_{s,x}}{\sqrt{a_{s,y}^2 + a_{s,z}^2}} \right) \right) \\ \bar{\phi}_s &= \frac{1}{N} \sum_{i=0}^N \left(\tan^{-1} \left(\frac{a_{s,y}}{\sqrt{a_{s,x}^2 + a_{s,z}^2}} \right) \right) \\ \bar{\theta}_s &= \frac{1}{N} \sum_{i=0}^N \left(\tan^{-1} \left(\frac{\sqrt{a_{s,x}^2 + a_{s,y}^2}}{a_z} \right) \right)\end{aligned}\quad (3)$$

where \mathbf{a}_s is the tilted and raw linear acceleration. x, y, z are the space axes in the reference frame of the tilted sensor. After determination of the tilt angles a 3×3 , 3D rotation matrix with Euler angles \mathbf{R} is applied to entire data. Finally the acceleration is calculated using (4) with the time-averaged acceleration magnitude

$\bar{a}_{s,i} = \frac{1}{N} \sum_{j=0}^N (a_{s,i,j})$ to obtain the gain factor q :

$$q_a = \frac{\sqrt{\bar{a}_{s,X}^2 + \bar{a}_{s,Y}^2 + \bar{a}_{s,Z}^2}}{g}\quad (4)$$

In a final step, the remaining offset is removed to achieve zero acceleration in X, Y and gravity g in Z . Previously calculated tilt angles (3) are used to reorient the angular velocities ($\boldsymbol{\omega}_s$) from the gyroscope. After reorientation, the rotational velocity n (sec. 2.5) is used to determine the gain q_ω using (5).

$$q_\omega = \frac{\frac{n}{60s} \cdot 360^\circ}{\bar{\omega}_{s,Z}}\quad (5)$$

with n the rotational speed (30 rpm) of the turbine. The gyroscope offset is calculated from the calibration data set, as it has no motion and it is known that $\boldsymbol{\omega}_{b,i}=0$. The total bias removal and calibration method is given by eq. 6.

$$\begin{aligned}\mathbf{a} &= \mathbf{R} \times \mathbf{a}_s \cdot q_a - \mathbf{o}_a \\ \boldsymbol{\omega}_b &= \mathbf{R} \times \boldsymbol{\omega}_s \cdot q_\omega - \mathbf{o}_\omega\end{aligned}\quad (6)$$

Fig. 4 shows the new reference system and sensor accuracy for acceleration Z (towards gravity). Maximal deviation (including outliers) from gravity is of ± 0.04 m/s^2 (relative deviation $\pm 0.42\%$, standard deviation 0.012 m/s^2 , relative standard deviation 0.12%). This corresponds to the manufacturer's technical data sheet values (tab. 1) and shows the very high accuracy of the sensor system.

2.4 Pressure data

The microtag’s pressure sensor measures the total pressure, which is of limited use for the current application as it includes the static pressure. To remove this effect, the static pressure was calculated and subtracted from the data to obtain only the remaining dynamic pressure share, as shown in eq. 7.

$$p_{\text{dyn}} = p_{\text{total}} - (p_{\text{ambient}} + \rho_{\text{water}}gh) \quad (7)$$

with water density $\rho_{\text{water}}=1000 \text{ kg/m}^3$ and averaged vertical distance from water level at flume inlet to sensor $h=300 \text{ mm}$. This hydrostatic share is $p_{\text{hydro}}=2452.5 \text{ Pa}$. Ambient pressure ($p_{\text{ambient}}=106401.66 \text{ Pa}$) is the ensemble average from calibration data. It includes the offset. Other terms for time-varying pressure inducing quantities like velocity gradients and added mass are neglected.

2.5 Measurement set up

A series of measurements has been carried out at $n=30 \text{ rpm}$ to demonstrate the usefulness of the system. This corresponds to $\lambda_r=1.01$ with a power coefficient $C_p=0.0516$ for a flume velocity $v_\infty=0.62 \text{ m/s}$. The operating point was chosen arbitrarily. However, at 30 rpm , a large angle of attack of the rotor blades and massive flow separation with strong fluid-structure interactions are likely to occur during each revolution. This was considered advantageous for the demonstration of the sensors. Additional rotor velocities will be considered in future. Turbine best point is at $\lambda_r=2.02$ with $C_p=0.22$. The period for one rotation is 2 s (200 samples). Data was captured for 90 s leading to $N=9004$ samples (microtag captures at 100Hz) and $N=90040$ (rotating platform at 1 kHz). The microtag data is interpolated to 1kHz and synchronized. Finally 34 full rotor revolutions are assessed.

3 Results & discussion

Tab. 2 shows the resulting measurement data. A cumulative phase lag of 2.2°

Table 2. Measurement data for 30 rpm , $\lambda = 1.1$, $C_p = 0.05$; if not expressed otherwise, the median value for 34 rotations is shown.

	Symbol	Unit	X	Y	Z
acceleration	a	$[\text{m/s}^2]$	-1.833	0.010	9.623
rotational speed		$[\text{r/s}]$	-16.71	12.53	-179.30
dyn. pressure	p	$[\text{Pa}]$	-1809.51 (min)	-547.03 (median)	405.09 (max)

per rotation is found for the microtag compared to the rotating platform. A simple adjustment method by adding the 2.2° for each revolution is applied for compensation. It is hypothesised that this phase lag as well as other inaccuracies origin from misalignment of the sensor (Z) compared to the rotor rotation axis. This leads to a tumbling motion compared to the rotor rotation for each rotation comparable to the obliquity of the earth ecliptic. For some of the parameters, a reference value is known. For the gyroscope in Z ($\omega_{b,Z}$) a median of 179.3° is measured ($\bar{n}=29.88 \text{ rpm}$). The drive system encoder (power take off) provides a rotational velocity $\bar{n}=30.17 \text{ rpm}$. This leads to an absolute difference to the reference of $-0.29^\circ/\text{s}$ (-0.96% relative). Centrifugal acceleration (a_x)

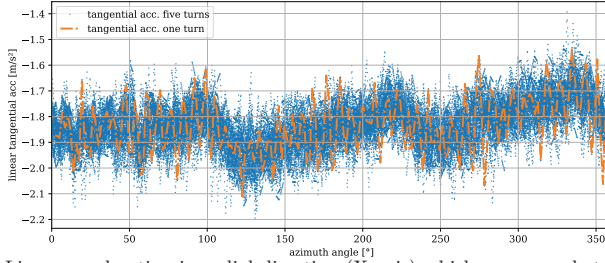


Fig. 5. Linear acceleration in radial direction (X -axis) which corresponds to the centrifugal load. The acceleration shows repeatable pattern of the three blades.

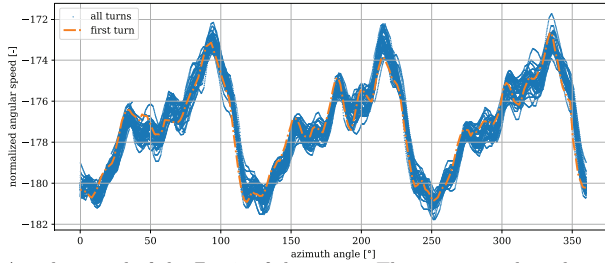


Fig. 6. Angular speed of the Z -axis of the sensor. The gyroscope data shows the rotational speed of the rotor which median is $-179.30^\circ/\text{s}$ which is equivalent to 29.88 rpm.

can be calculated for the distance of the sensor to the rotation axis $R=0.19$ m. The reference value is $a_X=1.90$ m/s^2 . Measured median is 1.833 m/s^2 (absolute difference 0.067 $\text{m}/\text{s}^2 = 6.4\%$). Finally a_Z has a reference of 9.81 m/s^2 . The measured median is of 9.623 m/s^2 (absolute difference -0.187 m/s^2 , -1.91%).

Fig. 5 shows the centrifugal acceleration (X -axis). A repeatable pattern is visible for each 120° . It includes not only the tumbling from misalignment but also blade bending due to hydrodynamic loads. However it should be noted that only one blade is shown. Measured data shows that alternating loads from the two other blades impact also the one with embedded sensors. The difference in the magnitudes of the three load alternation phases reflects this effect.

Angular velocity from the gyroscope is shown in fig. 6. This velocity is equivalent to $n=29.88$ rpm or $\omega_{b,Z}=179.3^\circ/\text{s}$ (see difference from expected value above). The pattern of the three blades becomes visible again while the rotational speed at the shaft (ω_r) remains almost at constant speed. This means that the torque ripple translates into a torsion of the runner which quantifies in the variation of the angular blade speed in Z . Pressure curves (fig. 7) show a significant decrease on the suction side for the first 55° and subsequent stalling of the profile with chaotic variations per turn. The curve stabilizes at 100° and forms a plateau for 150° . It finally increases from 250° to the maximum amplitude at 0° (pressure side). The slope is very useful for validation of 2D CFD simulations of such turbines as pressure is largely uninfluenced by 3D effects.

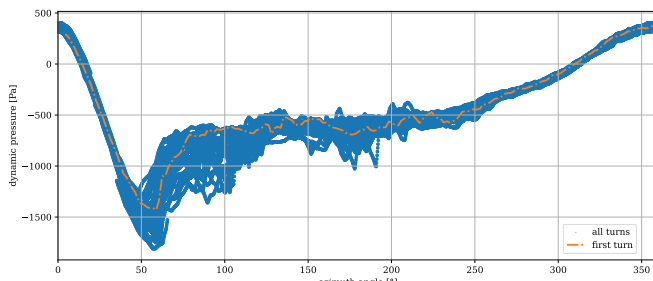


Fig. 7. Pressure over the azimuth angle for one turn (orange) and 34 turns (blue).

4 Conclusions & outlook

An embedded microsensor to capture the hydraulic loading and blade kinematics is placed in a flume scaled model of a CFFT. It measures pressure, accelerations and angular velocities in space.

A case adapted sensor calibration method is proposed and validated on a show-case dataset. Results show that the sensors provide insights in turbine deformation (torsion, bending) and show well-known load ripple from alternating loads. Pressure curves are of great interest for a better understanding of the FSI. Future work will investigate the data in more depth by using spectral and time-series analysis and by investigation of FSI effects on blade level for an entire characteristic curve. The spatial resolved free surface level in the rotor region will also be accounted when calculating dynamic pressure in future. This will lead to very important data for validation of 2D simulations for such turbine types. Pressure data combined with accelerations and angular velocities provide a rich database for the FSI characterization of such machines.

References

1. B. Barnier et al. Modelling the impact of flow-driven turbine power plants on great wind-driven ocean currents and the assessment of their energy potential. *Nat. Energy*, 5:240–249, 2020. doi:10.1038/s41560-020-0580-2.
2. T. Bennecke et al. A methodology to capture the single blade loads on a cross-flow tidal turbine flume model. In *Proceedings of 15th EWTEC, Bilbao, 2023*. doi:10.36688/ewtec-2023-501.
3. T. Bennecke et al. A weak coupled model for the fluid-structure interactions on cross-flow tidal turbine model. In *8th ECCOMAS Congress, Oslo, Norway, 2022*.
4. A.B. Bugnot et al. Current and projected global extent of marine built structures. *Nat. Sust.*, 2020. doi:10.1038/s41893-020-00595-1.
5. J.O. Dabiri. Potential order-of-magnitude enhancement of wind farm power density via counter-rotating vertical-axis wind turbine arrays. *J. Renew. & Sust. Energy*, 3(4), 2011. doi:10.1063/1.3608170.
6. P.-L. Delafin et al. Performance improvement of a darrieus tidal turbine with active variable pitch. *Energies*, 14(3):667, jan 2021. doi:10.3390/en14030667.
7. F. Ferraris et al. Procedure for effortless in-field calibration of three-axis rate gyros and accelerometers. *Sensors and Materials*, 7:311–330, 01 1995.
8. S. Hoerner et al. Passive flow control mechanisms (...) in cross-flow tidal turbines. *Exp. Fluids*, 62(104):1–14, 2021. doi:10.1007/s00348-021-03186-8.

9. T. Maître et al. Modelling (..) a Darrieus water turbine: Wall grid refinement (...) and comparison with experiments. *Ren. Energy*, 51:497–512, 2013. doi:10.1016/j.renene.2012.09.030.
10. I. Paraschivoiu. *Wind Turbine Design: With Emphasis on Darrieus Concept*. Presses Internationales Polytechnique, 2 edition, 2002.
11. P. Pelz. Upper limit for hydropower in an open-channel flow. *Journal of Hydraulic Engineering*, 137, 2011. doi:10.1061/(ASCE)HY.1943-7900.0000393.
12. K. Ruiz-Hussmann et al. A numerical fatigue failure assessment model to optimise cross-flow tidal turbines. *Ocean Engineering*, (under review).
13. S. Hoerner et al. Experimental optimization environment for developing an intra-cycle pitch control in cross flow turbines. *Int. Mar. Energy J.*, (accepted).
14. M. Shiono et al. An experimental study of the characteristics of a Darrieus turbine for tidal power generation. *Electr. Eng. Jpn.*, 132(3):38–47, 8 2000. doi:10.1002/1520-6416(200008)132:3<38::AID-EEJ6>3.0.CO;2-E.
15. Taltech. *MicroTag User Guide*, 2025. URL: <https://biorobotics.pages.taltech.ee/microtag/en/>.

Curriculum Vitae

Name	Wolf Iring Kösters
Date and place of birth	9. July 1993 Bonn, Germany
Nationality	German
Email	wolf.kosters@taltech.ee
ORCID	0000-0003-3538-7316
Etis	https://www.etis.ee/CV/Wolf_Iring_K%C3%B6sters/eng/

Education

2022-...	Tallinn University of Technology, School of Information Technologies, Computer and Systems Engineering, PhD studies
2022-2025	Otto von Guericke University, Institute of Fluid Dynamics and Thermodynamics, Fluid Dynamics and Technical Flows, PhD studies
2020-2021	Otto von Guericke University Magdeburg, Faculty of Process and Systems Engineering, Environmental and Process Engineering, MSc
2013-2020	Otto von Guericke University Magdeburg, Faculty of Process and Systems Engineering, Environmental and Process Engineering, BSc

Language competence

German	native
English	fluent
French	basic

Elulookirjeldus

Isikuandmed

Nimi	Wolf Iring Kösters
Sünniaeg ja -koht	9. Juuli 1993, Bonn, Saksamaa
Kodakondsus	Saksamaa
Email	wolf.kosters@taltech.ee
ORCID	0000-0003-3538-7316
Etis	https://www.etis.ee/CV/Wolf_Iring_K%C3%B6sters/est/

Haridus

2022-...	Tallinna Tehnikaülikool, Infotehnoloogia teaduskond, Arvuti- ja süsteemitehnika, doktoriõpe
2022-2025	Otto von Guericke Ülikool, Vedelikudünaamika ja Termodünaamika Instituut, Vedelikudünaamika ja tehnilised vood, doktoriõpe
2020-2021	Otto von Guericke Ülikool Magdeburg, Protsessi- ja süsteemitehnika teaduskond, Keskkonna- ja protsessitehnika, magistriõpe
2013-2020	Otto von Guericke Ülikool Magdeburg, Protsessi- ja süsteemitehnika teaduskond, Keskkonna- ja protsessitehnika, bakalaureuseõpe

Keelteoskus

Saksa	emakeel
Inglise	vilunud
Prantsuse	algteadmised

ISSN 2585-6901 (PDF)
ISBN 978-9916-80-502-2 (PDF)